AD-A072 011 SHEFFIELD UNIV (ENGLAND) POSTGRADUATE SCHOOL OF MINING F/G 20/11
PHOTOELASTIC INSTRUMENTATION. PRINCIPLES AND TECHNIQUES.(U)
MAY 79 A ROBERTS, I HAWKES DAJA37-70-C-0222
UNCLASSIFIED CRREL-SR-79-13 NL

1 OF 2
AD
A072 011

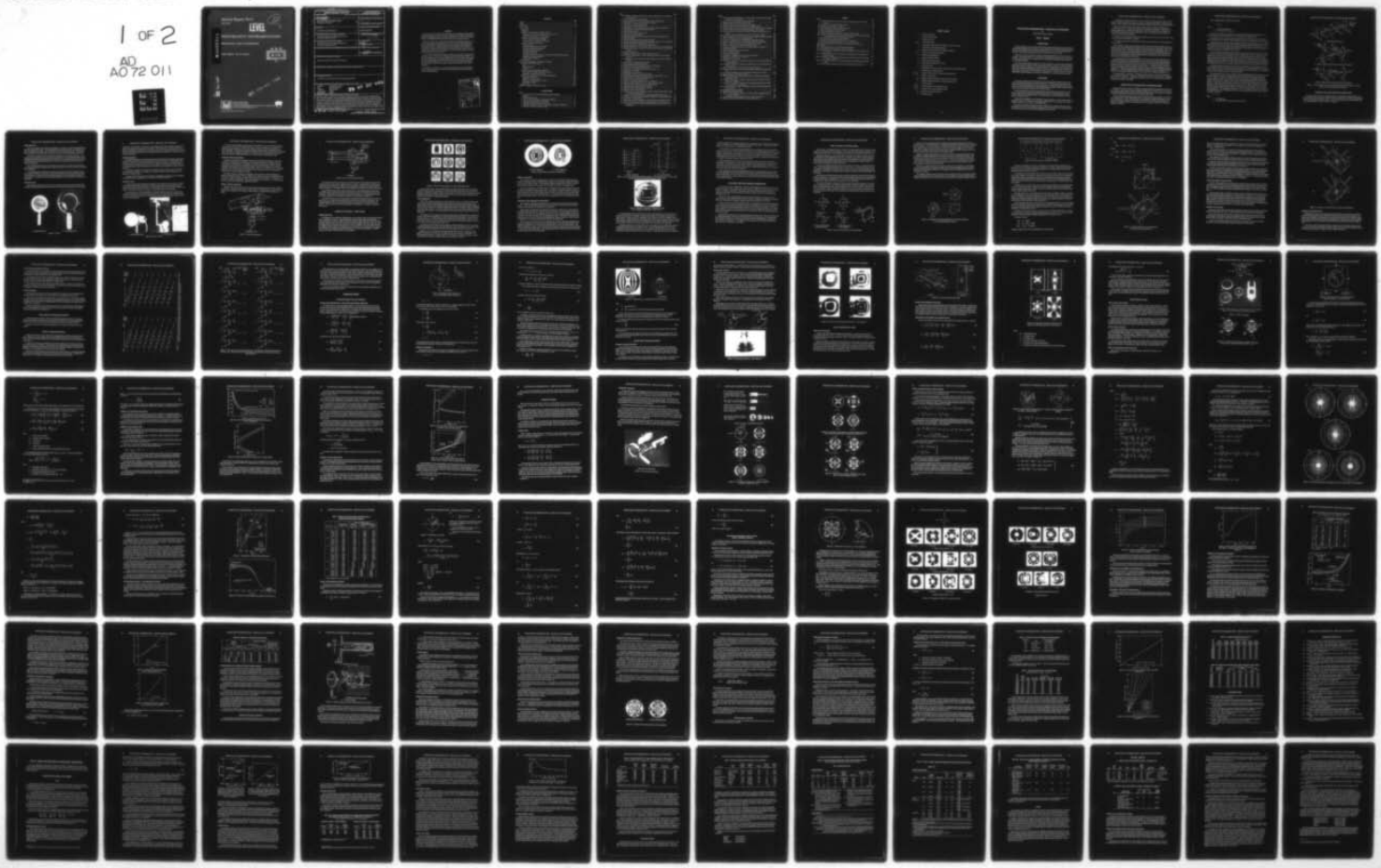

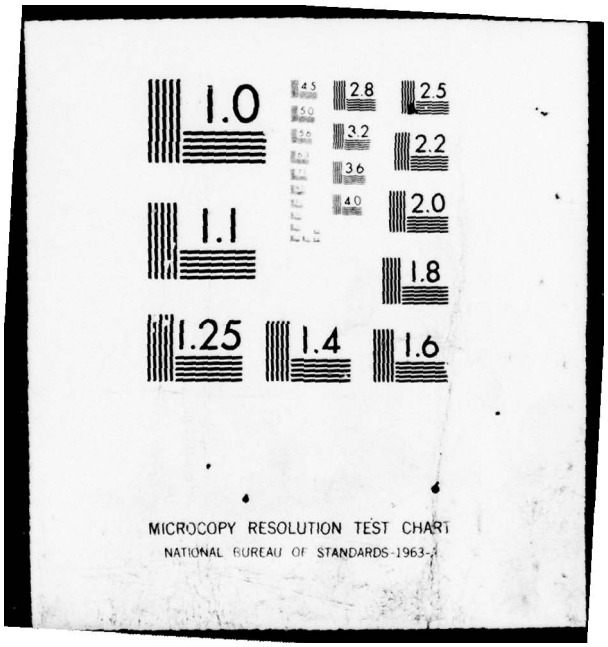
1.0
1.1
1.25
1.4
1.6
1.8
2.0
2.2
2.5
2.8
3.2
3.6
4.0
4.5
5.0
5.6
6.3
7.1
8.0
9.0
10.0
MICROCOPY RESOLUTION TEST CHART
NATIONAL BUREAU OF STANDARDS-1963-A

Special Report 79-13

May 1979

LEVEL

12

PHOTOELASTIC INSTRUMENTATION

PRINCIPLES AND TECHNIQUES

Albert Roberts and Ivor Hawkes

UNITED STATES ARMY
CORPS OF ENGINEERS
COLD REGIONS RESEARCH AND ENGINEERING LABORATORY
HANOVER, NEW HAMPSHIRE, U.S.A.

CRREL

Unclassified

SECURITY CLASSIFICATION OF THIS PAGE (When Data Entered)

REPORT DOCUMENTATION PAGE		READ INSTRUCTIONS BEFORE COMPLETING FORM
1. REPORT NUMBER Special Report 79-13	2. GOVT ACCESSION NO.	3. RECIPIENT'S CATALOG NUMBER SR-79-13
4. TITLE (and Subtitle) PHOTOELASTIC INSTRUMENTATION Principles and Techniques,		5. TYPE OF REPORT & PERIOD COVERED CRREL 6. PERFORMING ORG. REPORT NUMBER
7. AUTHOR(s) Albert Roberts and Ivor Hawkes		8. CONTRACT OR GRANT NUMBER(s) DAJA37-70-C-0222
9. PERFORMING ORGANIZATION NAME AND ADDRESS Cold Regions Research and Engineering Laboratory Hanover, New Hampshire 03755		10. PROGRAM ELEMENT, PROJECT, TASK AREA & WORK UNIT NUMBERS 161p.
11. CONTROLLING OFFICE NAME AND ADDRESS Cold Regions Research and Engineering Laboratory Hanover, New Hampshire 03755		12. REPORT DATE May 1979 13. NUMBER OF PAGES 160
14. MONITORING AGENCY NAME & ADDRESS (if different from Controlling Office)		15. SECURITY CLASS. (of this report) Unclassified 15a. DECLASSIFICATION/DOWNGRADING SCHEDULE

16. DISTRIBUTION STATEMENT (of this Report)

Approved for public release; distribution unlimited.

17. DISTRIBUTION STATEMENT (of the abstract entered in Block 20, if different from Report)

18. SUPPLEMENTARY NOTES

Dr. Roberts' work funded by U.S.Army European Research Office.

19. KEY WORDS (Continue on reverse side if necessary and identify by block number)

Detection	Measuring instruments
Gages	Mines (excavations)
Load cells	Photoelasticity
Loads (forces)	Stresses
Measurement	Theory

79 07 30 099

20. ABSTRACT (Continue on reverse side if necessary and identify by block number)

This report contains a detailed review of the theory and design of photoelastic transducers for measuring loads, strains, stresses and pressures. The measurement of engineering parameters under the adverse conditions normally encountered in the mining and civil engineering industries presents great problems, particularly where such measurements are to be made over long periods of time. Photoelastic transducers have distinct advantages over competing equipment in this respect in that the parameters to be measured are revealed as light interference fringes and the measuring gage itself often need consist of nothing more than simple steel and glass components. Examples of such gages are given in the report. The majority of the work reported here was carried out by the staff and students of the Postgraduate School of Mining, Sheffield University.

DD FORM 1 JAN 73 1473 EDITION OF 1 NOV 65 IS OBSOLETE

Unclassified 411 311

SECURITY CLASSIFICATION OF THIS PAGE (When Data Entered)

PREFACE

This report was prepared by Dr. Albert Roberts, Director, Postgraduate School of Mining, Sheffield University (now retired), and Dr. Ivor Hawkes, Expert, U.S.Army Cold Regions Research and Engineering Laboratory, President, Irad Gage Inc. Dr. Roberts' work was done under Contract DAJA37-70-C-0222 with the U.S.Army European Research Office.

The report is an attempt to summarize the basic theory of photoelastic transducers and present a few examples of their application in the fields of civil and mining engineering. The work described was conducted by members of the staff and post-graduate students of the Postgraduate School of Mining, Sheffield University, England, but the translation of the work into a practical system of instrumentation and measurement would not have been possible without the active interest and support of various consulting engineers, contractors, and industrial and government concerns.

In this connection the Postgraduate School of Mining was particularly indebted to Messrs. Horstman Ltd., the U.S.Army Corps of Engineers European Research Office, CRREL, the National Coal Board, the North of Scotland HydroElectric Authority, Messrs. Ove Arup and Partners, Sir William Halcrow and Partners, Messrs. Mott, Hay and Anderson, Nuttalls Ltd., and Stress Engineering Services Ltd. To all of these, and to many others associated with this work in one or other of its many aspects, the thanks and appreciation of the authors is expressed.

The contents of this report are not to be used for advertising or promotional purposes. Citation of brand names does not constitute an official endorsement or approval of the use of such commercial products.

CONTENTS

ILLUSTRATIONS

TABLES

NOMENCLATURE

δ	=	Relative retardation
C	=	Stress optic coefficient
t	=	Thickness of gage
σ_1, σ_2	=	Principal stresses
n	=	Isochromatic fringe order (white light) at a point in the gage
λ	=	Wavelength of light producing fringes
ϕ	=	Angular relative retardation in birefringent material
σ_x, σ_y	=	Stresses in rectangular coordinates
P	=	Diametrically applied force
a	=	Radius of gage or borehole
r	=	Radius of any point in gage
K	=	Strain/optical coefficient of the disk
η	=	Stress ratio (q/p)
f	=	Photoelastic unit material fringe value of gage (psi inch/fringe order)
S	=	Inclusion meter sensitivity factor
$\sigma_r, \sigma_\theta, \tau_{r\theta}$	=	Normal and shear stresses in gage (polar coordinates)
b	=	Radius of central hole
p, q	=	Greatest and least principal stresses in the host material
θ	=	Angular displacement relative to principal stress axis
ϵ_1, ϵ_2	=	Principal strains
E_h, E_g	=	Young's moduli of host material and gage
ν_h, ν_g	=	Poisson's ratio of host material and gage
L	=	Strain ratio in the host material
D	=	Diameter of gage

PHOTOELASTIC INSTRUMENTATION: PRINCIPLES AND TECHNIQUES

by

Albert Roberts and Ivor Hawkes

PART I: THEORY

INTRODUCTION

The determination of stress, strain and load in the strata surrounding earth excavations, and in underground support systems, presents special problems due to the need for long-term measurements in an environment that is particularly arduous and severe. In this environment delicate electronic and mechanical measurement systems are costly and prone to failure.

Within recent years measurement techniques employing photoelastic transducers have been devised to meet these problems. The photoelastic instrumentation system has also proved to be of value in observing stress, strain and load in civil engineering structures during construction and subsequent operation.

The system employs optical transducers in which the readout is in terms of the birefringence produced in cylinders or disks of glass, or sometimes of plastic, under load. The use of a glass disk loaded across its diameter is a well-known technique in photoelasticity for determining the stress-optic coefficient of birefringent materials. But its successful application as a load transducer, used in conjunction with an observation system devised by research workers at the former Postgraduate School of Mining at the University of Sheffield, is a relatively recent innovation.

BACKGROUND

That certain crystals, notably Iceland spar, possess the property of double refraction was well known before the beginning of the 19th century, and in 1816 Brewster[3] enunciated the principles of photoelasticity and was the first to use glass as a stress-birefringent material. Since that date numerous investigators have studied photoelastic techniques, which have today reached a high state of development for general use in stress analysis.

These developments have been mainly concerned with photoelastic model studies, at first with a two-dimensional technique using relatively thin sheets of stress-birefringent materials (usually plastics but occasionally glass), and subsequently by the three-dimensional "frozen stress" technique (Frocht[11]).

A more recent development is the photoelastic coating technique, in which surface strains are observed by means of a birefringent coating bonded continuously over the surface of the actual component under stress, and not on a birefringent model.

The idea of using glass components inserted or attached to a structure under load, so that birefringent effects in the glass could be observed and used, has occurred and reoccurred periodically throughout the years since Brewster published his original work.

In 1930 Mabboux published details of a system to observe strains through the medium of birefringent elements attached to the surface of concrete, masonry and other forms of structural components. Patents relating to this system were granted in Paris in 1931 and in the U.S.A. in 1935.[19] [20]

Maris devised a photoelastic blast pressure gage in 1944, and this was patented in the United States in 1947.[21] It used a glass element as a photoelastic transducer. Transient birefringence produced in the transducer by blast pressure waves was observed by the medium of reflected polarized light directed onto a photoelectric cell. The resulting electrical signal was observed by cathode-ray oscillograph.

In Europe in 1948 Coutinho carried out investigations into stress in concrete structures. Glass inserts were used as photoelastic inclusions.[7]

In Germany, Jobst outlined a photoelastic transducer system in 1949, and a German patent was issued in 1951.[18]

There is little evidence that these systems received more than sporadic attention, and none appears to have been systematically developed toward practical ends. Most of these devices used *reflected* polarized light, whereas the general and classical approach to photoelastic stress analysis was based on the use of *transmitted* polarized light on the laboratory photoelastic bench. It was not until the photoelastic coating technique became a practicable system of strain measurement that reflection polarimetry received serious attention and photoelastic stress analysis was taken out of the laboratory and into the field.

In 1957 Hiramatsu, Niwa and Oka published the first of a series of papers describing new equipment and techniques for measuring stresses in concrete structures using glass inclusions.[16] And in 1961 Zandman patented a photoelastic transducer system employing birefringent plastic elements attached to the surfaces of structural components.[30] Concurrently, Emery and Hawkes devised a photoelastic plastic transducer system for use on a rock bolt dynamometer and an extensometer.[10] Chakravarty[5] extended these transducer systems and also investigated the potential application of a cylindrical glass transducer designed by Roberts, Hawkes and Williams.[27] This device is a biaxial gage, following Hiramatsu, but is observed by transmitted polarized light.

This photoelastic "stressmeter" was studied in detail by Dhir,[8] and the associated polariscope systems by Williams.[29] A number of subsequent investigators at the University of Sheffield pursued various aspects of the photoelastic transducer system. The results of all these investigations form the basis of this report.

PRINCIPLES OF THE PHOTOELASTIC TRANSDUCER SYSTEM

Photoelastic stress analysis is essentially a technique whereby the differences in the principal stresses at various points within a transparent material can be studied in terms of the isochromatic fringes produced when the body is viewed under polarized light. The theory of the technique is well established (Frocht[11]) and will only be briefly reviewed here.

When a beam of polarized light passes through a stressed birefringent material it is split into two component beams. These emerge polarized in the planes of the principal stresses in the material and retarded in relation to one another by a phase difference which is proportional to the difference in magnitude between the principal stresses $(\sigma_1-\sigma_2)$ and the length of the light path through the material, t.

This relationship may be expressed in the form

$$\delta = Ct_2 \tau_{max} \tag{1}$$

where:

δ = the relative retardation
C = the stress optic coefficient.

The relative retardation is measured in terms of fringes (isochromatics) produced by interference between the two beams when they are resolved into one specific plane.

The polarizing of the incident beam and the resolution of the emergent beam are carried out using two filters, both of which are linear polarizers, referred to as the polarizer and the analyzer.

At points where one of the directions of principal stress in the birefringent material coincides with the axis of polarization, light passes through the material without being affected. If the axis of the analyzer is set at right angles to that of the polarizer then light of all wavelengths is extinguished and all such areas appear black (isoclinics). This enables the directions of principal stress to be identified at any point in the material.

The directions of principal stress are required for the measurement of fractional fringe orders at any point. But if these are already known, as for example when a disk is compressed across a diameter, the isoclinics are not required and they are therefore removed from the field of view. This is achieved by incorporating "quarter-wave" plates in both the polarizer and the analyzer, which has the effect of producing circularly polarized light. A quarter-wave plate is a permanently birefringent filter, with "slow" and "fast" axes at right angles to each other to produce a relative retardation between the two emergent beams equal to one quarter of some specific wavelength.

In circularly polarized light the light waves may be considered as being propagated through the birefringent material in the form of a helix, in which there is no specific linear plane of polarization. There is therefore no specific direction at which the axis of polarization is coincident with a direction of principal stress and of course no isoclinics.

The arrangements that have been standardized in the Sheffield photoelastic transducer system for illuminating and viewing the isochromatics in diametrically loaded disks are illustrated in Figure 1. Figure 1a shows the standard filter orientations relative to the loading direction for transmitted-light viewing. Figures 1b and 1c show the standard orientations for reflected-light viewing. In the latter two cases the disk is given a coating either of reflective cement or a mirror backing. It should be noted from Figure 1 that in each case the relative orientation of the linear analyzer with its adjacent quarter-wave plate remains the same. Thus, by producing an incident beam of the correct rotation, only one analyzer is required for viewing beams in both transmitted and reflected light. The arrangements shown give a "dark" field with zero stress in the disk, and the relationship between the isochromatics visible in the disk under load and the induced relative retardation is given by

$$\delta = n\lambda . \tag{2}$$

where:

n = the fringe order
λ = the wavelength of the light producing the fringes.

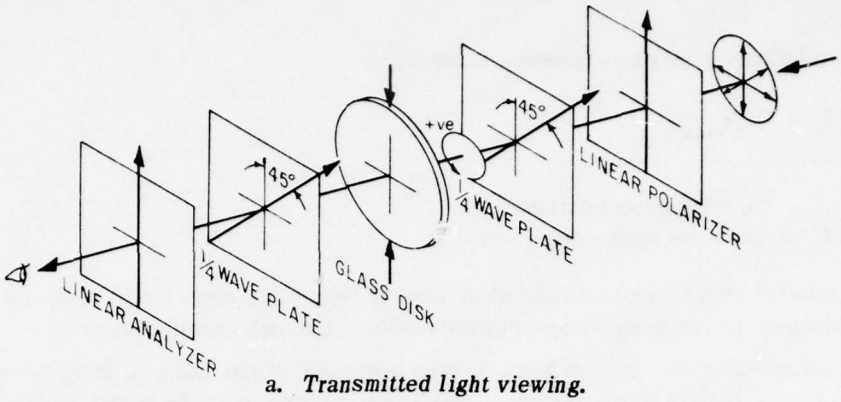

a. Transmitted light viewing.

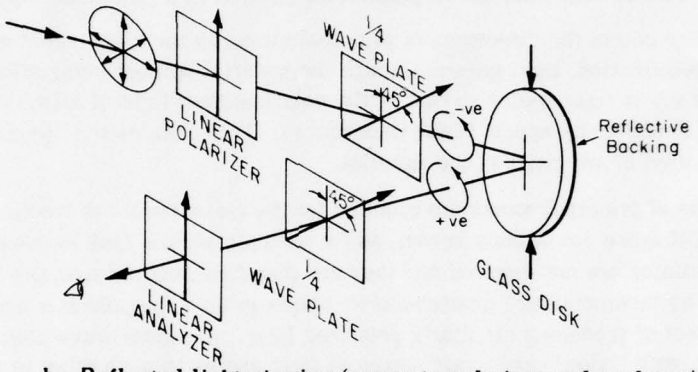

b. Reflected light viewing (separate polarizer and analyzer).

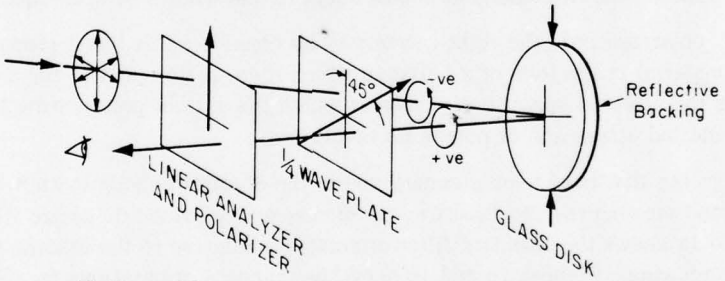

c. Reflected light viewing (combined polarizer and analyzer).

Figure 1. Viewing systems for use with photoelastic glass disk transducers. (Arrows indicate optical transmission axes of filters.)

Polariscopes used with the Photoelastic Transducer System

The instruments and viewing techniques used in the photoelastic transducer system have been designed to make operation as simple as possible, consistent with achieving precision adequate for the engineering problem in hand. A variety of polariscopes have been designed, each type being applicable to a particular form of transducer.

Simple hand-viewer

This is the simplest form of reflection polariscope. It consists of a sheet of plane-polarizing filter and a quarter-wave plate. These are aligned with the polarization axis of the quarter-wave plate at 45 degrees to the right (i.e. clockwise) of the axis of the plane polarizer. This arrangement is protected by thin sheet glass and is held in a frame with a handle attached (Figure 2a).

The viewer is intended for use with reflection transducers of the uniaxial disk type. If it is held against the transducer with the quarter-wave plate between the plane polarizing filter and the birefringent transducer the light incident on the transducer is circularly polarized and the observer sees the reflected circularly polarized beam. The same filter arrangement thus serves both as polarizer and analyzer.

The isochromatic pattern is read to the nearest unit fringe order, sometimes with estimation to the nearest half-fringe, the handle of the viewer being held in line with the direction of constraint on the transducer.

It is sometimes best to eliminate the isochromatic colors when making a simple line count. This is done by introducing a red filter, so that the isochromatics are seen as black lines against a red background. In some instruments the simple polariscope is fixed permanently in place on the transducer. The signal is then automatically displayed for observation when the transducer is illuminated.

Stressmeter viewer

The stressmeter viewer (Fig. 2b) is used with transducers operating under transmitted polarized light, with separate polarizer and analyzer, one on either side of the transducer. The viewer

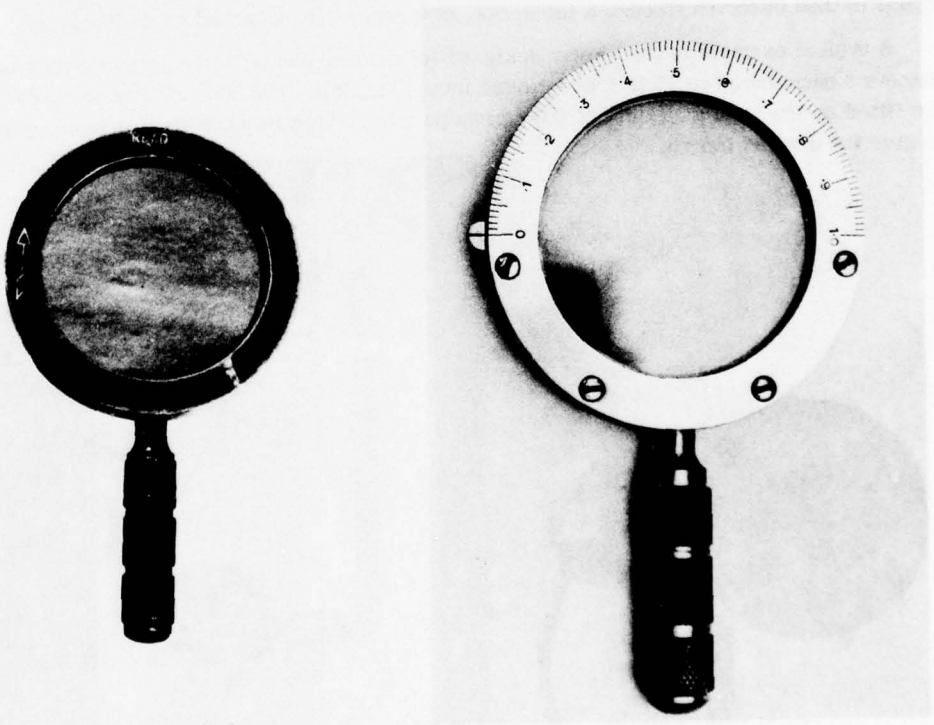

a. Simple hand-viewer. *b. Stressmeter viewer.*

Figure 2. Viewers.

serves only as the analyzer. It consists of a plane polarizing filter and a quarter-wave plate, with provision for rotating the filter relative to the plate. This rotation moves a scale on which 180 degrees is graduated into 100 units. The index of the scale is in line with the handle of the viewer and is held in register with the direction of constraint of uniaxial transducers, or with the zero axis of biaxial transducers.

Precision hand-viewer

The precision hand-viewer is designed for precision measurements with reflective transducers. The polarizer and analyzer are mounted separately, one on each side of the central handle. The polarizer consists of a combined linear polarizer and quarter-wave plate. It is mounted rigidly on the handle to the observer's right and has a cup into which an electric lamp can be inserted. In mining applications the light may conveniently be provided by the headpiece of a miner's cap lamp (Fig. 2c).

The polarizer, together with the light cup, is hinged so that the beam of light can be easily directed onto the transducer. The transducer is observed through the analyzer mounted on the handle to the observer's left.

The analyzer, with fixed quarter-wave plate and rotatable plane polarizing filter, is graduated for goniometric (Tardy) compensation, 0 to 100% over a 180-degree half-circle.

Periscope viewers.

In certain applications of photoelastic transducers the transducer may be fitted in a location that is either not accessible or too remote for direct viewing. Some of these installations may require the polarizer and the light source to be mounted integrally with the transducer fitment. The signal is then observed through a telescope, or a periscope, attached to the analyzer.

A typical example is the viewer designed for reading photoelastic gages on rock bolt dynamometers mounted up to 15 ft above ground level (Fig. 2d). The light source and polarizing filter are fitted on the head assembly of the periscope tube, which is made in sections coupled together to give the desired length.

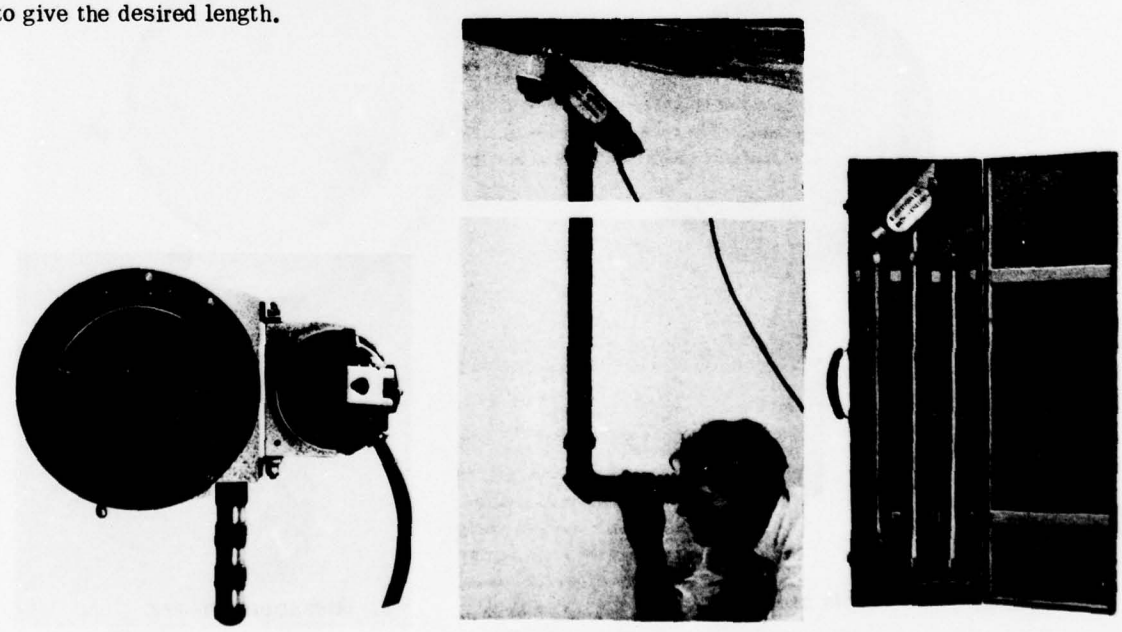

c. Precision hand-viewer. *d. Periscope viewer.*

Figure 2 (Cont'd). Viewers.

The head of the periscope is placed against the dynamometer, and circularly polarized light, incident upon the gage, is reflected back and down the tube to the analyzer and eyepiece unit, where the signal is observed. A prism in the eyepiece brings the image of the signal out at a convenient angle. The eyepiece also contains a quarter-wave plate and a rotatable plane polarizing filter. The rotation is graduated to measure to 1.0% fringe order. A fixed-focus lens system in the instrument gives suitable magnification, and a light filter gives monochromatic light.

Hiramatsu's reflection polariscope

Hiramatsu's polariscope, designed for use with his glass-insert stressmeters, is illustrated in Figure 3a. White light from a miniature electric lamp is converged by a condenser lens and converted into a polarized beam by a polarizer. The polarized light passes through a Babbinet compensator and is reflected by a half mirror placed at an angle of 45 degrees to the light path. The light is then projected into the photoelastic gage, which is of the reflective type. After being reflected by the silvered end-plate of the gage the light reenters the viewer, passes through an analyzer and is observed through an eyepiece.

The field of vision in Hiramatsu's stressmeter viewer consists of colored parallel lines arranged symmetrically on both sides of a straight line. Turning the dial of the compensator shifts these lines. When the dark line is brought onto the crosslines in the eyepiece the retardation in the gage is completely compensated. The scale reading on the dial then gives the relative retardation, one scale unit corresponding to approximately 500 A°.

Williams' reflection polariscope

Williams constructed a reflective stress plug viewer fitted for goniometric (Tardy) compensation (Fig. 3b). The primary light source is either a miner's cap lamp fitted into a cup with an extension to fit the light tube of the viewer, or alternatively a 12-v lamp with collimating lens as shown.

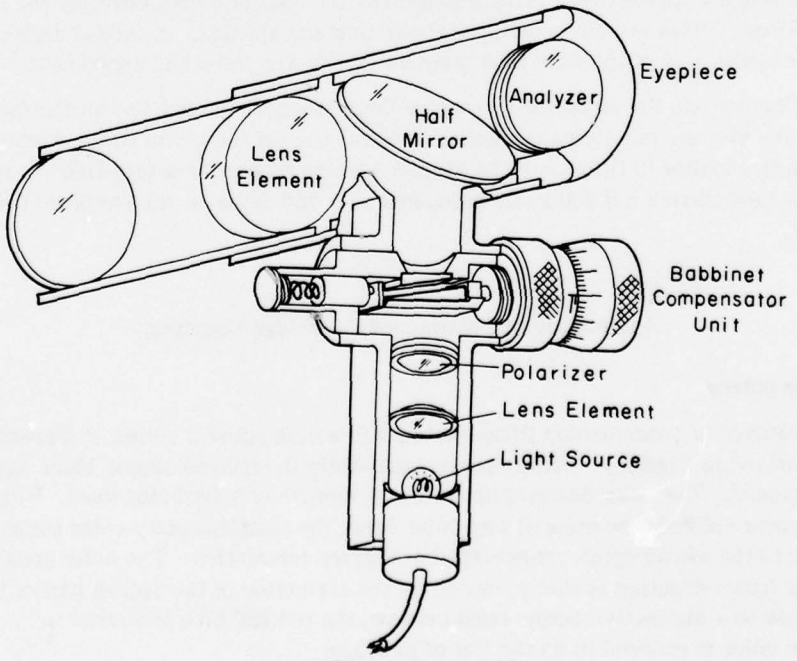

a. *Hiramatsu et al.*[16]

Figure 3. Reflection polariscopes.

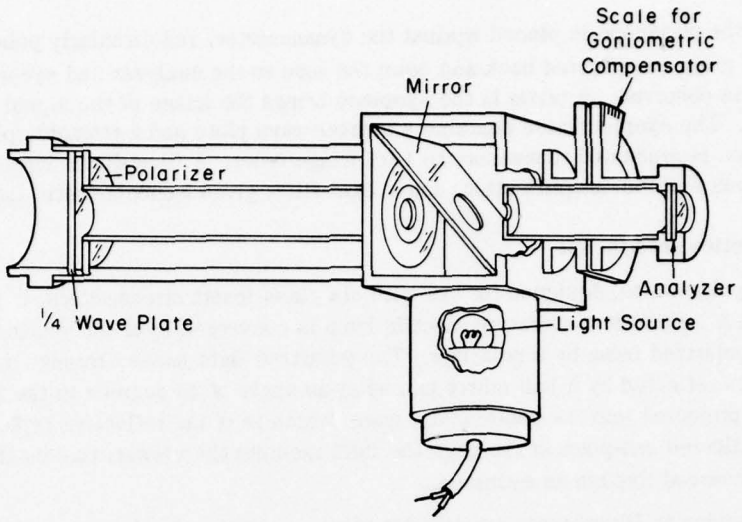

b. Williams.[29]

Figure 3 (Cont'd). Reflection polariscopes.

The instrument consists essentially of two concentric tubes (an outer light tube and an inner viewing tube) with a light source adaptor tube and an eyepiece. Light enters via the light source adaptor tube and is reflected by a stainless steel mirror down the annulus between the light tube and the viewing tube. An elliptical hole permits unobstructed vision down the central viewing tube.

Light reflected forward from the mirror is polarized by a plane polarizing filter annulus and then passes through a quarter-wave plate which takes the form of a disk covering the front of the instrument. These filters are protected by a glass disk and annulus. A second annulus of glass at the mirror-chamber end of the light tube protects the viewing tube and supports it.

Light reflected from the stress plug reenters the instrument through the quarter-wave plate and passes down the viewing tube, then through the central hole of the mirror to the eyepiece. An analyzing polarized filter is fitted into the eyepiece which rotates on a tube fixed to the mirror chamber. The tube carries a 0-100 scale graduated over 180 degrees, the eyepiece being fitted with an index.

Application of Polariscopes – Fringe Counting

Integral fringe orders

The appearance of isochromatic fringe patterns in a disk under a series of diametrically applied loads is illustrated in Figure 4. With monochromatic light the fringes appear black against a colored background. The color depends upon the wavelength of light being used. With white light the fringes appear colored, the color at any point being the complementary color minus those colors corresponding to the wavelengths extinguished at a given retardation. The color usually taken for the purpose of fringe counting is that produced by the extinction of the yellow part of the spectrum, and corresponds to a distinctive purple band between the red and blue isochromatics. In photoelasticity this color is referred to as the *tint of passage*.

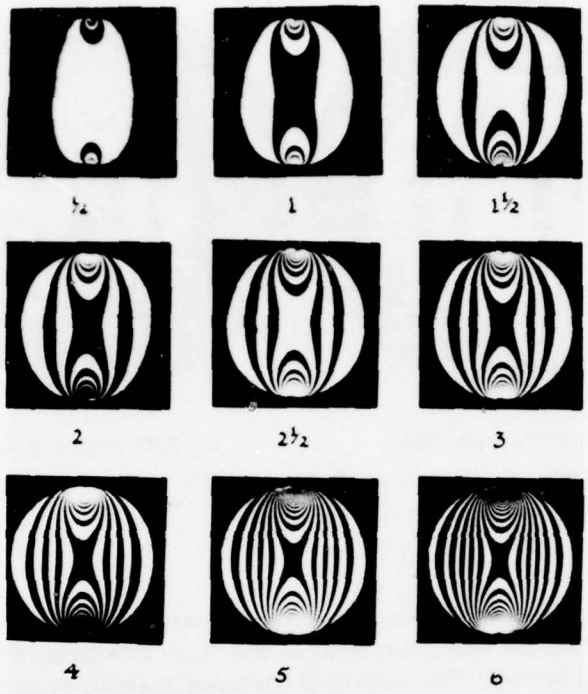

Figure 4. System of fringe counting for a diametrically loaded disk.

It is clear from Figure 4 that the fringe patterns are always symmetrical with isochromatics stacked on either side of the loading axis. The integral fringe order at the center of the disk is obtained by counting the number of fringes from one edge to the center along the transverse diameter. Fractional fringe orders are then measured by using either the Tardy system of goniometric compensation or the Babbinet compensation technique.

Tardy compensation

In the Tardy system the analyzer is rotated to optically retard or to advance the fringe order at the center of the disk, while keeping the two quarter-wave plates and the polarizer fixed in their positions relative to the direction of loading. With the filter orientations shown in Figure 1a and b the effect is to produce a complete wavelength retardation of the fringe order for 180 degrees of rotation of the analyzer. For the case shown in Figure 1c the same effect is produced by a 90-degree clockwise rotation of the combined polarizer and analyzer, again keeping the quarter-wave plate fixed.

The operation of this technique when using a separate polarizer and analyzer is illustrated in Figure 5 which shows fringe patterns in a disk before and after compensation. Figure 5a shows the fringe pattern as it normally appears with the analyzer aligned vertically in the direction of loading and the scale set at zero. Counting the fringes along the horizontal diameter, to one side of the center, gives an integral fringe count of 2.0.

To obtain the fractional fringe order the analyzer is rotated clockwise until the second fringe is optically retarded to the center of the disk (Fig. 5b). The scale reading of 0.70 is then added to the original integral fringe count, to give a total fringe order at the disk center of 2.7.

Hiltscher et al.[15] have found that by aligning fringes along the arms of a 60-degree cross marked at the center of the disk face, the fringe order can be measured to ±0.005 fringe. For practical purposes however, a reading accuracy of ±0.02 fringe is normally acceptable. This can be obtained by a relatively untrained observer with no marking on the disk.

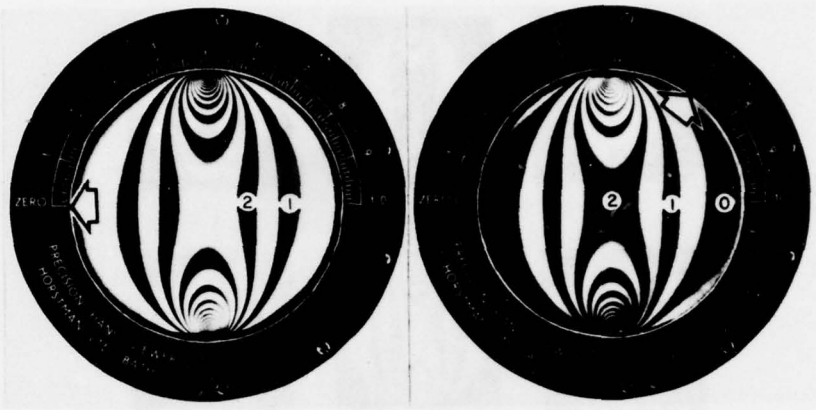

a. *Before compaction.* b. *After compaction.*

Figure 5. Tardy method of goniometric compensation.

Babbinet compensation

With the Babbinet method of compensation a variable amount of relative retardation can be added to or subtracted from the retardation being measured, by introducing a separate birefringent material into the optical system. This additional component normally takes the form of a pair of quartz wedges which can be moved relative to one another by means of a micrometer screw.

When the birefringence in the double wedge is of opposite sign and equal magnitude to that at the center of the disk, the region appears black. The number of revolutions required to obtain this dark field therefore gives a direct digital readout of fringe order without the need to count fringes. The technique is as accurate as the Tardy system. It is not widely used with photoelastic transducers in the Sheffield system. The Tardy system is preferred because of its simpler instrumentation.

Isochromatic fringe sharpening and multiplication

Two methods of modifying the fringe pattern in a birefringent material have been described by Post.[26] They are particularly applicable to disk transducers as they improve the accuracy of reading and also increase the sensitivity of the transducer.

Fringe may be both sharpened and multiplied by inserting a partial mirror on either side of a birefringent model positioned in a standard circular polariscope. In fringe sharpening the mirrors are parallel; their effect on light traversing the material is shown diagrammatically in Figure 6a. At each mirror surface some of the light is transmitted but most is reflected back through the birefringent material. (The rays have been drawn obliquely for clarity. In practice, normal incidence is employed; the rays are then parallel and emerge from the same point.)

The net result of this system is that the emergent rays combine to produce sharp peaks in the intensity/birefringence curve at integral and half-fringe orders. The entire fringe pattern is thus sharpened, which allows the center of any particular fringe to be more accurately located. This effect is illustrated in Figure 7 where a circular disk in diametral compression has been positioned in a dark field circular polariscope. Under monochromatic light the pattern consists of narrow light and dark fringes against a gray background.

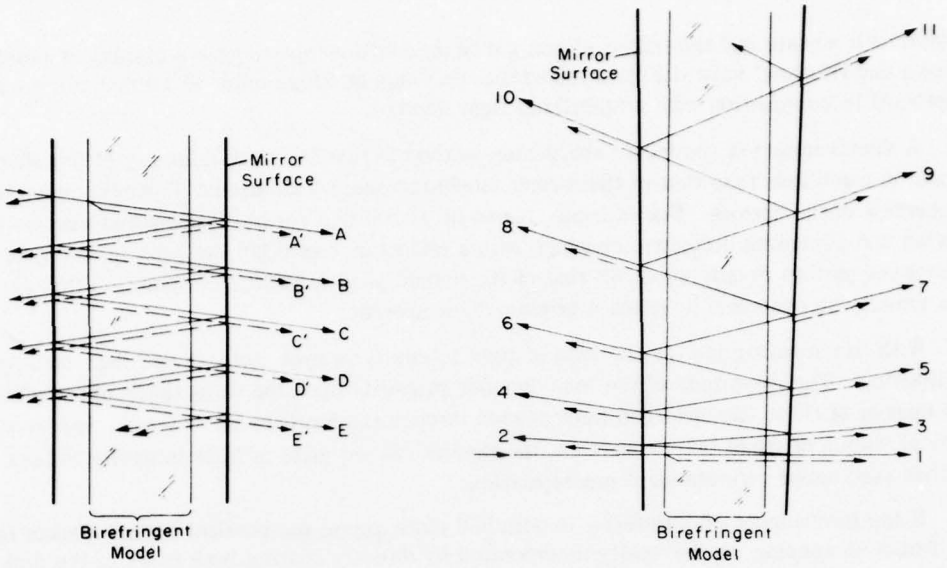

a. Fringe sharpening. *b. Fringe multiplication.*

Figure 6. *Light path through model and mirror system. (Full and dashed lines represent light polarized in mutually perpendicular planes.) (After Post[26].)*

Figure 7. *Sharpened isochromatic patterns for circular disk in diametral compression. (After Post[26].)*

The fringe multiplication technique differs from the above method in that the mirrors are inclined to each other at a small angle. The light path through the birefringent material and the mirror system is shown at a greatly exaggerated scale in Figure 6b. Each ray emerges from the mirror system in a different direction, according to the number of times it has traversed the material. The technique involves isolating that ray corresponding to the desired sensitivity, bearing in mind that the relative retardation is directly proportional to the total length of the light path.

It therefore follows that the fringe pattern in a disk transducer can be substantially altered by incorporating partial mirrors in the optical system. Fringe sharpening allows a more accurate assessment of the fractional fringe orders, and also presents the fringe pattern in a form more suitable for automatic recording, should this be desired. For example, the disk may be scanned by

a photocell mosaic and the output signal fed to an oscilloscope to give a display of isochromatics. Brown and Hickson[4] have obtained repeatable readings of fringe order to ±0.002 using a single photocell in conjunction with a stabilized light source.

A disadvantage of the fringe sharpening method is that the peak intensity of the sharpened fringe is much less than that of the normal isochromatics, by an amount depending upon the optical properties of the mirrors. For example, it can be shown that for high reflectance mirrors (typically having non-adsorbing dielectric coatings with a reflectance of 0.90) the peak intensity of the sharpened pattern is only about 5% that of the normal peak intensity. In practice this disadvantage can usually be overcome by using a brighter light source.

With fringe multiplication the loss of light intensity is even more severe than with fringe sharpening. The magnitude of the loss depends primarily upon the reflectance of the mirrors and the number of times the observed light passes through the birefringent material. However, for typical values of these two parameters, the theoretical estimate of light intensity is less than 1% of that associated with standard isochromatics.

If the birefringent disk material is polished plate glass, the parallel partial mirrors required for fringe sharpening can be easily incorporated by directly coating both faces of the disk. For fringe multiplication, on the other hand, one of the disk faces must be reground and polished before coating. Alternatively, a separate partial mirror is required to obtain the necessary nonparallelism of the reflecting surfaces.

ANALYSIS OF THE TARDY SYSTEM OF COMPENSATION

In the classical Tardy compensation method the crossed polarizer and analyzer plates are set parallel to the stress axes of the specimen, and a pair of "crossed" quarter-wave plates are interposed at 45 degrees to those axes. One quarter-wave plate is inserted between polarizer and specimen and the other between specimen and analyzer, forming a crossed circular polariscope arrangement (Fig. 1a).

The light is thus circularly polarized before entering the specimen and, provided that the relative position of the polarizer and its associated quarter-wave plate are maintained, no specific alignment would appear to be required between these filters and the rest of the system.

As long as the stress axes in the specimen (Fig. 1a) are horizontal and vertical, compensation to an integral fringe value can be achieved by rotating the analyzer until the point under observation is either black (monochromatic light) or exhibits a tint of passage (white light). The angle by which the analyzer has to be rotated to produce this effect is then equal to either half the angular phase difference produced in the specimen ($\phi/2$) or its complement ($180-\phi/2$), depending upon the direction of rotation.

For photoelastic specimens with a more complex stress system, with varying stress directions, the complete polariscope is normally rotated with respect to the specimen, so as to obtain alignment between the analyzer axis and one of the stress axes before compensation is attempted. It will be shown, however, that it is the alignment of the analyzer and its associated quarter-wave plate only which is important in this respect.

Effect of Variations in Polariscope Design

Commencing at the illumination source, the light is initially nonpolarized, vibration occurring randomly in directions normal to the light path. This light then passes through the polarizer, and plane polarized light with a vertical vibration plane then enters the quarter-wave plate (Fig. 1a).

Referring to Figure 8a, b let OS be the plane of vibration of the polarizer, and let OX, OY be the principal axes of the quarter-wave plate set at 45 degrees to that plane. Within the quarter-wave plate the initial vibration plane is resolved into two components, in the planes OX and OY. These vibrations are mutually at right angles and of equal amplitude, one being retarded by a phase angle of 45 degrees with respect to the other.

The axes of the quarter-wave plate may be set in either of two ways. In Figure 8a OX is the "fast" axis of the quarter-wave plate and OY the "slow" axis, i.e. the vibration on the OY axis is retarded by 45 degrees with respect to that on the OX axis. In this case the resulting circular polarization vector rotates in a counterclockwise (positive) direction, when observed towards the light source.

In Figure 8b the fast and slow axes of the quarter-wave plate are reversed and the rotation is clockwise (negative). In both cases therefore the phase difference between the rays emerging from the quarter-wave plate is 45 degrees, or $\pi/4$, except that in Figure 8a the OX vector leads OY by 45 degrees and in Figure 8b the OX vector lags OY by the same amount.

The circular polarization resulting from this arrangement of polarizer and quarter-wave plate can be resolved into two sets of vibrations mutually at right angles and oriented in any direction about a line perpendicular to the plane of Figures 8a and b, in which the slow ray lags the fast ray by 45 degrees. In effect, *no particular orientation of the polarizer and its associated quarter-wave plate is required with respect to the photoelastic specimen and the analyzer section of the polariscope.*

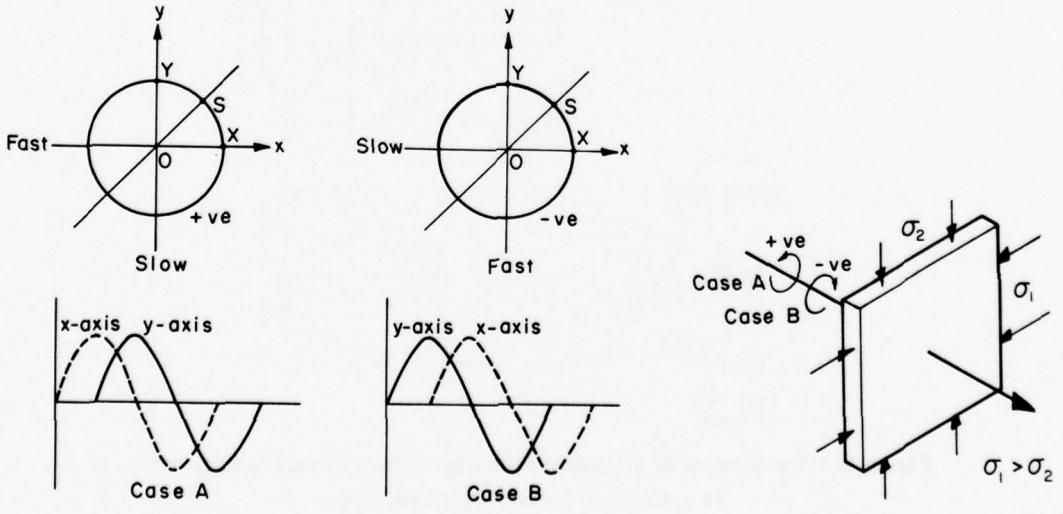

a. Vector rotation counter-clockwise (positive).

b. Vector rotation clock-wise (negative).

c.

Figure 8. The effect of variations in polarizer design.

However, correct orientation between the polarizer and its quarter-wave plate *is* essential. This conclusion is of vital importance in the use of many photoelastic measuring devices, especially when the polarizer, as part of the device, is embedded in the structure under examination and thus is in a position where it cannot be adjusted. In any case, where such gages are used, accurate alignment to an unknown stress direction cannot always be predicted before the gages are set, and the stress direction may change during the measurement period.

Suppose the polarized light impinges upon a loaded specimen of transparent material having the property of temporary birefringence, and having its stress axes vertical and horizontal. Consider the case in which the fast axis of the specimen is vertical and the rotation of the incident circularly polarized light is positive (Fig. 8c, Case A.) Let the circular polarization be resolved so that the fast or leading ray vibration coincides with the slow axis of the specimen, and the slow or lagging ray coincides with its fast axis.

The fast ray, initially leading the slow ray by a phase angle of 45 degrees, is now retarded by the stressed specimen by an amount ϕ (phase angle) which is dependent upon the specimen's thickness, the stress/optical properties of the specimen material, the applied stresses, and the wavelength of the light.

The emergent components are thus altered so that the lead of the fast ray is reduced to $(45^\circ\text{-}\phi)$. The light leaving the specimen therefore consists of two components of equal amplitude having an arbitrary phase difference, in which condition the general form of the vibration is elliptical (Fig. 9).

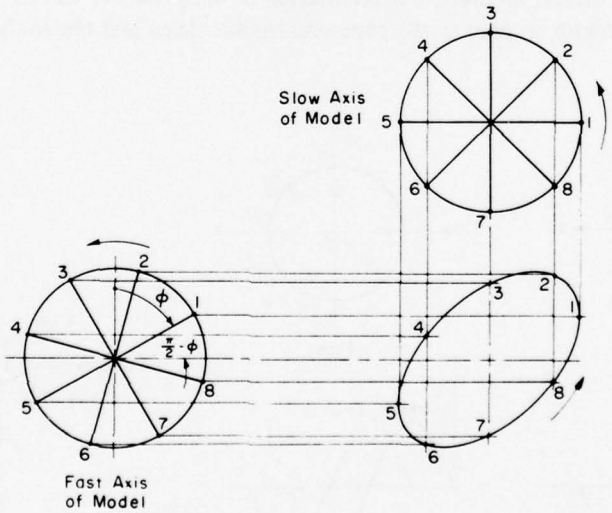

Figure 9. Development of elliptical polarization from circular polarization in a stressed photoelastic specimen.

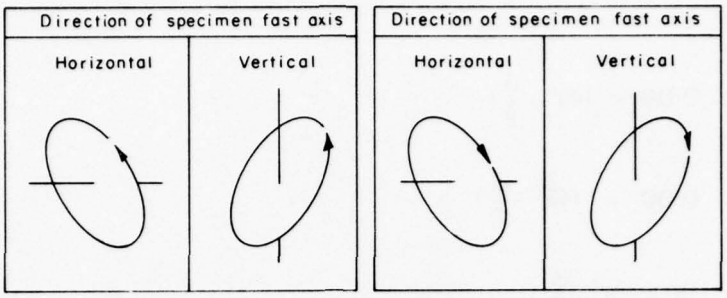

Figure 10. Vector orientation and rotation of ellipse.

The axes of this ellipse can only lie at 45 degrees to the stress axes in the specimen. At special values of ϕ the ellipse can become a straight line or a circle. The direction of rotation of the vector is the same as that of the circular generators in the example shown, but assumes an opposite direction for certain ranges of ϕ.

Consideration of the vector system with a polarizer setup as shown in Figure 8c and a similar stress system applied to the specimen, in both cases with the fast and slow axes of the specimen interchanged, gives the results shown in Figure 10, the retardation in the specimen being kept constant. The light emerging from the specimen passes on to the second quarter-wave plate, the axes of which are set at 45 degrees to the stress axes of the specimen, i.e. parallel with the axes of the ellipse.

Consider the case of Figure 10a showing a positive rotation polarizer and a specimen loaded so that the vertical axis is fast. Figure 11a shows the elliptical vibration and the generating circular vibrations superimposed. Figure 11b shows the relative positions of the vibration planes within the analyzer quarter-wave plate.

Referring to Figure 11b, on entering the quarter-wave plate the elliptical vibration is resolved into two components at right angles, OQ and OQ', in which OQ leads OQ' by a phase angle of 45 degrees. In traversing the plate arranged with its fast and slow axes as shown in the figure, the vector OQ is retarded with respect to OQ' by 45 degrees, i.e. on leaving the plate the vectors are in phase and the light emerges as a linear vibration OP'.

In order to produce extinction when viewing with monochromatic light, or to see a tint of passage when viewing with white light, the analyzer with its vibration plane initially on the line of OX must (using clockwise rotation) rotate through the angle BOA, so that its vibration axis lies perpendicular to the plane defined by OP'.

In Figure 11a the time for the vector to describe the arc KT of the ellipse KLK'L' will equal that for describing TL (K and L being symmetrically placed with respect to T). That is, arc XM equals MR. Thus angles MOX and MOR are equal and have the value ½ $(45^\circ - \phi)$.

In Figures 11a and b

$$OQ = OT = \sqrt{2}ON$$

$$OP' = OP = \sqrt{2}OX = \sqrt{2}OM$$

$$MNO = P'QO = 90 \text{ degrees}$$

therefore triangles QOP' (Fig. 11b) and NOM (Fig. 11a) are similar.

Thus

$$MON = P'OQ = (45° - \frac{\phi}{2})$$

Further,

$$Q'OA = P'OQ = (45° - \frac{\phi}{2})$$

and

$$BOA = 45° - (45° - \frac{\phi}{2})$$
$$= \phi/2 .$$

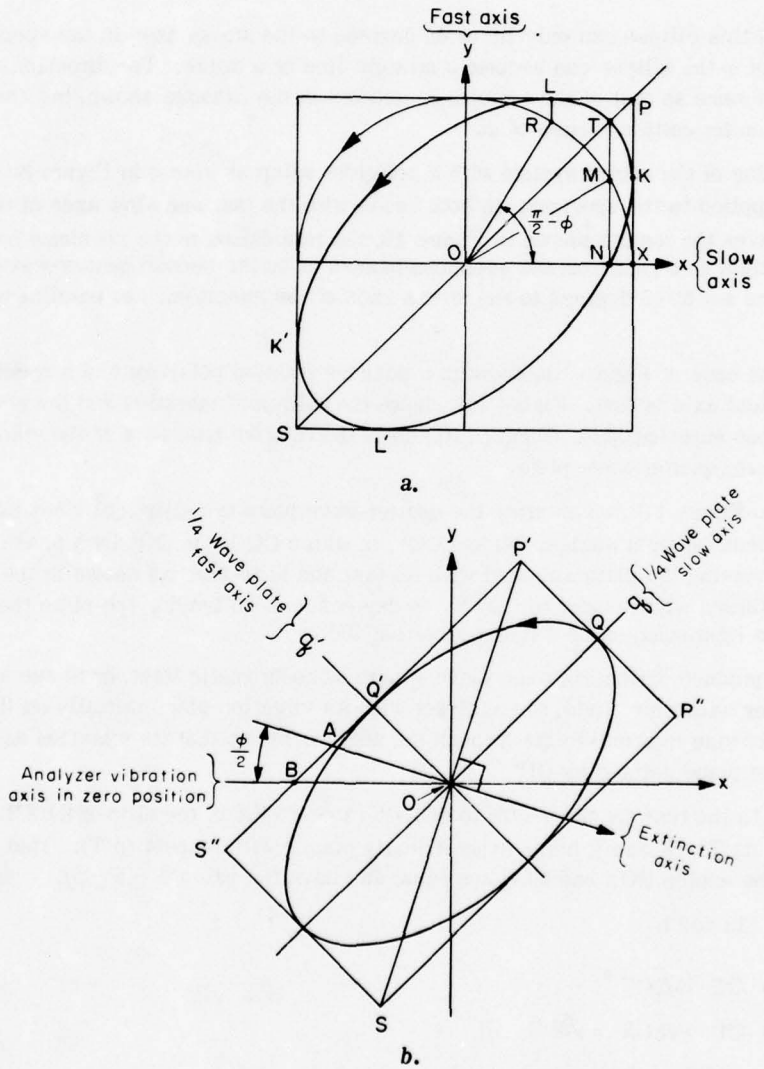

Figure 11. Elliptical vibration (a) and the generating circular vibration superimposed (b).

That is, the angle through which the analyzer must rotate in a clockwise direction to give extinction and to compensate for a retardation of ϕ in the specimen is $\phi/2$ when the polariscope is arranged as described above.

In an unstressed specimen ϕ is zero and the circularly polarized light beam entering the specimen leaves it to arrive at the analyzer quarter-wave plate unchanged. The ellipse then becomes a circle, and OP' (Fig. 11b) lies along OY. The analyzer in the zero position thus passes no light and the field appears dark.

Stress applied to the specimen, as shown in Figure 8c, results in integral fringe orders being observed, and a clockwise rotation of the analyzer causes a decrease in observed fringe values.

Coker and Filon[6] determined that for glass under load the fast axis corresponds to the principal stress direction having the greatest compression. In the case of biaxial tension, the principal stress direction showing the least tension would be the fast axis.

Thus the case illustrated by Figure 10a could represent a glass specimen under compression about a horizontal axis. The polariscope considered could therefore be used to measure fractional fringe orders in a specimen stressed in this way, provided always that the analyzer is rotated clockwise to measure the fraction. With this arrangement it is possible to dispense with the degree scale normally used with polariscope analyzers, and replace it with a 0 - 1.0 scale divided equally in fractions of a fringe and extending over an arc of 180 degrees.

Positive and negative circular polarizers

Consider a polariscope set up as in Figure 1a to observe a glass specimen under a horizontal compressive load. We have seen that integral fringe orders are observed and that clockwise rotation of the polarizer results in the observed fringe orders decreasing to a lower-order tint of passage. The effect of changing the positive circular polarizer for a negative type is shown in Figure 10a, b.

Assuming that initially the specimen is under no stress, the negative circular polarization is transmitted unchanged and the emergent rays are unaffected by the specimen. This means that the axis of vibration of the plane polarized light emerging from the quarter-wave plate is horizontal. Light thus passes through the analyzer when it is set in the zero position, and the fringe orders observed when the specimen is stressed are half-order colors. If the stress on the specimen is increased above the zero level, rotation of the analyzer in a clockwise direction, while maintaining a constant compressive stress, results in a lower fringe order being observed.

Orientation of the specimen

Rotating the polarization specimen under compression through a right angle rotates the ellipse through the same angle (Fig. 10a). The fast and slow axes of the specimen are interchanged.

Figure 12a shows that, with no stress, the extinction plan coincides with the OX axis, the vibration plane of the analyzer. That is, a dark field is observed at zero stress and the fringes observed when the specimen is under stress are the integral fringe orders.

A $(180°-\phi/2)$ clockwise rotation of the analyzer is now required to increase the observed fringe order to the next higher integral value, in the process of compensation.

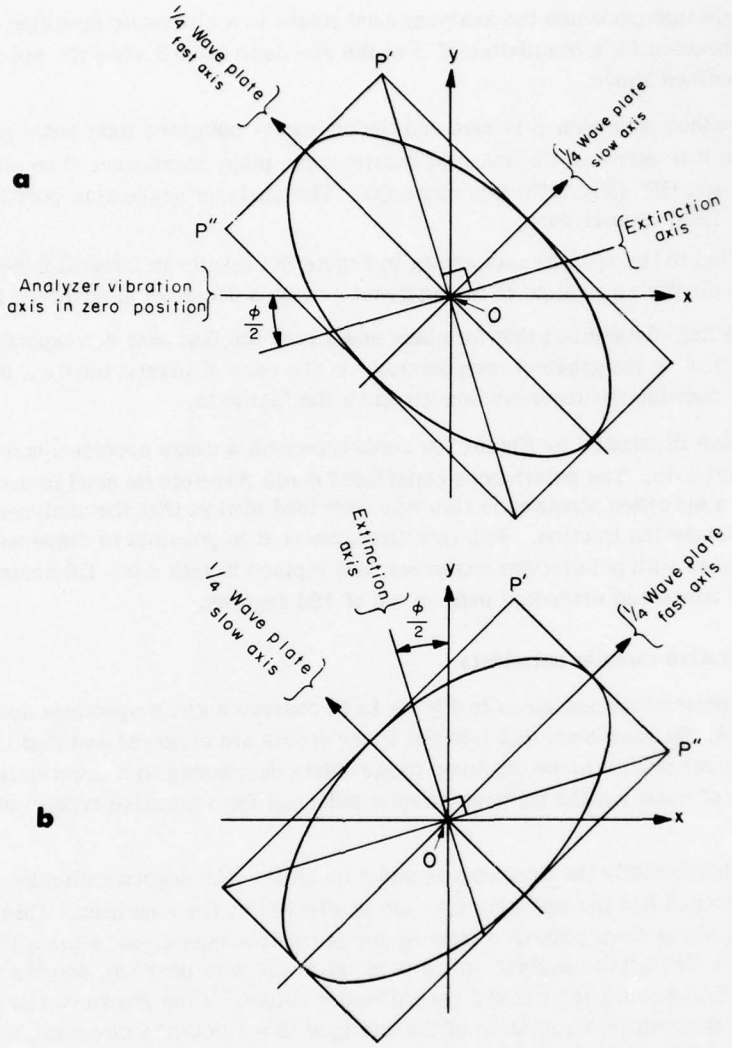

Figure 12. Reversal of fast and slow axes in tension and compression.

Compressive and tensile stresses

Maintaining the stresses in the original (horizontal) direction and replacing the compressive stress with an equal tensile stress also reverses the fast and slow axes of the specimen. The position of the analyzer is then exactly the same as that shown in Figure 12a. Again, the integral fringe orders are visible, and in the process of compensation a clockwise rotation of the analyzer by the amount $(180° - \phi/2)$ is required to increase the observed fringe order to the next higher integer.

In both these cases the original procedure of having to rotate the analyzer through an angle $\phi/2$ to gain extinction with a decrease in observed fringe order to the next lower integral value can be used by merely rotating the complete analyzer assembly through 90°.

Axis of the analyzer quarter-wave plate

Referring to Figure 11b, interchange of the slow and fast axes of the quarter-wave plate in the analyzer results in the vibration plane of the plane polarized light leaving the quarter-wave plate and entering the analyzer lying on the OP'' axis (Fig. 12b).

In the condition of zero stress the ellipse becomes a circle and OP'' lies along the OX axis. When the analyzer is placed in the zero position a bright field is observed, and when stress is applied to the specimen, half-order interference colors are seen.

With clockwise rotation of the analyzer an increasing value of ϕ results in a decrease in the rotation of the analyzer required to give extinction. This rotation increases the fringe order to the next higher integral value above that initially seen.

Axis of the analyzer

Referring again to Figure 11b, if the zero position of the analyzer is rotated through 90° the new zero position and vibration plane of the analyzer will correspond with the axis OY.

Zero stress in the specimen will result in OP' lying along this axis. The field will therefore be bright, and when the specimen is stressed half-order colors will be seen. If the stress increases the angle ϕ will increase, and correspondingly larger clockwise rotations of the analyzer will be required to give extinction.

Therefore, clockwise rotation of the analyzer results in the observed fringe order decreasing until, at full compensation, the observed color is the tint of passage at the next lower integral order below the fringe value initially seen.

General Behavior of Transmission Polariscopes

In the foregoing discussion the behavior of a single polariscope setup has been analyzed, together with the effects of making a series of individual alterations to the original arrangement. More than one of these changes could be incorporated at any time into a single instrument.

In Figure 13 the effect of all possible arrangements of a transmission polariscope are summarized.

Behavior of Reflection Polariscopes

Comparison of Figures 1a and b shows that the arrangement of polarizer and analyzer is the same. Therefore, if no phase change occurs at the reflection surface on the back of the photoelastic disk the reflection instrument (Fig. 1b) will behave identically with the transmission polariscope (Fig. 1a).

In Figure 1b the polarizing arrangement gives circular polarization with a positive vector rotation incident upon the transducer. If the transducer is not loaded this circularly polarized light undergoes a phase change of 90 degrees at the rear of the reflective transducer, so that the emergent light is circularly polarized but has a negative vector rotation.

Passage of this light through the analyzer quater-wave plate results in a horizontally polarized beam, which passes through the analyzer when the latter is in its zero position. A bright field is then observed. If the specimen is placed under load, half-order colors are seen.

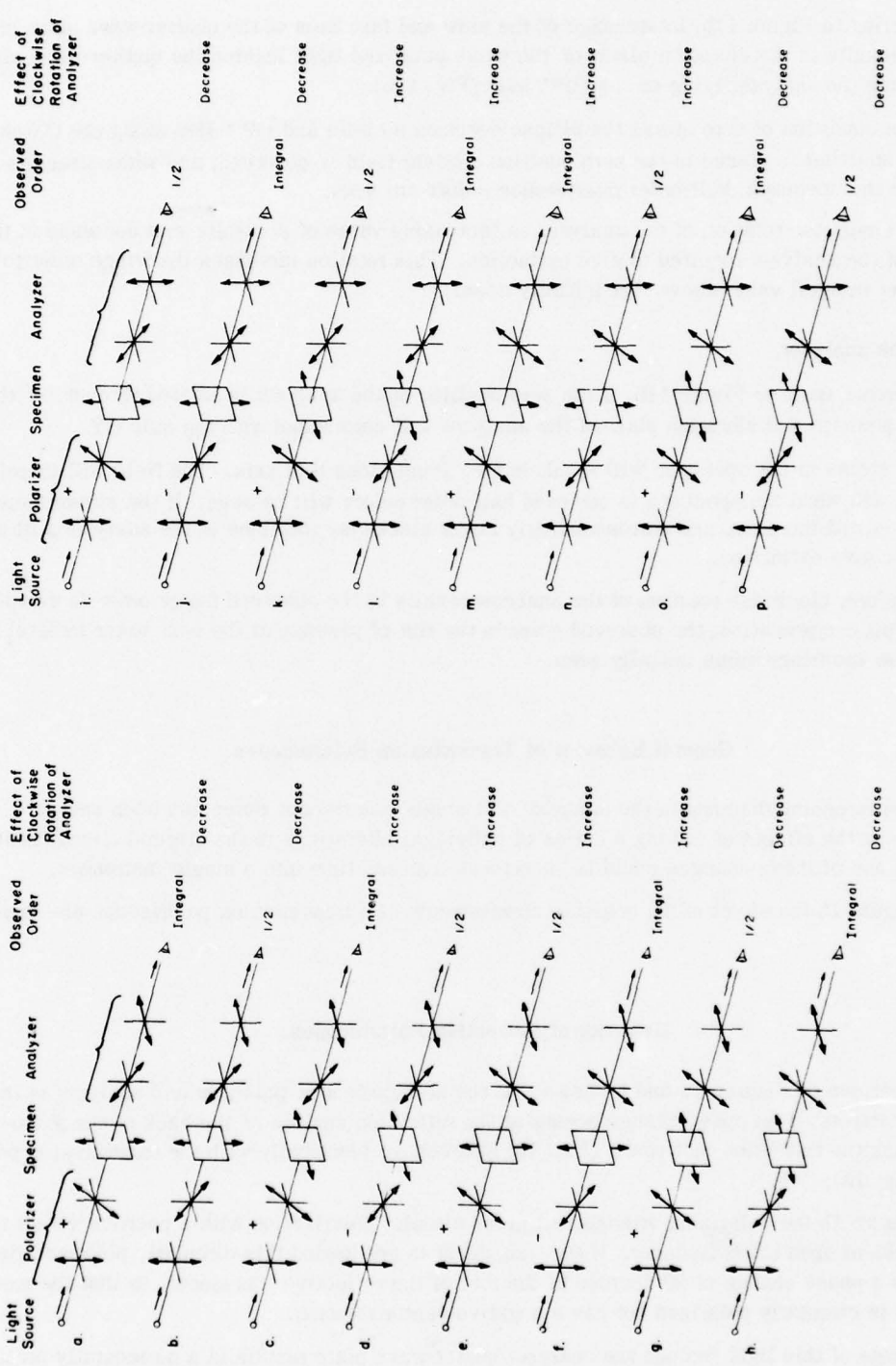

Figure 13. The behavior of transmission polariscopes. Axes marked on plane polarizing filters are vibration axes. Axes marked on quarter-wave plates and photoelastic specimens are fast axes. (After Williams[29].)

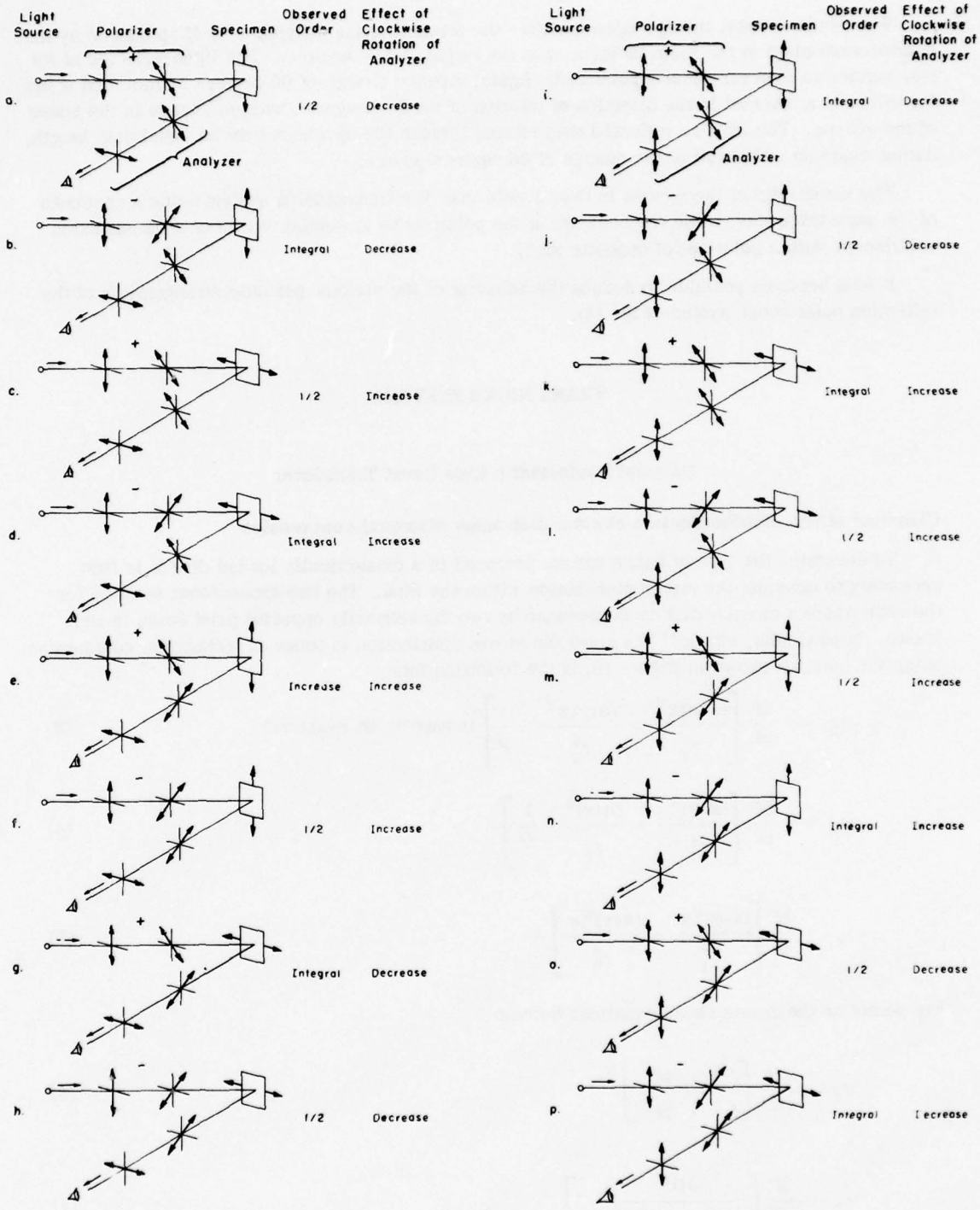

Figure 14. The behavior of reflection polariscopes. Axes marked on linear polarizing filters are vibration axes. Axes marked on quarter-wave plates and photoelastic specimens are fast axes. (After Williams[29].)

When under stress, the specimen modifies the original phase difference of 45° produced by the quarter-wave plate in the beam incident upon its surface by an angle ϕ. The light reflected at its rear surface is then elliptically polarized. Again, a phase change of 90 degrees occurs, and again the effect is a reversal in the direction of rotation of the light vector, with no change in the shape of the ellipse. The light so reflected then returns through the specimen over an equal path length, during which an additional phase change of 45 degrees occurs.

The sensitivity of the system is thus double that of a transmission system using a specimen of the same thickness, while the behavior of the polariscope is similar to that of a transmission polariscope with a polarizer of opposite sign.

It thus becomes possible to deduce the behavior of the various possible arrangements of the reflection polariscope system (Fig. 14).

TRANSDUCER SYSTEMS

Uniaxial Photoelastic Line Count Transducer

Classical stress distribution in a circular disk under diametral compression

To determine the type of fringe pattern produced in a diametrically loaded disk it is first necessary to consider the stress distribution within the disk. The two-dimensional solution for the case where a circular disk is compressed by two diametrically opposite point loads is well known. In particular, Frocht[11] has given the stress distribution in terms of rectangular coordinates, using the notation shown in Figure 15, in the following form:

$$\sigma_x = -\frac{2P}{\pi t}\left[\frac{(a-y)x^2}{r_1^4} + \frac{(a+y)x^2}{r_2^4} - \frac{1}{D}\right] \text{ (compression negative)} \tag{3}$$

$$\sigma_y = -\frac{2P}{\pi t}\left[\frac{(a-y)^3}{r_1^4} + \frac{(a+y)^3}{r_2^4} - \frac{1}{D}\right] \tag{4}$$

$$\tau_{xy} = \frac{2P}{\pi t}\left[\frac{(a-y)^2 x}{r_1^4} - \frac{(a+y)^2 x}{r_2^4}\right]. \tag{5}$$

For points on the x-axis, these equations become

$$\sigma_x = \frac{2P}{\pi t D}\left[\frac{D^2 - 4x^2}{D^2 + 4x^2}\right]^2 \tag{6}$$

$$\sigma_y = -\frac{2P}{\pi t D}\left[\frac{4D^4}{(D^2 + 4x^2)^2} - 1\right] \tag{7}$$

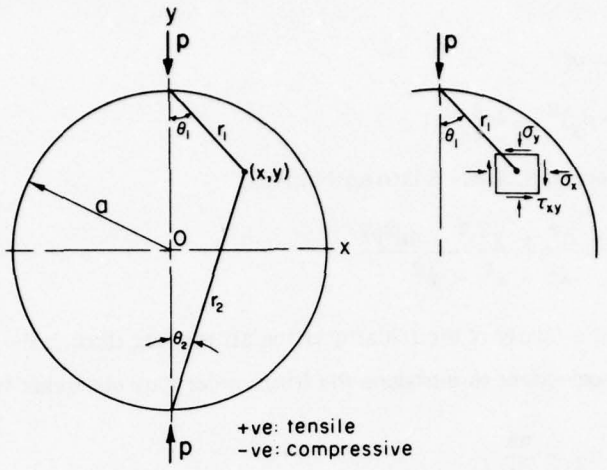

Figure 15. Rectangular stress components in a circular disk under diametral compression.

$$\tau_{xy} = 0 \, . \tag{8}$$

It is therefore evident that σ_x is always tensile and σ_y is always compressive along the entire x-axis, and that both stresses reduce to zero at the circumference.

The maximum stresses are developed at the center of the disk:

$$\sigma_x = \frac{2P}{\pi t D} \tag{9}$$

$$\sigma_y = \frac{-6P}{\pi t D} \, . \tag{10}$$

The stresses on the y-axis are:

$$\sigma_x = \frac{2P}{\pi t D} \tag{11}$$

$$\sigma_y = -\frac{2P}{\pi t}\left[\frac{2}{D-2y} + \frac{2}{D+2y} - \frac{1}{D}\right] \tag{12}$$

$$\tau_{xy} = 0 \, . \tag{13}$$

The classical theory therefore predicts a constant horizontal tension along the entire y-axis, and it implies infinite compressive stresses at the loading points.

Equation of isochromatics

Recalling the basic definition of a fringe or isochromatic curve as the locus of points of maximum and constant shear stress, the principal stress difference may be written as:

$$\sigma_1 - \sigma_2 = H$$

where H is a constant, or

$$H^2 = (\sigma_x - \sigma_y)^2 + 4\tau_{xy}^2 . \tag{14}$$

Substituting values from eq 3, 4 and 5 into eq 14 gives

$$\frac{4Pa}{\pi tH} = \frac{(x^2 + a^2 + y^2)^2 - 4a^2y^2}{a^2 - x^2 - y^2} . \tag{15}$$

Equation 15 represents a family of bicircular quartics all passing through the two points of loading.

It now becomes convenient to introduce the fringe order n by observing that, from eq 1 and 2,

$$H = \sigma_1 - \sigma_2 = \frac{n\lambda}{Ct} . \tag{16}$$

Equation 15 may then be written in the form

$$\frac{J}{n} = \frac{(a^2 + x^2 + y^2)^2 - 4a^2y^2}{a^2 - x^2 - y^2} \tag{17}$$

where

$$J = \frac{4PaC}{\pi\lambda}$$

and is constant for any given disk under a specific load.

The degree of agreement between theory and experiment is shown in Figure 16, which illustrates the observed fringe pattern in a plastic disk under a given diametral load, together with the theoretical fringe pattern corresponding to the same load. In this instance the fringe order at the center of the disk is 3.0.

The only discrepancy between the two patterns is that some of the observed fringes do not pass through the loading points in the two highly stressed zones. This can be explained by noting that the actual compressive load is applied over a finite width, due to flattening of the disk. This has the effect of displacing the zone of maximum shear stress away from the boundary.

It is important to note that the locus of the zero fringe, obtained by putting $n = 0$ in eq 17, is described by $a^2 = x^2 + y^2$, which also defines the circular boundary of the disk.

It therefore follows that, except at the loading points, shear stresses vanish at this boundary and the zero fringe is always present irrespective of the magnitude of the applied load. This dark zero fringe produced under a crossed circular polariscope is clearly evident in Figure 16.

During compression of the disk, fringes are generated at the two loading points; each successive pair of fringes approaches the center of the disk, merges temporarily, and then separates by moving outward toward the disk boundary. As these fringes can never reach the boundary, they stack along the x-axis.

One further consideration concerns the fringe order at the center of a diametrically loaded disk. Putting $x = y = 0$ in eq 17 and substituting for J gives

$$n = \frac{4PC}{\pi\lambda a} = \frac{AP}{D} . \tag{18}$$

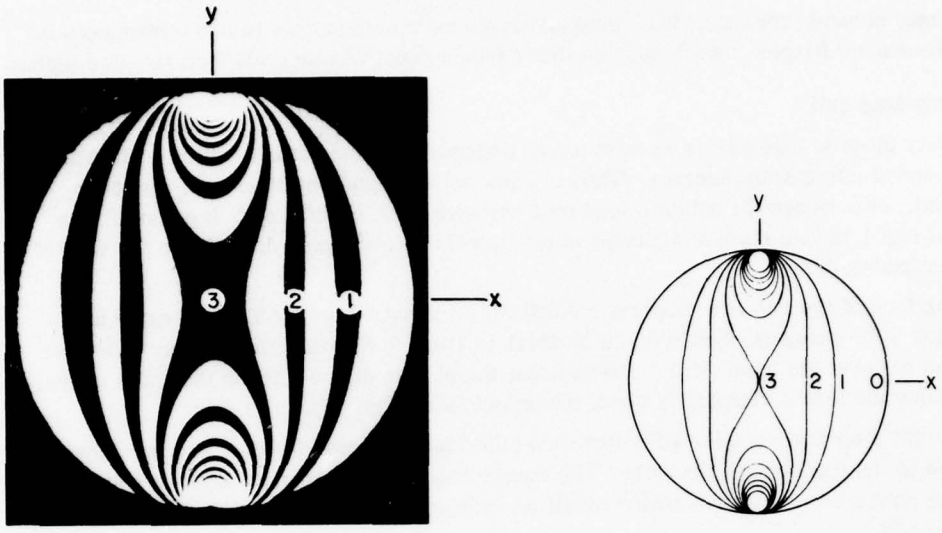

a. *Observed.* b. *Theoretical.*

Figure 16. Fringe patterns in a disk under diametral compression.

where

D = the disk diameter

and $A = \frac{8C}{\pi\lambda}$, a constant for a given disk material and light wavelength.

Thus for any given disk viewed under transmitted polarized light of a given wavelength, the fringe order at the center of the disk is *directly proportional to the applied load, inversely proportional to the diameter of the disk and independent of the thickness of the disk.*

For reflected light viewing the length of the light path is twice that for transmitted light viewing and eq 18 becomes

$$n = \frac{2AP}{D}. \tag{18a}$$

Thus a disk viewed under reflected light has twice the sensitivity of the same disk viewed under transmitted light.

As will be shown later the single glass disk can be used extensively as a photoelastic transducer, particularly as the fringe order at the center of the disk can be determined with a considerable degree of accuracy.

Uniaxial Central Fringe-Order Transducer

Hiramatsu's uniaxial stressmeter

As an alternative to the diametrically loaded disk described above, the stress birefringent material can be loaded so as to have a more or less uniform stress distribution. The fringes then appear as areas of uniform color which can be related to the applied load. Hiramatsu[17] has used such a system in which a solid cylinder of glass bonded into a body was used to monitor uniaxial stress changes.

As a practical tool for measuring, one of the greatest disadvantages of such a technique is that the fringe orders are transient, so that identification of the specific fringe value at the time of

observation may present problems. It is generally much more satisfactory to use transducers in which the successive fringes "stack up," so that a fringe count can be made from the zero datum.

Dowty pit-prop load cell

The Dowty pit-prop load cell is an example of a simple load indicator in which a birefringent material is bonded into a steel housing. The indicator was designed by Messrs Dowty Mining Equipment Ltd., as a fitment to indicate load on a cylindrical steel pit prop.[2] It consists of a circular steel cap 1.125 in. outside diameter which is welded into a hole drilled into the wall of the pit prop at mid-height.

The back face of the cup is a diaphragm 0.020 in. thick with a hole 0.375 in. square at its center. A disk of birefringent plastic 0.120 in. thick is fixed to the diaphragm, using reflective cement, so as to cover the hole. It is important that the plastic disk not touch the walls of the cap at any point and that it completely cover the square hole (Fig. 17).

When the pit prop is loaded the hole containing the load indicator deforms, and the deformation is transmitted to the cap through the weld. The square hole in the diaphragm acts as a stress raiser and the stress concentrations which result are transmitted to the birefringent plastic through the adhesive bond.

When viewed through the reflection hand viewer polariscope the interference fringes identify the loads on the prop by direct calibration. The appearance of the fringe pattern is shown in Figure 18.

Measurements can be refined by compensating between the integral fringe orders. However, the primary objective of this load cell was to provide a general indication of load at increments of 5 tons over the range 0-20 tons. For this purpose a simple hand viewer without compensation suffices. The characteristics of the optical signal are easily distinguishable at each 5-ton increment.

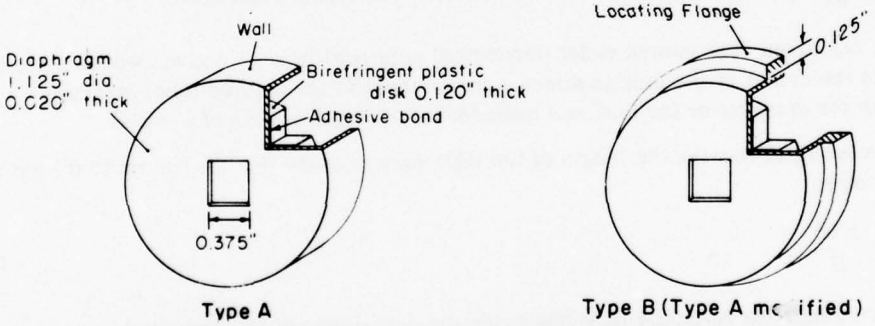

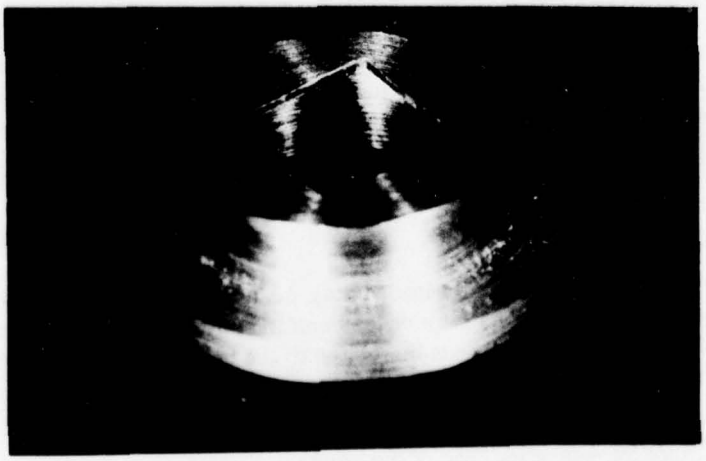

Figure 17. Dowty pit-prop load cell. (After Braiden.[2])

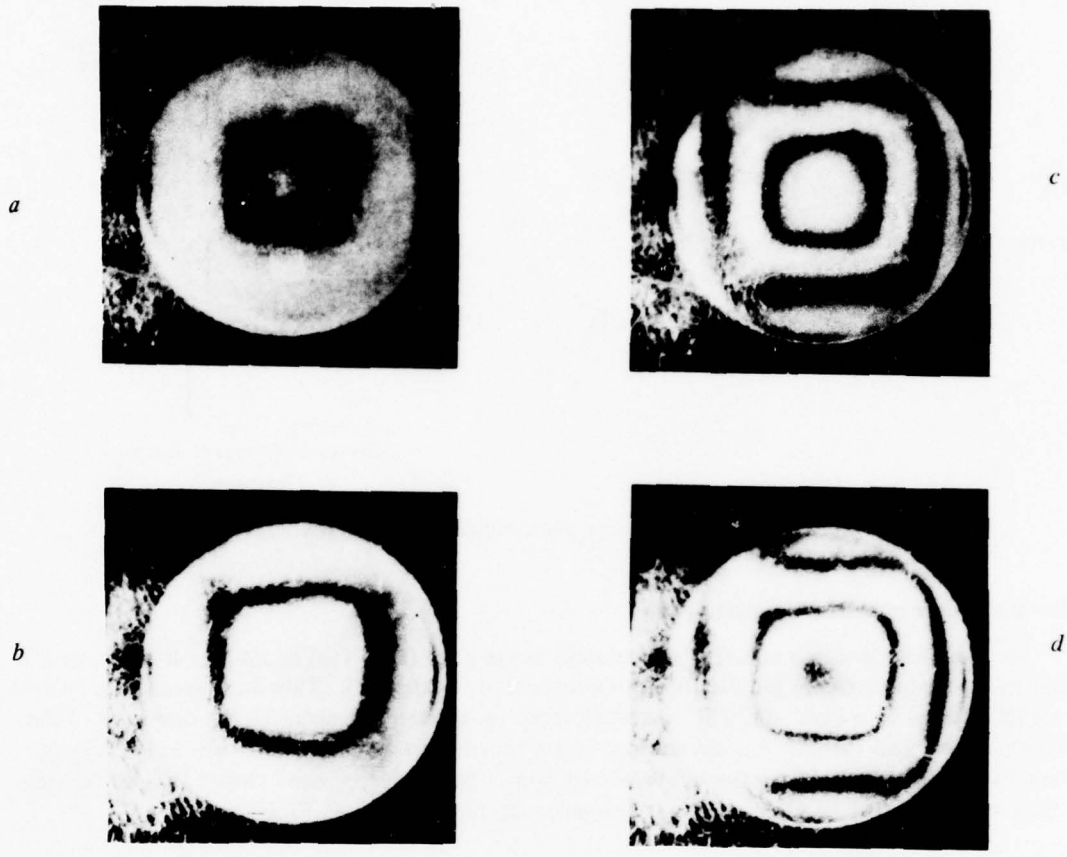

Figure 18. Optical scale of Dowty pit-prop load cell. (After Braiden[2].)

Uniaxial Photoelastic Strain Gages

Oppel's linear strain gage

A linear strain gage operating on photoelastic principles was designed and introduced by G.U. Oppel in 1956[24] (Fig. 19a). It consists of a thin strip of stress-birefringent plastic into which parallel interference fringes have been "frozen" by causing the plastic to polymerize under a condition of strain.

Strain of the surface to which the gage is cemented (at its ends only) is conveyed to the gage and observed as lateral displacement of the fringe pattern. The sensitivity of the gage depends directly on the stress optic coefficient of the plastic and its thickness calculated by equation 1. A typical gage would be designed to give a displacement of one fringe order for a strain of 1000 microinches per inch. The gages are available in a range of lengths and sensitivities. The maximum sensitivity ranges from 15 to 50 microinches per inch.

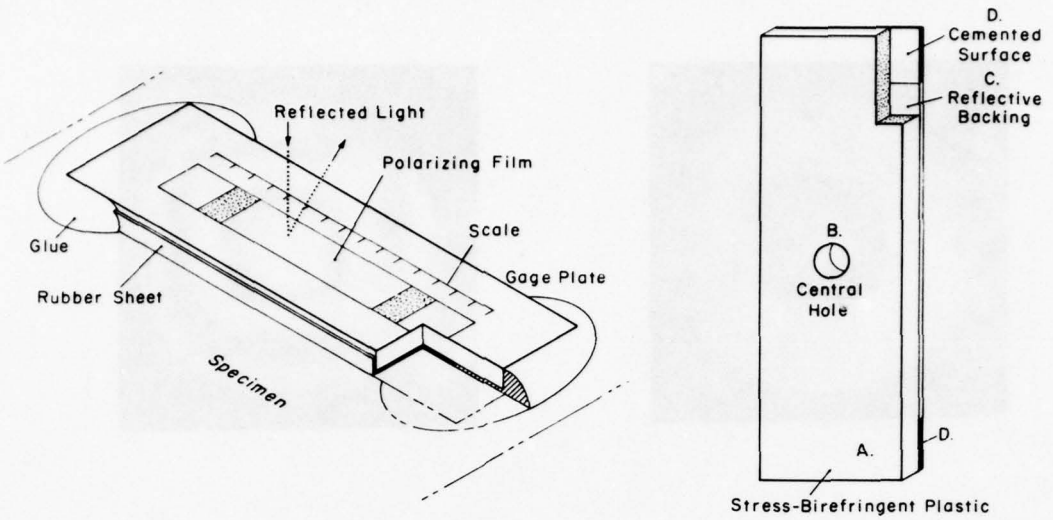

a. *Oppel*[24]. b. *Hawkes*[12].

Figure 19. Linear photoelastic strain gages.

Hawkes' linear photoelastic strain gage

Hawkes described his uniaxial photoelastic strain gage (Fig. 19b) in 1968[12]. It consists of a strip of stress-birefringent plastic (A) with a reflective backing (C). This strip contains a central hole (B) backed by a layer of PTFE non-stick tape. In use the two ends (D) are cemented to the surface under observation. Any subsequent strain is revealed as an isochromatic fringe pattern when the gage is viewed by reflected polarized light. The precision hand viewer is used for this. The interference fringes visible in the gage under strain are shown in Figure 20.

Characteristics of the Hawkes linear photoelastic gage

The stress distribution around a hole in a strip subjected to uniaxial stress, σ_1, is given by

$$\sigma_r = \frac{\sigma_1}{2}\left(1-\frac{b^2}{r^2}\right)+\frac{\sigma_1}{2}\left(1+\frac{3b^4}{r^4}-\frac{4b^2}{r^2}\right)\cos 2\theta \tag{19}$$

$$\sigma_\theta = \frac{\sigma_1}{2}\left(1+\frac{b^2}{r^2}\right)-\frac{\sigma_1}{2}\left(1+\frac{3b^4}{r^4}\right)\cos 2\theta \tag{20}$$

$$\tau_{r\theta} = \frac{\sigma_1}{2}\left(1-\frac{3b^4}{r^4}+\frac{2b^2}{r^2}\right)\sin 2\theta \tag{21}$$

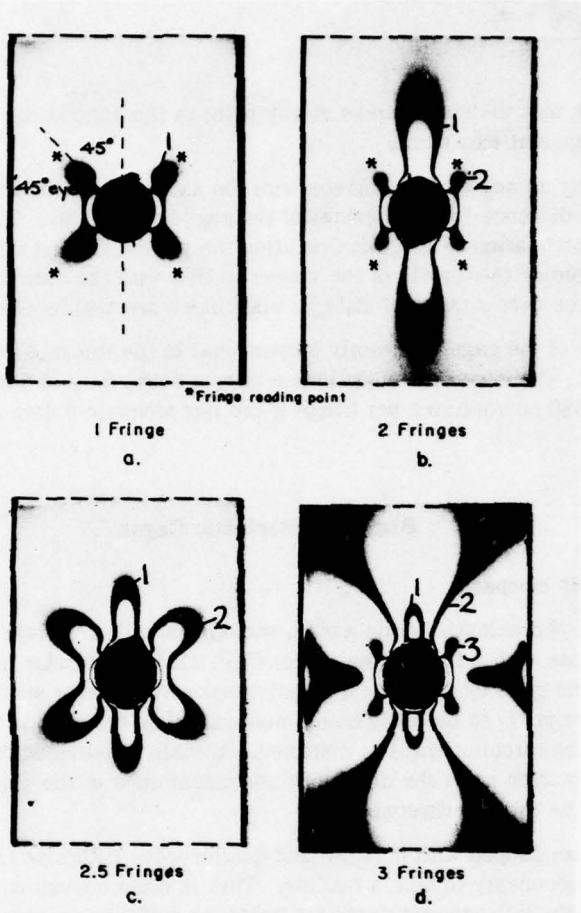

Figure 20. Fringe patterns displayed by Hawkes' linear photoelastic strain gage under load. (After Hawkes[12].)

where

σ_θ = the tangential stress

σ_1 = the applied stress

σ_r = the radial stress

b = the radius of the hole in the gage

r = the radius of the point being considered

θ = the angle of the point being considered, from the axis of the strip.

The maximum shear stress for any point r, θ is given by

$$\tau_{max} = \sqrt{\frac{\sigma_\theta^2 - \sigma_r^2}{2} + \tau_{r\theta}^2} \qquad (22)$$

It can be shown that the shear stress at any point in the gage is directly proportional to the axial strain in the gage at that point.

On a line making an angle of 45 degrees with the axis of the gage the shear stress reaches a maximum value at a distance from the center of the gage of $r = b\sqrt{3}$. This gives four precise points of fringe identification (Fig. 20). Operating the precision hand viewer by the Tardy compensation technique, holding the handle of the viewer in line with the axis of the strain gage, precise readings may be taken over a range of at least six fringes and within ±2% fringe order.

The sensitivity of the gage is directly proportional to the thickness and the stress-optic constant of the plastic. The gages currently in use have a sensitivity of 345 microstrains per fringe in white light, and 380 microstrains per fringe if the isochromatic colors are removed with a red filter.

Biaxial Photoelastic Gages

Oppel's biaxial strain compass

Oppel's biaxial photoelastic strain gages, sometimes called "strain compasses," take the form of a circular plate with a hole at the center (Fig. 21a). A circular fringe concentric to the hole is frozen into the gage by allowing it to polymerize while under strain. In use the gage is bonded around its periphery to the body being studied. When the gage is strained the hole acts as a stress raiser and the circular fringe is distorted. A scale is provided on the face of the gage, and by use of a calibration chart the directions and magnitudes of the principal stresses in the underlying body can be roughly determined.

Oppel's gages are capped with polaroid and quarter-wave filters so that only the application of a light source is necessary to take a reading. This is often convenient, but the system lacks the refinement possible with viewers fitted for Babbinet or Tardy compensation. More precise readings are possible using optical equipment and oil immersion, as described by Zandman[11].

Hawkes' biaxial strain gage

In the Sheffield photoelastic transducer system biaxial gages have been applied in three forms: 1) hollow cylindrical glass inclusions, 2) hollow cylindrical plastic or "low modulus" inclusions, and 3) flat circular disks of plastic with a central hole. The latter are Hawkes' biaxial photoelastic strain gages[13]. The Hawkes gage is cemented around its periphery to the surface of the body under examination. Although the dimensions may vary, the internal/external diameter ratio is maintained constant at ⅛ (Fig. 21b).

The isochromatic fringe patterns formed on such a gage when it is attached to a body under load and observed under polarized light are shown in Figure 22. The data required from these patterns are the directions, magnitudes, and signs of the major and minor principal strains.

Theory of the photoelastic biaxial strain gage

The theory of the photoelastic biaxial strain gage is described by Hawkes in the following terms[13]:

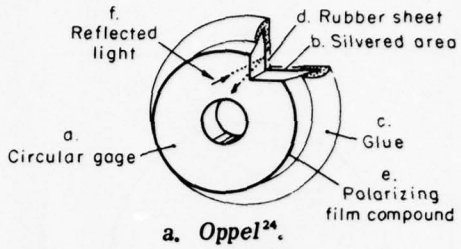

a. *Oppel*[24].

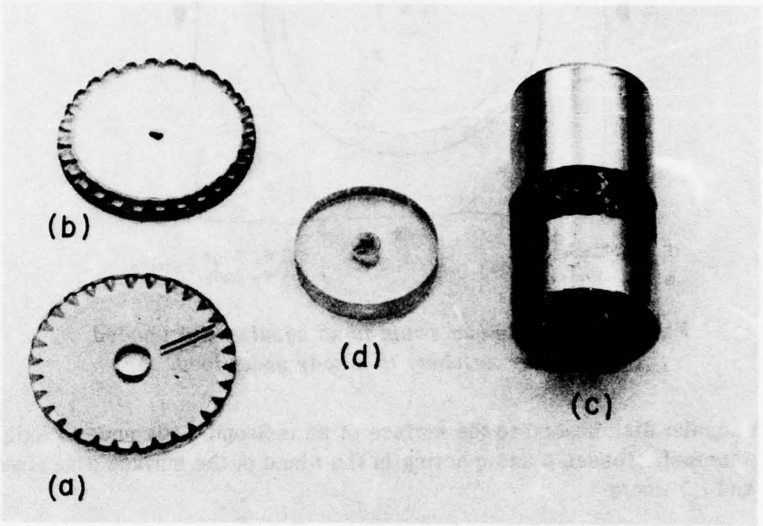

b. *Hawkes*[13]. *Biaxial gage (a, b), front and back views; soft inclusion gage (c, d), with and without front and back sleeves.*

Figure 21. Biaxial strain gages.

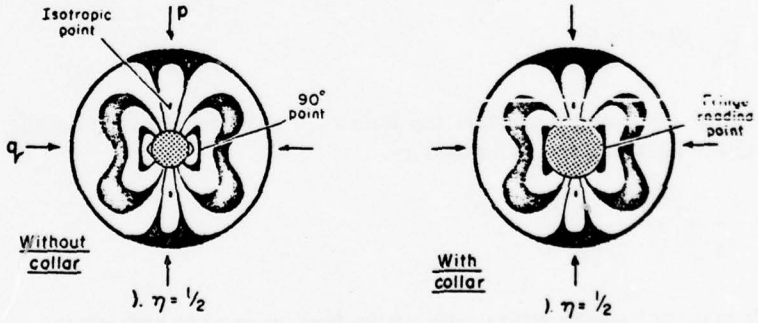

Figure 22. Isochromatic fringe patterns in an annular strain gage. Numbers refer to fringe order; η (stress ratio) = σ_2/σ_1.

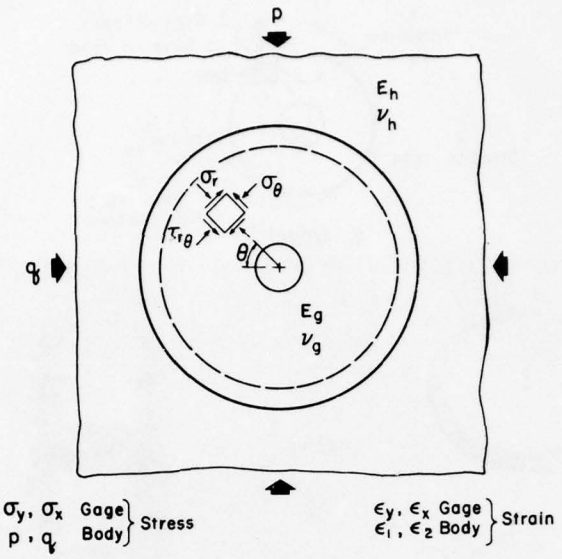

Figure 23. Stress and strain in an annular disk bonded around its periphery to a body under load.

Consider an annular disk bonded to the surface of an isotropic body under biaxial stress (Fig. 23). The principal stresses p and q acting in the plane of the surface give rise to two principal strains ϵ_1 and ϵ_2, where

$$\epsilon_1 = \frac{1}{E_h} (p - \nu_h q) \tag{23}$$

and

$$\epsilon_2 = \frac{1}{E_h} (q - \nu_h p) \tag{24}$$

where E_h and ν_h are the Young's modulus and Poisson's ratio, respectively, of the body. The strain ratio L in the host material is defined as

$$L = \frac{\epsilon_2}{\epsilon_1} = \frac{(q - \nu_h p)}{(p - \nu_h q)} \tag{25}$$

and L varies from ν_h to 1 as the stress ratio varies from uniaxial to hydrostatic.

The strains ϵ_1 and ϵ_2 are conveyed through the cement annulus to the body of the disk, where they set up stresses σ_y and σ_x given by:

$$\sigma_y = \frac{E_g}{(1 - \nu_g^2)} (\epsilon_1 + \nu_g \epsilon_2)$$

$$= \frac{E_g \epsilon_1}{(1 - \nu_g^2)} (1 + \nu_g L) \tag{26}$$

$$\sigma_x = \frac{E_g}{(1-\nu_g^2)} (\epsilon_2 + \nu_g \epsilon_1)$$

$$= \frac{E_g \epsilon_1}{(1-\nu_g^2)} (C + \nu_g) \tag{27}$$

where E_g and ν_g are the Young's modulus and Poisson's ratio, respectively, of the disk material.

The stresses σ_y and σ_x in the disk are now subjected to a stress concentration by the central hole, and the stresses σ_r, σ_θ, and $\tau_{r\theta}$ in polar coordinates, at any point, are given by

$$\sigma_r = \left(\frac{\sigma_x + \sigma_y}{2}\right)\left(1-\frac{b^2}{r^2}\right) + \left(\frac{\sigma_x - \sigma_y}{2}\right)\left(1-\frac{4b^2}{r^2} + \frac{3b^4}{r^4}\right) \cos 2\theta \tag{28}$$

$$\sigma_\theta = \left(\frac{\sigma_x + \sigma_y}{2}\right)\left(1+\frac{b^2}{r^2}\right) - \left(\frac{\sigma_x - \sigma_y}{2}\right)\left(1+\frac{3b^4}{r^4}\right) \cos 2\theta \tag{29}$$

$$\tau_{r\theta} = \left(\frac{\sigma_y - \sigma_x}{2}\right)\left(1+\frac{2b^2}{r^2} - \frac{3b^4}{r^4}\right) \sin 2\theta \tag{30}$$

where

σ_r = radial stress component

σ_θ = tangential stress component

$\tau_{r\theta}$ = shear stress

b = hole radius

r = radius of any point in gage

θ = angular displacement relative to major principal stress axis.

The relationship between the maximum shear stress τ_{max} at point r, θ and the birefringence under a crossed polariscope is given by:

$$\tau_{r\theta_{max}} = \sqrt{\left(\frac{\sigma_r - \sigma_\theta}{2}\right)^2 + \tau_{r\theta}^2} = \frac{E_g n \lambda}{2(1+\nu_g) 2 t K} \tag{31}$$

where

n = isochromatic fringe order

λ = wavelength of the light (2.27×10^{-5} in. for white light)

K = strain/optical coefficient of the disk*

t = thickness of the disk (length of light path = $2t$).

*For plastics it is usual to use the constant K as the material constant rather than C, where $K = (E_g C)/(1 + \nu_g)$.

When $\theta = 0°$ or $90°$ the relationship between the principal stress difference and the birefringence is given by:

$$\sigma_\theta - \sigma_r = \frac{E_g\, n\, \lambda}{(1+\nu_g)\, 2tK}. \tag{32}$$

From eq 25 – 31 it is possible to derive the complete distribution of the isochromatic fringes formed in a biaxial gage of given material properties when stress is applied to the body to which it is attached.

Analysis of the isochromatic fringe pattern

The distribution of the lines of constant principal stress difference (isochromatic fringes) in a biaxial gage under strain is symmetrical about two axes, given by $\theta = 0°$ and $90°$ (Fig. 22). The strain directions can therefore be obtained immediately by noting these directions of symmetry.

The direction of the major principal strain is identified by the alignment of two isotropic points (points of zero shear stress) which move outward as the strain ratio increases, until they are ultimately lost at the edge of the disk.

Magnitude of major principal strain

To determine the magnitude of the major principal strain, some optimum point in the disk must be specified at which the fringe order can be read. The two requirements governing the selection of the optimum points for reading are:

1. To give greatest possible sensitivity, it should be as close as possible to the point of maximum principal stress difference.

2. At the optimum point, variations in the magnitude of the minor principal strain should have no influence on the principal stress difference.

From eq 29 – 31 the point of maximum stress difference in a disk can be shown to be at the edge of the central hole, on the axis of the minor principal strain:

$$\left(\sigma_\theta - \sigma_r\right)_{max} = 3\,\sigma_y - \sigma_x .$$

The minor principal strain axis is easy to identify, which makes it an ideal line along which to count the fringes. Figure 24, derived from eq 26 – 29, gives the principal stress differences along the minor strain axis for maximum and minimum values of the principal strain ratio in the body to which the disk is bonded.

The principal stress difference is directly proportional to the Young's modulus of the disk material, and to the major principal strain magnitude. In the example shown in Figure 24 the Poisson's ratio of the disk material is taken as 0.38. For this ratio there is a point on the minor axis, at a distance of 1.83b from the center, at which the stress difference is independent of the strain ratio.

A reading of the isochromatic fringe order at this optimum point can therefore be related directly to the magnitude of the major principal strain, without reference to the magnitude of the minor principal strain.

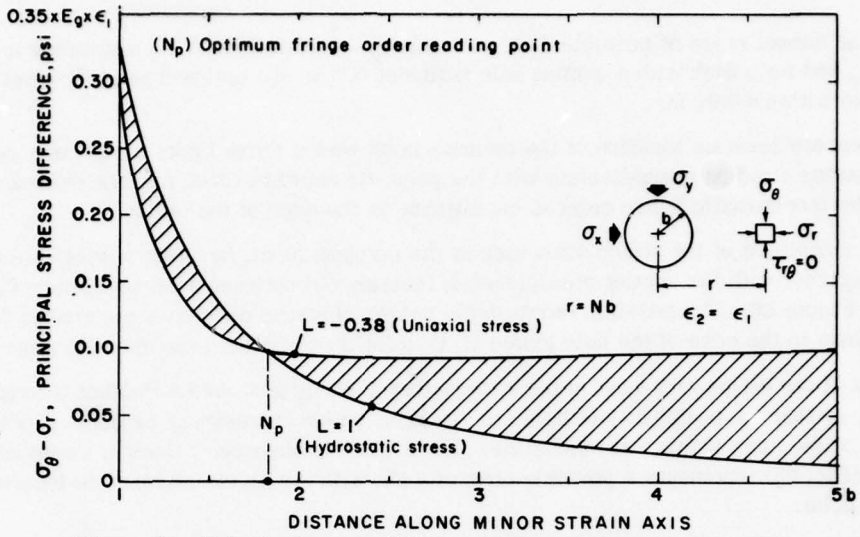

Figure 24. Principal stress difference along the minor strain axis for C = –0.38 and 1.

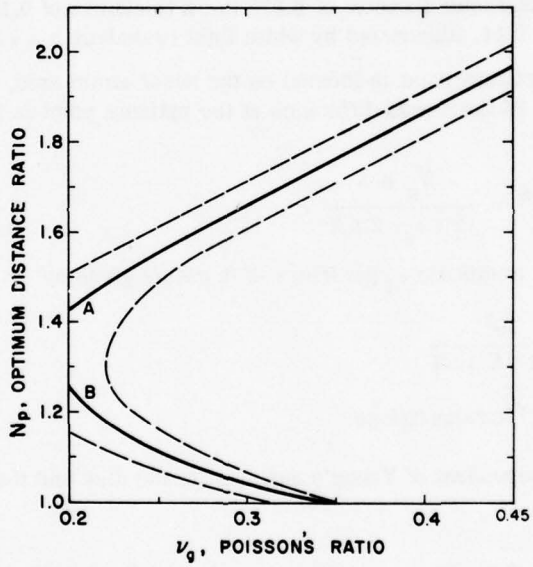

Figure 25. Optimum distance ratio vs Poisson's ratio of gage material.

The location of the optimum fringe order reading point is dependent only on the Poisson's ratio of the disk material. Figure 25 shows how the optimum point N_p moves as the Poisson's ratio varies from 0.2 to 0.45.

Below a Poisson's ratio of 0.35 there are two optimum points, representing a double intersection of the curves of principal stress difference plotted in Figure 24. Also shown in Figure 25 is the scatter band representing the accuracy with which the optimum point must be located, so that when the strain ratio changes from –0.38 to 1.0 the variation in stress difference is limited to ±2.5% of its average value.

In the normal range of possible disk materials $\nu_g = 0.25$ to 0.4. This represents a distance of $\pm 0.05\ N_p$ and for a disk with a central hole radius of 0.2 in. the optimum point N_p must therefore be located to within ± 0.01 in.

To ensure accurate location of the optimum point within these limits a soft, opaque plastic collar, having a radius commensurate with the point distance, is fitted into the central hole of the disk. The isochromatic fringe order is established at the edge of the collar.

The magnitude of the stress difference at the optimum point, for disks having different Poisson's ratios, together with the scatter possible when locating the optimum point to within ± 0.01 in., is given in Figure 26. The possible errors in the values of stress difference are greater for the optimum points close to the edge of the hole (curve B) than for those farther from the edge (curve A).

Most of the elastomers used in the manufacture of the gages have a Poisson's ratio greater than 0.3, so that the possibility of using the optimum points represented by curve B (Fig. 25, 26) does not arise, even if this were desirable. The scatter in observed values of stress difference for curve A (Fig. 25) represents a possible error of $\pm 4\%$, with the given tolerance in location of the optimum point.

The theoretical position of the optimum point, and the sensitivity (fringe order/principal strain magnitude) for any disk material, can now be calculated from Figures 24 and 25. For example, consider a gage having a central hole diameter of 0.375 in., a thickness of 0.132 in., a Poisson's ratio of 0.32, and a K factor of 0.14, illuminated by white light (wavelength $\lambda = 2.27 \times 10^{-5}$ in.).

From Figure 25 the optimum point is located on the minor strain axis, 0.32 in. from the center of the gage. From Figure 26 the stress difference at the optimum point is $10.3\ E_g \epsilon_1 \times 10^{-2}$. From eq 32 we have:

$$10.3\ E_g \epsilon_1 \times 10^{-2} = \frac{E_g\ n\ \lambda}{(1 + \nu_g)\ 2\ t\ K}\ .$$

The major principal strain magnitude ϵ_1 per fringe is therefore given by:

$$\epsilon_1 = \frac{\lambda \times 10^2}{(1 + \nu_g)\ 2\ t\ K\ 10.3}$$

$$= 455 \times 10^{-6} \text{ strains/fringe}\ .$$

The sensitivity is independent of Young's modulus for the disk and the radius of the central hole.

Magnitude of minor principal strain

To determine the magnitude of the minor principal strain it is necessary to measure some parameter that is independent of the major principal strain and which only varies as the ratio between the major and the minor principal strains.

Along the principal strain axis in the gage there are two points at which the stress difference is zero and therefore independent of the strain magnitudes. Figure 27 gives the relationship between the strain ratio L and the zero stress difference ratio N_0 for various values of the Poisson's ratio of the disk material.

The shaded area above a strain ratio of 0.6 indicates the general region in the disk where the zero stress difference point is not distinct and where it merges into a general background of very low stress difference. Also given in Figure 27 are the experimentally derived relationships for the disk (Hawkes and Moxon[14]). There is close agreement between the results of the experimental and theoretical studies.

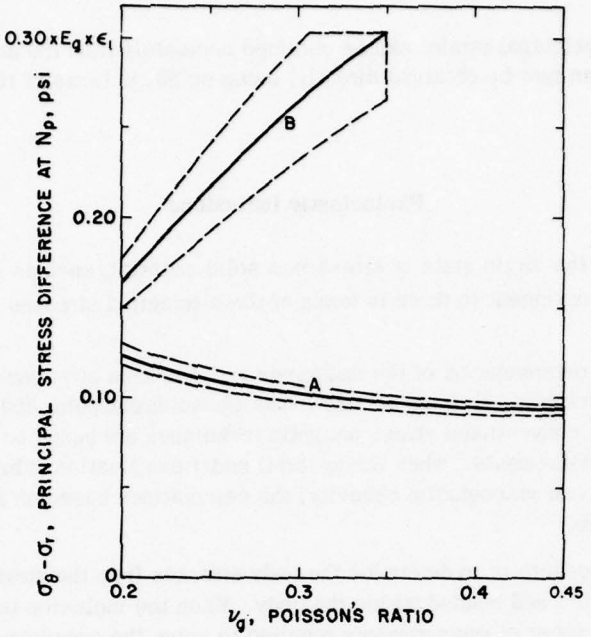

Figure 26. Principal stress difference at the optimum point vs Poisson's ratio of the gage material.

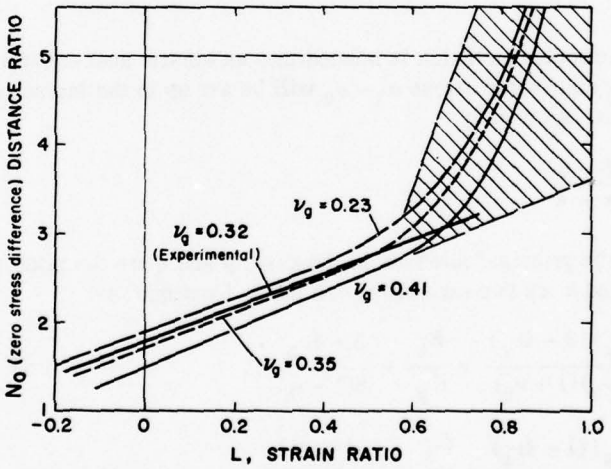

Figure 27. Isotropic point spacing vs strain ratio for various values of Poisson's ratio of the gage material.

It is not possible to derive the magnitude of the minor principal stress from Figure 27 with the same degree of precision as the major principal strain, especially as the strain ratio must be estimated above 0.6. In practice it is usually the major stress which is the more important. If an accurate value for the minor strain is required it must be obtained by using a solid disk, again bonded around its periphery to the body.

In this case the disk will be under a uniform stress, giving a constant fringe order over its area. From eq 26 and 27 we have:

$$\epsilon_1 (1 - L) = \frac{n\lambda}{2tK} . \tag{33}$$

As ϵ_1, the major principal strain, can be obtained accurately from the annular disk the value of the strain ratio L can now be obtained directly, using eq 33, in terms of the fringe order n in the disk.

Photoelastic Inclusions

When considering the virgin state of stress in a solid material, such as a rock mass or a concrete structure, it is convenient to think in terms of three principal stresses, one of which is assumed vertical.

The experimental determination of the magnitude and direction of stress changes within a solid mass presents many problems. Gaining access to the measurement point and fixing instruments may be difficult. Most conventional stress analysis techniques are based on the application of direct linear strain measurements. When the material under examination exhibits nonlinear stress-strain characteristics, and viscoelastic behavior, the calculations based on such measurements assume doubtful validity.

An alternative procedure is to determine the body stresses from the strains induced in an elastic inclusion inserted and bonded within the body. When the inclusion is of a type that displays a biaxial readout the number of measurements required to solve the complete stress field can be reduced from the usual six to three.

Inclusion theory

When an elastic circular inclusion is bonded into an elastic host material and the host material is stressed, a uniformly distributed stress $\sigma_1 - \sigma_2$ will be set up in the inclusion[23]. The stress difference in the inclusion is given by

$$\sigma_1 - \sigma_2 = \frac{p - q}{\kappa - k}$$

where σ_1 and σ_2 are the principal stresses in the gage, p and q are the principal stresses in the host material and κ and k are two constants, defined by Coutinho[9] as:

$$\kappa = \frac{(1 - \nu_g)(3 - 4\nu_g)}{8(1 - \nu_h)(1 + \nu_h)} \times \frac{E_h}{E_g} + \frac{5 - 4\nu_h}{8(1 - \nu_h)},$$

$$k = \frac{(1 + \nu_g)(1 - 4\nu_g)}{8(1 - \nu_h)(1 + \nu_h)} \times \frac{E_h}{E_g} + \frac{4\nu_h - 1}{8(1 - \nu_h)}.$$

Coutinho plotted values of κ and k against E_g/E_h and showed that for ratios of E_g/E_h greater than 2, κ and k change very little and when E_g is greater than $3E_h$ they are practically constant.

This means that if an elastic inclusion of high modulus is firmly cemented or otherwise fixed to the walls of a borehole in concrete or rock, changes in the host stress will produce corresponding changes in the inclusion that will have little dependence on changes in the modulus of elasticity of the host. That is, it is not necessary to know the host modulus precisely, and the more rigid the inclusion the less important becomes knowledge of the host modulus.

The inclusion may then be calibrated directly in terms of stress in the host, to become a "stressmeter."

Photoelastic stressmeter

The photoelastic inclusion stressmeter consists basically of a hollow-cored glass cylinder, bonded around its periphery in a hole drilled or cast in the body being studied. When illuminated, the end of the stressmeter is visible to an observer looking down the hole (Fig. 28).

Stresses generated in the body are transmitted to the meter, where they are revealed as an isochromatic fringe pattern when the meter is viewed under polarized light. In the plane of the meter, perpendicular to the axis of the cylinder, the fringe pattern identifies the directions, signs, and magnitudes of the two principal stress components.

The isochromatic fringe patterns are those illustrated in Figures 29-31.

In practice, to reduce the complexities of interpretation and to simplify observational procedures, it is sufficient to consider only those stress fields in which the major and minor principal stresses have the same sign. Owing to the low tensile strength of rocks and concrete it is rare to find appreciable tensile stresses in such materials. The glass inclusion stressmeter is used mainly to observe any increase of stress in a structure after the inclusion is inserted. In most applications both the principal stresses have been compressive.

Whether the principal stresses are both compressive or both tensile the procedure for interpretation of the isochromatic fringe pattern is similar. The sign of the major principal stress is clearly indicated by the direction in which the fringe pattern moves during the process of compensation.

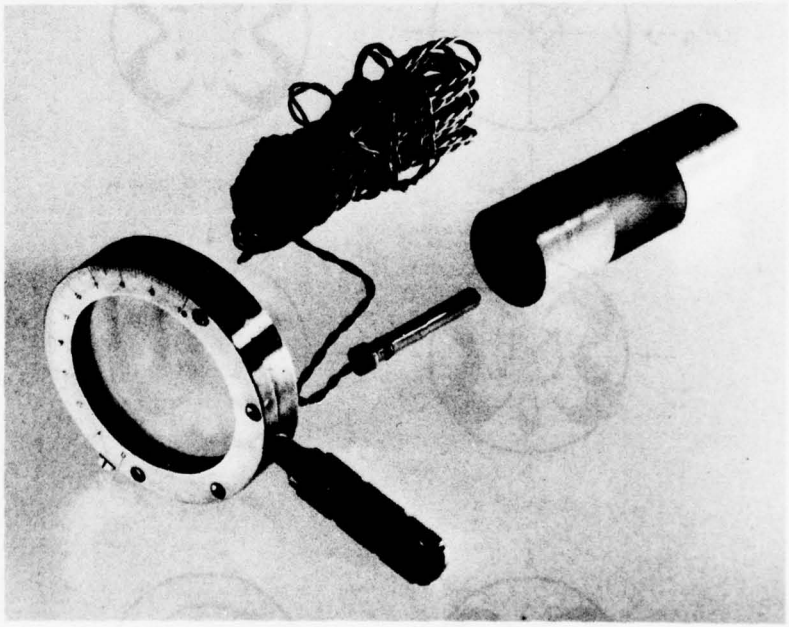

Stressmeter and accessories.

Figure 28. Photoelastic stressmeter.

For casting into concrete structures the adaptor holds the meter in the shuttering during casting. The source is a probe inserted through the central hole.

Used in drilled or cast holes more than 12 in. long. A 6-v bulb is incorporated.

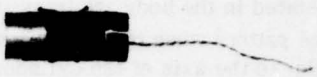

Reflective plug 1¼ in. diam used in shallow holes. The light source, polarizer and analyzer are held by the observer giving a sensitivity (psi/fringe) twice that of a normal plug.

Sizes available for setting in blocks or bricks which are built into a structure under investigation.

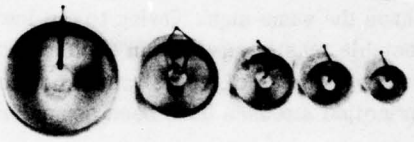

Figure 28 (Cont'd). Photoelastic stressmeter.

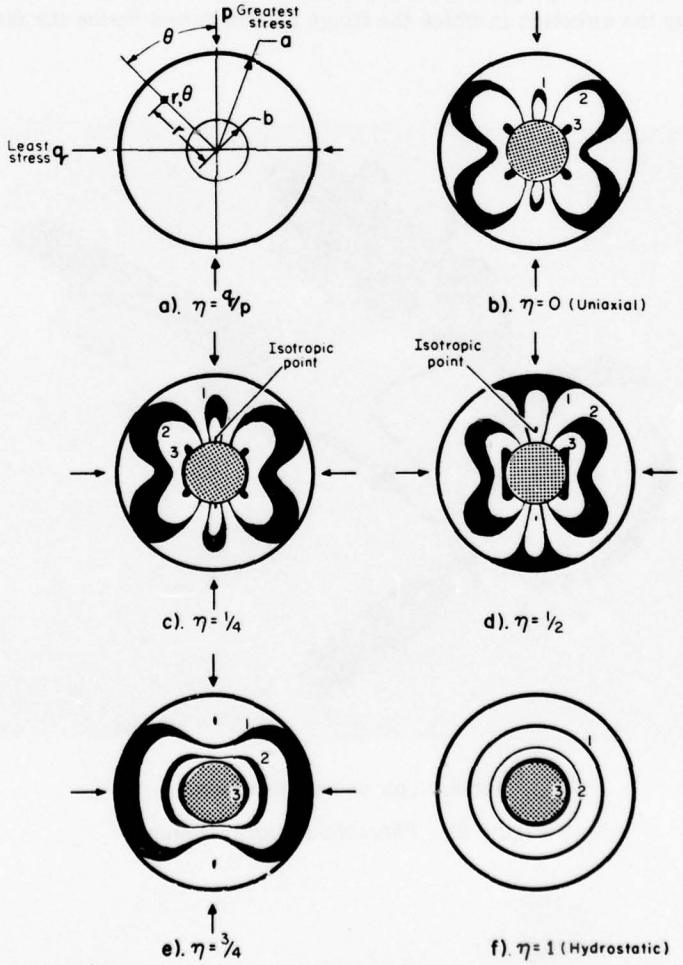

Figure 29. Isochromatic fringe patterns in a hollow cylindrical inclusion. (Fringe order 3.00.)

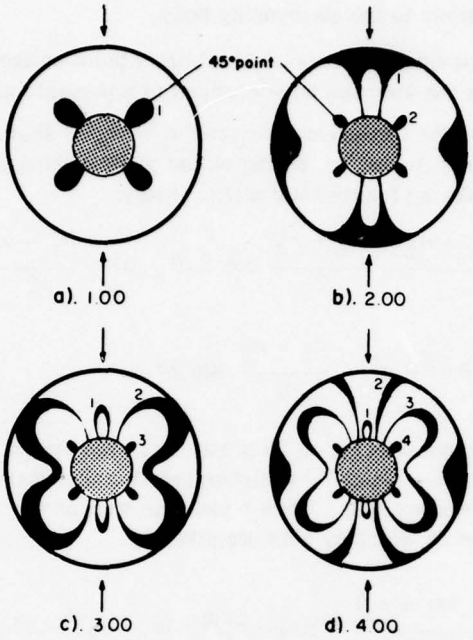

Figure 30. Isochromatic fringe patterns in a hollow cylindrical inclusion under increasing uniaxial stress. (Numbers give fringe order.)

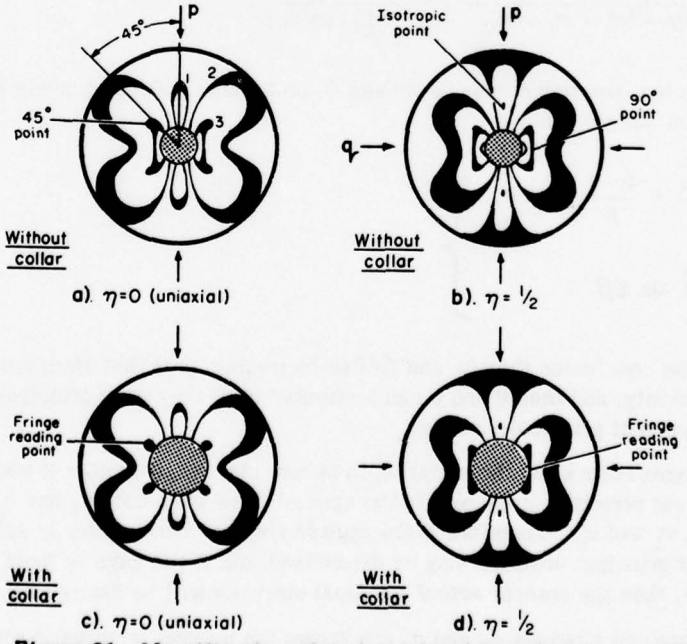

Figure 31. Identification of optimum isochromatic fringe reading point in a hollow cylindrical inclusion.

Theory of photoelastic hollow-cylinder inclusions

Hiramatsu, Niwa and Oka[17] made the following analysis of the stress in hollow cylindrical inclusions, in relation to the stress in the surrounding body.

It is assumed that the principal stresses at an arbitrary point on the surface of the body were previously σ_1 and σ_2 and that the stresses have changed to a present value of σ'_1 and σ'_2 respectively.

Denote the angle between the directions of σ_2 and σ'_2 by a, as shown in Figure 32. The variations in the stress components $\Delta\sigma$ and $\Delta\tau$, acting on the plane making an angle of θ with the plane on which σ_1 acted are, considering fundamental stress theory:

$$\Delta\sigma = \frac{\sigma'_1 + \sigma'_2 - \sigma_1 - \sigma_2}{2} + \frac{\sigma'_1 - \sigma'_2}{2} \cos 2(\theta - a) - \frac{\sigma_1 - \sigma_2}{2} \cos 2\theta, \tag{34}$$

$$\Delta\tau = \frac{\sigma'_1 - \sigma'_2}{2} \sin 2(\theta - a) + \frac{\sigma_1 - \sigma_2}{2} \sin 2\theta. \tag{35}$$

Differentiating eq 34 and considering eq 35 it may be shown that at any point there are two planes perpendicular to each other where $\Delta\tau$ vanishes and $\Delta\sigma$ takes maximum and minimum values. Let these values be p and q respectively. Then p and q as well as the angle θ_0 between the plane on which p acts and the plane on which σ_1 acts are given by:

$$\left.\begin{matrix} p \\ q \end{matrix}\right\} = \frac{(\sigma'_1 + \sigma'_2) - (\sigma_1 + \sigma_2)}{2} + \{(\sigma'_1 - \sigma'_2)^2 + (\sigma_1 - \sigma_2)^2 - 2(\sigma'_1 - \sigma'_2)(\sigma_1 - \sigma_2)\cos 2a\}^{1/2}$$

$$\tan\theta_0 = \frac{(\sigma'_1 - \sigma'_2)\sin 2a}{2p - \{\sigma'_1 + \sigma'_2 - 2\sigma_2 - (\sigma'_1 - \sigma'_2)\cos 2a\}}. \tag{36}$$

It can be shown that the magnitudes of $\Delta\sigma$ and $\Delta\tau$ on a plane making an angle β with the plane on which $\Delta\tau$ vanishes are given by:

$$\left.\begin{aligned} \Delta\sigma &= \frac{p+q}{2} + \frac{p-q}{2}\cos 2\beta, \\ \Delta\tau &= \frac{p-q}{2}\sin 2\beta. \end{aligned}\right\} \tag{37}$$

This leads to the conclusion that $\Delta\sigma$ and $\Delta\tau$ can be treated as if they were a normal and a shear stress respectively, and thus q and p can be treated as if they were principal stresses. Let p and q be called apparent principal stresses.

Photoelastic gages respond to the variation in normal stress. Therefore it may be possible to determine the apparent principal stresses. In the special case when both σ_1 and σ_2 are zero, p and q coincide with σ'_1 and σ'_2. Therefore if the gage is fixed in a body already subjected to stress the present *apparent* principal stresses may be determined, but if the gage is fixed in a body free from stress initially, then the present *actual* principal stresses will be determined.

If the initial principal stresses σ_1 and σ_2 are known the present principal stresses can be calculated from:

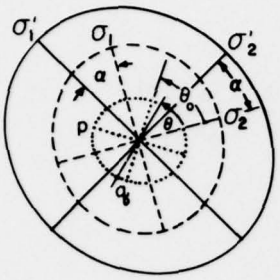

Figure 32. Initial, present, and apparent principal stresses. (After Hiramatsu[17].)

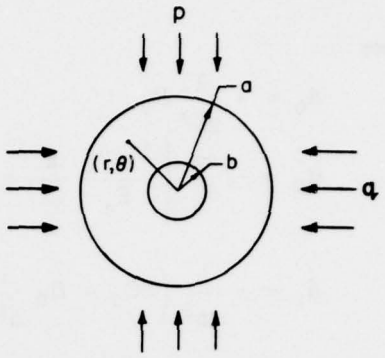

Figure 33. Coordinate system in Hiramatsu's[17] analysis.

$$\left.\begin{aligned} \left.\begin{matrix}\sigma'_1\\ \sigma'_2\end{matrix}\right\} &= \frac{\sigma_1+\sigma_2+p+q}{2} + \frac{1}{2}\{(\sigma_1-\sigma_2)^2+(p-q)^2+2(\sigma_1-\sigma_2)(p-q)\cos 2\theta_0\}^{1/2}, \\ \tan\alpha &= \frac{(p-q)\sin 2\theta_0}{2\sigma'_1-\{2\sigma_2+(p+q)-(p-q)\cos 2\theta_0\}} \end{aligned}\right\} \quad (38)$$

θ_0 is always greater than α, that is, the apparent principal stresses exaggerate the variation in direction, or change in direction, of the original principal stresses, especially when these are of a high magnitude.

Suppose the gage was inserted in an elastic body at a time when that body was free from stress. Suppose, further, that the body is now subjected to compressive stress, the principal stresses being p and q in the vicinity of the gage but outside the area of stress concentration produced by the gage. p is always assumed numerically greater than q.

The stress distribution in the gage will then depend upon p and q, the Young's modulus E_h and the Poisson's ratio ν_h of the containing elastic body. When the gage is observed under polarized light the isochromatics form contours of principal stress difference in the gage. Let the Young's modulus and the Poisson's ratio of glass be E_g and ν_g respectively, the outer and inner radii be a and b, and let us define the polar coordinates as shown in Figure 33. Assuming that the contact between the gage and the body is welded, without discontinuity, and that $q = 0$, the stress components σ_r, σ_θ and $\tau_{r\theta}$ at any point in the gage are:

$$\left.\begin{aligned} \sigma_r &= 2A_0 + B_0 r^{-2} - (6B_2 r^{-4} + 2C_2 + 4D_2 r^{-2})\cos 2\theta, \\ \sigma_\theta &= 2A_0 - B_0 r^{-2} + (12A_2 r^2 + 6B_2 r^{-4} + 2C_2)\cos 2\theta, \\ \tau_{r\theta} &= (6A_2 r^2 - 6B_2 r^{-4} + 2C_2 - 2D_2 r^{-2})\sin 2\theta, \end{aligned}\right\} \quad (39)$$

where

$$A_0 = -\frac{1}{2b^2} B_0 ,$$

$$B_0 = -\frac{ap}{E_h}\left\{\frac{1-\nu_g}{E_g}\frac{a}{b^2} + \frac{1+\nu_g}{E_g}\frac{1}{a} - \frac{1+\nu_h}{E_h}\left(\frac{1}{a} - \frac{a}{b^2}\right)\right\}^{-1} ,$$

$$A_2 = -\frac{1}{3b^2}\left(2C_2 + D_2\frac{1}{b^2}\right),$$

$$B_2 = -\frac{b^4}{3}\left(C_2 + 2D_2\frac{1}{b^2}\right),$$

$$C_2 = (\beta'\gamma - \beta\gamma')/(\alpha\beta' - \alpha'\beta) ,$$

$$D_2 = (\alpha'\gamma - \alpha\gamma')/(\alpha'\beta - \alpha\beta') ,$$

$$\alpha = 4\left(1 - \frac{a^2}{b^2}\right)\left(\frac{3-\nu_h}{E_h} + \frac{1+\nu_g}{E_g}\right),$$

$$\beta = \frac{2}{a^2}\left\{\frac{3-\nu_h}{E_h}\left(1 - \frac{a^4}{b^4}\right) - \frac{1+\nu_g}{E_g}\frac{a^4}{b^4} - \frac{3-\nu_g}{E_g}\right\} ,$$

$$\gamma = -4p/E_g ,$$

$$\alpha' = -\frac{2(1+\nu_h)(3-\nu_h)}{E_h}\left(\frac{b^4}{a^4} - \frac{4a^2}{b^2} + 3\right) + \frac{8(3+\nu_h\nu_g)}{E_g}\frac{a^2}{b^2}$$
$$+ \frac{2(1+\nu_g)(3-\nu_h)}{E_g}\frac{b^4}{a^4} - \frac{6(1+\nu_h)(1+\nu_g)}{E_g} ,$$

$$\beta' = -\frac{4(1+\nu_h)(3-\nu_h)}{E_h}\left(\frac{b^2}{a^4} - \frac{a^2}{b^4}\right) + \frac{4(3+\nu_h\nu_g)}{E_g}\frac{a^2}{b^4}$$
$$+ \frac{4(1+\nu_g)(3-\nu_h)}{E_g}\frac{b^2}{a^4} + \frac{12(\nu_h-\nu_g)}{E_g}\frac{1}{a^2} ,$$

$$\gamma' = \frac{6p(1+\nu_h)}{E_h} .$$

Should the principal stress p be zero but the other one q have a finite magnitude, the stress components at any point in the gage may be obtained by substituting q and $\theta + \pi/2$ respectively in eq 39.

When both q and p are not zero the stress components in the gage are given by the algebraic sums of the corresponding components under the two assumed stress states.

Once the stress components at any point in the gage have been found, the difference between the principal stresses $\sigma_1 - \sigma_2$ is calculated from:

$$\sigma_1 - \sigma_2 = \{(\sigma_r - \sigma_\theta)^2 + 4\tau_{r\theta}^2\}^{1/2} . \tag{40}$$

Figure 34 shows theoretical isochromatics, drawn under the assumptions that the Young's moduli of glass and the containing body are 6.3×10^5 and 2.1×10^5 kg/cm respectively, that the Poisson's ratio for both is 0.2, and that the gage is welded to the body.

The shape of the isochromatics is much affected by the ratio q/p, but only little affected by E_h and ν_h. When q is equalto p, all the isochromatics become concentric circles.

Barron[1], using the basic equations derived by Hiramatsu, has also determined the stress distribution in a hollow cylindrical inclusion bonded into an elastic host material and subjected to biaxial stress. Referring to Figure 29, the isochromatic fringe order n at any point in the inclusion is given, for plane stress, by:

$$n_{(r,\theta)} = \left\{\frac{t}{f^*}\left[p\,k_1\,(1+\eta) - p\,k_2\,(1-\eta)\cos 2\theta\right]^2 + p^2\,k_3^2\,(1-\eta)^2\sin^2 2\theta\right\}^{1/2} \tag{41}$$

where k_1, k_2 and k_3 are functions of a/b; the elastic moduli and Poisson's ratio of the meter and host material and the radius to the point in the meter being considered.

These constants are derived by Barron as follows:

$$k_1 = 2B_0\,r^{-2}$$

$$k_2 = 4\,(3\,A_2 r^2 + 3\,B_2 r^{-4} + C_2 + D_2\,r^{-2})$$

$$k_3 = 4\,(3\,A_2 r^2 - 3\,B_2 r^{-4} + C_2 + D_2 r^{-2})$$

where

$$A_0 = \frac{-b^{-2}B_0}{2}$$

$$B_0 = \frac{-a}{E}\Bigg/\left[\frac{(1-\nu_g)}{E_g}\,ab^{-2} + \frac{(1+\nu_g)}{E_g}\,a^{-1} - \frac{(1+\nu_h)}{E_h}\,(a^{-1} - ab^{-2})\right]$$

$$A_2 = -\frac{b^{-2}}{3}\,(2\,C_2 + b^{-2}\,D_2)$$

$$B_2 = -\frac{b^4}{3}\,(C_2 + 2\,b^{-2}\,D_2)$$

where

$$C_2 = \left(\frac{\beta'\gamma - \beta\gamma'}{\alpha\beta' - \alpha'\beta}\right)$$

*f is the material fringe value where $f = [(\sigma_1 - \sigma_2)t]/n$.

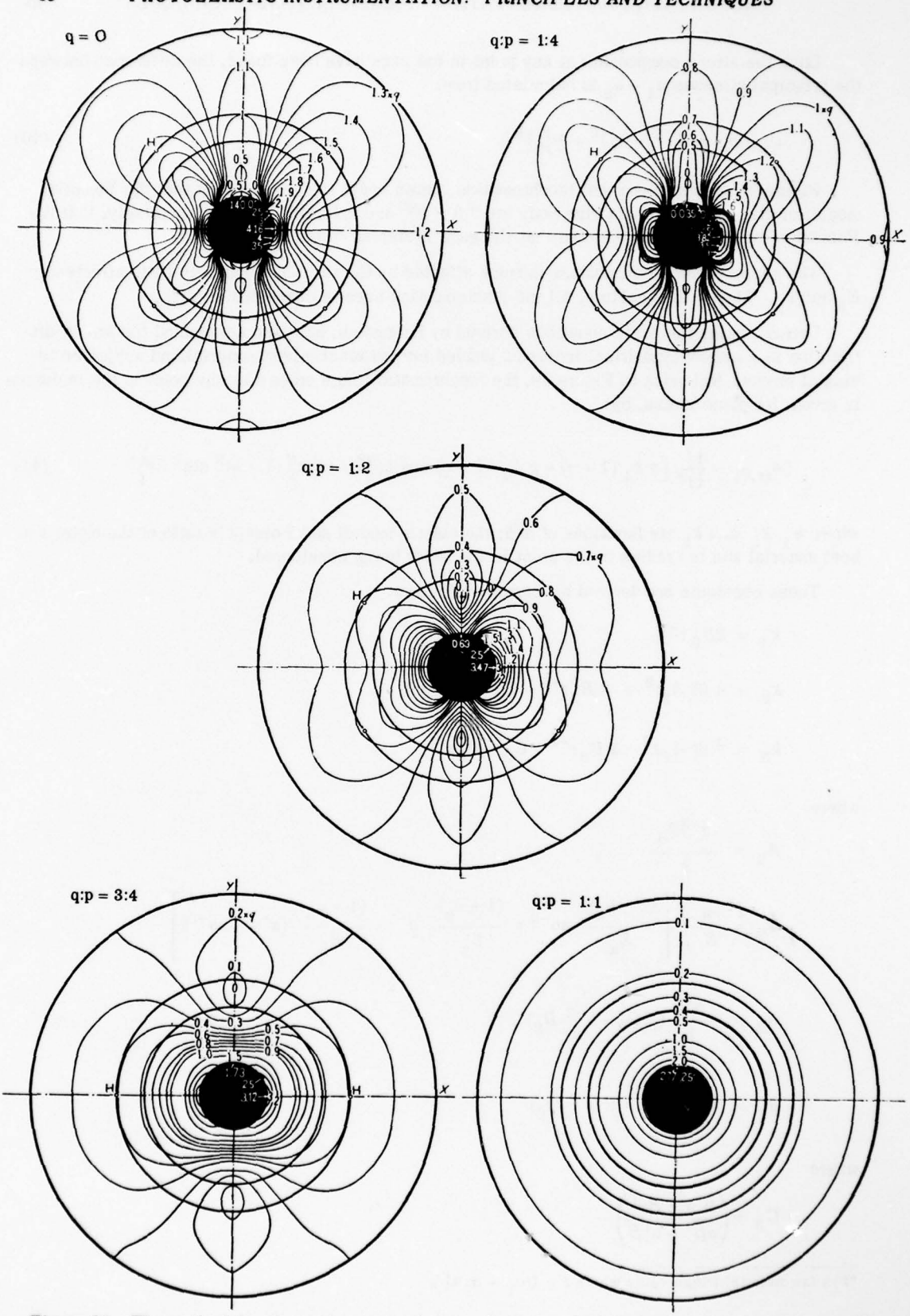

Figure 34. Theoretical isochromatics appearing in a hollow cylindrical gage. (After Hiramatsu[17].)

$$D_2 = \left(\frac{\alpha'\gamma - \gamma'\alpha}{\alpha'\beta - \alpha\beta'}\right)$$

where

$$\alpha = 4\,(1 - a^2b^{-2})\left[\frac{(3 - \nu_h)}{E_h} + \frac{(1 + \nu_g)}{E_g}\right]$$

$$\beta = 2a^{-2}\ \frac{(3 - \nu_h)\,(1 - a^4\,b^{-4})}{E_h} - \frac{(1 + \nu_g)\,a^4b^{-4}}{E_g} - \frac{(3 - \nu_g)}{E_g}$$

$$\gamma = \frac{-4}{E_h}$$

$$\alpha' = \frac{-2\,(1 + \nu_h)\,(3 - \nu_h)\,(a^{-4}b^4 - 4a^2\,b^{-2} + 3)}{E_h} +$$

$$+ \frac{8\,(3 + \nu_h\nu_g)\,a^2\,b^{-2} + 2\,(1 + \nu_g)\,(3 - \nu_h)\,a^{-4}b^4 - 6\,(1 + \nu_h)\,(1 + \nu_g)}{E_g}$$

$$\beta' = \frac{-4\,(1 + \nu_h)\,(3 - \nu_h)\,(a^{-4}b^2 - a^2b^{-4}}{E_h} +$$

$$+ \frac{4\,(3 + \nu_h\nu_g)\,a^2b^{-4} + 4\,(1 + \nu_g)\,(3 - \nu_h)\,a^{-4}b^2 + 12\,(\nu_h - \nu_g)\,a^{-2}}{E_g}$$

and

$$\gamma' = \frac{6\,(1 + \nu_h)}{E_h}.$$

Roberts et al. have shown experimentally,[27] and Barron theoretically,[1] that there are two points at which the fringe order may be measured for the evaluation of the major principal stress, depending upon the stress ratio η:

When $\eta < \frac{1}{3}$, the point is $r = 2b$, $\theta = 45°$ (45° point)

When $\eta > \frac{1}{3}$, the point is $r = 1.75b$, $\theta = 90°$ (90° point)

Three axes can be readily identified: $\theta = 0°$ (major), $\theta = 45°$ and $\theta = 90°$ (minor). The major axis is not suitable for fringe order measurements as the stress gradient along it changes too slowly, giving very low sensitivity.

For the minor and the $\theta = 45°$ axes eq 41 simplifies to:

$$p = n_{(r,\,\theta=90°)} \frac{f}{t[(k_1 + k_2) + \eta\,(k_1 - k_2)]} = \frac{nf}{tJ_1} \tag{42}$$

$$p = n_{r,\,\theta=45°)} \frac{f}{t[(k_1^2\,(1+\eta)^2 + k_3^2\,(1-\eta)^2]^{1/2}} = \frac{nf}{tJ_2}\,. \tag{43}$$

When $n = 1$ and $t = 1$, $1/J_2$ becomes equal to the meter sensitivity factor S, which, when multiplied by the unit material fringe value f, gives the meter sensitivity in terms of psi in./fringe of inclusion length.

Using eq 42 and 43 the meter sensitivity factor S, in terms of the material fringe value f, can be calculated for all points along the 45° and minor axes for various stress ratios η, various values of the Poisson's ratios ν_g and ν_h, and Young's modulus ratio E_h/E_g. This has been done by Hawkes et al.[32] and the results are shown in Figure 35.

The most common stress change encountered in practice is uniaxial ($\eta = 0$). From Figure 35 it will be noted that for uniaxial stress fields there is a point on the 45° axis at which the gage sensitivity is a maximum (i.e. the meter sensitivity factor is a minimum). The "45° point" is so clearly defined (see Fig. 30, 31) that it would be convenient to have the sensitivity determined by measuring the fringe order at that point for all stress fields, biaxial as well as uniaxial. This would then be the "standard sensitivity factor" for the gage. The 45° point cannot be used when the stress ratio $\eta > \frac{1}{3}$ as it is not easily identified, and measurements must be made on the minor axis in such biaxial stress fields.

For the sensitivity factor to remain constant the measurement point on the minor axis should be fixed so that the average sensitivity when the stress ratio η varies from 0 to 1 will equal the sensitivity determined by measuring the fringe order at the 45° point for uniaxial stress fields. For the example shown in Figure 35, with values $E_h/E_g = 10^{-1}$ and $\nu_h = \nu_g = 0.25$, the optimum 90° point is at a radius of $1.32b$ and the standard sensitivity factor, S_0, is $0.470f$ psi in./fringe.

Figure 36 shows the variation of the J_2 factor of eq 43 for the 45° point ($\eta = 0$), and illustrates the influence of the ratio E_h/E_g and the Poisson's ratio of the host and gage material ν_h and ν_g.

The variation of the optimum 90° point radius with the Poisson's ratio of the inclusion and the host material, and with different values of the modular ratio E_h/E_g, is given in Table I, together with the various sensitivity factors, for stress ratios of unity and zero.

Soft birefringent inclusions – The photoelastic strainmeter

The state of stress in an elastic medium in situ may be deduced from measurements of strain on a soft elastic inclusion inserted into a hole in the structure under observation. If it may be assumed that the inclusion has a sufficiently low elastic modulus relative to that of the surrounding medium, the hole into which the inclusion is set must deform as though the inclusion were not present.

The soft inclusion thus acts as a strainmeter, and if it consists of an optically stress-birefringent material it will form a photoelastic biaxial gage.

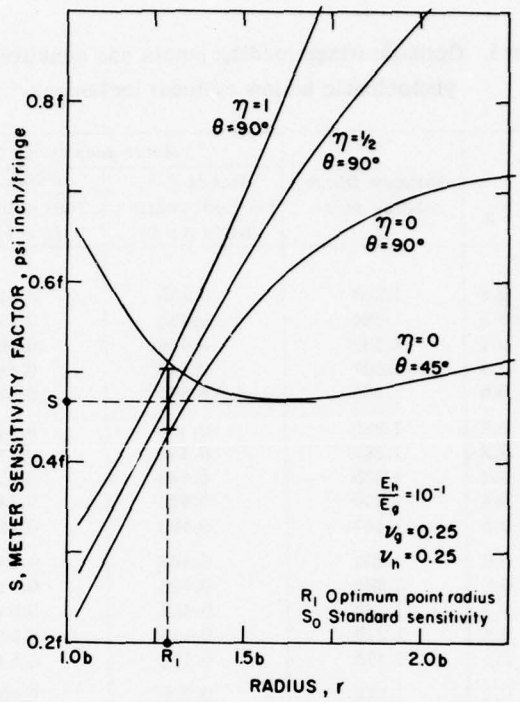

Figure 35. Determination of optimum fringe reading point.

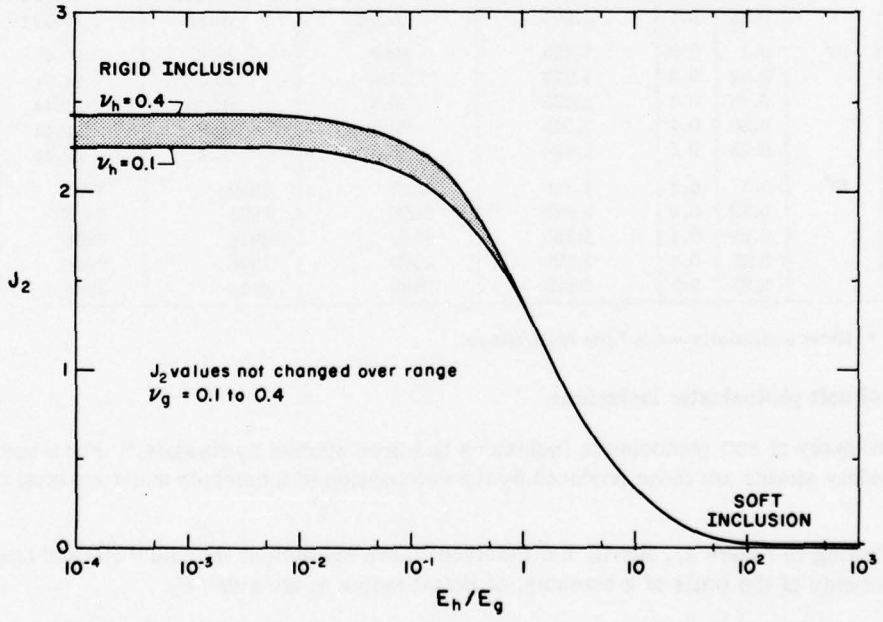

Figure 36. Variation of J_2 factor against E_h/E_g ratio for two values of ν_g.

Table I. Optimum fringe reading points and sensitivities of photoelastic hollow cylinder inclusions.

E_h/E_g	ν_g	ν_h	Optimum fringe reading point	Meter sensitivity factor, S *		
				Standard S (at "45° point," when $\eta = 0$)	Biaxial stress values	
					"90° point," ($\eta = 1$)	"90° point," ($\eta = 0$)
10^{-4}	0.1	0.2	1.28*b*	0.435	0.472	0.392
	0.32	0.2	1.28*b*	0.435	0.472	0.392
	0.25	0.1	1.33*b*	0.445	0.469	0.419
	0.25	0.4	1.20*b*	0.410	0.484	0.342
	0.25	0.5	1.16*b*	0.397	0.483	0.311
10^{-2}	0.1	0.2	1.28*b*	0.438	0.472	0.392
	0.32	0.2	1.28*b*	0.439	0.472	0.393
	0.25	0.1	1.33*b*	0.448	0.471	0.420
	0.25	0.4	1.20*b*	0.414	0.486	0.344
	0.25	0.5	1.16*b*	0.400	0.486	0.314
10^{-1}	0.1	0.2	1.28*b*	0.467	0.510	0.426
	0.32	0.2	1.29*b*	0.469	0.510	0.428
	0.25	0.1	1.34*b*	0.483	0.510	0.358
	0.25	0.4	1.21*b*	0.448	0.521	0.375
	0.25	0.5	1.17*b*	0.430	0.519	0.343
1	0.1	0.2	1.24*b*	0.709	0.805	0.619
	0.32	0.2	1.30*b*	0.741	0.795	0.681
	0.25	0.1	1.31*b*	0.745	0.795	0.691
	0.25	0.4	1.22*b*	0.701	0.798	0.596
	0.25	0.5	1.20*b*	0.685	0.805	0.571
10^{2}	0.1	0.2	1.12*b*	23.6	29.8	17.4
	0.32	0.2	1.27*b*	27.4	30.0	24.54
	0.25	0.1	1.22*b*	26.3	30.16	22.44
	0.25	0.4	1.22*b*	26.3	30.3	22.44
	0.25	0.5	1.22*b*	26.3	30.3	22.44
10^{4}	0.1	0.2	1.12*b*	2320	2959	1707
	0.32	0.2	1.27*b*	2690	2955	2413
	0.25	0.1	1.22*b*	2580	2976	2206
	0.25	0.4	1.22*b*	2580	2976	2206
	0.25	0.5	1.22*b*	2580	2976	2206

* Meter sensitivity = $S \times f$ psi inch/fringe.

Theory of soft photoelastic inclusions

The theory of soft photoelastic inclusions has been studied by Hawkes.[32] For a soft inclusion the boundary strains are those produced by the deformation of a borehole under uniaxial or biaxial stress.

Referring to Figure 37, Merrill and Peterson[22] have shown that the radial (U) and tangential (V) displacements of the walls of a borehole, of initial radius a, are given by:

$$U = \frac{a}{E_h} [(q+p) + 2(q-p)\cos 2\alpha] \qquad (44)$$

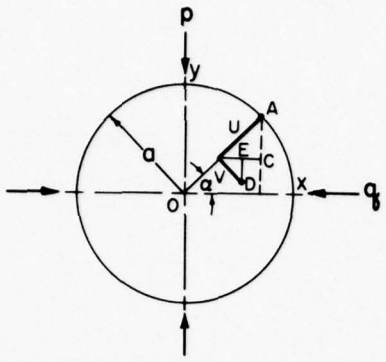

Figure 37. Deformation of a borehole.

and

$$V = -\frac{2a}{E_h}(q-p)\sin 2\alpha \tag{45}$$

where E_h is the modulus of the material into which the borehole is drilled and p and q are the principal stresses acting.

Let us now determine the strains ϵ_y and ϵ_x, assuming that the inclusion is solid.

At any point A on the surface of the borehole (Fig. 37):

$$\epsilon_y = \frac{AC + ED}{AB} = \frac{U\sin\alpha + V\cos\alpha}{a\sin\alpha}. \tag{46}$$

Substituting for U and V from eq 44 and 45, and letting

$$\frac{q+p}{E_h} = W_1 \text{ and } \frac{q-p}{E_h} = W_2$$

$$\epsilon_y = \frac{(W_1 a + 2a W_2 \cos 2\alpha)\sin\alpha - 2W_2 a \sin 2\alpha \cos\alpha}{a\sin\alpha}.$$

Using

$$\cos 2x = 1 - 2\sin 2x$$
$$\sin 2x = 2\sin x\cos x$$
$$\sin^2 x + \cos^2 x = 1$$
$$\epsilon_y = W_1 + 2W_2 - 4W_2\sin^2\alpha - 4W_2\cos^2\alpha$$
$$= W_1 - 2W_2$$
$$= \frac{3p-q}{E_h}. \tag{47}$$

Similarly

$$\epsilon_x = \frac{3q-p}{E_h}. \tag{48}$$

This means that the strains ϵ_x and ϵ_y are independent of the angle α, i.e. the strain in the inclusion is uniform and independent of the Poisson's ratio of the material surrounding the borehole.

We must now determine the principal stress difference $(\sigma_2 - \sigma_1)$ at any point in the inclusion, assuming that it has a central axial hole small enough that the boundary stresses are not changed by its presence. From eq 47 and 48:

$$p = \frac{3}{8} E_h \left(\epsilon_y + \frac{\epsilon_x}{3}\right) \tag{49}$$

$$q = \frac{3}{8} E_h \left(\epsilon_x + \frac{\epsilon_y}{3}\right). \tag{50}$$

Putting $L = \frac{\epsilon_x}{\epsilon_y}$ in eq 44

$$p = \frac{3}{8} E_h \epsilon_y \left(1 + \frac{L}{3}\right) = \frac{E_h}{8} \epsilon_y (3 + L). \tag{51}$$

Putting $\eta = \frac{q}{p}$ in eq 47

$$\epsilon_y = p \frac{(3 - \eta)}{E_h}. \tag{52}$$

Substituting for ϵ_y in eq 51 we have

$$(3 - \eta)(3 + L) = 8$$

i.e.

$$L = \frac{3\eta - 1}{3 - \eta}. \tag{53}$$

The boundary strains ϵ_y, ϵ_x on the inclusion set up stresses given by

$$\sigma_y = \frac{E_g}{(1 - \nu_g^2)} (\epsilon_y + \nu_g \epsilon_x) = \frac{E_g}{(1 - \nu_g^2)} \epsilon_y (1 + \nu_g L) \tag{54}$$

and

$$\sigma_x = \frac{E_g}{(1 - \nu_g^2)} (\epsilon_x + \nu_g \epsilon_y) = \frac{E_g}{(1 - \nu_g^2)} \epsilon_y (L + \nu_g). \tag{55}$$

Substituting for L and ϵ_y

$$\sigma_y = \frac{E_g}{(1 - \nu_g^2)} \frac{p}{E_h} (3 - \eta) \left[1 + \nu_g \frac{(3\eta - 1)}{3 - \eta}\right]$$

$$= p \frac{E_g}{E_h} Q_1 \tag{56}$$

and

$$\sigma_x = \frac{E_g}{(1-\nu_g^2)} \frac{p(3-\eta)}{E_h} \left[\nu_g + \frac{(3\eta-1)}{3-\eta}\right]$$

$$= \frac{E_g}{E_h} Q_2 \tag{57}$$

The stresses are now concentrated by the central hole, radius b, and become, in polar coordinates:

$$\sigma_r = p \frac{E_g}{E_{hr}} \left[\frac{Q_1+Q_2}{2}\left(1-\frac{b^2}{r^2}\right) + \frac{Q_1-Q_2}{2}\left(1-\frac{4b^2}{r^2}+\frac{3b^4}{r^4}\right)\cos 2\alpha\right]$$

$$= p \frac{E_g}{E_h} N_1 \tag{58}$$

$$\sigma_\theta = p \frac{E_g}{E_h} \left[\frac{Q_1+Q_2}{2}\left(1+\frac{b^2}{r^2}\right) - \frac{Q_1-Q_2}{2}\left(1+\frac{3b^4}{r^4}\right)\cos 2\alpha\right]$$

$$= p \frac{E_g}{E_h} N_2 \tag{59}$$

$$r_{r\theta} = p \frac{E_g}{E_h} \left[\frac{Q_1-Q_2}{2}\left(1+\frac{2b^2}{r^2}-\frac{3b^4}{r^4}\right)\sin 2\alpha\right]$$

$$= p \frac{E_g}{E_h} N_3 . \tag{60}$$

The principal stress difference at any point is now given by:

$$\sigma_1 - \sigma_2 = p \frac{E_g}{E_h} [(N_1-N_2)^2 + 4N_3^2]^{1/2}$$

$$= p \frac{E_g}{E_h} M . \tag{61}$$

The relationship between the isochromatic fringe order at the point r, α and the principal stress difference is given by:

$$\frac{nf}{t} = p \frac{E_g}{E_h} M . \tag{62}$$

And for unit length and fringe order eq 62 becomes:

$$S = M f \frac{E_h}{E_g} \tag{63}$$

where S is the meter sensitivity.

Interpretation of Birefringent Pattern on Hollow-Cylinder Photoelastic Inclusions

The birefringent pattern in a hollow-cylinder photoelastic inclusion completely and instantaneously identifies the biaxial stress field in the plane of measurement, perpendicular to the longitudinal axis of the gage.

Separation of the biaxial stresses

Several methods have been proposed by various authorities to determine the separate stresses p and q from the optical pattern displayed by a hollow-cylinder photoelastic inclusion under load.

Measurement at two points. Barron[1] shows that if two measurements are made, one on the $\theta = 0°$ axis and one on the $\theta = 90°$ axis, and both at the same radius, then:

$$p = f/4\, t\, k_1 k_2 [k_2 (n_x + n_y) + k_1 (n_x - n_y)] \tag{64}$$

and

$$q = f/4\, t\, k_1 k_2 [k_2 (n_y + n_x) - k_1 (n_y - n_x)] \tag{65}$$

where t is the length (thickness) of the cylinder, f is the material fringe value, n_x, n_y and n_{xy} are the fringe orders on the $\theta = 0°$, 90°, and 45° axes.

The method is discounted as being too complicated and liable to inaccuracy, except under high stress, unless precision optical equipment is used, preferably incorporating Babbinet compensation. This is also one of two methods suggested by Hiramatsu.[17]

Determination of the stress ratio q/p: Hiramatsu's method. Hiramatsu's method is to use the shape of the pattern, over which certain points A, B, C etc., are defined, as shown in Figure 38a. At point H the fringe order is the maximum that occurs on the outer circle and at point X it has the same value. At point Y the fringe order is the minimum occurring in the meter.

From the radial position of point X or of point Y the stress ratio q/p is determined by referring to the relationship shown in Figure 38b. Young's modulus and Poisson's ratio of the host rock have very little effect on this relationship. When η varies from 0 to 0.5 the position Y is used to define the ratio of stresses.

Unfortunately the position X does not vary very much in radius as η changes. Hence errors could be significant. This criticism does not apply to point Y, where the radial variation of position is quite large in the range $\eta = 0.5$ to 0.9.

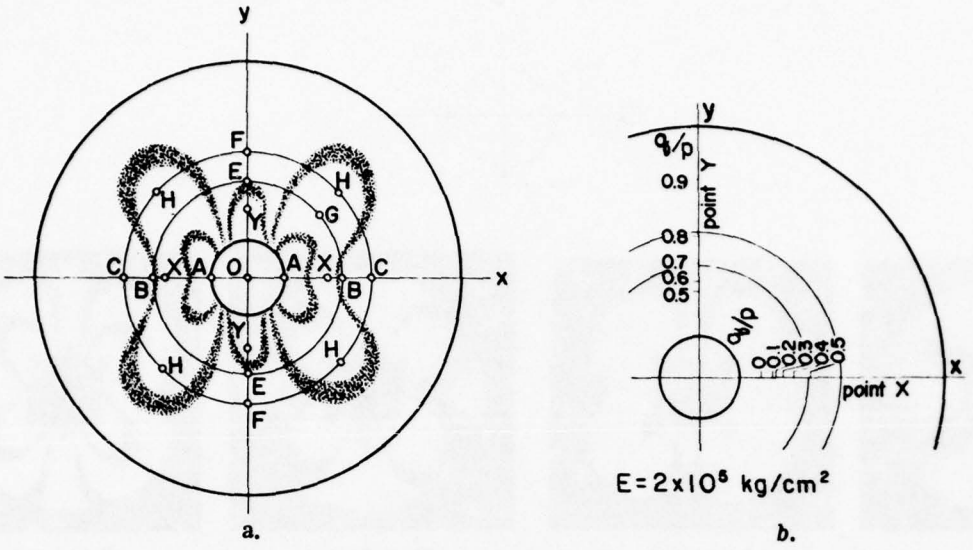

Figure 38. Determination of the ratio q/p. (After Hiramatsu[17].)

Determination of the stress ratio q/p: Sheffield method (A). The ratio of the applied stresses may be estimated from the overall shape of the fringe pattern. Figure 39 shows fringe patterns obtained for ratios of η of 0, 0.2, 0.6, 0.9 and 1.0. It can be seen from these photographs that it is quite feasible to obtain an estimate of η from the variations in the overall shape of the fringe pattern.

However, not only does the pattern shape change with η but it also varies with the magnitude of p. Hence, to identify the ratio η by inspection over a range of both p and q the observer must remember a series of standard fringe patterns and be able to readily distinguish between them. Until the observer can make these estimations with confidence he must carry photographs of standard fringe patterns for use as a visual comparator.

The accuracy of such a system is adequate for many practical field problems.

Determination of the stress ratio q/p: Sheffield method (B). The ratio of the applied stresses may be estimated by observation of zero points on the p axis. Figure 40 shows the variation of $[(k_1 - k_2) + \eta\,(k_1 + k_2)]$ with radius for various values of η when $E = 10 \times 10^6$ psi. In the range $0.2 \leq \eta \leq 0.9$ there is some radius at which this proportionality constant is zero, i.e. the fringe order is zero. Hence there is a black spot on the fringe pattern and the radial position of this spot varies with η. Since this is a zero point it should always be visible regardless of the magnitude of the stress level p.

Hence a measure of this radial position of the zero point is a potential measure of η, which, theoretically, should be equally suitable at both high and low stress levels.

Now it can be shown that $n_x = 0$ when

$$\eta = \frac{k_2 - k_1}{k_2 + k_1} \quad . \tag{66}$$

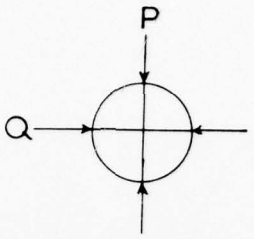

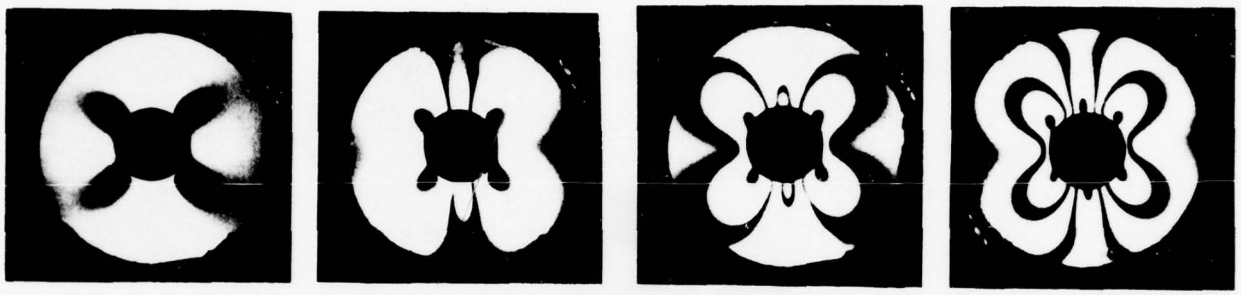

One fringe *Two fringes* *Three fringes* *Four fringes*

a. *Biaxial fringe patterns q = 0.*

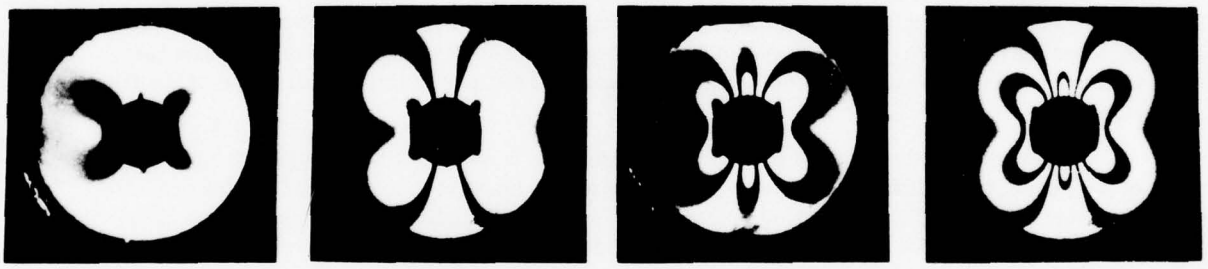

One fringe *Two fringes* *Three fringes* *Four fringes*

b. *Biaxial fringe patterns q = p/4.*

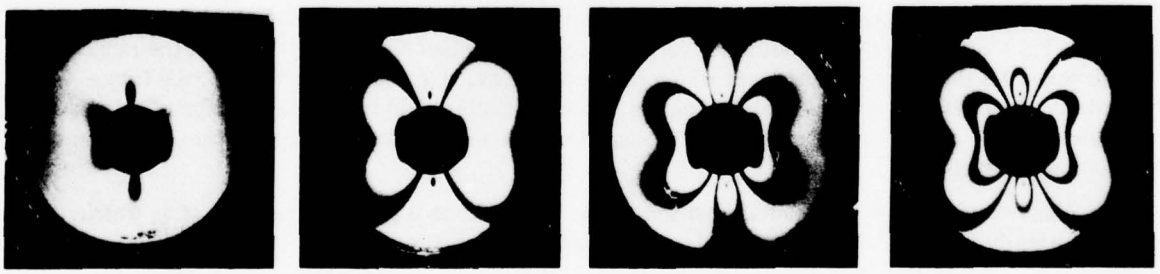

One fringe *Two fringes* *Three fringes* *Four fringes*

c. *Biaxial fringe patterns q = p/2.*

Figure 39. Photographic comparator of stressmeter patterns.

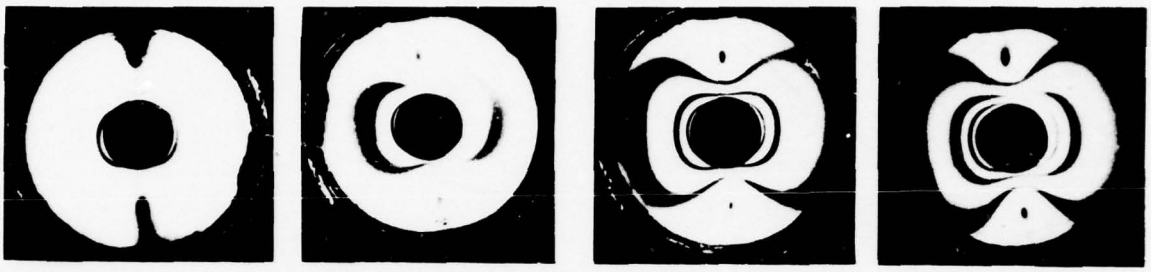

One fringe | Two fringes | Three fringes | Four fringes

d. Biaxial fringe patterns q/p = ¾.

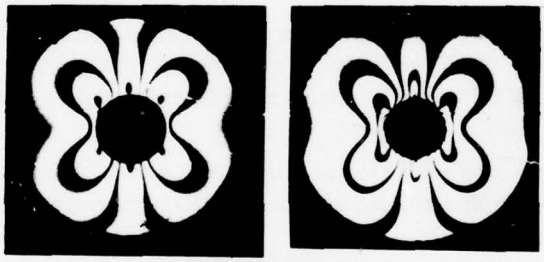

q = 0 | q = 0.2 p

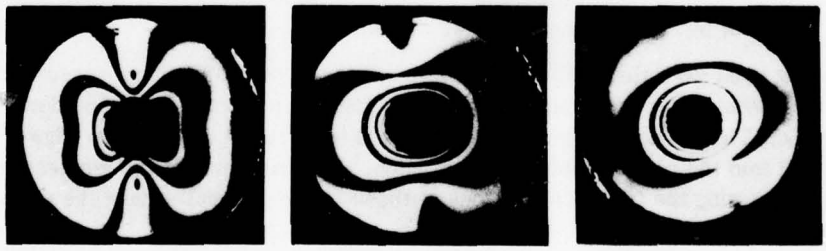

q = 0.6 p | q = 0.9 p | q = p

e. Behavior of zero points with principal stress ratios.

Figure 39 (Cont'd).

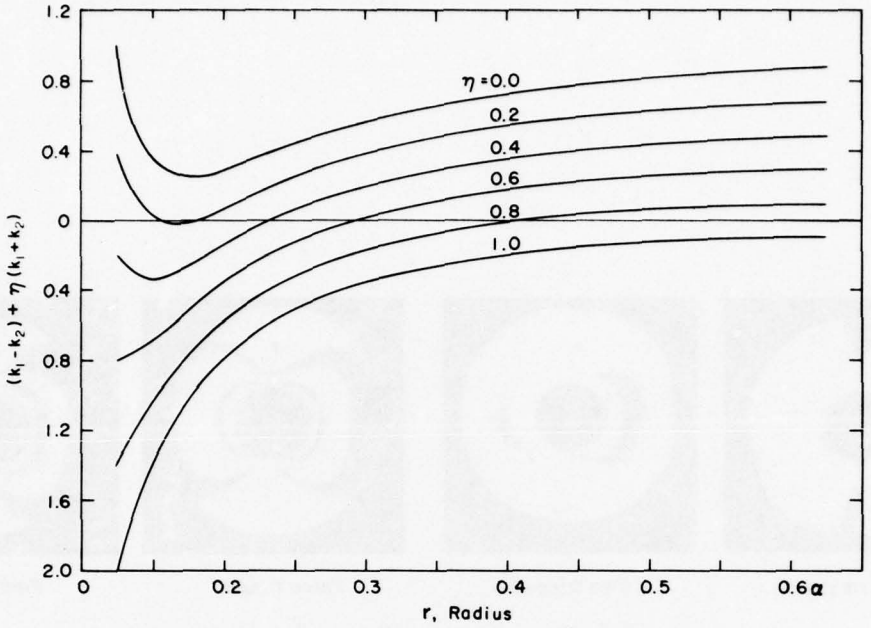

Figure 40. Variation of proportionality constant with radius, for various values of q/p (Barron).

Hence the radial position of the zero point can be calculated for all ratios of η. Figure 41 shows the radial position of the zero point for the range of η from 0.2 to 0.9. It can also be shown that the radial position of this point is almost entirely unaffected by variations in the host rock modulus.

Figure 39 shows the zero point clearly at values of η of 0.25, 0.50 and 0.75, and measurements from these photographs are in excellent agreement with the theoretical graph.

Determination of the magnitude of the greatest stress p

After the stress ratio η is determined the magnitude of the greatest stress p is evaluated by relating the fringe order at a specific point of measurement to the major principal stress, either by direct calibration or by calculation (see eq 42 and 43).

Depending upon the value of the stress ratio either one of two optimum measurement points is used. The 45° point is very precisely defined as a discrete point and is self-evident on the relevant fringe patterns. The 90° point is not self-evident and is therefore fixed as the edge of an opaque collar inserted into the central hole of the inclusion. The magnitude of the greatest stress is obtained by measuring the fringe order at one of these points and multiplying the measured value by the meter sensitivity factor.

Determination of the sign of the greatest stress p

Whether the greatest stress is tensile or compressive is determined by observing if the fringe order at any point on the minor axis is advanced or retarded when the Tardy compensation procedure is carried out.

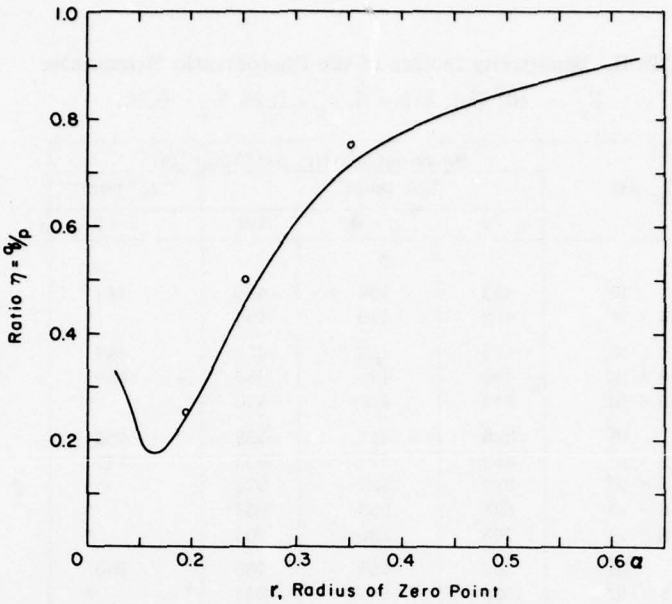

Figure 41. Radial variation of zero point with biaxial stress ratio (Barron). Experimental points are from photographs in Figure 39.

Sensitivity of the photoelastic stressmeter

From Figure 36 and the results quoted in Table I the following conclusions may be drawn concerning the photoelastic stressmeter:

1. The Poisson's ratio of the inclusion plays no part in determining the optimum 90° point radius and the standard sensitivity factor.

2. The optimum 90° point radius increases from 1.16b to 1.33b as the Poisson's ratio of the host material decreases from 0.5 to 0.1.

3. The standard sensitivity factor increases by roughly 10% as the Poisson's ratio of the host material decreases from 0.5 to 0.1.

4. In a host material with a Poisson's ratio of 0.1 an error of up to 5% is possible when applying the standard sensitivity factor for fringe order/stress conversions in biaxial stress fields. The possible error increases to 20% when Poisson's ratio of the host material falls to 0.5.

The glass photoelastic stressmeter described by Roberts et al.[27] has a Young's modulus of 10^7 psi, a Poisson's ratio of 0.25, an inner hole/inclusion diameter ratio of 0.2 (i.e. b/a = 0.2), and a material fringe value *f* of 1024 psi inch/fringe in white light illumination.

The theoretical sensitivity factors of this gage when set into various materials with different Young's moduli are given in Table II, and plotted in Figure 42. In this example the Poisson's ratio of the host material ranges from 0.2, an average value for rocks, to 0.5, the maximum theoretical value for a material creeping under load without volume change. When Poisson's ratio for the host material is 0.2 the sensitivity (uniaxial value) remains constant at 450 psi inch/fringe, as the modulus of the host material increases up to 5×10^6 psi. This indicates that the stressmeter is acting as a "rigid inclusion" over this range.

Table II. Sensitivity factors of the Photoelastic Stressmeter

$E_g = 10^7$ psi, $a/b = 5$, $\nu_g = 0.25$, $\nu_h = 0.20$.

E_h, psi	Meter sensitivity, psi/fringe/in.			
	"90° point"			"45° point"
	$\eta = 1$	$\eta = 0$	Avg	$\eta = 0$
10^4	491	409	450	447
5×10^4	492	410	451	*
10^5	494	412	453	449
2×10^5	498	415	456	454
6×10^5	511	428	470	*
10^6	525	441	483	482
2×10^6	559	471	515	515
4×10^6	627	527	577	*
6×10^6	695	582	639	*
8×10^6	763	636	700	*
10^7	832	689	760	750
1.5×10^7	1000	821	911	*
2×10^7	1170	951	1060	1021

Note: Radius of "90° point = 1.29b.

* Not calculated.

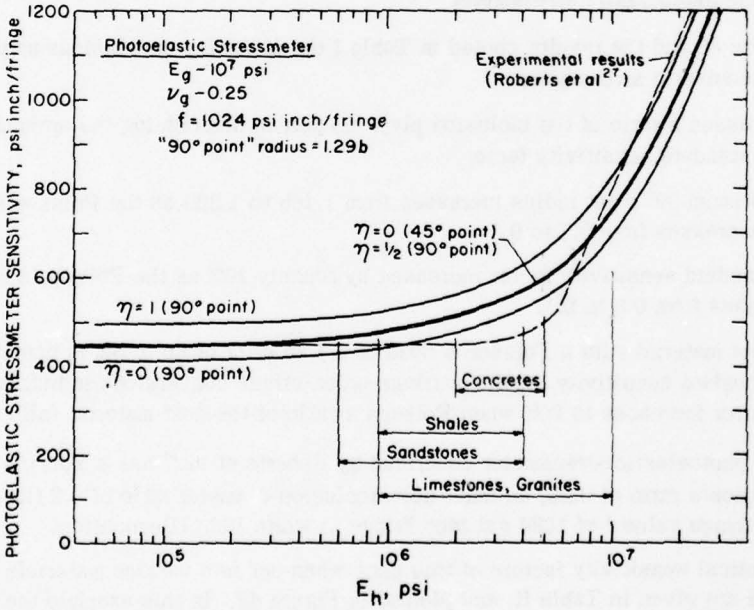

Figure 42. Sensitivity of the photoelastic stressmeter.

The choice of a value for the standard sensitivity of the photoelastic stressmeter depends primarily on the range of material types in which it is to be used. The experimental curve for the uniaxial sensitivity of the photoelastic stressmeter, for various rock types and other materials (reproduced from Roberts et al [27]), is shown plotted with the theoretical curve in Figure 42. There is some divergence between the theoretical and experimental results over a host material modulus range of 10^6 to 6×10^6 psi. This is probably due to the difficulty in defining the modulus of such materials. The moduli quoted in reference 27 are the average tangent values up to failure. These are almost always several times higher than the initial tangent moduli, which would be the most appropriate values for plotting against the meter sensitivity.

It is therefore not possible to have one specific value of the standard sensitivity for all the materials in which the photoelastic stressmeter is likely to be used. Common sense must be applied in selecting an appropriate value for the particular purpose concerned. For example, from Figure 42 the appropriate value for soft shales and sandstones would be 450 psi inch/fringe, while that for high-strength concretes would be 550 psi inch/fringe.

An optimum 90° point radius of 1.29b has been selected for the photoelastic stressmeter as this is the average of the values over a range of the ratio of Young's modulus of the host to that of the inclusion from 1 to 10^{-4} for host materials having a Poisson's ratio of 0.1 to 0.2 (see Table I).

The overall accuracy of the fringe order/stress conversion, using a standard sensitivity for the general class of materials being studied, and for biaxial stress fields, will normally be within 15%. The accuracy is much greater for uniaxial stress fields by adjusting the sensitivity factor, using the values given in Table I or Figure 42.

Sensitivity of the photoelastic strainmeter

The strain induced in a "soft inclusion" by stress changes in the surrounding host body is independent of the material properties of the inclusion. The hole into which the inclusion is set thus deforms as if the inclusion were not present, i.e. the inclusion behaves as a strain gage.

From the values in Table I the following conclusions may be drawn regarding soft inclusions:

1. The location of the 90° point and the value of the standard sensitivity factor are not affected by changes in the Poisson's ratio of the host material.

2. The optimum 90° point radius and the standard sensitivity factor are functions of the Poisson's ratio of the inclusion material.

3. When the Poisson's ratio of the meter is approximately 0.2 to 0.3, an error of up to 12% is possible when applying the standard sensitivity factor for fringe order/stress conversion in biaxial stress fields.

The variation of the standard gage sensitivity factor with the modulus ratio $E_h/E_g > 1$, for an inclusion having a Poisson's ratio ν_g of 0.32, is illustrated in Figure 43. Numerical values are given in Table III. It will be noted that for modulus ratios $E_h/E_g > 20$ the slope of the curve plotted logarithmically is unity. Therefore a standard sensitivity factor may be used, where:

$$\text{Standard sensitivity factor} \qquad S = F\ f\ E_h/E_g\ . \tag{67}$$

The relationship between the Poisson's ratio of the gage and the sensitivity constant F is given in Figure 44. Over the range ν_g from 0.1 to 0.4 the relationship is reasonably linear and can be expressed as:

$$F = 0.215 + 0.167\,\nu_g\ . \tag{68}$$

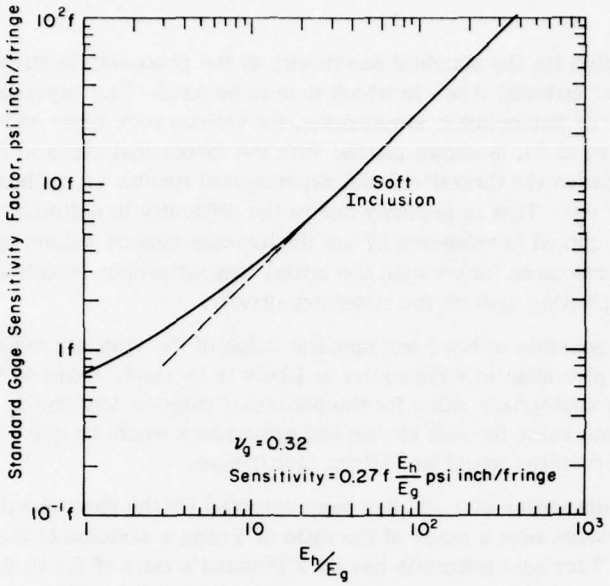

Figure 43. Variation of strainmeter sensitivity factor vs modulus ratio E_h/E_g.

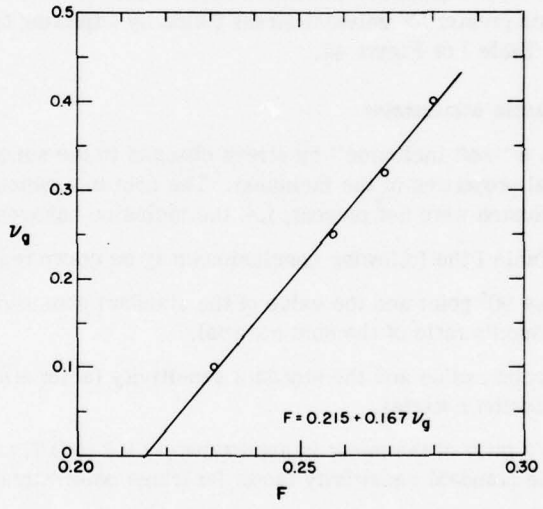

Figure 44. Sensitivity constant F vs Poisson's ratio ν_g for a photoelastic soft inclusion.

Therefore the standard sensitivity factor of a soft inclusion photoelastic meter having the ratio $b/a = 0.2$ can be expressed as:

$$S_0 = (0.215 + 0.167\,\nu_g)\, f\, E_h/E_g \tag{69}$$

Table III. Sensitivity of photoelastic soft inclusions.

	Standard sensitivity factor		Sensitivity constant F				
			Inclusion theory			Elementary theory for soft inclusions	
	Diam ratio = 0.2				Diam ratio = 0.02	Diam ratio = 0.2	
E_h/E_g	$\nu_g = 0.32$	$\nu_g = 0.25$	$\nu_g = 0.32$	$\nu_g = 0.25$	$\nu_g = 0.32$	$\nu_g = 0.32$	$\nu_g = 0.25$
1	0.742	0.732	0.762	0.732	0.713	0.240	0.229
2	1.02	0.997	.501	.498	.477	.240	.229
10	3.18	3.07	.318	.307	.287	.240	.229
2×10^2	54.4	52.1	.272	.260	.243	.240	.229
10^3	270	259	.270	.25ℰ	.240	.240	.229
2×10^3	539	517	.269	.258	.240	.240	.229
10^4	2690	2580	.269	.258	.240	.240	.229

Viewing system used with photoelastic hollow-cylinder inclusions

The optical system applied in the hollow-cylinder photoelastic inclusions (Fig. 45) has not previously been applied to any great extent in photoelastic studies. The inclusion has three components: an aluminum shield to keep the bonding cement off the face of the meter, a hollow-cored glass or plastic cylinder (the photoelastic transducer), and a parabolic aluminum reflector.

A probe containing a light bulb and a circularly polarizing filter fits into the hole in the center of the meter. Polarized light from the probe is reflected from the end of the meter and passes through the transducer, to be viewed by the observer using a hand-analyzer.

The polarizing element in the probe consists of a combined quarter-wave plate and a linear-polarizing filter set to produce left-hand circularly polarized light. Upon reflection from the back end of the meter the direction of polarized rotation is reversed and the light becomes right-hand polarized.

The quarter-wave plate and the linear polarizing filter in the analyzer are set to produce left-hand polarized light. The probe filter and the viewing analyzer therefore act as a crossed polariscope, giving a dark field in the meter when it is stress-free.

To carry out Tardy compensation for exact fringe order measurement the linear polarizing filter in the analyzer must be aligned with a direction of principal stress in the photoelastic inclusion. As the directions of principal stress are the axes of symmetry of the fringe pattern this is self-evident and is easily done, without the need to generate isoclinics. It is not necessary to have any predetermined angular alignment of the polarizing filters in the probe and the directions of principal stress in the inclusion.

The system thus differs essentially from that normally employed in conventional photoelastic stress analysis, where the directions of principal stress are determined from observed isoclinics.

Reading the Photoelastic Stressmeter

The procedure for viewing the fringe patterns displayed by a photoelastic stressmeter under load, and interpreting these patterns as a measured value of stress, may now be summarized:

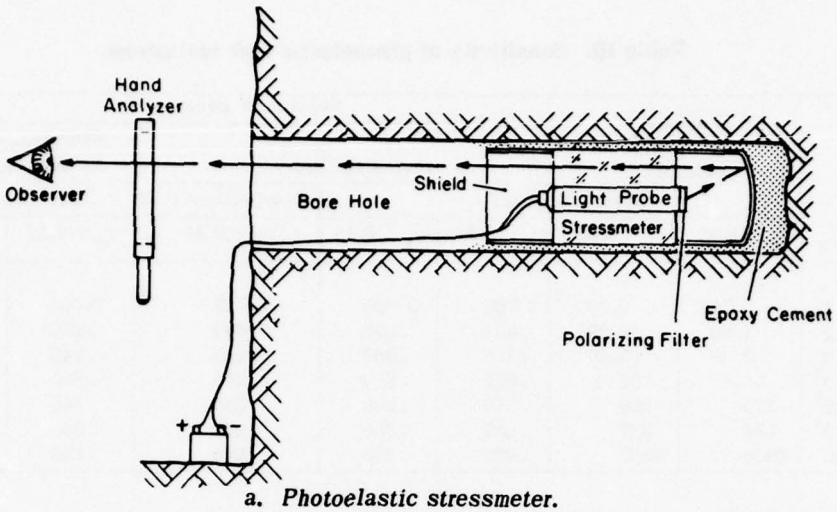

a. Photoelastic stressmeter.

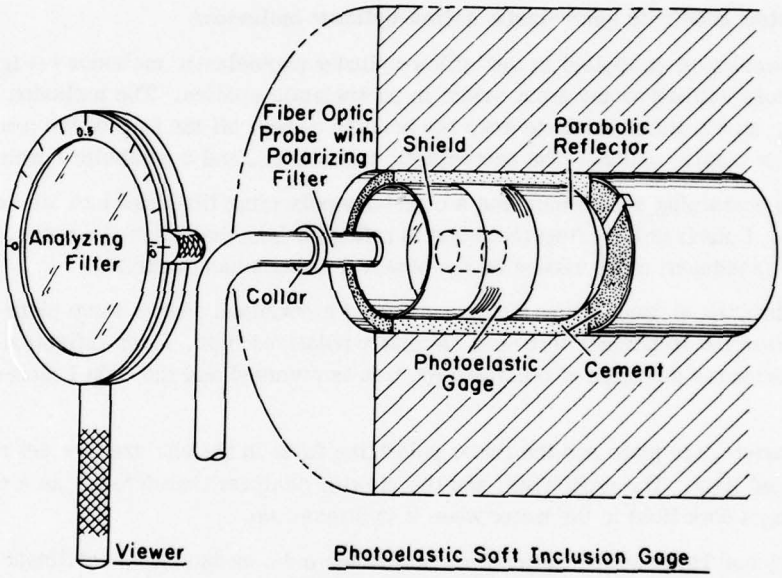

b. Soft inclusion gage.

Figure 45. Viewing systems for hollow-cylinder photoelastic inclusions.

Insert the polarized probe into the stressmeter until the face of the meter appears to be uniformly illuminated. At this point the collar of the probe should be in contact with the face of the stressmeter. (When the meters are of the type to be set in deep holes the light probe is fixed permanently in place.)

Set the scale of the stressmeter viewer to zero, and observe the stressmeter through the viewer. (Hold the viewer by its handle so that the scale faces the operator.) The orientation of the handle of the viewer is not critical at this stage. If the stressmeter is at depth it can be sighted through a telescope with the handviewer held between the telescope and the mouth of the hole.

On observing the stressmeter through the viewer there will be either:

1. A uniformly colored field, which can be dark or light but in which the colors do not form a definite pattern. In this case the fringe order is less than one.

2. A definite fringe pattern consisting of a series of colored lines. In this case the fringe order is greater than one. Figure 39 illustrates the possible range of patterns, from 1 to 4 fringes, in biaxial stress fields ranging from uniaxial to hydrostatic (both principal stresses having the same sign). The patterns display an exact fringe order, e.g. 1.00, 2.00, 3.00. The analysis in the following section may be carried out on each pattern.

Pattern symmetry

The pattern should be symmetrical about two axes at right angles to each other, if the meter is correctly set in a stress situation such that there is a relatively small stress gradient in the vicinity of the meter.

The most common causes of asymmetrical patterns are:

1. Unsatisfactory bonding of the meter into the host material. Setting tools and setting procedures have been devised and proved in practical applications. If they are properly used the possibility of defective setting will be remote.

2. Stress-raisers in the vicinity of the meter. This effect is sometimes associated with measurements in concrete, where steel reinforcement members embedded in the concrete and hidden from view cause local stress gradients. The stress gradients associated with beams in bending will also show up as asymmetrical patterns in the meter. Stress gradients are also produced in the vicinity of "flat jacks" used in certain forms of in situ rock stress and load measurement operation. These will be seen as asymmetrical patterns.

3. Heterogeneities in the host material. The aggregate in concrete causes stress variations on a local scale. If the aggregate size is greater than the external diameter of the meter this can result in nonuniform patterns. When being used in concrete the meter should always be at least as large as the largest aggregate.

Even when the pattern is not symmetrical and uniform, the readings rarely have to be completely rejected. A considerable amount of information can still be extracted, with reference to relative stress changes and general stress directions, even from irregular patterns.

Directions of the principal stresses

The axes of symmetry of the pattern in a photoelastic stressmeter are the directions of the principal stresses in the host material, in the plane of measurement, perpendicular to the optical axis of the meter. In Figure 39 all the axes of symmetry are self evident, except for the hydrostatic case where there are no preferred directions of principal stress.

The directions of the principal stresses can be thus determined for any system of loading from 0.05 fringe upward. As the stress level increases from zero the background of the meter lightens, and two dark spots appear at diametrically opposite edges of the inner hole. If the hand-viewer is then rotated bodily about its optical axis (keeping the index at zero), these spots will change color and oscillate slightly but they will not orbit around the central hole (as they would if the stresses were zero). The line joining these two spots, and the line perpendicular to this, are the two principal stress directions in the plane of measurement of the meter.

At higher stress levels, i.e. 0.5-1.0 fringe, the two spots of color may not be present, because the whole meter appears light yellow or colorless. The procedure now is to set the viewer scale to approximately 0.5 and then rotate the whole handviewer about its optical axis while observing

the meter. At one specific position of the viewer a definite pattern will appear. Further rotation of the viewer causes this pattern to distort and blur. One of the axes of symmetry of the pattern seen will be coincident with the handle of the viewer. This direction and that at right angles to it are the directions of the principal stresses.

Difficulties will be experienced when the stress fields approach hydrostatic because then there are no well-defined directions of principal stress. This type of stress field is difficult to recognize below 0.5 fringe but above the level of stress the circular nature of the fringe pattern is seen when the scale of the viewer is rotated. This is then easily identified.

Direction of the major principal stress

The direction of the major principal stress cannot be found from stressmeter readings below 0.5 fringe without some knowledge of the loading conditions. If the stress field is known to be uniaxial the line joining the two colored spots, mentioned previously, is the direction required. However, in biaxial stress fields this is not necessarily so.

If it is definitely known that the major stress is compressive its direction can be identified by aligning the handle of the viewer alternately with the two stress directions and then rotating the scale of the viewer clockwise. The alignment direction which retards the fringe order (i.e. the colored areas shrink towards the edge of the central collar) is the direction of the major principal stress. The reverse happens if the major stress is tensile.

At higher fringe orders the difficulties are much less. In Figure 39 the major principal stress direction is vertical (i.e. top to bottom of the figures). As the stress level increases the fringes first appear successively at the point where the minor (horizontal) axis runs into the central collar and they then move out and around towards the major axis.

In biaxial patterns with a stress ratio $\eta > \frac{1}{4}$ the major axis is clearly identified by the appearance of two black spots (isotropic points) above and below the central hole, and directly in line with the major axis.

At fringe orders between 1.0 and 1.5 in uniaxial stress fields there is sometimes difficulty in distinguishing between the major and minor stress axes because the pattern shape at these fringe orders is almost symmetrical with both axes. In such cases, however, it is usually known whether the major stress is compressive or tensile, and the major stress direction can be identified by applying the Tardy compensation technique.

Ratio between the principal stresses

When the two principal stresses have the same sign two methods are available for finding the stress ratio: 1) Approximate assessment by deduction from the general shape of the fringe pattern (see Fig. 39). 2) Refined assessment by measurement of the isotropic point spacing (see p. 55).

Sign of the principal stresses

When the direction of the major principal stress has been determined the handle of the stressmeter is aligned with that direction. The fringes are observed at the point where they cross the minor stress axis, i.e. at right angles to the handle of the viewer. Clockwise rotation of the meter scale will now move these fringes, either towards the central hole (i.e. retarding the fringe pattern), or away from the central hole (i.e. advancing the fringe pattern). If the fringe order is retarded the major principal stress is compressive; if the fringe order is advanced it is tensile.

Magnitude of the major principal stress

The procedure used to determine the magnitude of the major principal stress is as follows:

The handle of the viewer is held in line with the major principal stress direction and, with the scale set to zero, the number of fringes visible in any quadrant of the pattern, between the major and the minor stress directions, is counted. The fringes are counted beginning on the major axis and then moving out and around to the minor axis (see Fig. 39).

The fringes in patterns resulting from near-uniaxial stress conditions appear first near the edge of the collar at points lying 45° radially from the axes of symmetry. As the stress field approaches hydrostatic, however, the fringes first appear at the edge of the collar on the minor stress axis.

When the fringes have been counted the viewer scale is rotated clockwise until the last fringe to develop (i.e. that nearest the collar edge on the minor stress axis) is just about to disappear behind the collar. At this point the pattern will have been retarded to an integer fringe order, and it will be similar to one of those illustrated in Figure 39. The operation is illustrated in Figure 46 which shows a uniaxial stress pattern before and after retardation. To obtain the exact fringe order the fractional scale reading after retardation is added to the original unit fringe count.

To carry out this operation when the major principal stress is tensile the hand-viewer must be held with its handle aligned along the minor principal stress axis, after which the procedure is as before.

When the fringe order is read it is essential to make the count of integer fringes with the scale set at zero. This is because the pattern is compensated to the lower integer fringe order when the increment is less than ½ fringe, but for fractions greater than ½ the pattern is compensated to the next higher fringe order.

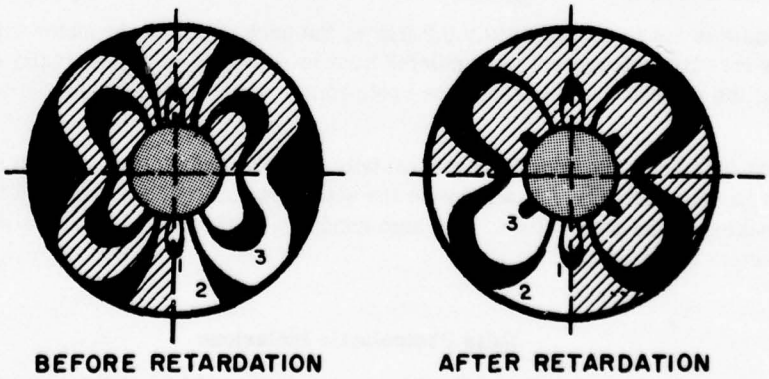

Figure 46. Uniaxial stress pattern before and after retardation.

For example, if the fringe order is 2.35 the pattern will be retarded upon compensation to the unit integral pattern at 2.00 fringes, but if the fringe pattern is registering 2.65 on first viewing, compensation will move the pattern to 3.00 fringes. This need cause no confusion if the cardinal rule is obeyed: make the integer fringe count with the scale set to zero and make it before performing the compensation procedure.

The magnitude of the major principal stress may now be obtained by multiplying the measured fringe order by the meter sensitivity factor. The value of this factor depends upon whether the meter is acting as a "rigid inclusion" or not, and on the length of the glass cylinder of the meter. The validity of the rigid inclusion assumption depends upon the magnitude of the modulus of elasticity of the material in which the meter is set. Rocks and concrete rarely have a fixed modulus which is independent of time or the rate of loading and it is seldom possible to quote a precise value for materials of this type.

The range of values for E_h normally accepted for various rocks and concrete is given in Figure 42 and an average sensitivity over this range of materials is given as 480 ±20 psi inch/fringe. For soft materials whose modulus is less than 1×10^6 psi it is more realistic to assume a meter sensitivity of 460 psi inch/fringe and for high modulus concretes a value of 500 psi inch/fringe.

For all but the most precise work, however, the errors introduced by assuming a standard meter sensitivity, S_0, of 480 psi inch/fringe are very small.

To obtain the sensitivity factor of any given stressmeter it is only necessary to divide the standard meter sensitivity by the length of the glass cylinder in the meter. The magnitude of the major principal stress is thus given by:

$$\text{Stress} = \frac{\text{Fringe order} \times 480 \text{ psi}}{\text{Length of glass cylinder (inches)}}$$

Fringe orders less than unity

To interpret the readings of a stressmeter when the fringe order is less than one usually requires some knowledge of the loading conditions. Under zero stress, and with the index of the scale set to zero, the general field of an illuminated stressmeter is dark blue or gray-brown, with a lighter colored region around the central hole. If the viewer (not the scale) is then rotated bodily around its central axis these background colors change from dark blue to gray-brown, or vice versa.

If the scale is set to approximately 0.2 fringe, the background of the meter will be either very light blue or very light brown, with two colored blue/brown spots at diametrically opposite points, just touching the edge of the collar. These spots rotate around the collar as the whole viewer is rotated.

The light colored areas around the central hole, and the colored spots which appear when the scale is set to approximately 0.2, are due to the small residual stresses induced into the glass during the making of the stressplugs. The zero condition of the meters should always be observed before the meters are inserted.

Solid Photoelastic Inclusions

Solid inclusions of photoelastic material are sometimes used when the shear stress in a body is required rather then the principal stresses.

Solid cylindrical inclusion stressmeter

The stress difference $(\sigma_1 - \sigma_2)$, equal to twice the maximum shear stress, in a solid cylindrical inclusion bonded into a body subject to stresses p and q, is represented by Hiramatsu et al.[17] as:

$$\sigma_1 - \sigma_2 = \frac{E_g (5 + \nu_h) - E_h (1 + \nu_g)}{E_g (3 - \nu_h) + E_h (1 + \nu_g)} (p - q) \tag{70}$$

where E_g and ν_g = Young's modulus and Poisson's ratio of the inclusion
E_h and ν_h = Young's modulus and Poisson's ratio of the containing body.

From this it follows that $\sigma_1 - \sigma_2$ is proportional to $p - q$ and $\sigma_1 - \sigma_2$ is uniform over the whole area of the gage.

A solid cylindrical birefringent inclusion thus presents a uniform fringe order which can be measured and calibrated to give $p - q$.

The individual magnitudes of p and q cannot be deduced by using circularly polarized light alone in a solid photoelastic stressmeter. However, if two stressmeters, one annular and one solid, are set in the same stress field, the annular instrument will yield the magnitude of the major principal stress, and its direction, while the solid cylinder will give the arithmetical difference between the major and minor stresses. Hence the minor principal stress is identified. The value so found should check with the magnitude of minor principal stress indicated by the isochromatic pattern observed on the annular instrument.[28]

Observational procedures on the solid cylindrical birefringent inclusion

Except for a narrow zone near the peripheral boundary the isochromatic pattern seen in a solid cylindrical inclusion is one of uniform color. The exact color is a function of the principal stress difference in the glass.

Readings are taken as with the annular stressmeter. The analyzer is aligned with the major stress direction in the inclusion, and the fringe pattern is compensated at the center of the inclusion to the tint of passage, this being the datum point between integral fringe orders.

The direction of the major stress in the inclusion is not readily apparent, but the directions indicated by a neighboring annular stressmeter, and the vehavior of the fringe pattern during compensation, will provide this information. If the axis of the analyzer is not aligned with a direction of principal stress then when compensation to a tint of passage is attempted the colors will wash out. By trying the compensation technique with the analyzer aligned in different directions, the direction where the colors do not wash out (principal stress directions) can readily be identified. Care has to be taken during the compensation process to avoid miscounting the integral fringe order. The Tardy method allows observed fringe orders to be compensated to the nearest integral value, which in turn has to be identified by inspection of the color sequence during compensation, or by the overall fringe pattern shown by the inclusion. When a uniform state of shear stress exists in the inclusion the duplication of colors in the interference color scale can produce ambiguous interpretations of the integral fringe orders.

Compensation by the Babbinet method would avoid this difficulty, since fringe orders are then compensated to a datum of zero fringe order, but the compensator has to be aligned accurately with the principal stress directions in the inclusion and the instrument itself obstructs the field of view around the point of inspection.

The Tardy method is more convenient for use with photoelastic stressmeters, and the use of additional filters, in the manner suggested by Pant[25], allows the integral fringe orders to be identified without ambiguity.

Identification of integral fringe orders in a solid inclusion, applying Pant's method

The stress-optic law relating observed fringe orders to the principal stresses in a birefringent material can be written:

$$n = \frac{Ct}{\lambda} (\sigma_1 - \sigma_2) \tag{71}$$

where

n = observed fringe order in light of λ wavelength

C = stress optic coefficient (constant for the material)

t = length of the light path in the material

σ_1 and σ_2 = principal stresses in the material.

Similarly for two other observations employing monochromatic radiations of wavelengths λ_1 and λ_2:

$$n_1 = \frac{Ct}{\lambda_1} (\sigma_1 - \sigma_2) \tag{72}$$

$$n_2 = \frac{Ct}{\lambda_2} (\sigma_1 - \sigma_2) \tag{73}$$

n, n_1 and n_2 are measured at the same point in the material, for the same stress conditions. From eq 71 – 73:

$$n = Q (n_1 - n_2) \tag{74}$$

where

$$Q = \frac{\lambda_1 \lambda_2}{\lambda (\lambda_2 - \lambda_1)} . \tag{75}$$

If the wavelengths λ_1 and λ_2 are produced from light of wavelength λ by colored filters from neighboring positions in the spectrum, n_1 and n_2 will generally have the same integral value and the term $(n_1 - n_2)$ will be small. The required fringe order n can be found, therefore, by identifying the fractional fringe orders involved in n_1 and n_2.

When applying Pant's method Rose[26] found that two additional points must be considered. First the filters used, which were commercially available color filters, did not produce unique values of λ_1 and λ_2, so that an approximation was involved in eq 74.

Second, the observed fringe orders n_1 and n_2 have different integral values when they lie on different sides of a full fringe order. Since there must be no confusion in measuring the correct value of $(\Delta n_1 - \Delta n_2)$ the filter producing the higher reading of fringe order must be carefully noted.

If the wavelengths λ, λ_1 and λ_2 are not known with precision the constant Q can best be found by direct calibration. The following example illustrates the method. Four color filters were used (Table IV).

Table IV. Color filters used in calibration of solid stressmeter.

Ilford filter no.	*Color*	*Nominal transmission wavelength*
602	Spectrum blue	440 Å - 4900 Å
603	Blue green	4700 Å - 5200 Å
606	Spectrum yellow	5600 Å - 6100 Å
608	Spectrum red	6200 Å - infrared

The stressmeter, 1.25 in. diameter by 1.5 in. long, was bonded into a sandstone slab (8 × 8 × 1.5 in.) loaded in uniaxial compression. Upon application of incremental loads the fringe orders displayed by the meter were observed, first in white light and then with combined white light and the individual filters.

The experimental readings are given in Table V. The results showed substantial agreement with those obtained by Rose[28] (see Fig. 47).

Table V. Observed fringe orders in a solid stressmeter.

Meter dimensions 1½ in. diam × 1½ in. long

Load on slab (lb)	*Applied stress (psi)*	*Fringe orders*				
		White light	*White light + filter 602*	*White light + filter 603*	*White light + filter 606*	*White light + filter 608*
4000	304	0.65	0.82	0.76	0.64	0.58
8000	608	1.28	1.72	1.63	1.38	1.18
12000	912	1.98	2.56	2.43	2.04	1.76
16000	1216	2.62	3.33	3.15	2.72	2.34
20000	1520	3.22	4.12	3.90	3.30	2.84
24000	1824	3.78	4.87	4.61	3.95	3.39
28000	2128	4.31	5.57	5.27	4.51	3.86
32000	2432	4.89	6.27	5.93	5.10	4.37
36000	2736	5.45	7.06	6.66	5.68	4.88

Figure 48 shows Rose's data in calibration form for values of Q obtained by using the six possible filter combinations. Individual values for the fringe order difference are given in Table VI. Differences between readings from two filters have been plotted against the observed white light fringe order, and the values of the constant Q in each case are shown in Figure 48.

Table VII shows comparison values of observed and calculated white light fringe orders, using the Q factors of Figure 48, and the observed fringe-order difference for three of the filter combinations. The calculated values agree with the observed fringe orders to within 10%. Such a standard of agreement can be regarded as satisfactory for identifying integral values, although the possible error is large enough to produce discrepancies when the required fringe order is close to a full integral value.

To minimize errors in observation, attention must be paid to the transmission characteristics of the filters used. The calculated fringe orders must be carefully compared with the fringe orders seen in white light, without color filters added.

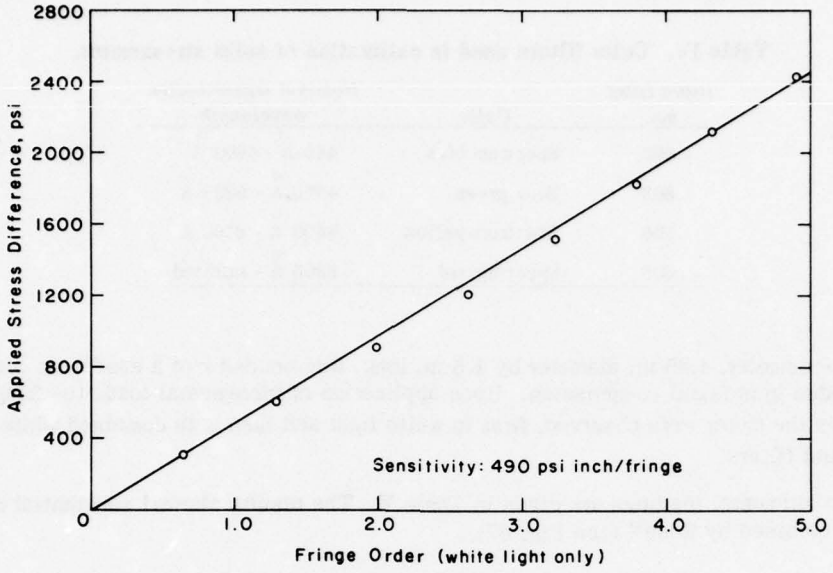

Figure 47. Calibration data for solid photoelastic stressmeter. (After Rose[28].)

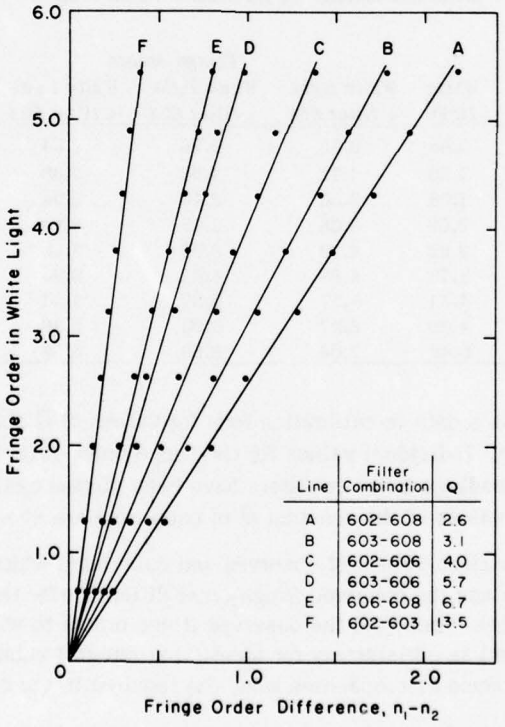

Figure 48. Calibration data for solid stressmeter (Pant's method). (After Rose[28].)

Table VI. Fringe order differences from Table V.

Load on slab (lb)	Fringe order in white light	Fringe order difference $(\bar{u}_1-\bar{u}_2)$ filters 602-608	$(\bar{u}_1-\bar{u}_2)$ filters 603-608	$(\bar{u}_1-\bar{u}_2)$ filters 602-606	$(\bar{u}_1-\bar{u}_2)$ filters 603-606	$(\bar{u}_1-\bar{u}_2)$ filters 606-608	$(\bar{u}_1-\bar{u}_2)$ filters 602-603
4000	0.65	0.24	0.18	0.18	0.12	0.06	0.06
8000	1.28	0.54	0.45	0.34	0.25	0.20	0.09
12000	1.98	0.80	0.67	0.52	0.39	0.28	0.13
16000	2.62	0.99	0.81	0.61	0.43	0.38	0.18
20000	3.22	1.28	1.06	0.82	0.60	0.46	0.22
24000	3.78	1.48	1.22	0.92	0.66	0.56	0.26
28000	4.31	1.71	1.41	1.06	0.76	0.65	0.30
32000	4.89	1.90	1.56	1.16	0.83	0.73	0.34
36000	5.45	2.18	1.78	1.38	0.98	0.80	0.40

Table VII. Observed and calculated fringe orders compared by Pant's method.

Load on slab (lb)	Observed fringe order in white light n	Filter combinations – fringe orders 603-606 Obs. (n_1-n_2)	603-606 Calc. n	606-608 Obs. (n_1-n_2)	606-608 Calc. n	602-603 Obs. (n_1-n_2)	602-603 Calc. n
4000	0.65	0.12	0.68	0.06	0.42	0.06	0.81
8000	1.28	0.25	1.43	0.20	1.34	0.09	1.21
12000	1.98	0.39	2.22	0.28	1.88	0.13	1.76
16000	2.62	0.43	2.45	0.38	2.54	0.18	2.43
20000	3.22	0.60	3.42	0.46	3.08	0.22	2.97
24000	3.78	0.66	3.76	0.56	3.75	0.26	3.51
28000	4.31	0.76	4.33	0.65	4.35	0.30	4.05
32000	4.89	0.83	4.73	0.73	4.89	0.34	4.59
36000	5.45	0.98	5.58	0.80	5.36	0.40	5.40

LITERATURE CITED

1. Barron, K. (1964) Glass-insert stressmeters. Department of Min. Tech. Surv. Div. Rept. FMP 64/123/MRL. Mines Branch Ottawa.
2. Braiden, P.M. (1964) The application of optical measurement techniques to the determination of loads on hydraulic pit props. M. Eng. Thesis, University of Sheffield.
3. Brewster, Sir David (1816) On the communication of the structure of doubly refracting crystals to glass and other substances by mechanical compression and dilatation. Phil. Trans. Roy. Soc., p. 156-178.
4. Brown, A.F.C. and V.M. Hickson (1950) Improvements in photoelastic technique obtained by the use of a photometric method. Brit. J. Appl. Phys. vol. 1 (2), p. 39-44.
5. Chakravarty, P.K. (1963) Photoelastic techniques applied to the study of rock mechanics. Ph.D. Thesis, University of Sheffield.
6. Coker, E.G. and L.N.G. Filon (1931) A treatise on photoelasticity. Cambridge University Press, Cambridge, England.
7. Coutinho, A. (1948) Determination of stresses in concrete by the photoelastic tensometer method. Annales d'Inst. Tech. Bat. Trav. Pub. no. 4, p. 20, (May).
8. Dhir, R.K. (1966) A study of the photoelastic stressmeter. Ph.D. Thesis, University of Sheffield.

LITERATURE CITED (Cont'd)

9. Durelli, A.J., V.J. Park, N.C. Feng, and F. Chiang (1967) Stresses and strains in matrices with inserts. Contract no. Nonr. 2249 (06), C.U.A. Project no. 4, 147, 05.

10. Emery, C.L. (1961) A study of instrumentation applied to the determination of physical properties of rocks in mines. Ph.D. Thesis, University of Sheffield.

11. Frocht, M.M. (1948) Photoelasticity. vols. 1 and 2, New York: Wiley and Sons.

12. Hawkes, I. (1968) Moduli measurements on rock cores. Ist. Intn. Conf. Int. Soc. Rock Mech. Lisbon, vol. 1, p. 655-660, Oct.

13. Hawkes, I. (1968) Theory of the photoelastic biaxial strain gage. Int. J. Rock Mech. Min. Sci., vol. 2, p. 405-419.

14. Hawkes, I. and S. Moxon (1965) The measurement of in-situ rock stress using the photoelastic biaxial gage with the core relief technique. Int. J. Rock Mech. Min. Sci. vol. 2, p. 405-419.

15. Hiltscher, R., G. Florin and L. Strindall (1966) Arbeitsangleitung zur spannungoptischen messung ebener spannungszustande mit polariscop und lateralextensometer. Die Bautechnik, vol. 43, p. 3-12.

16. Hiramatsu, Y., Y. Niwa, and Y. Oka (1957) Measurement of stress in the field by application of photoelasticity. Technical Report, Kyoto University, no. 37, p. 49-63.

17. Hiramatsu, Y., Y. Niwa, and Y. Oka (1967) Measurement of variation in stress by a photoelastic stressmeter. Mem. Faculty Engr. Kyoto, vol. 29 (1), p. 58-75, Jan.

18. Jobst, Gunther (1951) Spannungfenster. Deutsches Patentschrift, no. 817044, Oct.

19. Mabboux, Georges (1931) Perfectionnements apporte's aux pro èdes et dispositifs pour la photo elasticimetrie. Brevet d'Invention Francaise No. 728,632, Dec.

20. Mabboux, Georges (1935) Process and device for the application of elasticimetry, particularly photoelasticimetry. U.S. Patent no. 2,014,688, Sept.

21. Maris, Harry, B. (1947) Photoelastic blast pressure gage. U.S. Patent no. 2, 415,436, Feb.

22. Merril, R.H. and J.R. Peterson (1961) Deformation of a borehole in rock. U.S. Bureau of Mines R.I. 5881.

23. Muskhelishvili, R.H. (1953) Some basic problems of the mathematic theory of elasticity. P. Noordhoff Ltd., Groningen (Holland).

24. Oppel, G.U. (1961) Photoelastic strain gages. Exp. Mechs. Vol. 1 (3), p. 65-73, March.

25. Pant, B. (1963) A method for determining integral fringe orders in photoelastic analysis. Proc. S.E.S.A., p. 173, July.

26. Post, D. (1955) Isochromatic fringe sharpening and fringe multiplication in photoelasticity. Proc. S.E.S.A., vol. 12 (2), p. 143-156.

27. Roberts, A., I. Hawkes, F.T. Williams, and R.K. Dhir (1964 and 1965) A laboratory study of the photoelastic stressmeter, vol. 1 and Field applications of the photoelastic stressmeter, vol. 2. Int. J. Rock Mech. Min. Sci.

28. Rose, H. (1969) Practical aspects of the photoelastic stressmeter in concrete. Res. Rept. (unpublished). University of Sheffield.

29. Williams, F.T. (1964) The measurement of stresses and strains in concrete structures and in strata in underground excavations. Ph.D. Thesis, University of Sheffield.

30. Zandman, F. (1961) Dispositif photoélastique. Exposé d'invention Suisse, no. 35592.

31. Zandman, F. (1962) Concepts of the photoelastic stress gage. Exp. Mechs. vol. 2 (8), p. 225-233, August.

32. Hawkes, I. (1969) Biaxial stress and strain measurements using photoelastic hollow cylinder inclusion meters. CRREL Special Report 133.

PART II: DESIGN AND OPERATION OF PHOTOELASTIC TRANSDUCERS

The major application of photoelastic transducers has been to evaluate loads, stresses and strains in civil engineering type structures and in mines. This section of the report deals with the basic photoelastic materials used and the design, calibration and general methods of use of photoelastic transducers.

PHOTOELASTIC MATERIALS AND CEMENTS

Glass

The two basic photoelastic materials used for photoelastic transducers are glass and stress-birefringent plastics. Glass is a relatively strong material, having stable time-dependent qualities at low ambient temperatures. It behaves as an almost perfectly linear elastic solid up to stresses very nearly approaching its breaking strength.

The birefringent properties of glass were recognized long ago by Brewster,[3] and early photoelastic experiments were made on glass models by Mesnager[56] and by Coker and Filon.[6] More recently, biaxially loaded glass plates were used by Hoek[44] in connection with studies on rock fracture and related rock stress problems. Hooper[50 51] made a comprehensive study of glass as a photoelastic transducer element, and much of the following discussion and theory is taken from his work.

Glass is an extremely variable material with physical properties which differ widely according to its chemical composition. For the applications detailed in this report, soda-lime plate glass has been found eminently suitable. It is relatively cheap and easily obtained, and it can be cored without difficulty using thin-walled diamond drills.

Except where stated otherwise, the material used for all the work on disk transducers described in this report is soda-lime glass with the following approximate composition by weight:

Sio_2	73.3%	CaO	9.2%	Al_2O_3	0.8%	SO_3	0.3%
NaO	12.6%	MgO	3.2%	K_2O	0.3%		

Measured values of the static Young's modulus and Poisson's ratio of this material are 10.2×10^6 psi and 0.24 respectively. The thermal softening temperature and the coefficient of linear expansion are given by the glass manufacturers as 739°C and 8.0×10^{-6}/°C respectively.

Birefringent properties of glass

The stress-optic coefficients of different glasses are known to vary considerably; Coker and Filon[6] have quoted values ranging from −2 to +4.5 Brewsters.* Tests on 1-in.-thick disks of soda-lime glass 2 in. in diameter and 1 in. in diameter, using sodium light, were made by Hooper[50] and gave a disk sensitivity of 970 lb/fringe. Inserting this value into eq 18 for $\lambda = 5900$ Angstrom units (Å) gives a stress optic coefficient C of 1.882×10^{-8} in.^{2}/lb and converting to metric notation a value of +2.72 Brewsters. This estimate of +2.72 Brewsters is identical to a value obtained by Waxler[73] and close to the value of +2.68 Brewsters measured by Van Zee and Noritake[72] for a similar glass plate.

---

* A Brewster is the scientific unit for the stress-optic coefficient and is equal to 10^{-3} cm^2/dyne.

This estimate of +2.72 Brewsters is identical to a value obtained by Waxler[73] and close to the value of +2.68 Brewsters measured by Van Zee and Noritake[72] for a similar glass plate.

It is more convenient to express the stress-optic coefficient in terms of a material or unit fringe value f, which is the stress difference required to produce one fringe in a model of unit thickness. For any given model the stress difference is given by

$$\sigma_1 - \sigma_2 = \frac{fn}{t} \tag{76}$$

where n is the fringe order and t the model thickness at the point of interest. The unit fringe value f for soda-lime glass is equal to 1234 psi (stress difference) per fringe per inch thickness when viewed in sodium light (Å = 3900). From eq 76 and eq 1 and 2 (Part I) it is easy to derive that $f = \lambda/C$. It is also implied from eq 1 that the stress-optic coefficient is the same for both compressive and tensile stress fields, a fact that has been verified experimentally by Savur.[68]

For time intervals in the region of 20 years there is the possibility of some change in the stress-optic coefficient, associated with internal changes in the structure of the glass. Harris[38] reported increases of between 1% and 19% over this length of time for a number of different glasses. He suggests that the stress-optic coefficient increases fairly rapidly during the first few years after the glass is cast, and then settles down to a steady value. However, over the periods of time involved in field investigations in mining and civil engineering it is reasonable to expect that the effect of time on the birefringent properties will be minimal, so that it should not greatly influence the accuracy of the glass disk as a practical load transducer.

The effect of moderate time intervals on the stress-optic coefficient of soda-lime glass was checked by Hooper,[50] who applied a constant diametrical load to disks for a period of two years. During this time no discernible change in fringe order from the original five fringes at the disk center was observed.

The effect of temperature on the stress-optic coefficient of glass was also studied by Harris,[38] who found variations in the coefficient to be strongly dependent upon chemical composition. Most coefficients increased with a rise in temperature, but for one glass containing a large proportion of lead oxide the coefficient decreased relative to its value at room temperature.

For a soda-lime glass, Van Zee and Noritake[72] found that the stress-optic coefficient increased approximately linearly by 5% as the temperature was increased from 20°C to 540°C, but increased very rapidly with further rise in temperature.

From eq 18 it is possible to express the disk load sensitivity in terms of either the light wavelength or the disk diameter. The effect of light wavelength on the sensitivity of a 2-in.-diam, 1-in.-thick disk is shown in Figure 49. These results show satisfactory agreement with corresponding points on the theoretical line, which may be defined as $S = 0.165\ \lambda$ lb/fringe (λ in Angstroms). It is thus possible to increase the sensitivity of any disk by up to about 50%, based on the red light value, by varying the wavelength of the light passing through it.

To limit the disk stresses, and for ease of reading, the operating range of a glass transducer is normally limited to five fringes, under transmitted light. It is found in practice that while white light gives the most distinctive fringe pattern up to about three fringes, it is unsuitable for use beyond this point because at the higher fringe orders the effect of extinction occurring at periodic wavelengths gives rise to a "washing out" of the colors. For this reason it is normal practice to illuminate the disk by monochromatic light.

In field applications it is seldom possible to use a truly monochromatic light source, and it is generally more convenient to use white light in conjunction with a colored filter with a specified band width. In a high quality optical filter the band width may be about 100 Å, but cheaper

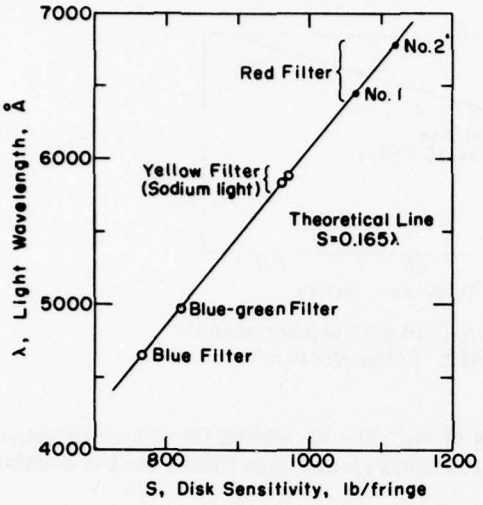

Figure 49. Variation of sensitivity (load/fringe order) with wavelength of light for a diametrically loaded 2-in.-diam, 1-in.-thick soda-lime glass disk. Fringe order measured at the center of the disk, transmitted light. (From Hooper.[50])

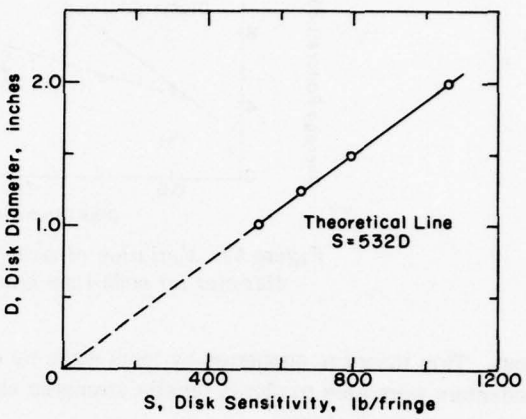

Figure 50. Variation of sensitivity with diameter of soda-lime glass disks using red filter (λ = 6450 Å). Disks loaded diametrically, fringe order measured at the center of the disk, transmitted light. (From Hooper.[50])

filters with a band width of around 500 Å have proved satisfactory for field instruments. The light produced by a sodium vapor lamp has its visible energy concentrated in the spectrum 5890 to 5896 Å and is recommended for laboratory tests.

Values of disk sensitivity corresponding to mean filter wavelengths are plotted in Figure 49. Each filter has a band width of between 500 and 600 Å, and the maximum difference between measured and specified mean wavelengths is 25 Å. The two red filters do not give an abrupt final cutoff because of their capacity to transmit infrared radiation. When red filters are used, a separate disk calibration should be carried out in order to determine the predominant wavelength of the particular filter used.

The variation of disk sensitivity S with diameter for light of a given wavelength is shown in Figure 50. Values of sensitivity obtained using a red filter ($\lambda = 6450$ Å) are seen to lie in close proximity to the corresponding theoretical line, $S = 532\,D$ lb/fringe (diameter D measured in inches).

Strength of glass

A commonly accepted theory of glass failure is that of Griffith[36] who suggested that failure initiates at preexisting cracks or flaws within or on the surface of the specimen. The relatively low strength of ordinary glass can then be attributed to the presence of these so-called Griffith cracks, which act as stress raisers and readily propagate under applied load. If such cracks are absent, as in freshly drawn glass fibers, the measured tensile strength is sometimes on the order of 2×10^6 psi, which is in reasonable agreement with the strength calculated on the basis of intermolecular forces. In contrast, Holland and Turner[47] found the bending strength of 2300 soda-lime glass specimens to be from around 7000 to 16,000 psi, depending on the test conditions and the surface condition of the specimen.

The strengths obtained in uniaxial tensile tests are usually lower than those obtained in bending, due to the relatively greater volumes subjected to maximum tensile stress in the former

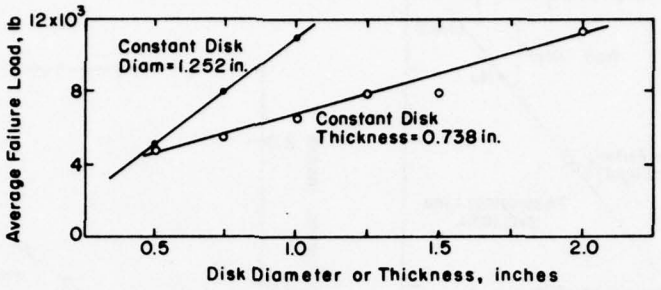

Figure 51. Variation of mean failure load with thickness and diameter for soda-lime glass disks. (After Hooper.[50])

test. This theory is supported by tests made by Argon et al.[33] who by loading through small spherical indenters were able to obtain tensile strengths about 100 times greater than those found in bending and direct tensile tests.

Glass disk failure loads

One way to determine the tensile strength of a brittle material is by the Brazil test, in which a disk or cylindrical specimen is loaded to failure across a diameter. Glass disks are loaded in a similar manner when used as transducers, and it is possible from such tests to obtain both the fracture load for a given disk and the nominal tensile strength* of the glass. This method of testing disks has the added advantage that the entire contact area is directly visible and thus provides a means of checking the uniformity of loading.

The results of strength tests on soda-lime glass disks of various sizes are given in Table VIII. Ten disks of each size were diametrically loaded to failure between ground steel platens at the rate of 4000 lb/minute. Mean values of failure load are plotted against disk thickness and diameter in Figure 51.

Table VIII. Variation of mean failure load and nominal tensile strength with thickness and diameter for soda-lime glass disks loaded between steel platens.

Vickers diamond pyramid hardness 220. (After Hooper.[50])

a) Diameter 1.252 in., varying thickness

Thickness t (in.)	*Failure load P_o (lb)*	*Std dev (lb)*	*Tensile strength σ_c* (psi)*
0.697	5200	530	5320
0.738	7940	1110	5460
1.000	11070	1800	5630

b) Thickness 0.738 in., varying diameter

Diameter D (in.)	*Failure load P_o (lb)*	*Std dev (lb)*	*Tensile strength σ_c* (psi)*
0.507	4780	900	8130
0.743	5470	1120	6350
1.000	6510	620	5620
1.252	7960	1120	5460
1.698	3000	570	4610
1.996	11390	1600	4920

* Calculated from $\sigma_c = 2P_o/\pi Dt$ from eq 9

* Nominal because the assumption must be made that failure initiates at the center of the disk.

According to eq 9 the failure load is directly proportional to both thickness and diameter, for a given tensile strength. This is seen to be the case in Figure 51 for 1.25-in.-diam disks, where the mean tensile strengths for each set of specimens are related linearly. Figure 51 also illustrates the proportionality between failure load and diameter for 0.738-in.-thick disks. Table VIIIb shows a wide variation in observed tensile strength as compared with that deduced from classical theory. This suggests the possibility of an alternative failure criterion related to the method of loading, as will be discussed later.

It is apparent from these tests that the safety factor of a loaded glass disk depends to a large extent upon its geometry. For a disk 1.25 in. in diameter and 0.75 in. thick, commonly used in photoelastic transducers, the mean failure load corresponds to a nominal tensile strength of 5460 psi, equivalent to a fringe order at the center of the disk of 12.0 (transmitted light, $\lambda = 6450$ Å).

When using these transducers in load gages the disks are not usually loaded above about five fringes, giving (in this instance) a safety factor of 2.4. Assuming a normal frequency distribution for the failure load, the chance of a uniformly loaded disk failing at five fringes is remote (less than 0.002%).

Static fatigue of glass

Glass is a material whose strength is very much dependent upon the duration of loading. The fatigue effect exhibited by glass under static load is in some ways analogous to the dynamic fatigue experienced by metals under cyclic loading. In both cases it is the gradual spread of flaws which eventually causes failure of the specimen.

Gurney and Pearson[37] measured the bending strength of soda-lime glass rods under static and cyclic loading. In contrast to the behavior of metals, they found little difference in the times to fracture between the two cases when specimens were subjected to the same applied stress. This is consistent with the hypothesis that both static and cyclic failure in glass are caused by the propagation of cracks in tensile stress fields. The mode of failure under cyclic loading in glass is quite different from that displayed in polycrystalline metals, where flow and work-hardening preceding the formation of cracks substantially alter the inherent structure of the metal.

Few observations have been made on the long-term strength of glass, but experimental work by Holland and Turner[46] and later by Baker and Preston,[34] indicated a fatigue limit for glass. This suggestion finds support in the experiments described by Shand,[69] who loaded 0.24-in.-diam soda-lime glass rods in bending for periods of up to 10 years. The applied load was maintained constant for each test, and it was found that a high proportion of the rods which did not fail during the first few weeks remained intact for the duration of the test. Results from the initial stages of one series of tests are shown in Figure 52, from which it is evident that a lower limit for the breaking strength is approached after a period of 16.5 weeks. It is reasonable to assume that this form of relationship applies to diametrically loaded glass disks, and in experiments where loads have been maintained for periods of up to two years at the maximum working stress of five fringes, no fractures have been observed.

Plastic flow in glass

Glass is commonly considered not to exhibit the property of plastic flow which is common to metals, and it is often regarded as an ideal brittle solid having no yield point. Under very high pressures, however, plastic flow and permanent deformation have been observed in glass disks loaded across the flats between hardened steel dies (Bridgman and Simon[35]). On soda-silicate glasses the threshold pressure, below which no permanent effect was evident, was approximately 0.4×10^6 psi. Early experiments by Phillips[61] on the stretching of glass fibers have demonstrated the property of time-dependent behavior. Also, Jessop[53] detected small changes in Young's modulus

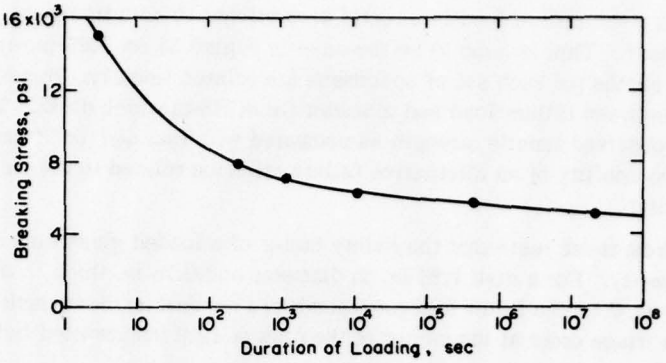

Figure 52. Static fatigue of soda-lime glass; data from bending tests on ¼-in.-diam annealed rods. (From Shand.[69])

for specimens of glass in bending, while experiments by Murgatroyd and Sykes[59] showed delayed elastic strain on soda-lime glass rods in torsion.

The possibility of plastic flow in glass under high pressures is significant in relation to the design and performance of instruments embodying disk transducers, in which high stresses are generated at the platen contact region at working loads.

The problem is complicated by the three-dimensional stress state that exists in the platen contact region. Hooper[51] has suggested that some idea of the yield stress of glass in the plate area can be obtained by static indentation tests. He made Vickers hardness tests on soda-lime glass, commonly used in photoelastic transducers, and calculated values for the yield stress in the range of 260,000 to 440,000 psi.

As will be shown later the diametral compression of glass cylinders does generate high stresses in the platen contact region but these are well below the flow stress levels and do not give rise to stability problems in photoelastic transducers.

Chemical durability of glass

Chemical attack on glass by water or acids differs from attack by alkaline solutions in that the effects of the former are limited to constituents other than silica, whereas the latter attack all constituents. Attack by neutral or acid solutions involves the selective extraction of certain constituents within the surface layer, while attack by alkaline solutions tends to remove an entire layer of the surface. When glass is subjected to atmospheric moisture, fogging and occasionally pitting may occur and this becomes more pronounced with increasing alkali content in the moisture.

As they are applied in practice, disk transducers may be subject to normal atmospheric conditions, or sometimes totally submerged in water. Hooper[50] submerged ten soda-lime glass disks (1.252 in. diam, 0.736 in. thick) under water for a period of 11 weeks, and then loaded them to failure between flat steel platens. The groundwater used in this experiment was taken from a construction site in London clay, and had an average pH of 6.6. The average strength of the glass specimens was approximately 20% less than the corresponding value obtained on disks tested at room temperature and at a relative humidity of about 55%. Tests by Baker and Preston[34] also indicate a small decrease in the strength of glass with increasing relative humidity.

Table IX. Selected properties of a range of different glasses. (After Hooper.[50])

Values relate to disks 1.25 in. in diameter, 0.75 in. thick; fringe values relate to sodium light.

Glass type	*Failure load P_I (lb)*	*Load for 5 fringes (lb)**	*Stress optic constant C (Brewsters)*	*Fringe value, f (psi in./fringe)*	*Vickers hardness V*
Soda-lime	8060	3040	+2.72	1234	554
Borosilicate (Pyrex)	4630	2090	+3.95	854	498
Borosilicate crown	2440	2870	+2.88	1164	536
Zinc crown	2890	2230	+3.70	910	572
Dense barium crown	2310	4420	+1.87	1776	556
Barium light flint	2290	3060	+2.70	1242	508
Dense flint	2500	2940	+2.81	1194	525
Double extra dense flint	--	6720	-1.23	-2710	270
Irtran 5	--	4130	+2.00	+1684	421

* Extrapolated values where reported load exceeds failure load.

Selection of glass for photoelastic transducers

Soda-lime glass has been chosen as the standard material for photoelastic transducers due to its easy availability at low cost, but there is no reason why other types of glass should not be used, provided they satisfy the necessary requirements of strength and stability. Load test results on different glasses are summarized in Table IX. Three 1.25-in.-diam, 0.75-in.-thick disks were cored from each blank and loaded to failure between flat steel platens. A fourth disk was cored and its faces polished to facilitate the measurement of birefringence. The relatively low strength of the optical glass disks is immediately apparent, and it is this property which normally precludes their use as disk transducers.

Values of the stress-optic constant varied considerably, ranging from +3.95 Brewsters for the low-expansion borosilicate glass to -1.23 Brewsters for the double extra dense flint, a glass containing a high percentage of lead oxide. Vickers hardness tests also showed this glass to be comparatively soft in relation to the other glasses. Material fringe values, as defined by eq 76 and corresponding to sodium light (λ = 5893 Å), are included in Table IX.

Some of the glasses can be used at elevated temperatures, up to around 350°C for borosilicate glass. Higher temperatures would require materials other than glass. One material has so far been found which satisfies the requirements of transmittance and temperature resistance: Irtran 5, a transparent ceramic (polycrystalline magnesium oxide) manufactured by the Eastman Kodak Co. The results of a test on a small sample are included in Table IX. Although this material is expensive, its high melting point (2800°C) suggests the possible application of photoelastic disk transducers in the field of high temperature load measurement.

Apart from possible high temperature work, ordinary soda-lime plate glass is thus by far the most suitable material for photoelastic disk transducers and photoelastic hard inclusions.

Birefringent Plastics

Birefringent plastics have long been used in conventional photoelastic stress analysis. Their application has obvious limitations so far as long-term use is concerned because of creep problems. Nevertheless, when used on a short-term basis they have considerable merit, notably ease

Table X. Properties of typical photoelastic plastics at room temperature.

Material	*Trade name*	*Tensile strength (psi)*	*Young's modulus E (psi)*	*Poisson's ratio*	*Unit fringe value f (psi in./fringe)*	*Figure of merit (E/f)*
Epoxy resin	Araldite CT 200	10,500	420,000	0.35	59	7,130
Epoxy resin	Araldite MY 753	9,000	450,000	0.35	45	10,000
Glyptal resin	Bakelite BT-61-893	17,000	615,000	0.36	91.0	6,750
Phenolformaldehyde	Catalin-800	7,000	300,000	0.42	39	7,600
Polystyrene	Castolite	8,100	705,000	0.36	158	4,460
Cellulose nitrate	Celluloid	7,000	300,000	0.4	225	1,350
Acrylic resin	Perspex	7,000	450,000	0.38	856	584
Allyl diglycol	CR-39	--	300,000	--	85	4,120
Gelatine 13 percent	--	--	6	--	0.15	--

of fabrication, simplicity in application and, when used as coatings, the capability of presenting a complete picture of the surface strain distribution on heterogeneous materials. By a suitable choice of coatings, material deformations may be studied throughout the elastic and into the plastic range.

The properties of a number of materials commonly used for photoelastic coatings and models are listed in Table X. Materials used as photoelastic coatings are commercially available in sheet form, from which photoelastic transducers, in the form of biaxial and linear strain gages, may easily be cut. Such materials are listed in Table XI.

The properties of epoxy resins used by Trumbachev and Katkov[71] at the Skochinsky Mining Institute, Moscow, are listed in Table XII. The hardeners used with these resins are maleic and phthalic anhydrides, polyethylene polyamine, metapheniline diamine, and hexamethylene diamine. Suitable plasticizers are dibutyl phthalate, castor oil, and certain polyesters.[60]

Hogg[45] examined the properties of four transparent plastics for use as low modulus photoelastic inclusions, with the trade names Araldite CT 200, Columbia Resin CR39, Catalin BT 61-893, and Makrolon. Araldite has a slight yellow coloration, but the amount of light absorbed is small and in no way interferes with its use as a photoelastic material.

None of the materials is difficult to machine although sharp tools must be used to eliminate edge effects. Residual strain can easily be removed by annealing Araldite and Columbia Resin but this is more difficult with Catalin. Extruded sheet Makrolon displays considerable residual strain which is very difficult to remove.

Makrolon is the most sensitive of these materials, for which Hogg quotes unit fringe values as follows:

Makrolon	43 psi/fringe-in.
Catalin	91 psi/fringe-in.
Araldite	65 psi/fringe-in.
Columbia Resin	108 psi/fringe-in.

Table XI. Typical commercial photoelastic plastic model and sheet materials.
Data and descriptive material from manufacturers' catalogues.

Source - PHOTOLASTIC INC.

Coating materials

Type	K min.	C	Max. elong. (%)	E (1000 psi)	Nominal thickness available	Tolerances	Sensitivity constant to °F	Max. usable temp. °F
PS-1	.14	40	10	360	.120,.080,.040 .020.,010	±.002 ±.001	300	300
PS-2	.12	--	3	450	.120,.080,.040	±.003	350	500
PS-3	.02	--	30	30	.080	±.003	110	400
PS-4	.005	3-5	150	1	.120	±.003		350
PS-5	.11	60	3	420	.250	±.005	250	Model material

The following description suggests the typical uses for each of the different photoelastic sheets:

PS-1 General purpose for accurate stress analysis in elastic and elasto plastic ranges. Can be used in almost every case where the structure to be coated is of equal or higher modulus. It is normally supplied with a reflective or processed backing which has been designed to increase the bond strength of the material.

PS-2 An economical plastic where wider thickness tolerances are acceptable. Its exceptionally good thermal characteristics make it useful for high temperature tests.

PS-3 Generally used in application on non-metallic materials, also on post yield investigations on metals. It is used very successfully on fiberglass structures, and for crack propagation studies.

PS-4 Analysis of parts made of very soft materials (low modulus) and rubbers. It is also very useful as a model material as it requires very low forces for straining.

PS-5 A good model material for two-dimensional photoelasticity, exhibits good sensitivity with low edge effects.

Model materials

PS-5 Cast Epoxy sheet	This material has very low creep and edge effects.
PS-1 Polyester sheet	An excellent material for two dimensional model work. It is characterized by complete freedom of creep and edge effects, and has a high photoelastic sensitivity.
PS-4 Polyurethane sheet	A low-modulus material that requires very low forces for straining. It is desirable for making dynamic or wave propagation studies. It can also be used for hand loaded demonstration applications.
PL-4 Liquid epoxy resin	A plastic designed for casting of thick sections, sheets or three-dimensional models. It is characterized by a very low exothermic reaction, and consequently, casting of large section models without creating residual stresses is considerably simplified. It exhibits excellent machining characteristics and low humidity absorption.

Table XI (cont'd). Typical commercial photoelastic plastic model and sheet materials.

BUDD, S.A.

Plastic selection chart

Plastic	*Type*	*Young's modulus E (psi)*	*Thickness*	*Max. strain (%) (1)*	*K (2)*	*First fringe occurs at micro in./in. (3)*	*Easily contoured to (inches radius) (4)*
Sheets			1 mm			3,000	
	S-09	450,000	2 mm	2.5	0.09	1,500	40
			3 mm			1,000	
			1 mm			2,700	
	SC-10	480,000	2 mm	2.5	0.10	1,350	40
			3 mm			900	
			1 mm			15,000	
	S-02	37,100	2 mm	85	0.02	7,500	10
			3 mm			5,000	
	S-16	540,000	.042 in.	2.5	0.16	1,700	50
			.072 in.			850	
Liquid Brushed on	L-08	450,000	.01 in.*	2.5	0.08	14,100	All curvatures
			.02 in.			7,050	
	G	40,100	.01 in.	50	0.02	56,400	All curvatures
			.02 in.			28,200	
	L-02	40,100	.01 in.	85	0.02	56,400	All curvatures
			.02 in.			28,200	
	L-11	510,000	.01 in.	1.5	0.11	10,250	All curvatures
			.02 in.			5,125	
Contoured	L-08	450,000	.08 in.*	2.5	0.08	1,760	0.25†
	L-02	40,100	.08 in.	85	0.02	7,050	0.25†
	L-11	510,000	.08 in.	1.5	0.11	1,030	0.25†
Spray-on	Special spray equipment applies it in uniform coatings 0.005 in. (0.125 mm) or thicker						

(1) Limit of linear strain-optical response.

(2) The value of K factor and thickness is indicated on each sheet, but must be determined for liquid and contoured applications.

(3) The value of principal strain difference $(\epsilon_1 - \epsilon_2)$ in the metal which will produce one fringe in the plastic, using crossed polaroids. A fringe is the dividing line between red and blue or green, and is called "tint of passage."

(4) Radius of curvature to which plastic can be applied.

* Any thickness can be used; these values chosen for illustration.

† Take square root of radius for double curvature.

Table XII. Physical and mechanical properties of material for photoelastic coatings. (After Trumbachev and Katkov.[71])

No.	Composition (parts by weight)	Modulus of elasticity E (kg/cm^2)	Poisson's ratio (μ)	Bending strength δb (kg/cm^2)	Proportional limit σpb (kg/cm^2)	Stress band of material δ^{11} (kg/cm^2)	Max. ϵ(%)
1	Resin ED-6—100 Maleic anhydride—30	3.5×10^4	0.37	1400	500	11	0.7
2	Resin ED-6—100 Maleic anhydride—30 Dibutyl phthalate—17.5	3.0×10^4	0.37	1200	500	11	0.9
3	Resin ED-5 or E-40—100 Maleic anhydride—30 Unsaturated polyesters—25	1.6×10^3	0.36	--	450	10	2.2
4	Resin ED-5 or E-40—100 Maleicanhydride—30 Saturated polyesters—25	1.2×10^3	0.36	--	400	10	12.0

The Hawkes biaxial gage, and also his linear strain gages, are cut from commercially available polyester sheet (Photolastic PS-1 sheet) which is easy to machine, shows good stability, and has a high sensitivity.

Cements

The feasibility and reliability of photoelastic plastics as strain-indicating devices, in common with bonded strain gages of all types, depends on the character of the cement bond between the strain gage and the work-piece, and upon the stability of the cement itself. Ideally, the cement should permit complete transference of strain, as at a welded contact, without shrinkage or creep.

Similarly, the effectiveness of photoelastic inclusions hinges on the character of the cement bond around the periphery of the inclusion. Such gages are usually set into holes in the host materials, and the cement must fill the annulus between the meter and the host material with sufficient rigidity to transmit the stresses without creep. The uncured cement must be fluid enough to enable the meter to be set, yet viscous enough to hold the meter in position while the cement polymerizes. During this time the cement must neither expand nor shrink to such an extent that visible stress is introduced into the meter.

Epoxy resins are the most commonly used two-component cements but some of these are significantly exothermic during the curing period; the temperature rise depends upon the rate at which heat can be dissipated from the epoxy mass. Cure times decrease with rise in temperature, so that high exothermic resins quickly achieve working strength. However, they can also cause local thermal strains around the bonded interface, which become locked in and can produce a "no-load" fringe order in the glass.

Table XIII. Adhesives.

a. Adhesives used with photoelastic plastics. (Photolastic Inc.)

Type	Cure time (hr)	Cure temp.	Elong. (%)	E (1000 psi)	Max. usable temp. (°F)	Use with plastic types	Standard package
PC-1	12	Room	3-5	450	180	PS-1,PS-2,PL-1	1 oz.,Pt.,Qt.,Gal.
PC-6	24	Room	50	30	400	PS-3,PL-2	3 oz.,Pt.,Qt.,Gal.
PC-7	*	Elevated	3-5	450	500	PS-2	3 oz.,Pt.
PC-8	48	Room	10	500	180	PS-1	3 oz.,Pt.
PC-10	3-4	Room	3-5	450	180	PS-1,PS-2,PL-1	1 oz.,Pt.,Qt.,Gal.

* Cure time dependent on temperature chart of temp. vs time included in instructions.

b. Adhesives used with photoelastic coatings. (Trumbachev and Katkov.[71])

No.	Composition (parts by weight)	Time of polymerization (hr) 5-10°C	20°C	50-60°C	Shear strength (kg/cm²)
1	Resin ED-5(6)–100 Acetone–10 Polyethylene polyamine–6.5	48	36	4	100-150
2	Resin ED-5(6)–100 Dibutyl phthalate–20 Polyethylene polyamine–15	32	24	2	250-275
	Resin ED-5(6)–100 Polyethylene polyamine–15	30	24	1-2	200-230

Cements used with photoelastic coatings

The properties claimed for the cements sold by Photolastic Inc. for use with photoelastic sheet materials and the epoxy cements used by Trumbachev and Katkov[71] are given in Table XIII. The adhesives included Araldite, Epone, Epicote, Epoxite, etc., the hardening time of which mostly varied from 24 to 30 hours at room temperature. To shorten the polymerization time and to strengthen the bond Trumbachev and Katkov applied accelerators such as dimethyl aniline, or raised the temperature of the mixture to from 50° to 60°C.

Cements for photoelastic plastic strain gages and inclusions

Any of the cements used with photoelastic coatings may also be used with photoelastic strain gages. However with this type of device a rapidly acting cement is attractive in that considerable time can be saved during laboratory tests when they are used. For certain field operations, when using linear and biaxial photoelastic gages, a rapid-hardening cement is virtually essential.

For laboratory work, Photolastic Inc. PC-10, which cures in 3-4 hours, may be used. For the in-situ determination of stress by the core relief technique, and for field determinations of Young's

modulus and the stress-strain characteristics of rock cores, a dental cement, of unknown composition, trade name F88 (Tridox Products, 212 N. 21st St., Philadelphia, Pa. 19103) which has a very rapid hardening rate (1-2 minutes) has been used.

Rapid-hardening cements generally have rapid exothermic reactions and should only be applied as thin coats to enable the heat to be dissipated, and avoid shrinkage strains. The same effects occur with all bonded strain gages, but with photoelastic materials they lead to extraneous birefringence, whereas with other techniques they sometimes go unobserved. Upon polymerization rapid-hardening, cements sometimes tend to become brittle and hence, although giving a strong static bond, they can be dislodged by mechanical impact.

The cements used by Hogg[45] and Hawkes[39] to set photoelastic plastic inclusions into boreholes are identical to that designed by Moore[57] (FR type) for glass inclusions (photoelastic stressmeters) and are described below.

There are certain cardinal principles in relation to bonding photoelastic plastic gages:

1. Establish the time-temperature-humidity characteristics of both the gage and cement, and thereafter apply them only within their limitations, for the particular environmental conditions involved. As a general rule, only use photoelastic plastics for short-term investigations.

2. Always use control gages set on similar specimens to those under observation, but left unloaded in the same time-temperature-humidity environment. This will allow extraneous birefringence to be detected, and the appropriate corrections made.

Cements for photoelastic glass inclusions (Photoelastic Stressmeters)

Considerable work has been carried out on properties of cements suitable for bonding photoelastic glass stressmeters into rock and concrete host materials.

Theoretically the stiffness of the cement should be taken into consideration when calculating the stress concentration factors k_1, k_2 and k_3 for evaluation of the stressmeter sensitivity (see page 45). However, in practice the modulus of the cement at around 10^6 psi is not significantly different from that of cement grout on low modulus rocks, so stiffness effects can generally be neglected. In the theoretical derivation of the stress meter sensitivity laid out in Part 1, it is assumed that the meter is "welded" to the surrounding body, i.e. all stresses, compressive, tensile and shear, are transmitted across the interface. The cement layer must have a finite radial thickness and therefore a perfect welded boundary is not possible. With 1.25-in.-diam stressmeters the adhesive thickness is usually about $^1/_{16}$ in., i.e. adhesive thickness is $a/10$, where a is the outer radius of the meter. With larger stressmeters it is possible to have smaller ratios of adhesive thickness.

It has been found by Dhir[8] that for epoxy resin type cements the readings of photoelastic stressmeters are remarkably unaffected by the presence of thin layers of cement. The tests made to determine this will be discussed later in the section on stressmeter calibrations.

For compressive stress evaluation the interface bonding between the meter and the surrounding is not critical, but where tensile stresses are expected bonding is essential. Tests by Moore[57] indicate that a bond tensile strength of around 1000 psi can be expected between glass and rocks using the epoxy type cements. A similar value was also obtained by Rose[64] although he showed that in favorable circumstances (steel bonded to steel with a very thin cement layer) the tensile strength of epoxy cements can be as high as 4000 psi. Very little experimental work has been undertaken using stressmeters in tensile fields or in conditions where there is a significant (>2 fringe) reduction in compressive stress after the meter has been set. However, some tests by Hogg[45] have shown that the photoelastic stressmeter will accurately respond to tensile stress changes on the order of 300 psi before cement failure.

The selection of cements for setting stressmeters is essentially governed by their creep properties and considerations involved in the actual setting operations, i.e. time to set, viscosity, moisture effects.

Dhir[8] tested several cements for use with the photoelastic stressmeter before choosing epoxy resin Araldite AV121 with HY951 hardener (proportions 100 parts resin to 4.5 parts of hardener, by weight 25 parts 200 mesh carborundum powder). The setting time of this cement is about 1 hour at 18°C, but its life is considerably increased at lower temperatures. Its full cure time is approximately 24 hours, and when cured its elastic properties are $E = 1.37 \times 10^6$ psi and $\nu = 0.32$ (loading range 0 - 2500 psi, strain range 200 microstrains/min, age 1 week at 18°C).

While the fully cured resin is not affected by moisture, polymerization of the mix is. Therefore the mix is only suitable for dry holes. For field work this cement has three major drawbacks:

1. It will not set completely in wet conditions. However, if the cement dries out later then the curing process will continue to completion.

2. The uncured mix is too viscous for setting stressmeters at low temperatures. It freezes before curing at 0°C.

3. The hardener is hygroscopic and deteriorates over a period of about 3 months, unless stored in ideal conditions.

Rose[64] used Araldite AV121 with X83/144 hardener (100 parts resin to 13 parts hardener by weight) to set stressmeters in a concrete buttress dam. This epoxy mix will polymerize in the presence of water and has a usable life of about 15 minutes at 18°C. Initial solidification occurs after about 2 hours and a full-strength cure is achieved in about 48 hours. However, for a similar application at low temperatures, Rose found it better to use AV121 with Ancamine LT hardener and 400 mesh carborundum filler, in the proportions 100:20:50, respectively. The setting time of this mix is 20 to 30 minutes, which gives ample time to set the meter, and the cure time is 5-7 days at -4 to +5°C. This cement will cure in the presence of water and its elastic properties when fully cured are: $E = 0.82 \times 10^6$ psi, and $\nu = 0.35$ (range 0 - 2000 psi at a constant strain rate of 200 microstrains/min, age 1 month).

Moore[57] also tested various cementing materials for stressmeters. He found no significant differences in the calibration results of stressmeters set with different epoxy cements and finally selected an epoxy resin FR 1131A with hardener FR 1131B for his field studies. This cement, which also sets in wet conditions, is now generally recommended for use with the photoelastic stressmeter and can be obtained prepackaged for this use.* The composition is as follows:

Epoxy resin (FR 1131A)	20 parts by weight
Hardener (FR 1131B)	10 parts by weight
Carborundum (400 mesh)	40 parts by weight
Barytes	10 parts by weight
Aerosil	1 part by weight

The reaction between resin and hardener is exothermic and only small amounts, enough for one inclusion, should be mixed at one time. The purpose of the barytes and the carborundum is to help absorb the heat generated, to give the necessary stiffness for setting, and to give increased rigidity when set. Aerosil, a fine siliceous powder, is also used to absorb the heat of polymerization and to increase the viscosity of the cement mix.

---

* Stress Engineering Services Ltd., Midsomer-Norton, Somerset, England.

AD-A072 011 SHEFFIELD UNIV (ENGLAND) POSTGRADUATE SCHOOL OF MINING F/G 20/11
PHOTOELASTIC INSTRUMENTATION. PRINCIPLES AND TECHNIQUES.(U)
MAY 79 A ROBERTS, I HAWKES DAJA37-70-C-0222

UNCLASSIFIED CRREL-SR-79-13 NL

2 OF 2
AD
A072 011

END
DATE FILMED
8-79
DDC

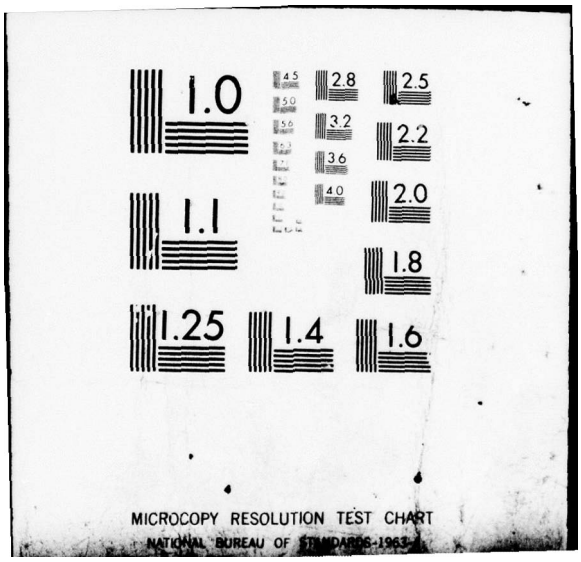
1.0
1.1
1.25
1.4
1.6
1.8
2.0
2.2
2.5
2.8
3.2
3.6
4.0
4.5
5.0
5.6
MICROCOPY RESOLUTION TEST CHART
NATIONAL BUREAU OF STANDARDS-1963-A

This mix gives a cement which can be used for setting inclusions in the temperature range 5° to 20°C. Below 5°C the resin needs to be warmed to aid mixing. Above 20°C more carborundum and Aerosil should be added, in the ratio of 40:1.

The mix has a workable pot life of 35 minutes at 15°C, increasing to 1 hour at 0°C, and decreasing at higher temperatures. It is hard after 4 hours, but requires at least 24 hours before it can be regarded as fully cured. Its modulus and Poisson's ratio are 1.35×10^6 psi and 0.35 respectively.

Tests to investigate the magnitude and effects of cement creep on stressmeter readings have been made by Moore,[57] Hooper,[49] Rose[64] and Rabbets.[63] The general conclusion of these studies is that for meters set into concrete-like materials, with the FR cements, at temperatures to 18°C the change in fringe order with time is relatively insignificant. However, at temperatures over 29° there is a tendency for the fringe order readings to fall at the high fringe order (4 to 5). For stressmeters set in high temperature environments (>38°C), Rabbets recommends the use of Portland cement grout incorporating an agent to reduce shrinkage.

LOAD MEASUREMENT BY PHOTOELASTIC TRANSDUCERS

Photoelastic load cell designs can be broken down into two main categories: those which induce the direct loading of a glass disk and those in which the glass disk is located in a hole passing through a steel body and diametrically loaded by deformation of the body. Load cells of the first category, where the total load is carried by the glass disk, are very easy to design and construct and their use will be discussed in detail in a later section on applications. The sensitivity of such cells is determined by eq 18 or 18a, depending upon whether transmitted or reflected light is used, and as the load range is controlled by the strength of the glass disk, their range is very limited. The majority of photoelastic load cells are of the second category in which the load is carried by a steel body with the glass disk measuring the body deformation. To be able to design steel bodied load cells it is necessary to understand the deformational behavior of both the steel body and the glass disk.

Deformation and Strength of Glass Disk Transducers

On p. 22 (Part 1) the stress distribution was given for a disk diametrically loaded across two points. In practice, with the disk set in a deforming steel body, the load is applied to the disk over a finite area and so a more detailed treatment is necessary to predict the disk stresses and deformation.

Stress distribution in a disk loaded diametrically over finite areas

Where uniform radial loading is applied over two opposite arcs of a solid circular disk, equations for the stresses along the two principal diameters are given by Hondros.[48]

Applying a load P over diametrically opposite arcs, as in Figure 53, and taking the loading diameter along the vertical (y) axis, the principal stresses (tensile positive) along the loading axis at any radius r are:

$$\sigma_\theta(y) = + \frac{P}{\pi R t a} \left\{ \frac{[1-(r/R)^2]\sin 2a}{1-2(r/R)^2 \cos 2a + (r/R)^4} - \tan^{-1}\left[\frac{1+(r/R)^2}{1-(r/R)^2} \tan a \right] \right\} \tag{77}$$

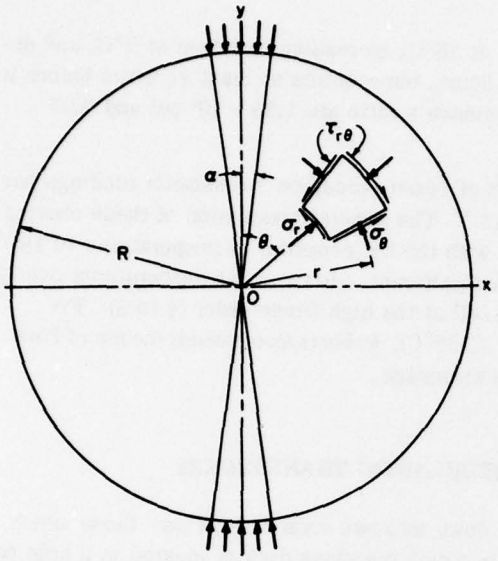

a. Radial Stresses

Figure 53. Notation for polar stress components in circular disk under radial applied stresses.

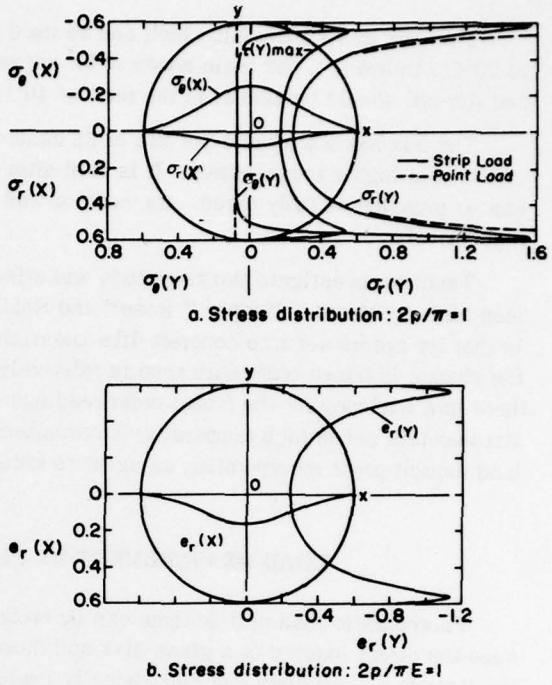

Figure 54. Theoretical stress and strain distribution along loading (OY) and transverse (OX) diameters. (From Hondros.[46])

$$\sigma_r(y) = -\frac{P}{\pi R t \alpha}\left\{\frac{[1-(r/R)^2]\sin 2\alpha}{1-2(r/R)^2\cos 2\alpha+(r/R)^4} - \tan^{-1}\left[\frac{1+(r/R)^2}{1-(r/R)^2}\tan\alpha\right]\right\}. \tag{78}$$

Along the x-axis the principal stresses are:

$$\sigma_\theta(x) = +\frac{P}{\pi R t}\left(\frac{\sin 2\alpha}{\alpha}\right) - 1 \approx +\frac{P}{\pi R t} \tag{79}$$

$$\sigma_r(x) = -\frac{P}{\pi R t}\left(\frac{\sin 2\alpha}{\alpha} + 1\right) \approx -\frac{3P}{\pi R t}. \tag{80}$$

From symmetry, the shear components along both axes are zero.

These four equations, together with the radial strain distribution, are plotted in Figure 54 for the case where the loading width equals $D/12$, i.e.

$$\alpha = \tan^{-1} 1/12 .$$

Comparison of this stress distribution with that given on p. 22-23 for a point-loaded disk shows that the vertical compressive stress attains a maximum value, equal to the applied pressure, at the loaded surface, instead of taking on an infinite value as before. It is also evident that the tensile stress along the vertical diameter no longer remains constant, as predicted by the point load theory, but changes to compression for values of $r/R \geq 0.85$.

Also shown in Figure 54 is the distribution of maximum shear stress along the loaded diameter. This is directly proportional to the variation in fringe order along the same axis. Its minimum values are located at the points $r/R = \pm 0.92$, which is the same result as for a uniform strip load on a semi-infinite solid.

From St. Venant's principle the stress distribution within the disk, except in the vicinity of the loading platens, will be largely independent of whether the load is considered to act at a point or over a small but finite area. From eq 77 and 78 the difference in principal stresses at the center of the disk is:

$$\sigma_r(y) - \sigma_\theta(y) = -\frac{4P \sin 2\alpha}{\pi Dt\, a} \tag{81}$$

and from the point load equations (eq 11 and 12)

$$\sigma_r(y) - \sigma_\theta(y) = -\frac{8P}{\pi Dt}\,. \tag{82}$$

Hence, by assuming a point load, the calculated principal stress difference would be in error by an amount

$$1 - \frac{2\alpha}{\sin 2\alpha}\,. \tag{83}$$

For $\alpha = \tan^{-1} 1/12$, the error is -0.3%, so the effect of loading a disk over this finite width is to reduce the principal stress difference by 0.3%. The corresponding reduction in fringe order, with five fringes at the center of the disk, would be only 0.015, or less than the reading accuracy of 0.02. For the smaller loading arcs or contact widths normally used in practice this difference in central fringe order becomes less than 0.1% and may therefore be neglected.

Deflection of a glass disk diametrically compressed between flat platens

In many transducer applications the glass disk is diametrically loaded between flat steel platens. The required surface displacements in both the disk and platens can be obtained by adding the disk deformations to those of the platen at the contact area. Hooper[50] has done this and has shown that the mutual approach (deformation) Δ_z of two points on the loading axis of a disk, each at a distance $(R + z)$ from the cylinder center, with the disk loaded between two elastic flat platens, is given by

$$\Delta_z = \frac{P}{\pi t}\left[\frac{1-\nu_g^2}{E_g}\left(2 \ln \frac{2D}{a} - 1\right) + \frac{1-\nu_s^2}{E_s}\left(2 \ln \frac{4z}{a} - \frac{\nu_s}{1-\nu_s}\right)\right] \tag{84}$$

where subscripts g and s refer to glass and platen (steel) respectively and a, the contact half width, is given by

$$a^2 = \frac{2PD}{\pi t}\left(\frac{1-\nu_g^2}{E_g} + \frac{1-\nu_s^2}{E_s}\right). \tag{85}$$

Figure 55 is a plot of eq 84 for a range of z values, with values of $D = 1.25$ in., $t = 1$ in., $E_g = 10.7 \times 10^6$ psi, $\nu_g = 0.24$, $E_s = 30 \times 10^6$ psi, and $\nu_s = 0.30$, which are typical for a glass disk

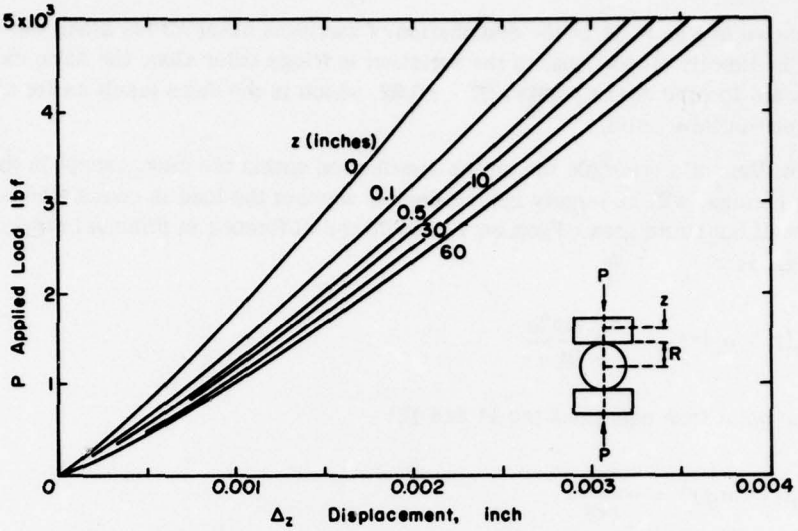

Figure 55. Plane-strain deformation for a 1/25-in.-diam, 1.0-in.-long glass cylinder diametrically compressed between flat steel platens, computed from eq 84. (From Hooper.[50])

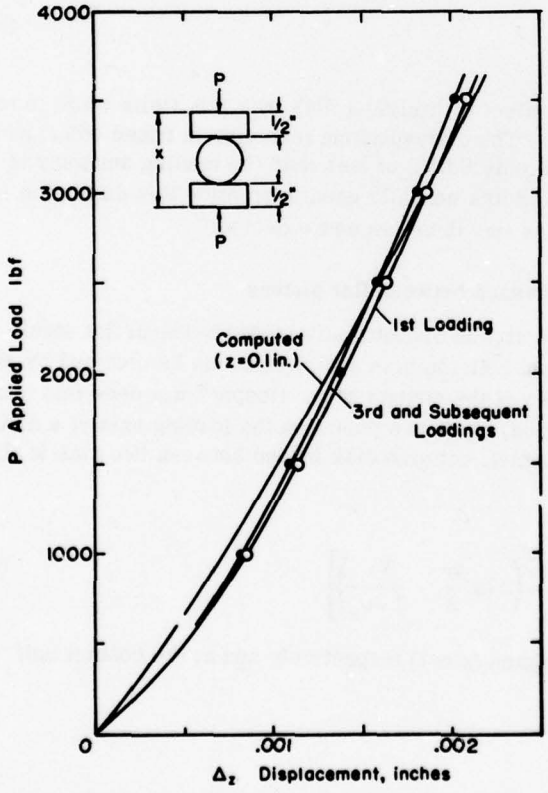

Figure 56. Measured and calculated displacements for 1.25-in.-diam, 1.0-in.-long glass cylinder loaded in diametral compression between flat steel platens. (From Hooper.[50])

transducer assembly used in a photoelastic load cell. It is apparent from Figure 55 that the deformation of the platens is a significant factor.

Measured load-deformation curves for the above glass disk transducer assembly are shown in Figure 56. The slight shift between the curves obtained on first and subsequent loadings is due principally to permanent deformation in the steel platens. This effect can be overcome in practice by proof-loading the cells, and bedding-in the glass disks, before the cells are installed for service. The measured deformation curves are only linear for loads greater than those corresponding to about two fringes. This accounts for the slight departure from linearity which is sometimes observed in the load/fringe order characteristic of photoelastic load cells as will be shown later.

Also included in Figure 56 are theoretical values of overall disk deformation calculated from eq 84 and with a value of $z = 0.1$ in. The measured and calculated values are in fairly close agreement for this value of z.

Values of deformation (first loading cycle) for disks of various sizes measured by Hooper[50] are summarized in Table XIV, and correspond to loads producing approximately five fringes in

Table XIV. Measured deformations of 1-in.-thick soda-lime glass disks. (From Hooper.[50])

Disk diam (in.)	*Applied load (lb)*	*Measured disk def. (10^{-3} in.)*
1.0	2500	2.0
1.25	3500	2.1
1.5	4000	2.1
2.0	5000	2.2

Table XV. Elastic and shakedown load limits for EN 57 steel platens. (From Hooper.[50])

Disk glass diam (in.)	*Load for 5 fringes* (lb)*	*Elastic limit (lb/in.)*	*Shakedown limit (lb/in.)*
0.5	1,330	3,100	12,000
1.0	2,660	6,100	24,000
1.25	3,330	7,700	30,100
1.5	3,990	9,200	36,100
2.0	5,320	12,300	43,900

* Under transmitted red light ($\lambda = 6450$ Å).

each case. It is interesting to note that in all cases the deformation required to produce about five fringes at the disk center is around +0.002 in. and is virtually independent of disk diameter.

Elastic and shakedown limits for steel loading platens

In a photoelastic load gage, where the transducer is under diametral loading imposed between steel loading platens, and the load taken by the disk is small, the contact stresses in the steel fall within the elastic range. As the load is increased a yield point is reached somewhere in the contact region, and this may be predicted by combining the elastic stresses with a suitable yield criterion. The applied load corresponding to the yield point is termed the *elastic limit* P_e.

At any higher load plastic deformation will occur, and if this load is subsequently removed some residual stresses will remain in the contact zone. If the same load is then reapplied, the combination of elastic and residual stresses in the contact region may not reach the yield point of the material. In such a case the stress state is said to "shake down" to an entirely elastic system, and the maximum load at which this takes place is referred to as the *shakedown limit* P_s. It follows, therefore, that in designing photoelastic load cells the load transmitted by the internal platens must never be allowed to exceed the shakedown limit, otherwise cumulative plastic flow will occur.

Hooper[50] has studied the literature on the subject in detail. He concludes that the elastic limit P_e for platens loaded by a cylinder is given by

$$P_e = 2.8\, a\, t\, Y \tag{86}$$

and the shakedown limit P_s in rolling contact by

$$P_s = 3.6\, a\, t\, Y \tag{87}$$

where a is the contact half width, t the cylinder thickness and Y the yield stress in compression.

Hooper was unable to determine the theoretical shakedown limit for static loading other than to conclude that it occurs at appreciably higher loads than with rolling contact. Thus the use of eq 87 provides conservative values for the shakedown limits.

Table XV shows theoretical loads for the elastic limit and shakedown limit from eq 86 and 87 calculated for 1-in.-long glass disks with typical diameters and loaded by a steel platen having a yield stress of 152,000 psi (EN 57 steel, 320 Vickers hardness number). For these calculations, the half width contact a was calculated from eq 85 at the load required to produce five fringes at the disk center using transmitted red light ($\lambda = 6450$ Å). From Table XV it is apparent that there is an adequate safety factor of approximately 2.2 with respect to the elastic limit for these conditions. Although the use of loads up to the shakedown limit is permitted to retain subsequent elastic behavior, it is more practical to consider the elastic limit as the upper design criterion.

Fracture mechanism in glass disks under diametrically applied loads

Hooper[51] has made a detailed study of the failure mechanism of glass disks diametrically loaded between flat platens. He has shown that the mode of fracture can be explained in terms of the tensile stresses generated in the contact region. The classical two-dimensional Hertz analysis of the problem predicts only compressive stresses in the contact region, but a more detailed treatment of the problem after Kunert[54] predicts tensile stresses along the edges of the contact region. The predicted tensile stresses are a minimum at the center of the contact edge and rise to a pronounced peak near the ends of the contact rectangle. In general Hooper found that failure initiated at the predicted points. Hooper[51] points out that Kunert's equation gives the stresses in an elastic half space due to a Hertzian pressure uniformly distributed along the contact length and cannot be applied literally to a case where the cylinder has finite rigidity. However, Kunert's equations are useful in that they predict the region of highest tensile stress (at the disk ends) and give the general orders of magnitude.

It follows logically that if the peak tensile stresses at the disk ends can be reduced, the load required to produce failure should increase. (Tapering the ends of roller bearing rollers to increase the load bearing capacity is common practice.)

Hooper[51] showed that by chamfering the edges of glass disks to an angle of 5° over a length of 0.125 in., the load to failure of disks 1.125 in. in diameter and 0.738 in. long could be increased 53% over similar nonchamfered disks.

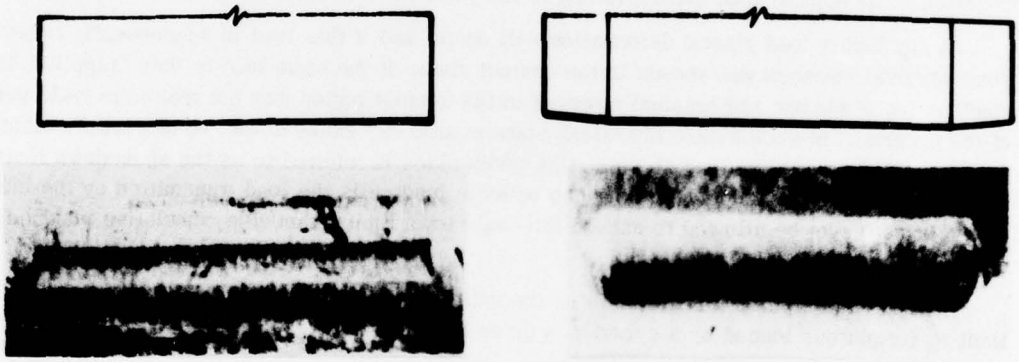

a. Impression from normal disk. *b. Impression from chamfered disk.*

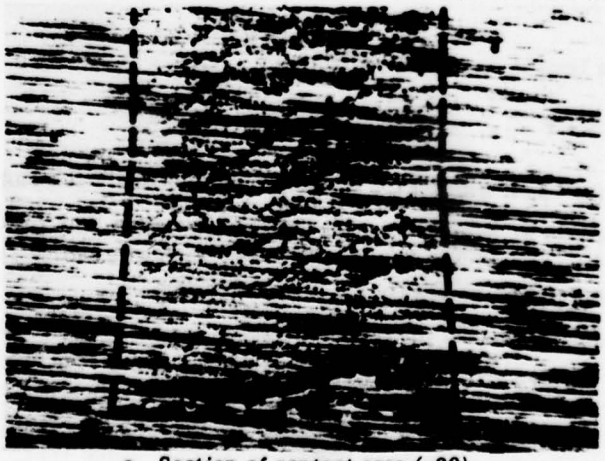

c. Section of contact area (×30).

Figure 57. Contact zones in flat steel platens used with 1¼-in.-diam, ¾-in.-thick glass disks. (From Hooper.[50])

Figure 57 illustrates part of the impression made by loading a 1.25-in.-diameter, 0.75-in.-thick disk between ground steel platens (V = 220) to 6000 lb, equivalent to about twice the working load of the disk when it is used as a transducer. The lack of uniformity of loading, on a microscopic scale, is apparent. By tracing the original grinding marks through the contact area it can be seen that zones of appreciable size exist in which there is no contact with the glass. This is despite the very high normal stresses generated over the area of contact, in this case amounting to about 180,000 psi at the center.

Influence of platen material and lubrication

When a glass disk is pressed against a platen of different elastic properties, one contact surface tries to contract more than the other and interfacial forces are generated between the two bodies. These surface transactions induce additional stresses that reduce the tensile stresses and thus beneficially increase the disk failure load.

Hooper[51] has made a detailed study of the problem; some of his results are given in Table XVI. Generally, as the rigidity of the platen material increases so does the surface traction and the disk failure load. However, higher failure loads were obtained with glass platens than with any other platen material. This has been explained by Hooper as being due to interfacial friction and slip effects. With glass platens, interfacial friction is theoretically zero, but with metal platens slip between the glass and platens causes the interfacial stresses to be reduced. Hooper confirmed this by making tests on two sets of glass disks loaded between greased and "dry" flat steel platens. The average failure load when using the dry platens was 35% higher than the corresponding value using greased platens.

Table XVI. Mean failure loads of 1.25-in.-diam, 0.738-in.-long soda-lime glass cylinders compressed between flat platens of various materials. (From Hooper.[51])

Ten tests per platen.

Platen material	*E(10⁶ psi)*	*ν*	*P(lb)*	*Spread (lb)*
Solid cylinders				
Glass	10.7	0.24	8920	1440
Steel	30	0.30	7940	1110
Brass	14	0.37	6980	350
Aluminum	10	0.34	6910	610
Perspex	0.43	0.35	5630	770
Hollow cylinders				
Glass	10.7	0.24	1630	130
Perspex	0.43	0.35	1760	210

Design Aspects of Photoelastic Load Cells

For loads up to about 3000 lb a glass disk transducer can be used with the load applied directly to the disk, while still retaining an acceptable factor of safety against fracture. Higher loads require a separate elastic body with the disk measuring distortion and thus indicating the load on the body. Figure 58 illustrates the general design principles of such load cells.

Cylindrical body load cells

One of the most common load cell bodies consists of a solid steel cylinder containing a transverse hole at mid-height (Fig. 58a). Load applied to the ends of the cylinder causes distortion

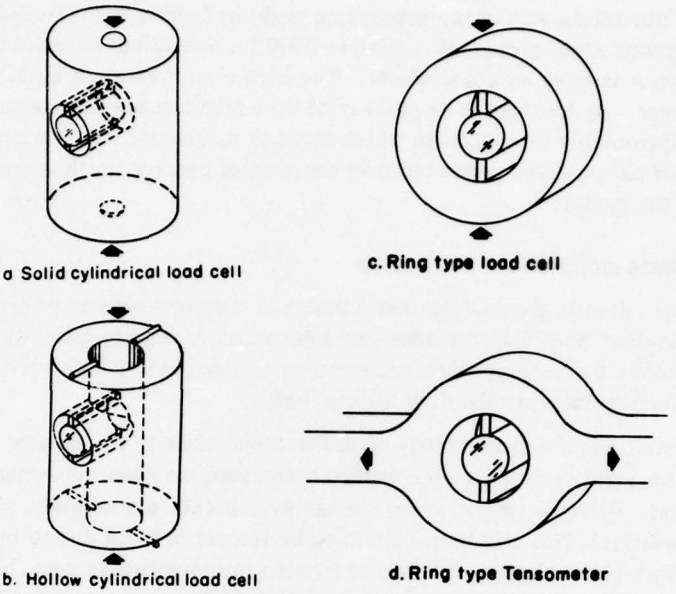

Figure 58. Loading arrangements for photoelastic load cells.

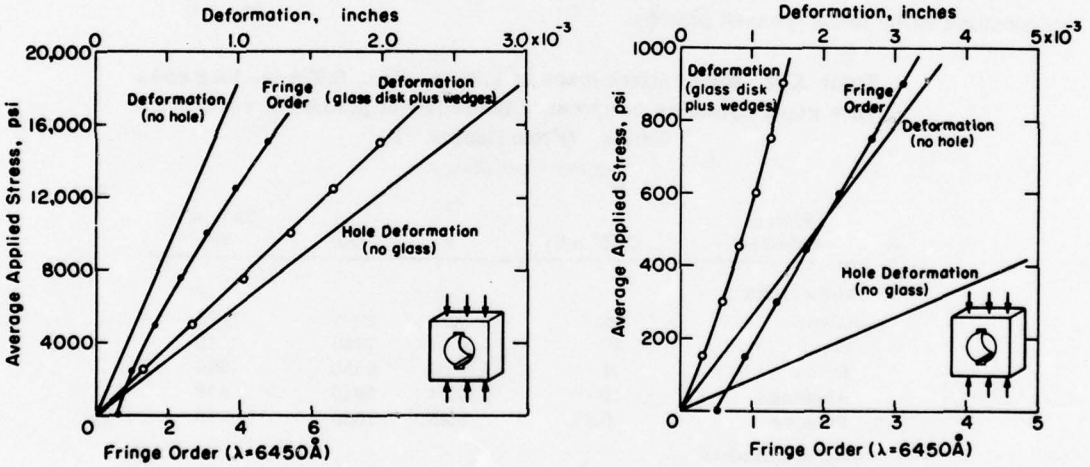

a. In steel slab. *b. In acrylic resin slab.*

Figure 59. Calibration and deformation characteristics of 1.25-in.-diam, 1-in.-thick glass disk. (From Hooper.[50])

of the central hole which in turn leads to deformation of a glass disk transducer located within the hole. The gage body must be capable of withstanding the stress concentrations produced by the hole, with an adequate safety margin, and the deformation of the central hole must be known with sufficient accuracy to enable the load cell geometry to be calculated for any specified sensitivity.

Hooper[51] has made a detailed study of the basic principles of photoelastic load cells and reference should be made to his paper for the detailed design guidelines.

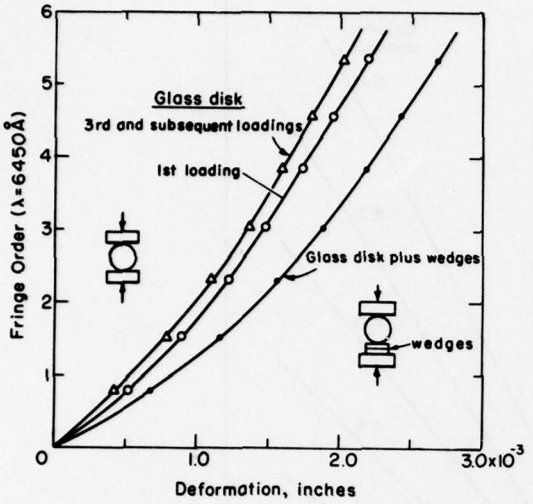

Figure 60. Measured diametral deformation of 1¼-in.-diam, 1-in.-thick glass disk and wedge assembly. (From Hooper.[50])

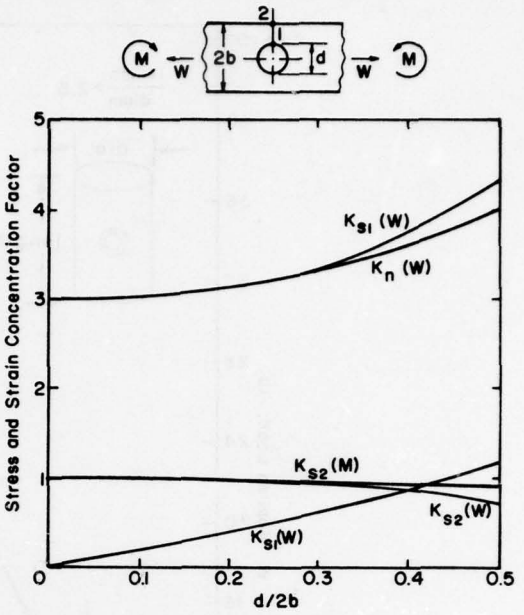

Figure 61. Stress and strain concentration factors for strip of finite width in tension and bending. (From Howland and Stevenson.[52])

Hooper experimented with glass disks set in holes in both steel and acrylic resin bodies. To simulate plane stress conditions in a load cell he used two 1.5-in.-thick, 8-in.-square slabs, one of steel and the other of acrylic resin. A hole 1.624 in. in diameter was drilled centrally in each slab and then slotted to give flats 0.5 in. wide at diametrically opposite points, in line with the intended loading direction. A 1.25-in.-diameter, 1-in.-thick soda-lime glass disk was set in each of the slots, the clearance between the disk and slot surfaces being taken up by an upper steel platen and a lower sliding wedge assembly. The relationships between fringe order at the center of the disk and the average applied stress for the two slabs are given in Figure 59. The wedge mechanism was used to preload the disks to approximately 0.5 fringe, resulting in a displacement of the calibration curve (applied stress/fringe order) away from the stress axis. Values of unrestrained hole deformation, calculated after Muskhelishvili,[23] are included in Figure 59, as are the deformations that would have occurred if the slabs had not been perforated. For the steel slab, the calibration curve is sensibly linear beyond the second fringe, and this is typical for all steel-bodied load gages having a preload below about one fringe.

Hooper made further tests to obtain the fringe order/deformation curve for the glass disk loaded in the wedge mechanism (Fig. 60). From these data the overall deformation of the glass and wedges can be obtained for a given fringe order.

The presence of a circular hole in a loaded body gives rise to considerable stress gradients, which ultimately determine the strength of the body. Figure 61 shows the stress and strain concentration factors at the edge of a circular hole located at the center of a uniaxially loaded strip of finite width. The stress concentration factor K_s is the ratio of the stress in the loading direction at the required point to the stress that would have occurred without the hole. The strain concentration factor K_n is the ratio of the hole deformation along the loading axis to the corresponding deformation with no hole present (see Hooper for the derivation of K_n). Also shown in Figure 61 are the theoretical stress concentration values obtained by Howland and Stevenson[52] for the case where a bending moment is applied in the plane of the strip.

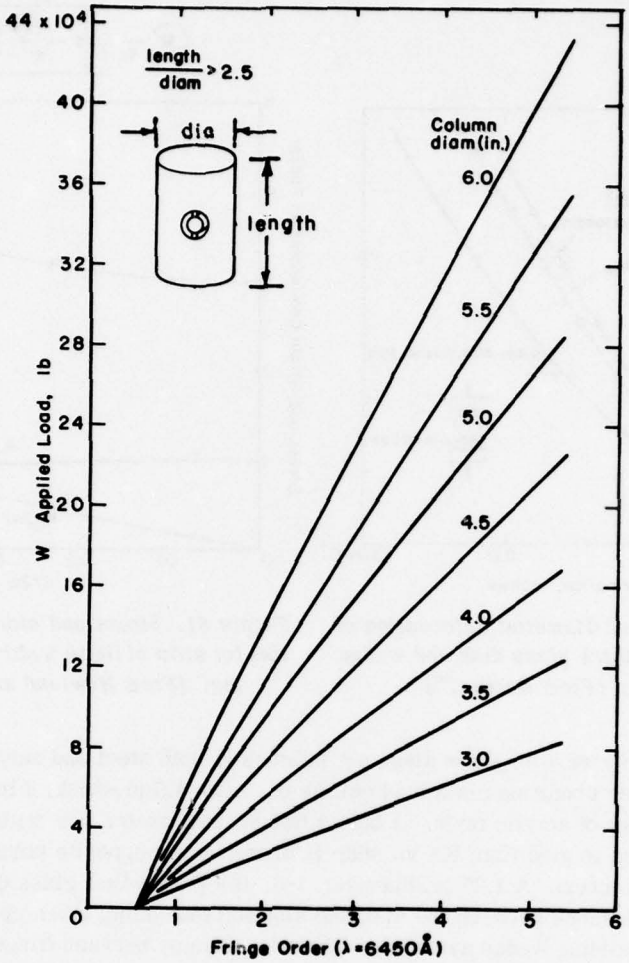

Figure 62. Computed calibration curves for steel-body load gages of various shapes. Constant internal bore 1.625 in. diam; constant glass cylinder shape, 1.25 in. diam, 1.0 in. long; transmitted light. (From Hooper.[50])

In most photoelastic load cells of the steel cylindrical type the ratio of hole to cylinder diameter is around 0.4.

When the load-bearing member in a load cell is a steel cylinder, with the glass disk transducer measuring the deformation of a transverse hole passing at mid-height through the body, the hole deformation is not quite uniform along its length. This is because plane stress conditions prevail at the ends while conditions at the center are closer to those of plane strain.

Hooper[50] made a series of diametral measurements along the length of a hole traversing a loaded cylinder. At a deformation sufficient to produce five fringes in a 1¼-in.-diam glass disk (approximately 2×10^{-3} in.) the differential deformation was around 10^{-4} in. maximum. This is a relatively insignificant amount and in designing cylindrical-type photoelastic load cells the influence of the

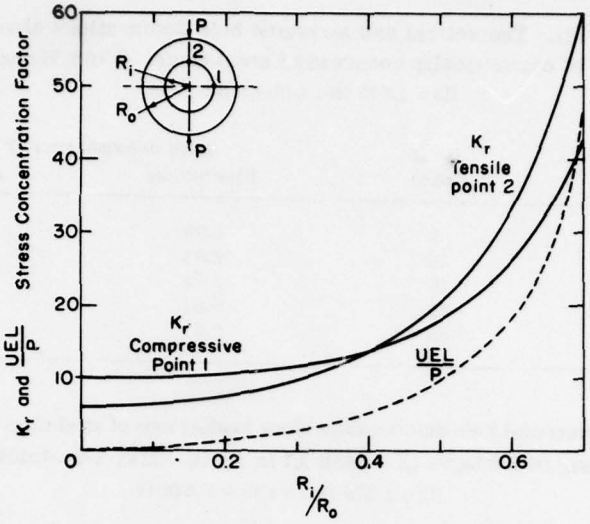

Figure 63. Stress concentration factors and hole deformation for elastic ring in diametral compression. (From Hooper.[50])

circular cross section on the hole deformation can be ignored.

Figure 62 shows calibration curves computed by Hooper for cylindrical-type load gages with a length to diameter ratio greater than 2:5.

Ring-type photoelastic load cells

The lower limit of the working range of photoelastic load cells of the cylindrical type is about 50 tons. The lower range can be extended by adopting a steel tube or ring as the deforming elastic body. Such a loading system is analogous to the well-established proving ring technique, with ring deflections being measured by the glass disk instead of a dial gage.

The relation between load P and measured hole deformation in a ring-type load gage is almost perfectly linear, the change in internal diameter U along the loading axis of a ring of rectangular section being given by Morley[58] as

$$U = \frac{3P}{EL}\left(\frac{1+\rho}{1-\rho}\right)^3\left[\frac{\pi}{8} - \frac{2(1-\rho)}{\pi(1+\rho)\ln(1/\rho)}\right] + \frac{1}{\pi\ln(1/\rho)} \tag{88}$$

where ρ is the ratio of outer to inner radius, L is the width of the gage, and E is the modulus. It is interesting to note that for a given applied load per unit length and elastic modulus, the ring deflection is dependent only upon ρ. Figure 63 gives the value of UEL/P as a function of ρ.

Calculated hole deformations, based upon the mean values for generalized plane stress and plane strain conditions, are listed in Table XVII and are all within 5% of the corresponding measured displacements. Thus eq 88 is entirely satisfactory for the purpose of predicting the values of hole deformation required for the design of ring-type photoelastic load cells.

In cylindrical-type load cells it is possible to neglect the effect of glass disk resistance on the hole deformation. This is not necessarily so for ring-type gages, however, as the load carried by the disk may amount to a substantial proportion of the total applied load.

Table XVII. Theoretical and measured hole deformations along loading axis of diametrically compressed steel rings. (From Hooper.[50])

ID = 1.875 in., width = 3.510 in.

OD (in.)	*Load (tons)*	*Hole deformation (10^{-3} in.)*	
		Theoretical	*Measured*
3.000	7	2.98	3.02
3.250	10	2.81	2.98
3.626	15	2.74	2.77
4.002	20	2.61	2.60
4.490	25	2.41	2.52

Table XVIII. Theoretical hole deformations along loading axis of steel rings at loads corresponding to 5 fringes (λ = 6450 Å) in 1¼-in.-diam, 1-in.-thick glass disk.

ID = 1.875 in., width = 3.510 in.

OD (in.)	*Without disk*		*With disk*	
	Total applied load (10^3 lb)	*Hole deformation (10^{-3} in.)*	*Net applied load (10^3 lb)*	*Hole deformation (10^3 in.)*
3.000	15.5	2.95	12.2	2.32
3.626	21.3	2.68	18.0	2.27
3.626	32.3	2.63	29.0	2.36
4.002	42.0	2.45	38.7	2.26
4.490	54.7	2.35	51.4	2.21

The applied loads necessary to produce five fringes in a 1¼-in.-diameter, 1-in.-thick glass disk set in a ring-type load cell body have been calculated by Hooper[50] and are given in Table XVIII. A load of roughly 3300 lb is required to produce five fringes in the glass disk itself and this value must be deducted from the total applied load to give the net load carried by the steel ring itself. In designing load cells below 20 tons capacity, the effect of disk rigidity becomes significant and an iterative process is used to calculate calibration curves for this type of gage. Values of fringe order are first calculated on the assumption that no resistance is offered by the glass disk. Then the cylinder loads corresponding to these fringe orders are deduced from the applied load to give a net diametral load across the ring. New values of fringe order are then obtained, and the procedure is repeated until the variation between successive values of fringe order is acceptably small. This typically takes three iterations.

Figure 64 shows the results of such a procedure for predicting the calibration characteristics of a steel ring load cell, ID 1.625 in., OD 3.0 in., length 3.5 in., fitted with a glass disk 1.25 in. in diameter and 1 in. long, viewed by transmitted light (λ = 6450 Å). The measured load/fringe order curve is also given in Figure 64 and shows that the calculation procedures as laid out are adequate for design purposes.

Figure 65 summarizes the results of calculations on a range of ring-type gage bodies, given the necessary parameters for gages with ranges from 8 to 30 tons.

Another important consideration in the design of ring-type load cells is the distribution of stress within the body of the gage. Of particular interest are the maximum tensile and compressive stresses which result from the application of diametrically opposite line loads.

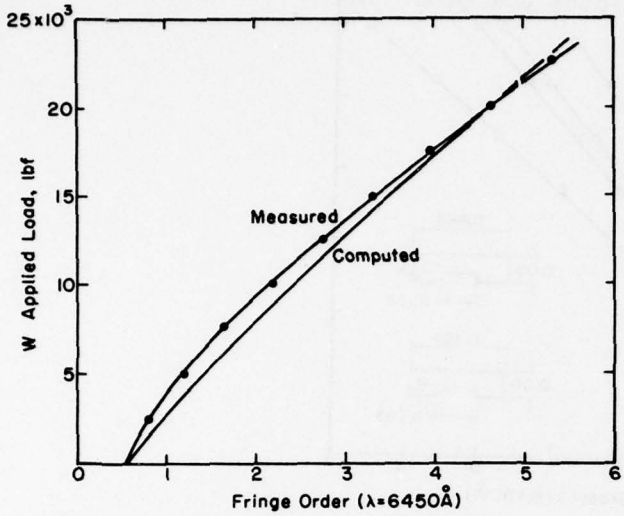

Figure 64. Computed and measured calibration curves for 10-ton ring-type load gage. Steel ring: ID 1.625 in., OD 3.0 in., length 3.5 in.; glass cylinder: 1.25 in. diam, 1.0 in. long; transmitted light. (From Hooper.[50])

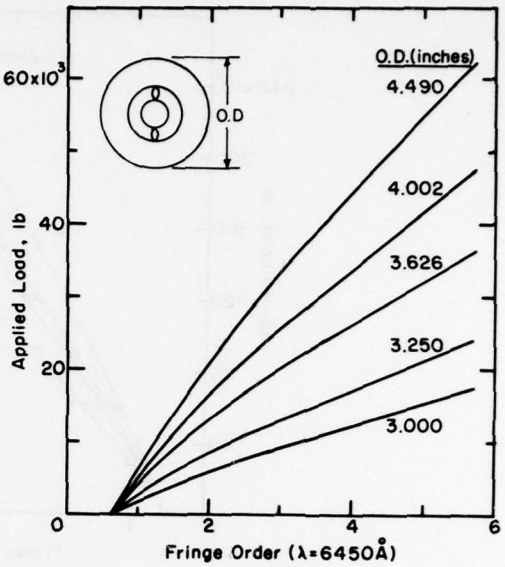

Figure 65. Computed calibration curves of ring-type steel body load gages containing a 1¼-in.-diam, 1-in.-thick glass disk (ID 1⅞ in., ring width 3.510 in.). (From Hooper.[50])

These maximum stresses occur at points where the hole boundary intersects the loading and transverse axes. Popov[62] gives numerical values for the stress concentrations at these points, relative to the corresponding values for a solid disk. Tangential stresses at the hole boundary are given by

$$\sigma_\theta = \frac{PK_r}{\pi L R_0} \tag{89}$$

where R_0 is the inner radius. The relevant stress concentration factors, K_r, are plotted in Figure 63.

For the ring geometry normally encountered when making photoelastic load cells the maximum tensile stress along the axis of loading is the most critical. It is essential to ensure that this stress is well within the elastic limit of the material from which the gage body is constructed.

Working range and sensitivity of steel-bodied load cells

Figures 62 and 65 show the working range of typical steel-bodied load gages. The initial fringe order at zero applied load represents the glass disk preload. The disk is preloaded to ensure that no movement can take place between it and the loading platens and also to minimize the nonlinearity of the fringe order/load relationship at low applied loads. Typical preloads are between 0.5 and 1.0 fringe.

The precise calibration characteristic for any other load gage will, as described, depend upon the stiffness of the wedge mechanism and the degree of flatness and surface finish of the slots and internal platens, but Figures 62 and 65 may safely be used to give an initial estimate of load-carrying capacity. Thus, by interpolation, a convenient body size may be chosen to cover load ranges from 0 to 200 tons.

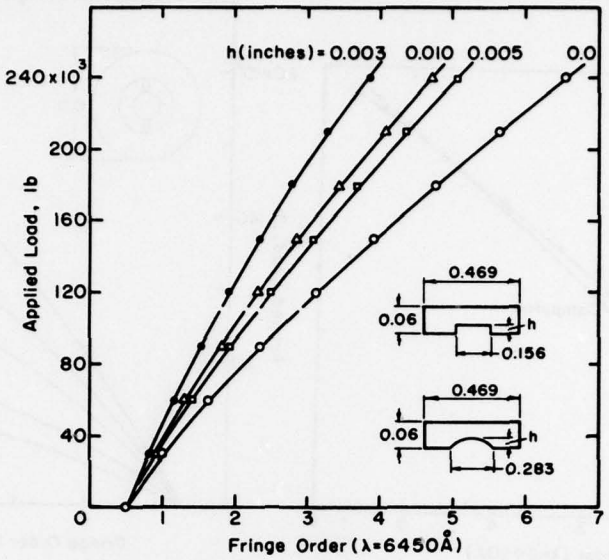

Figure 66. Effect of slotting top platen on load gage sensitivity. Column length 12 in., diam 4½ in., hole diam 1⅝ in.; disk 1¼ in. diam., 1 in. thick. (From Hooper.[50])

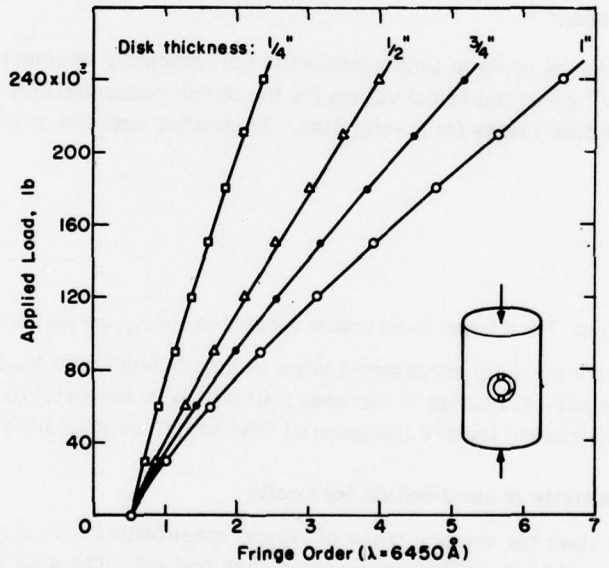

Figure 67. Variation of load gage sensitivity with thickness of glass disk transducer. Column length 12 in., diam 4½ in., hole diam 1⅝ in., disk diam 1¼ in. (From Hooper.[50])

The sensitivity of a photoelastic load gage is primarily dependent upon the geometry of the gage body, but it may also be changed by adjusting the stiffness of the various components which are inserted into the transverse hole containing the transducer. One method is to modify one of the internal platens so that it acts as a point-loaded beam or arch. Calibration test results using slotted top platens of high-tensile steel (EN57), in conjunction with a high tensile steel body, are plotted in Figure 66.

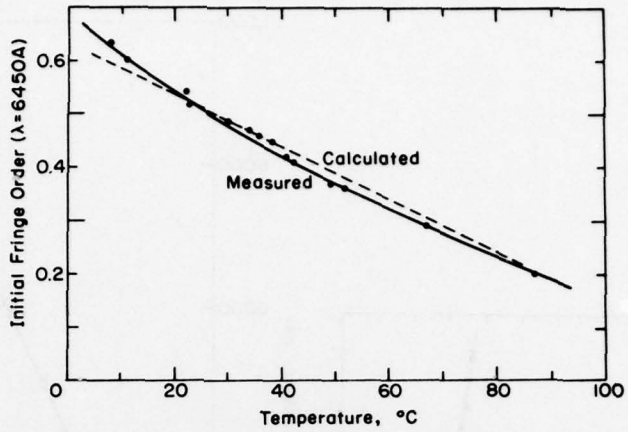

Figure 68. Variation of initial fringe order with temperature for 100-ton pile load gage (disk preload 0.52 fringe at 23°C). (From Hooper.[50])

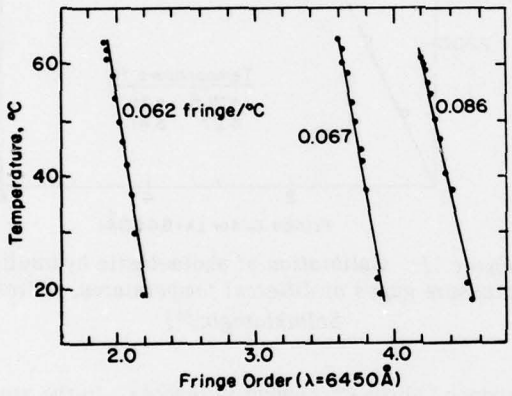

Figure 69. Effect of temperature variation on rock bolt dynamometer readings. (From Saltuklaroglu.[66])

Another method of regulating the sensitivity of a gage is to vary the thickness of the glass disk transducer. Although for a given load applied to a disk the observed fringe order is independent of the disk thickness, when the disk is located at the center of a traverse hole in a load gage and constrained by platens, the thickness of the gage affects the displayed fringe order. The disk is now subjected to a load per unit length, because the traverse hole deforms more or less uniformly over its length. An example of the effect of varying the thickness of a 1.25-in.-diameter disk in a load gage is shown in Figure 67.

Effects of temperature on load cell calibration

In common with many other forms of load-measuring instruments, photoelastic load gages have some sensitivity to temperature change. As the coefficient of linear expansion of glass is less than that of steel, change in temperature will result in slight differential movement of the internal gage components.

Hooper investigated the effects of temperature on a 100-ton load gage preloaded to 0.52 fringe order at 23°C. His observed results are shown in Figure 68, where it will be noted that a change in temperature from 10° to 90°C changes the fringe order from around 0.6 to 0.2. In practice it will be sufficiently accurate to read off the initial difference in fringe order due to difference in temperature from Hooper's observed relationship, and then assume that the modified calibration characteristic lies parallel with that observed at laboratory temperature.

Saltuklaroglu[66] has recorded the results of temperature variation on the readings of ring-type load gages, as shown in Figure 69 for a rock bolt dynamometer* and Figure 70 for a steel joist load gage.

* Described in section on applications.

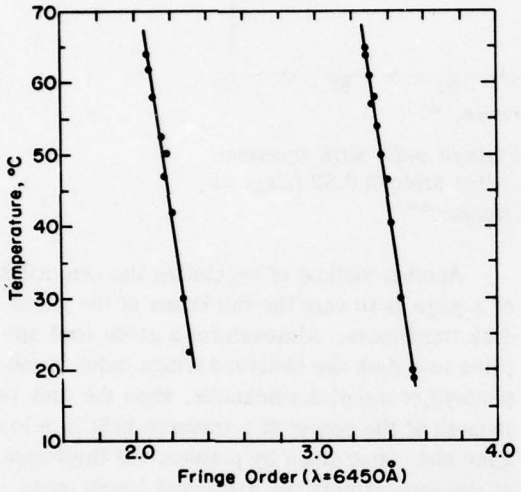

Figure 70. Effects of temperature on readings of steel joist load meter. (From Saltuklaroglu.[66])

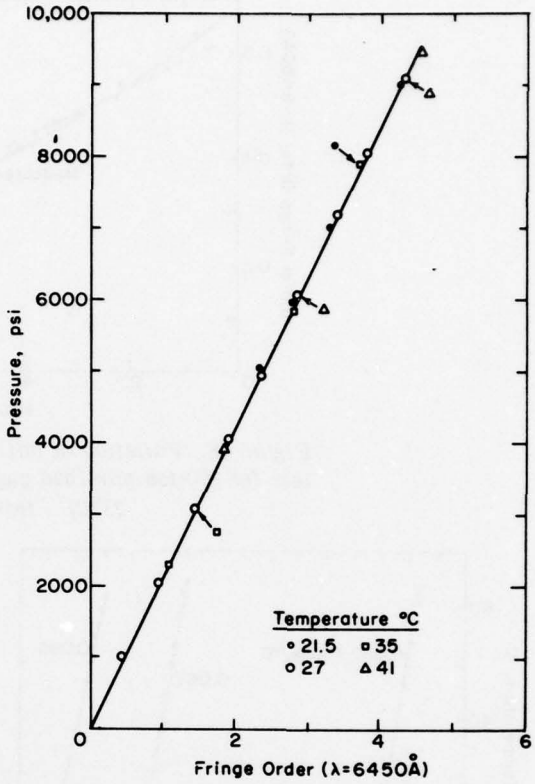

Figure 71. Calibration of photoelastic hydraulic pressure gages at different temperatures. (From Saltuklaroglu.[66])

In rock bolt dynamometers a change of 5°C produces about 6% change in reading. In the steel joist load cell the fringe order difference due to variation in temperature is 0.006 fringe/°C. In both cases, for all practical purposes under the conditions prevalent in mining and civil engineering operations, this temperature effect is relatively unimportant and may be neglected.

The effects of temperature on the photoelastic fluid pressure gage* are shown in Figure 71. Although in a closed hydraulic circuit the internal pressure must change as a result of thermal expansion of the fluid with change of temperature, these changes have no effect on the pressure/fringe sensitivity constant of the photoelastic pressure gage.

Effects of moisture on the stability of photoelastic load cells

The conditions under which instruments have to be applied in the field, in civil and mining engineering, necessitate that they be capable of functioning in adverse circumstances of atmospheric and groundwater corrosion. Wherever possible, methods of protecting the gages by enclosures and O-ring seals, etc., are adopted, with corrosion-resistant materials used in the methods of construction.

Corrosion will modify the stiffness of the disk and wedge assembly, and so can be expected to alter the calibration characteristic of load gages which embody these items in their construction. The degree to which corrosion protection is successful will be shown by the change in calibration characteristic with time.

*Described in the Appendix.

Table XIX. Periodic calibration values (λ = 6450 Å) for 100-ton pile load gage left submerged under 10 ft head of water. (From Hooper.[50])

Applied load (10^3 lb)	*Date*			
	9/10/67	*11/12/67*	*10/4/68*	*9/9/68*
0	0.51	0.53	0.53	0.53
30	1.16	1.18	1.14	1.17
60	1.86	1.89	1.86	1.88
90	2.65	2.67	2.65	2.65
120	3.43	3.44	3.45	3.44
150	4.31	4.30	4.29	4.28
180	5.16	5.15	5.17	5.15
210	6.08	6.07	6.09	6.05
240	7.01	6.99	7.03	6.99

Hooper submerged a 100-ton load gage under a 10-ft head of water over a period of 10 months, the gage being calibrated and recalibrated periodically during this period. His results are shown in Table XIX.

Saltuklaroglu[66] submerged rock bolt dynamometers and steel joist load gages in saline water for periods of 6 months and 2 weeks, respectively, but noted no change in the load/fringe order sensitivity over this time.

Long-term stability of photoelastic load cells

The following is reprinted from Hooper.[50]

> Perhaps the most important attribute of photoelastic load gages is their excellent long-term stability. In the majority of applications, these gages are used in field constructions where load changes occur over lengthy periods of time. This is particularly true in civil and structural engineering, for example, where significant variations in applied load commonly occur over a period of years rather than weeks or months. It would clearly be unwise in such cases as these to spend time and effort installing instrumentation of doubtful long-term stability. With photoelastic load gages, however, laboratory and field experience gained over a period of several years has shown them to be exceptionally stable.
>
> One of the principal reasons for this state of affairs is that the gages contain no "moving parts" in the conventional sense. All the gages consist essentially of components of glass and steel which, if properly annealed and not overstressed, are two very stable materials. The basic principle to be applied in aiming for long-term stability is to ensure that the stresses applied to these two materials are kept well within their respective elastic ranges. It also follows that the degree of success achieved in this respect depends to a great extent upon performing a detailed and reliable analysis on each gage component. But provided that these stresses are accurately known, there is every reason to expect good stability. The auxiliary equipment used to read the gages is, of course, inherently stable as it simply consists of a light source and filters in the form of a standard circular polariscope. In addition, the overall reliability of this equipment is assured as the light source and polarizer are portable and in no way fixed to the gage, and can therefore be easily replaced if necessary.
>
> The selection of soda-lime glass as the most suitable transducer material has already been mentioned, but the choice of gage body material also has an important bearing upon overall gage stability. For both column-type and ring-type bodies,

the material commonly used is En 24 (1.5 per cent nickel-chromium-molybdenum) steel, hardened and tempered to condition T. The minimum specified yield of stress of this steel is 100,000 lb/in.² [Note: this is much higher than the maximum stresses ever operated in load cell bodies]... The material generally used for the internal wedges and platens is En 57 (martensitic chromium-nickel rust-resisting) steel, which has a very similar yield stress and machinability to the En 24 steel used for the gage bodies,... Bimetallic corrosion at the interfaces between the two types of steel is virtually eliminated by plating the surface of the transverse slotted hole with a comparatively thick layer of chromium, which substantially reduces the electrochemical potential between adjacent surfaces as well as providing smooth hard surfaces to receive the internal platens. In addition, the ends of the transverse hole itself are always (usually) sealed off, usually with a removable cover plate, in order to prevent the deposition of dirt and moisture onto the internal gage components.

In a laboratory test carried out to assess long-term stability, a 10-ton ring-type photoelastic gage was kept under sustained loading for 1 year, with the applied load slightly greater than the maximum working load for the gage.

Over the 1-year test period, the fringe order at maximum working load changed from 5.29 to 5.19 at a fairly even rate, which represents a drop of less than 2 per cent. These test results were considered most encouraging, and subsequent experience in field applications where predominantly constant loads have been applied indicates quite definitely that photoelastic load gages do display excellent long-term stability.

DETERMINATION OF STRESSES AND STRAINS USING PHOTOELASTIC GAGES

Photoelastic Stressmeters

A wide variety of photoelastic gages have been developed for the evaluation of stresses in structures and rock masses and for measuring surface strains. Of these only two, the photoelastic stressmeter and the photoelastic biaxial gage, have found widespread use.

The photoelastic stressmeter consists basically of a glass cylinder with an axial hole. To make it into a practical tool additional components are required and the nature of these is determined by the particular application. Four different designs have been evolved:

Type B – when the polarizing filters are built permanently into the meter.

Type P – when the polarizing filters can be introduced for reading the meter.

Type R – for meters having a reflective backing.

Type T – for the simple glass cylinder intended for use with transmitted polarized light.

Figure 72 shows the basic B/P type meter with permanent and removable probes. The type R meter is similar except that the back of the glass cylinder is given a reflective coating of aluminum-filled epoxy paint.

An aluminum ferrule is mounted at one end of the stressmeter to protect the front of the glass from cement which might otherwise run down over the glass face during the setting operation. At the other end is an aluminum parabolic reflector. In type B meters the light polarizing probe is mounted permanently in the axial hole through the glass. Thus polarized light is reflected from

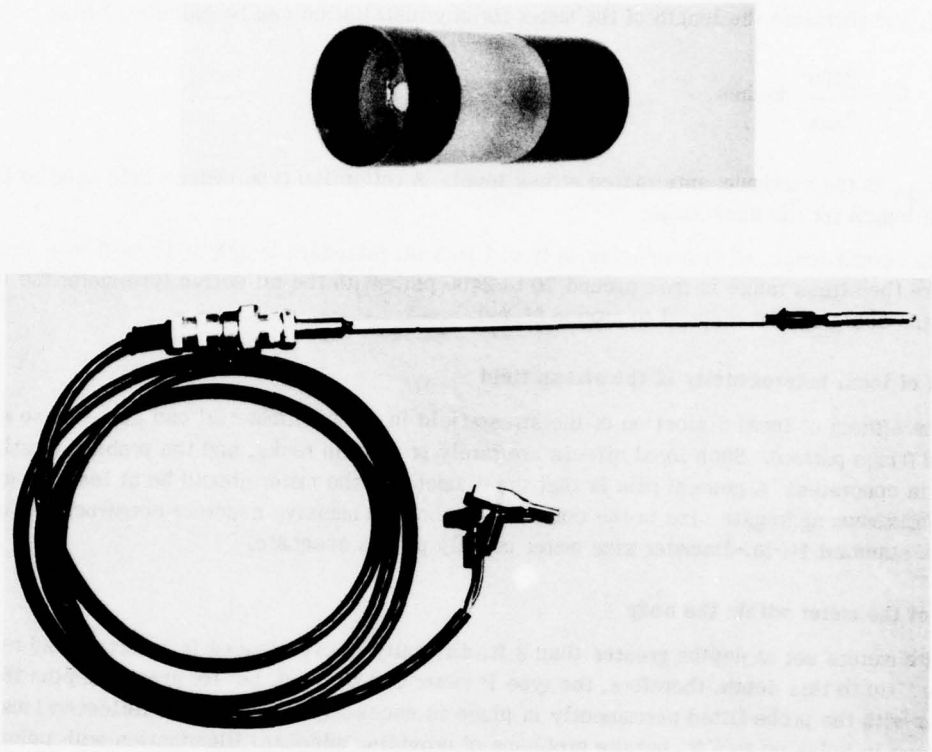

Figure 72. Photoelastic stressmeter.

the reflector and passes back down the bore hole through a hand-held analyzer (Precision Hand Viewer) to the observer. For type P meters intended to be set near the surface, the probe is designed to be inserted for reading and then removed. The end face of the type R meter, which has a reflective coating, is intended for use where high sensitivity is required and a reflection polariscope is available. Using this system light travels twice through the meter and the sensitivity for a particular meter length is doubled. Type T meters are primarily intended for laboratory calibrations, and for use where access is readily available to both sides of the meter. In addition to these basic forms of stressmeter, other specialized configurations have been developed for specific applications, e.g. for mounting behind concrete shuttering, as will be described later.

Stressmeters have been built in a range of diameters from ¼ to 3 in. and in lengths up to 6 in., again depending upon the application.

Anticipated stress levels

As discussed in Part 1, the average sensitivity of the stressmeter S in typical rocks and concrete is

$$S = \frac{480}{L} \text{ psi/fringe}$$

where L is the length of the meter in inches. The maximum fringe order which can be reasonably read in a stressmeter is five fringes (a monochromatic filter is required for readings above four fringes), and therefore the length of the meter for any installation can be calculated from

$$L = \frac{2400}{\sigma_{max}} \text{ inches}$$

where σ_{max} is the maximum anticipated stress level. A reflective type meter would need to have half the length for the same range.

The normal length of stressmeters is from 1 to 3 in. (standard length of 1½ or 3 in.), and therefore the stress range is from around 70 to 2400 psi. With the reflective type meter the lower end of the scale can be reduced to around 35 psi.

Degree of local heterogeneity of the stress field

The effects of local distortion of the stress field in the host material can give rise to a non-uniform fringe pattern. Such local effects are rarely present in rocks, and the problem mostly arises in concretes. A general rule is that the diameter of the meter should be at least as great as the maximum aggregate size in the concrete. Except in massive concrete construction such as dams, a standard 1¼-in.-diameter size meter usually proves adequate.

Depth of the meter within the body

With meters set at depths greater than 3 ft, difficulty is experienced in inserting and removing a probe. Up to this depth, therefore, the type P meter can be used, but for greater depths the type B meter with the probe fitted permanently in place is necessary. The type R (reflective) meter has been used in holes up to 6 ft, but the problems of providing adequate illumination with polarized light are very great at this depth, and the usual recommended limit for reflected light is around 2 ft.

The only limitation on depth for the type B meter is the need to keep a line of sight for observation.

Stressmeter Setting Techniques

Stressmeters can be set into bodies using one of three techniques: casting them directly in place, setting them into holes drilled or cast into the structure, or setting them into blocks to be cast or built into the structure.

Casting stressmeters in place

The simplest technique for setting stressmeters is to cast them directly in place. Unfortunately this method is limited to use in concrete structures. Figure 73 illustrates a type P stressmeter with attachments to enable it to be cast into concrete behind shuttering. For this type of use the parabolic reflector on the stressmeter is modified to accept a threaded bolt and the front ferrule is replaced by a rubber stopper. The action of clamping the meter to the shuttering squashes the rubber stopper so that later when the shuttering is stripped the stopper unstrains and can be removed.

Setting stressmeters into holes

The great majority of stressmeters are set into holes drilled or cast into the structure. The object when setting stressmeters in boreholes is to provide a uniform annulus of cement around

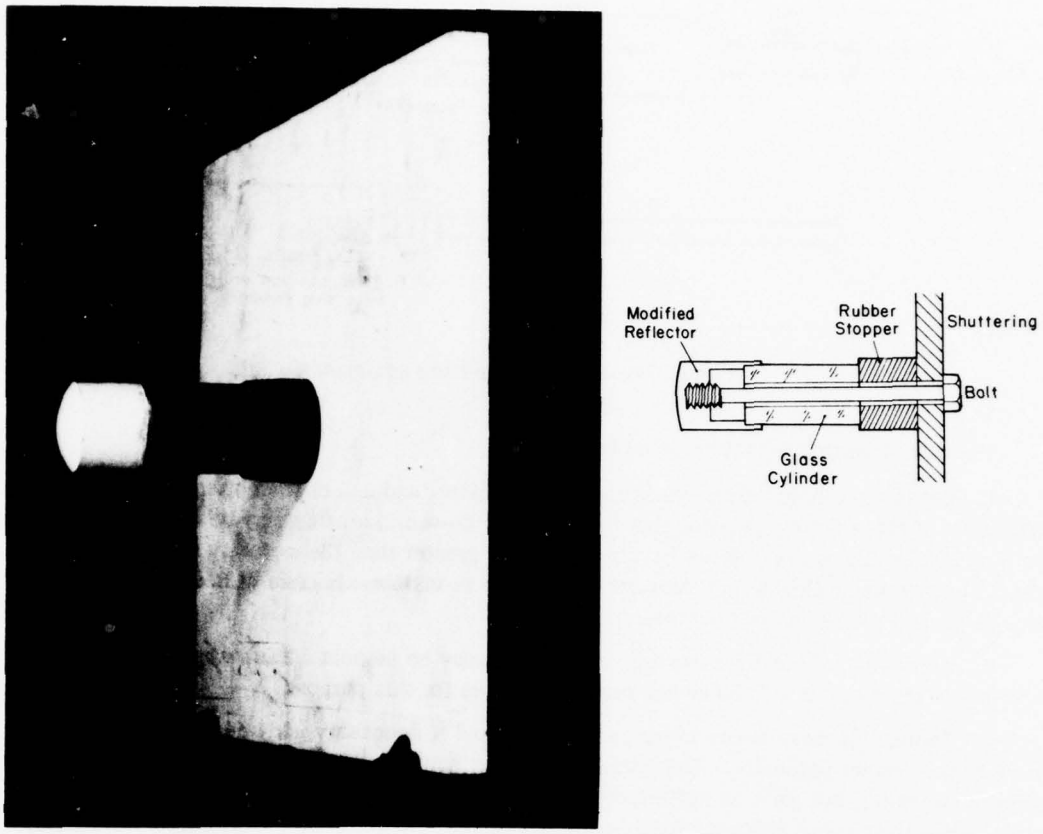

Figure 73. Type P stressplug with shuttering attachments.

the meter to bond it to the sides of the hole. Two techniques have been developed to achieve this in short (less than 3 ft) and long (greater than 3 ft) holes.

Ideally, the diameter of the hole into which a meter is to be set, for the standard meter range, should be the meter diameter plus $\frac{1}{8}$ in. As it is not possible to drill exact hole diameters, the acceptable range is meter diameter plus $\frac{1}{8}$ to $\frac{1}{4}$ in.

Various techniques have been used to form holes for stressmeters. In concrete it is sometimes convenient to cast the holes into the wet mix using polished steel bars which are removed after the concrete has partially set. However, the most universal and most satisfactory technique is to use diamond core drills, which give a smooth, straight hole of very closely controlled diameter. Many meters have been set in holes drilled by conventional Y type rotating bits and percussive drilling techniques, but care must be taken to ensure that the diameter of the hole is constant and within the correct tolerances.

Short hole setting technique. The standard short hole setting tool is illustrated in Figure 74. It is matched to the diameter of the individual meter and consists of a stressmeter carrier mounted on a push rod, and a sleeve to centralize the meter in the hole and act as a cement container. A lock nut clamped to the push rod fixes the location of the meter in the sleeve. Two sleeves are provided for each specific meter size to allow for variations in hole size, and the largest diameter sleeve which will slide in the hole is used.

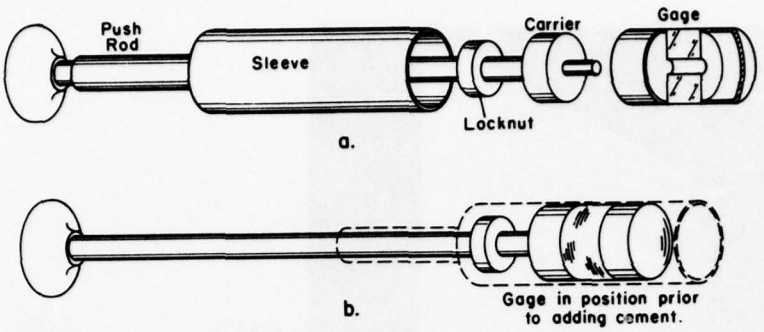

Figure 74. Short hole setting equipment.

The actual setting technique is as follows:

1. Measure the hole depth, check the hole diameter, and select the correct sleeve for the setting tool. If there is any question that the hole may be oversize, this may be checked by inserting bars of various diameters. Holes having a diameter greater than the meter diameter plus ¼ in. should be rejected. Check that the back of the hole is visible. In case of doubt a small light bulb can be passed to the end of the hole.

2. Clean the hole and remove any water which may be present. Washing the hole out with acetone or other suitable solvent has proved effective for this purpose.

3. Thoroughly mix the two-component cement and if necessary add additional filler to bring it up to the correct viscosity. The cement should be sufficiently fluid to be extruded around the side of the meter, but must be sufficiently viscous to hold the meter in place during polymerization. When the cement holds its form during mixing but slumps or settles down under vibration, it is usually at the correct viscosity.

4. The position of the lock nut must now be set such that the volume of cement to be placed in the cup (formed by the back of the stress plug and the sleeve when the plug is pulled fully into the sleeve) will be sufficient to fill the annular gap between the plug and the hole walls. The amount of cement is not critical, and large amounts of excess cement can be tolerated. In practice, the aim should be to work with a large excess of cement initially and then, with experience, alter the position of the lock nuts to give the optimum amount for the specific conditions.

5. Fit the stressmeter onto the carrier and draw it down into the sleeve to a position determined by the lock nut (the stressmeter should be an easy slide fit onto the carrier.

6. Fill the cup, formed by the back of the stressmeter and sleeve, with cement, taking care not to include any air bubbles. The cement can be induced to settle uniformly by tapping the side of the sleeve or by holding it against a source of vibration.

7. Insert the setting tool into the hole and push it in until the sleeve contacts the back of the hole. Exert a steady pressure of the order of 40-80 lb on the push rod and slowly rotate the sleeve clockwise, while keeping the push rod stationary, to ensure an even distribution of cement around the meter. During this operation the push rod should be moving into, and the sleeve out of, the hole. The operation is continued until the sleeve clears the carrier head, as judged from the relative movement of the push rod and sleeve extension tube. During the operation, the end of the sleeve must always be kept in contact with the moving annulus of cement, and in many cases it will be found that the movement of the cement will actually eject the sleeve.

8. When the carrier head has cleared the end of the sleeve, the setting tool should be carefully withdrawn, leaving the meter held in place by the cement annulus. The amount of excess should be noted and, if necessary, the lock nut position can be altered to increase or decrease the cement volume used.

9. The bond between the plug and hole wall may now be checked by inserting the light probe and observing the cement/glass interface. Any air bubbles will be shown up as areas of lighter color against a general dark background. Small air bubbles can be tolerated, but where any doubt exists it is best to withdraw the meter using a hooked rod passing through the central hole and start the operation again. The zero pattern in the meter can also be checked at this stage, as previously described.

10. It is essential to clean the setting tool with acetone or other suitable solvent after every setting.

Long hole setting technique. The standard long hole setting equipment (Fig. 75) is made up of three separate components: a cement chamber, setting head, and forcing tool.

The function of the cement chamber is to act as a receptacle to carry the cement to the end of the borehole and to provide means for extruding the cement around the meter. It is made up of a tube, open at both ends and containing a solid wooden ejector sealed to the inner surface of the tube by an O-ring seal. The end of the tube facing the seal and through which the cement is to be ejected has a strut mounted diametrically across it. To fill the cement chamber, the ejector is pushed into the tube to contact the strut and then slowly withdrawn as cement is fed into the open end. The cement is applied with a spatula and must be sufficiently viscous to enable it to stay in place over the end until it is drawn into the tube by the movement of the ejector. With care the tube can be completely filled with cement free from air bubbles. The cement chamber is full when the O-ring seal is just inside the tube end.

The function of the setting head (Fig. 75b) is to hold the stressmeter centrally in the hole as it is being forced against the cement chamber and to eject back away from the meter after setting. The unit consists of three main parts: a plunger, a main body, and a spacing sleeve. To set the head, the plunger is pushed into the body against an ejector spring until a peg can be pushed into a groove in the plunger. If the pressure on the plunger is then released it will be held in its set position by the peg. Additional pressure on the plunger forces it further into the body, and the peg springs out of its groove by the action of a leaf spring, allowing the plunger to eject when the pressure is released after the meter has been set. A spacing sleeve screwed into position over the leaf spring keeps out dirt. Sleeves of various sizes should be provided to ensure that the setting head is a slide fit into the borehole.

The function of the forcing tool is to grip the inside of the borehole to enable the setting head, through its extension rods, to be forced into the hole against the cement chamber. It consists of three main units: an expanding anchor, screw head, and rod clamp and cup. In operation the anchor is passed over the setting rods and partially inserted into the borehole. The clamping nut is then rotated to expand the anchor and grip the inside of the borehole. The rod clamp is then clamped to the rods at a preset distance from the anchor extension and the cup screwed over the clamp and onto the screw head. Rotation of the screw head will then force the setting rods into the hole. The rod clamp contains a thrust bearing so that the rods are not constrained and can be rotated independently of the screw head.

The setting operation using the long hole equipment is as follows:

1. Check and clean the hole as with the short hole equipment.

2. Fit various sleeves to the setting head until one is found which will just slide to the back of the hole. Oversize holes must be rejected.

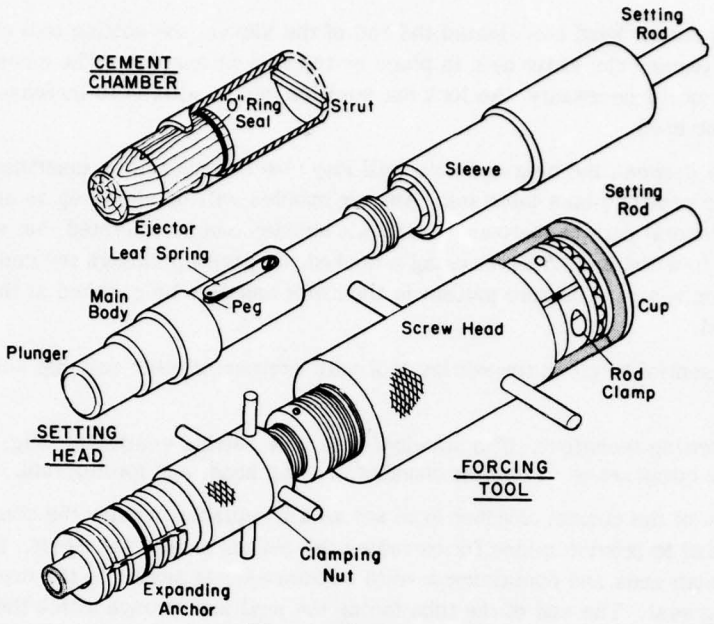

a. Three main components.

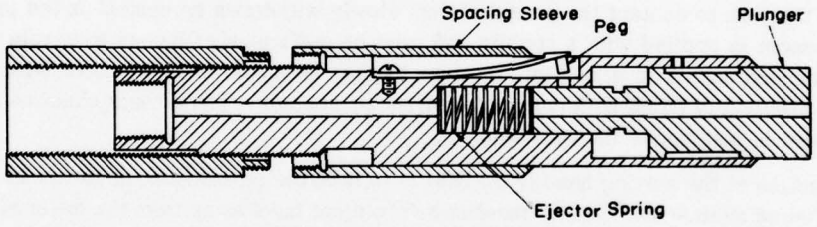

b. Details of setting head.

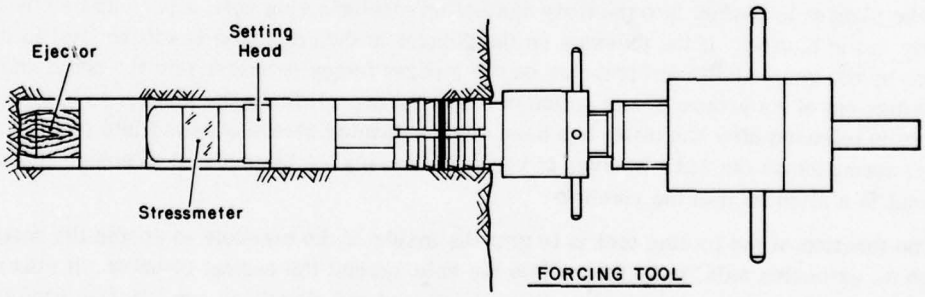

c. Equipment in use.

Figure 75. Long hole setting equipment.

3. Set the setting head ejecting mechanism as previously described, thread the probe leads through the setting head, and mount the stressmeter over the end of the plunger which just protrudes from the main body in its set position. Check the release mechanism and then reset and remount the meter. Depending upon the working space available at the mouth of the hole, thread together the setting rods, couple them to the setting head, and thread the probe lead wires through the rods.

Figure 76. Equipment for setting large diameter photoelastic stressmeters.

4. Thoroughly mix the two-component cement, check the viscosity (see short hole setting technique), and fill the cement chamber as described. The mixing cup should be left on site to check polymerization.

5. Measure the ejector travel into the cement chamber, as this is required to be marked out later on the forcing tool.

6. Place the cement tube and ejector into the hole with the ejector leading and push the assembly to the end of the borehole with the stressmeter mounted on the setting head. The cement chamber should be a loose slide fit in the hole, and as it is usually undersize to ensure this the

Figure 77. Building brick containing type T stressmeter.

outside diameter may be built up using adhesive tape. If the hole tapers to the back, care must be taken not to jam the chamber in the hole, and its diameter should be checked against the spacing sleeve on the setting tool. Check that the cement chamber is at the end of the hole by reference to the original hole depth measurement.

7. Place the expanding anchor of the forcing tool over the setting rods and expand the anchor to grip the inside surface of the borehole.

8. Measure off a distance equal to the ejector travel plus ½ in. from the end of the anchor extension and clamp the rod clamp firmly in this position. To make this measurement the screw head must be screwed back for attachment to the cup.

9. Slowly and carefully rotate the screw cap to force the setting rods into the hole. During this operation the thrust should be less than the pressure required to operate the ejection mechanism. As the rods move into the hole the ejector will move into the cement chamber, extruding the cement past the strut and around the meter. If the meter is allowed to rotate two or three times during its forward travel, this is sufficient to ensure a uniform cement annulus.

10. When the full travel of the cement chamber ejector has been taken up (checked by noting the travel of the screw head), resistance to rotation will increase rapidly and the plunger will be forced back into the setting head and into the released position. At this point the screw head rotation should be reversed to allow the rods to move back from the meter. The rod clamps can now be removed and the rods pulled back to enable the setting head to completely clear the meter.

11. The forcing tool and setting head can now be completely removed from the hole, taking care to feed the probe lead wires through the setting rods as they are withdrawn. When the setting head is withdrawn, it should be carefully examined to ensure that the excess cement is uniformly distributed around its periphery. This should always be the case and indicates a uniform cement annulus between the meter and the hole.

12. The stressmeter can now be illuminated to check visibility and the zero fringe pattern.

13. The excess cement should always be cleaned off the setting head immediately after use, using acetone or another suitable solvent.

Large stressmeters such as those used in dam installations measure up to 3 in. in diameter and require considerable force for extrusion of the cement when being set, particularly at low temperatures. In these circumstances the screw feed mechanism on the setting tool can be replaced by a down-the-hole hydraulic ram which is clamped into the mouth of the hole using an expanding wedge system. Figure 76 illustrates such equipment.

Setting stressmeters into blocks

In some structures such as dams or brick walls it is very convenient to set stressmeters into concrete blocks or bricks to be subsequently cast or built into the structure to be studied. Figure 77 shows a building brick containing a type T stressmeter prior to being bricked into a wall. Figure 78 a-c shows concrete cubes prepared in the laboratory to receive type T and P stressmeters. Figure 78d shows instrumented concrete cubes being cast in place on site.

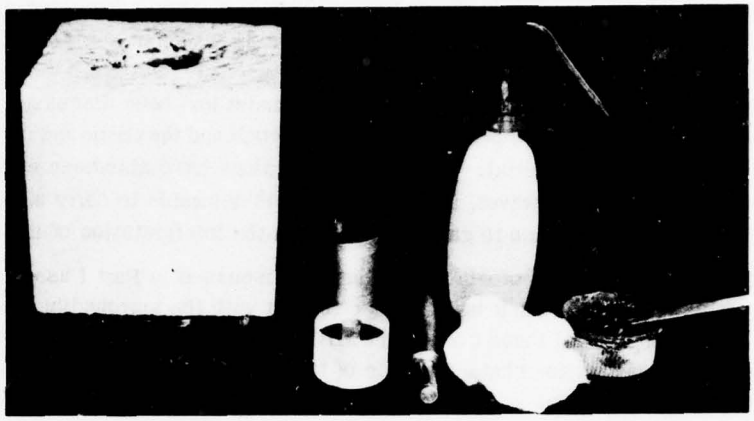

a. Concrete cube, type T stressmeter, and jig for assembly.

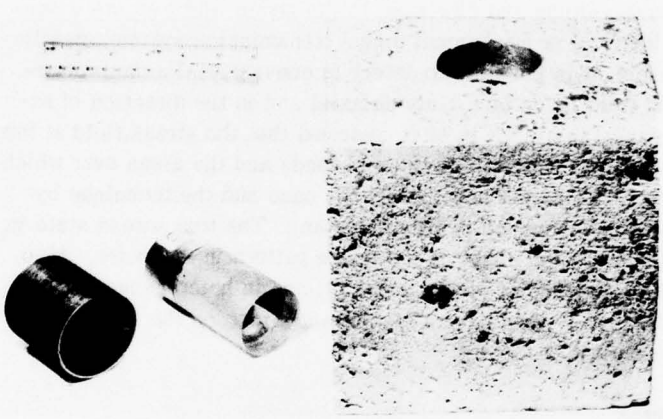

b. Concrete cube and type P stressmeter.

c. Assembled cube and stressmeter showing sleeve for attachment of viewing tube.

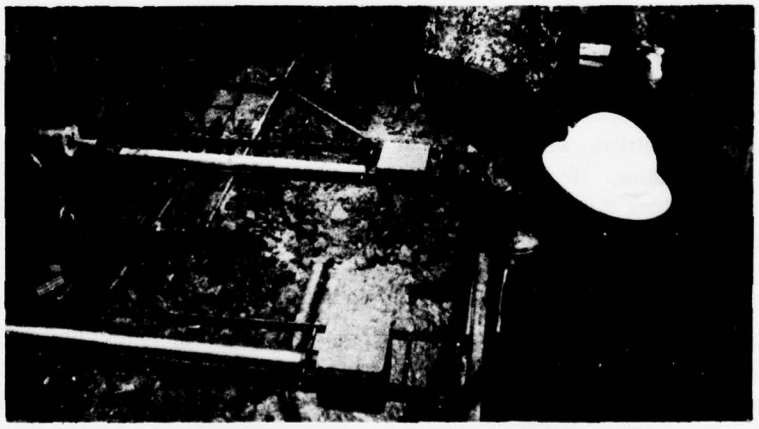

d. Cubes containing stressmeters being cast into place.

Figure 78. Instrumented concrete cubes.

Calibration of the Photoelastic Stressmeter

The theoretical sensitivity of the photoelastic stressmeter has been discussed in detail in Part I, in terms of the relevant elastic properties of the host materials and the elastic and photoelastic properties of the meter material. The theoretical values have also been experimentally verified by numerous researchers. However, in many cases it is desirable to carry out direct calibration in a particular material and also to gain experience in the interpretation of the fringe pattern.

The theoretical treatment of photoelastic inclusions discussed in Part I assumes that the inclusion is perfectly elastic and that it is in perfect contact with the surrounding medium, which is also perfectly elastic. Since all these conditions will rarely, if ever, occur in practice, an exhaustive examination of the calibration characteristics of the photoelastic stressmeter set in a wide range of materials has been made.

It became apparent at an early stage of the work that the stressmeter's unique property of providing a direct visual response, both in magnitude and direction, to the strain which exists within itself, unaffected by any intervening electrical or mechanical signal transmission system, greatly aids the calibration validity. For example, it is possible to detect in conventional uniaxial compression tests whether or not the stress field is, in fact, truly uniaxial and in the direction of external loadings on the test piece. In biaxial testing it is often assumed that the stress field at the center of the specimen is determined solely by the ratio of external loads and the areas over which these loads are applied to the specimen. This is not necessarily the case and the technique by which the individual loads are applied to the specimen is very important. The true stress state in the vicinity of the meter is always revealed by the shape of the fringe pattern in the meter. Also, when testing homogeneous materials the existence of platen restraint, and in heterogeneous materials the added existence of material anisotropy, can have a significant effect on the form and fringe order magnitudes of the fringe pattern in the meter.

Shape, size and loading of test specimens

The theory of photoelastic inclusions detailed in Part I is based on plane stress loading conditions, i.e. zero stress along the axis of the inclusion. A technique for applying different known stresses in three orthogonal directions to a test piece has not yet been developed to the best of the writer's knowledge. Thus, most of the calibrations on photoelastic inclusions have been made in idealized plane stress conditions using slabs roughly equal to the length of the inclusion. Dhir[27] has calibrated glass photoelastic inclusions in cubes where the conditions are somewhere between plane strain and plane stress, with results that do not significantly differ from those obtained under plane stress (slab) loading. He also made a series of tests in which test cubes were loaded so as to produce stresses along the axis of glass photoelastic inclusions, again with no significant effects on the gage readings. Similarly, tests made in cubes with blind holes drilled into them show that provided the inclusion is at least one diameter away from the back of the hole the stress concentrations associated with the back of the hole do not affect the gage readings.

The size of the test specimens in relation to the size of the inclusion is determined primarily by the area of influence of the inclusion. There is considerable literature on the theoretical distribution of stresses around holes and inclusions, and much of this has been confirmed by photoelastic model studies. From this work, which has been summarized by Savin[67] it can be concluded that the influence of the hole itself does not significantly affect the stress field in the surrounding material beyond a distance greater than $2d$ (where d is the diameter of the hole) from the edge of the hole.

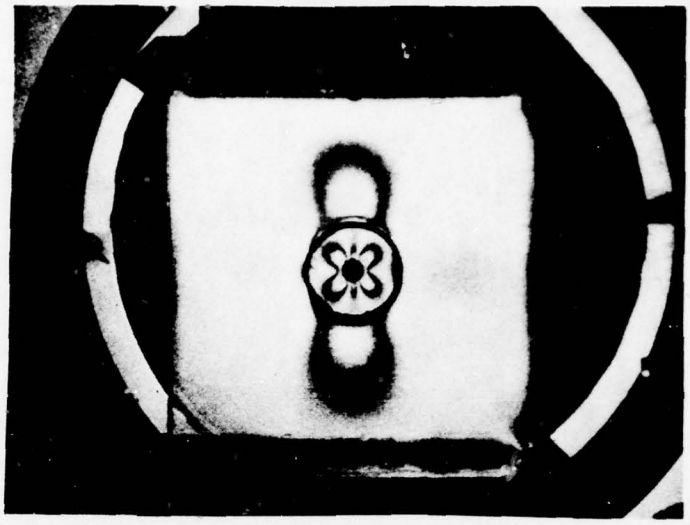

Figure 79. Fringe pattern observed in a photoelastic stressmeter set in an acrylic resin slab, under uniaxial compression.

When the hole is filled by an inclusion with the same modulus as the surrounding material, the inclusion obviously has no effect on a stress field applied subsequent to filling the hole. When the inclusion has a modulus greater than four times that of the surrounding material the area of influence of the inclusion is limited to roughly one diameter from the edge of the hole.[70]

Calibration tests of the photoelastic stressmeter have confirmed these general conclusions. Figure 79 shows a stressmeter set in a slab of acrylic resin under plane stress uniaxial compression. It can be seen that the stress concentration in the material surrounding the meter extends for approximately one diameter above and below the meter. Stress relief in the acrylic, to each side of the meter, was seen not to extend beyond a similar distance. Another factor influencing the size of the test specimen in relation to that of the inclusion is the degree of heterogeneity of the test material. Figure 80 shows a photoelastic stressmeter set in a concrete slab which has a photoelastic plastic coating to reveal its strain distribution under load. Despite the almost random strain distribution in the test specimen the meter shows a clean uniaxial pattern. This condition was found to generally apply in concretes, provided that the diameter of the meter was at least that of the largest aggregate and that the test slab face dimensions were at least ten times the largest aggregate diameter.

Dhir[27] studied the effects on the calibration characteristic of inclusion as a function of the size of the slab for slabs of fine grained material. Meters were calibrated repeatedly as slabs were reduced in side length from 10 to 4 in. in stages of 1 in., the diameter of the stressmeter being 1.25 in. No significant change in the stress/fringe-order sensitivity constant were observed until the slab side lengths were reduced below 5 in. Thus, to be sure that the edges of the test specimen do not influence the stress field around an inclusion set on the central axis, the width of the specimen must be at least five inclusion diameters.

When calibrating inclusions in blocks where the thickness is comparable to the width, the shear stresses associated with the loading platen can have a large effect on the stress distribution around the inclusions. As a general rule the nonuniform stresses associated with the boundary condition at the loaded interface penetrate the specimen to a depth roughly equal to one half the width of the loaded surface.[43] To be sure that a predictable stress state exists in the area

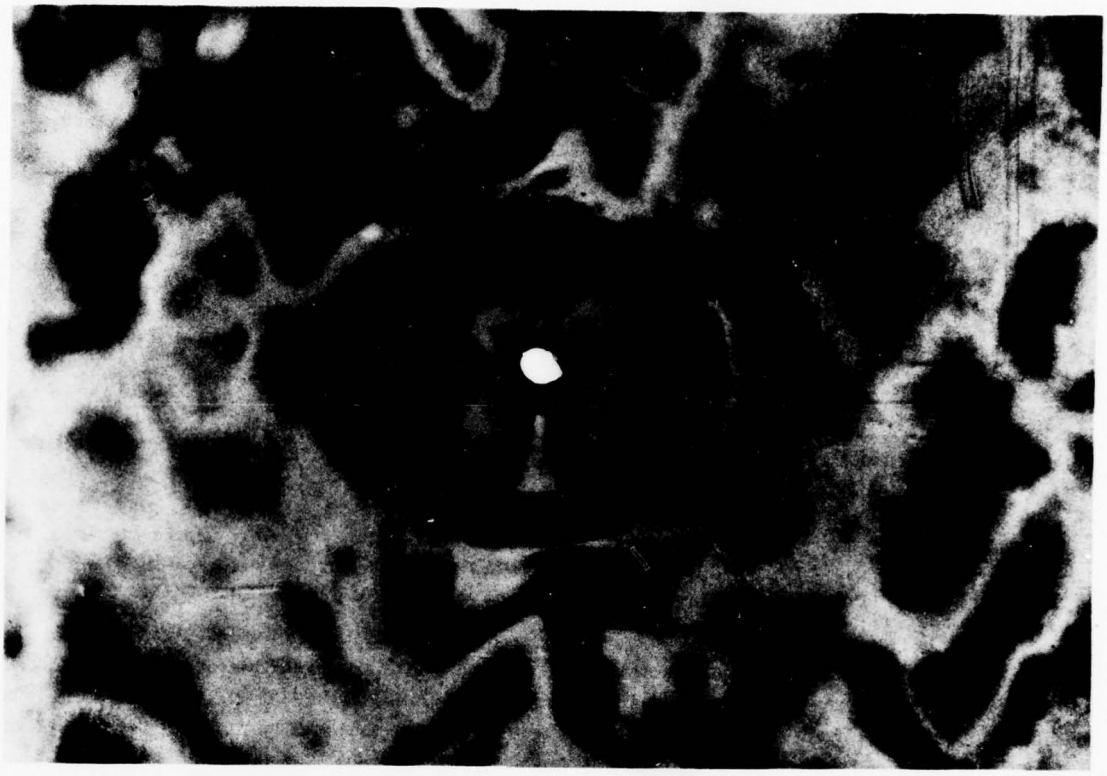

Figure 80. Fringe patterns observed in a photoelastic stressmeter set in a concrete slab under uniaxial compression. Concrete coated with photoelastic plastic.

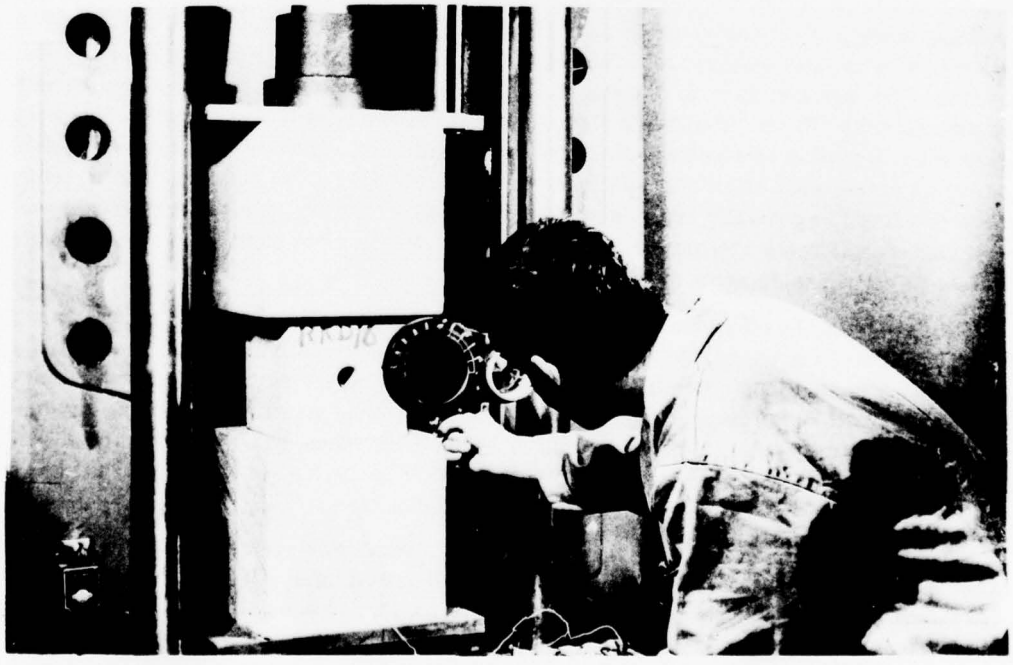

Figure 81. Meter being calibrated in a cube of rock, set between rock platens.

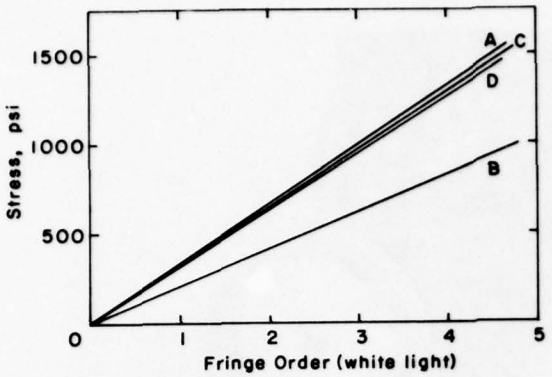

Figure 82. Calibration characteristics of a photoelastic stressmeter (length 1½ in.) under uniaxial loading conditions. (From Roberts et al.[27])
A: meter set in a cube, between rock platens.
B: meter set in a cube, between steel platens.
C: meter set in a slab, between rock platens.
D: meter set in a slab, between steel platens.

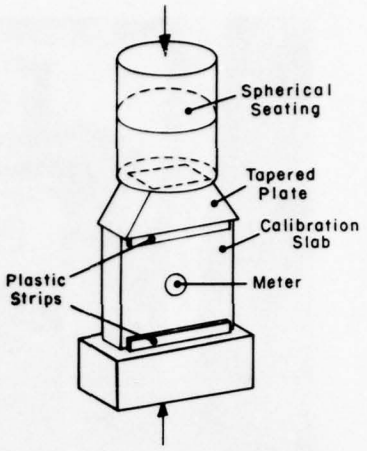

Figure 83. Recommended calibration set-up for photoelastic stressmeters set into slabs.

where the inclusion is to be set for calibration the height of the specimen should be at least three times the width. Figure 81 shows a system devised by Dhir[27] to insure uniform stress in a test cube by loading it between cubes of similar material. Figure 82 shows the calibration characteristics of a photoelastic stressmeter when calibrated in a rock cube in this manner as compared to loading the cube between steel platens. The calibration error introduced by using steel platens and assuming uniform stress can be of the order of 50%.

The errors when calibrating in cubes are largely due to the frictional effects between the steel and rock, and the different Poisson's ratios of these materials. In all calibration tests it is also essential that the loading surfaces of the test specimens are flat, smooth and parallel. In the tests reported by Dhir[27] the end loading faces were cut in one pass, using a 2-ft-diameter diamond saw, and the resulting faces were surface-ground and tested for flatness.

To further demonstrate the effects of specimen shape in relation to condition of the loaded boundary Dhir[27] cut down the cube shown in Figure 81 to a slab with a thickness equal to the length of the inclusion and recalibrated the meter. The results are included in Figure 82. It will be noted that when calibrating with slabs similar results are obtained with both rock and steel platens and that the inclusion stress/fringe order sensitivity in slabs (plane stress) is not significantly different from that in cubes (partly plane stress, partly plane strain) when they are correctly loaded.

Hawkes[39] has found that bonding a strip of photoelastic plastic onto each face of the test slabs adjacent to loading surfaces and observing the uniformity of the fringe orders in the plastic is an effective way of ensuring uniformity of loading during calibration. The recommended set-up for calibration inclusion in uniaxial compression is illustrated in Figure 83. Figure 84 shows a similar set-up for biaxial calibrations. When making biaxial stress calibrations it is essential to increase the loads along the two axes simultaneously, keeping the required ratio between the loads constant.

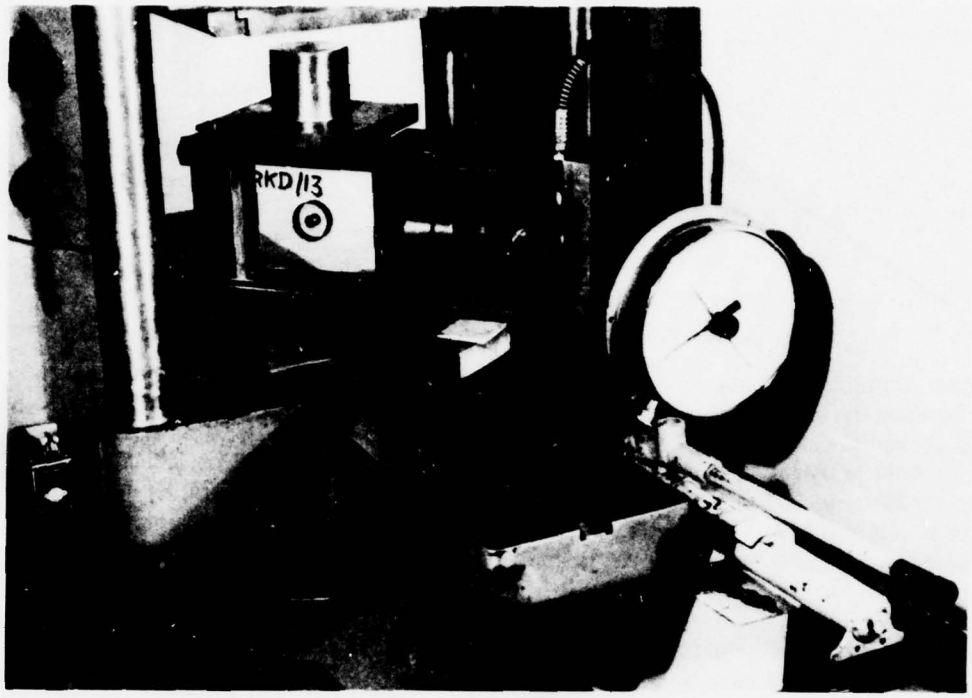

Figure 84. Biaxial calibration of photoelastic stressmeter.

Observed calibration characteristics

The theoretical stresses generated in a photoelastic inclusion, discussed in great detail in Part I, are based on the assumption that the inclusion is "welded" into the body. If a thin layer of adhesive is to produce a welded boundary condition then it must withstand and transmit shear, tensile and radial stresses from the host body to the inclusion.

The effects of the cement layer on the stressmeter sensitivity for short time loading have been investigated by Dhir.[27] A welded boundary condition was simulated by drilling a 1/4-in.-diameter hole in a rectangular glass slab and observing the fringe orders around the hole as the slab was loaded. The hole was subsequently overcored using a 1.25-in. internal diameter diamond drill having a wall thickness of 1/32 in. and the annulus so formed (a stressmeter) was then cemented back in place in the slab using Moore's standard epoxy resin mix (page 88). The slab was again loaded and the fringe orders around the central hole noted as a function of the load. The results of the tests (Fig. 85) indicate that this particular cement has no influence on the stressmeter readings. The tests were repeated with different cement thicknesses but with a stressmeter cemented into an acrylic resin slab. These results are also given in Figure 85; again it will be noted that the cement layer thickness has no noticeable effect on sensitivity.

The sensitivity of the photoelastic stressmeter when set into different materials and subjected to uniaxial and biaxial stress fields has been discussed in considerable detail in Part I. Reference should be made to this section for the appropriate sensitivity factors to use under specific loading conditions. As discussed earlier the sensitivity of a photoelastic stressmeter of given material is determined by its geometry, the length of the light path, the nature of the stress field and the type of host material. The calibrations carried out have been aimed principally at evaluating the influence of the last two factors.

In relation to meter geometry the stress field around a hole in a body only influences the general stress field for a distance of roughly one hole diameter. Thus it may be expected that meters having an outer diameter to inner ratio greater than 3 would exhibit similar stress/fringe order characteristics. Dhir[27] made

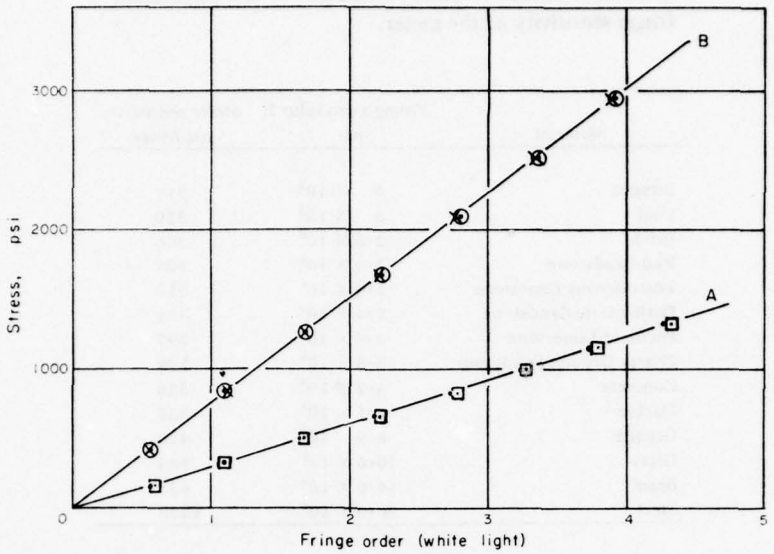

Figure 85. Calibration characteristics of stressmeters in different materials and with different thicknesses of cement.

A Meter set in 'perspex' slabs 1½ in. thick.
⊡ with 1/32 in. cement layer.
• with 1/16 in. cement layer.

B Meter set in glas slab 1 in. thick.
⊙ with no cement.
X with 1/32 in. cement layer.

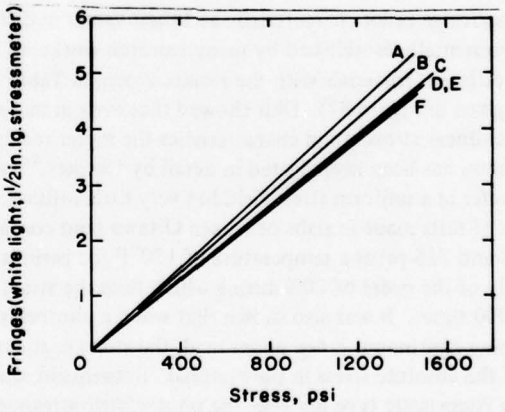

Figure 86. Calibration characteristics of 1½-in.-long stressmeters with various ratios of external to internal diameter in white light (uniaxial stress field). (From Roberts et al.[27])

A: ratio 3.2:1.
B: ratio 3.33:1.
C: ratio 5:1.
D: ratio 6:1 (1.5:0.25).
E: ratio 6:1 (3.0:0.5).
F: ratio 6.66:1.

Table XX. Effect of Young's modulus of test piece upon fringe sensitivity of the meter.

Material	*Young's modulus* E *psi*	*Meter sensitivity psi/fringe*
Perspex	4×10^5	317
Coal	5×10^5	320
Brick	$2{\cdot}0 \times 10^6$	306
Red Sandstone	$2{\cdot}0 \times 10^6$	304
Fossiliferous Limestone	$2{\cdot}4 \times 10^6$	318
Darley Dale Sandstone	$2{\cdot}4 \times 10^6$	316
Portland Limestone	$3{\cdot}6 \times 10^6$	297
Coarse Ground Sandstone	$3{\cdot}8 \times 10^6$	299
Concrete	$4{\cdot}2 \times 10^6$	320
Marble	$6{\cdot}1 \times 10^6$	430
Granite	$8{\cdot}5 \times 10^6$	470
Glass	$10{\cdot}0 \times 10^6$	504
Brass	$14{\cdot}0 \times 10^6$	635
Steel	$30{\cdot}0 \times 10^6$	1270

a series of tests to confirm this general conclusion, in which he calibrated a range of different meter geometries in acrylic resin slabs. The results are given in Figure 86. It will be noted that there is a slight change in the sensitivity as the hole to meter diameter ratio changes from 3 to 5 but the readings do not significantly change at higher ratios. From Figure 86 it will also be noted that there is no scale effect, and a meter 3 in. in diameter with a ½-in.-diameter central hole gives exactly the same reading as a 1¼-in.-diameter meter with a ¼-in. hole. Tests on meters ranging in length from 1 to 6 in. verified that the sensitivity of the meter is directly proportional to the length of the light path in the glass. The standard photoelastic stressmeter is 1.50 in. long with an OD of 1.25 in. and an ID of 0.25 in.

The linearity of the stress/fringe order characteristic and their values in different materials under uniaxial stress fields have been experimentally established by many research workers. In particular, Dhir[27] made detailed calibrations in 14 different materials with the results shown in Table XX. (Stressmeter sensitivity plotted against modulus is given in Figure 87). Dhir showed that even in materials exhibiting noticeable viscoelastic behavior and nonlinear stress/strain characteristics the meter readings still remained linear with stress. This latter phenomenon has been investigated in detail by Hawkes,[40] who showed that creep of the host material around the meter in a uniform stress field has very little influence on the meter readings. Figure 88 shows the results of tests made in slabs of frozen Ottawa sand containing photoelastic stressmeters and loaded to between 618 and 725 psi at a temperature of 150°F for periods up to 200 hours. The greatest fringe order change was only of the order of 20% during which time the strain change, assuming an initial modulus of 10^6 psi, was 1000 times. It was also shown that when a photoelastic stressmeter is bonded into a material which is undergoing continuous creep under load, the stress in the meter will eventually build up to a value representative of the absolute stress in the material. Subsequent studies by Skilton[74] have generally confirmed that in viscoelastic type material the photoelastic stressmeter is only responsive to stress changes. He determined that a photoelastic stressmeter bonded into siltstone maintained its calibration figure to within ± 5% even though the host material underwent appreciable viscous creep during the period of observation. This condition applied under a constantly applied load and under a gradually increasing load. Also, when installed in a specimen of rock salt that was already under load, the photoelastic stressmeter was observed to pick up the ambient stress in the host material over a period of time. Concurrently it responded immediately and automatically to an incremental increase of stress imposed upon the host material after the time of stressmeter insertion. Buswell et al.[75] have used the photoelastic stressmeter to evaluate stresses in highly viscoelastic solid rocket propellant fuels and generally reached the same conclusion that in such materials the stressmeter readings are governed only by the stresses.

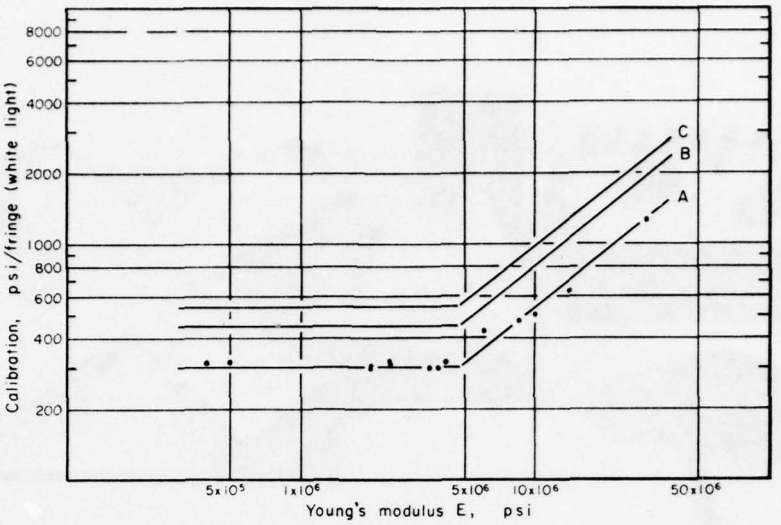

Figure 87. The effect of the Modulus of elasticity of the surrounding material upon the calibration characteristics of the stressmeter.

A 1½ in. long stressmeter in white light, read at the 45° compensation points. Uniaxial stress field.
B 1 in. long stressmeter in white light, read at the 45° compensation points. Uniaxial stress field.
C 1 in. long stressmeter in white light, biaxial stress field (ratio of principal stresses 1 : ½) compensated to collar edge on minor stress axis.

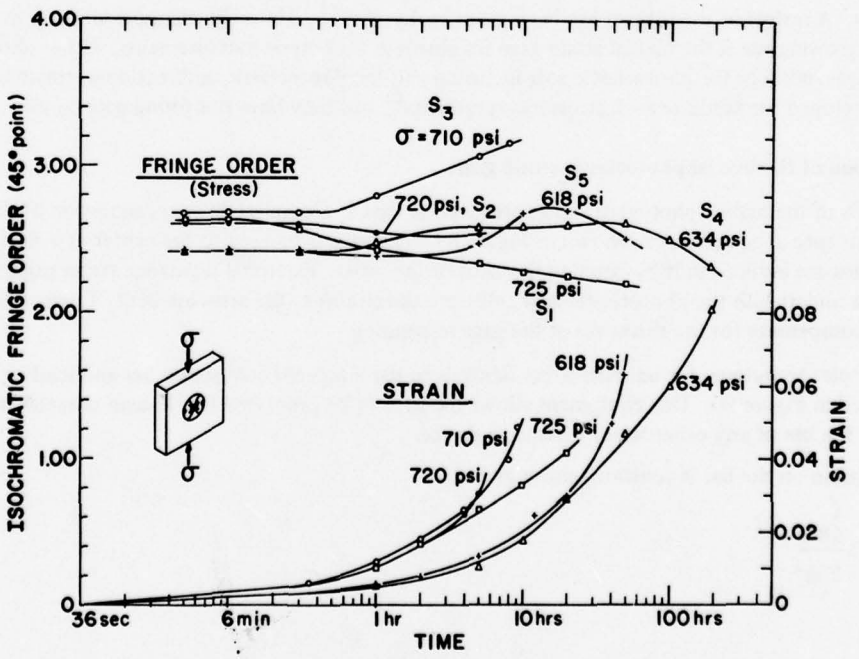

Figure 88. Strain and isochromatic fringe-order readings in instrumented frozen-sand slab creeping under stress.

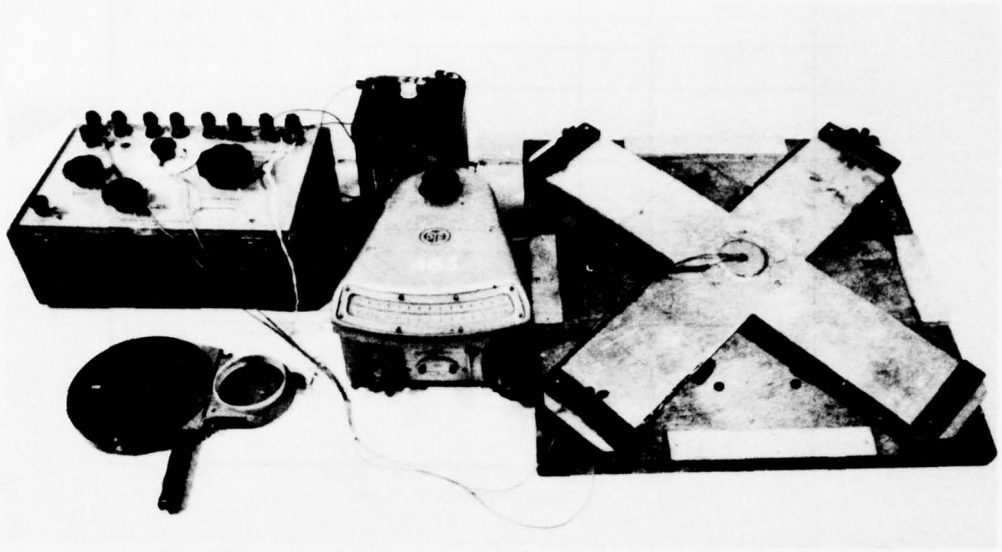

Figure 89. Biaxial gage calibration equipment.

Photoelastic Strain Gages

As described in Part I, a variety of photoelastic strain measuring gages have been developed for specific purposes. A review of the subject has been given by Leeman[55]. However, the only strain gage which appears to be in growing use is the biaxial strain gage for absolute rock stress measurements. Other photoelastic strain gages, notably the photoelastic soft inclusion and the photoelastic undirectional stressmeter, have also been developed for absolute rock stress measurements[41] but they have not found general use.

Calibration of the biaxial photoelastic strain gage.

Details of the biaxial photoelastic gage are given in Part I. Complete biaxial calibration of the gage requires the use of special equipment as shown in Figure 89. The gage is bonded to the center of a sheet-metal cross, and strains are induced in it by bending the arms of the cross. Electrical resistance strain gages, mounted on the cross underneath the photoelastic gage, measure the strains as the arms are bent. Corrections are necessary to compensate for the thickness of the gage in bending.

A simpler technique, for uniaxial stress fields, is to use a tapered calibration bar and loading weight, as illustrated in Figure 90. This equipment allows the gage to be calibrated in a known uniaxial stress field, without the use of any other strain measuring device.

The strain on the bar is constant, and is given by

$$\epsilon = \frac{6Wx}{Ebh^2} \tag{90}$$

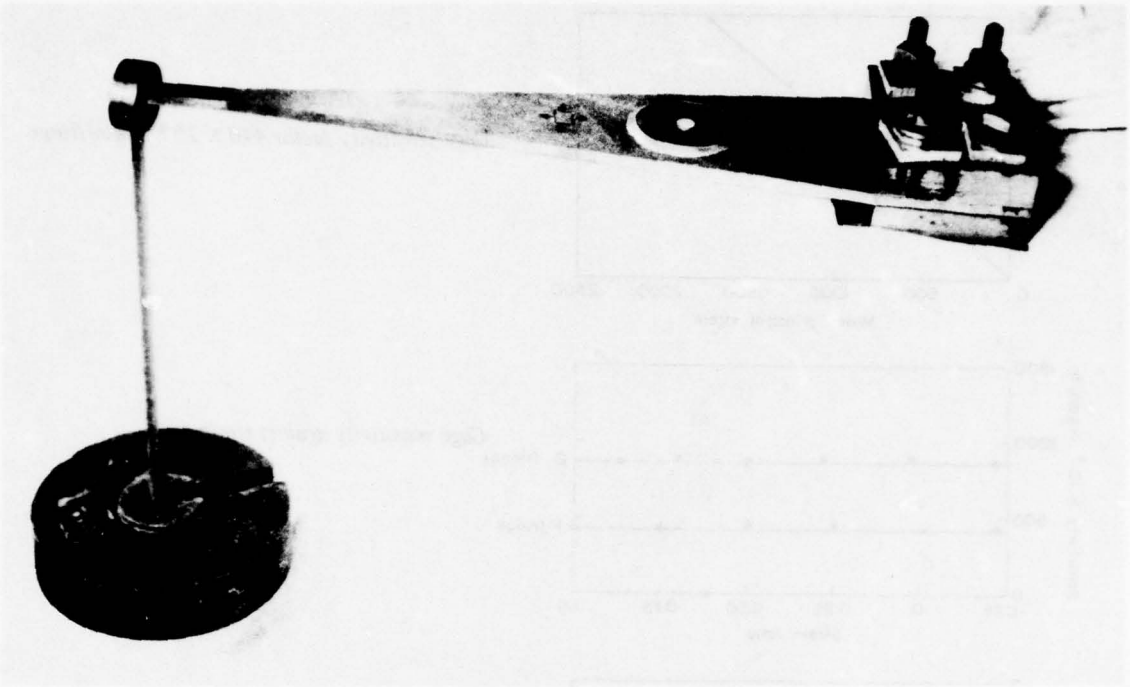

Figure 90. Calibration bar and loading weight.

where

W = loading weight
b = width of the bar at point x (in.)
h = thickness of the bar (in.)
x = distance measured between the point of observation and the point of application of the weight
E = Young's modulus of the bar material.

For a tapered bar x/b is constant.

Because the gage is being calibrated in bending a correction factor is necessary to compensate for the thickness of the gage:

$$\epsilon \text{ (true)} = \epsilon \text{ (calculated)} \times \frac{t/2 + h}{h} \tag{91}$$

where t = the thickness of the gage.

The calibration characteristics of a standard 2-in.-diameter plastic biaxial gage with a 0.2-in.-diameter central hole are shown in Figure 91.

The experimental sensitivity of 440×10^{-6} strain/fringe is very close to the theoretical value of 450×10^{-6} calculated earlier in Part I. Similarly the ratio of principal strain as a function of isotropic point spacing is close to that predicted theoretically.

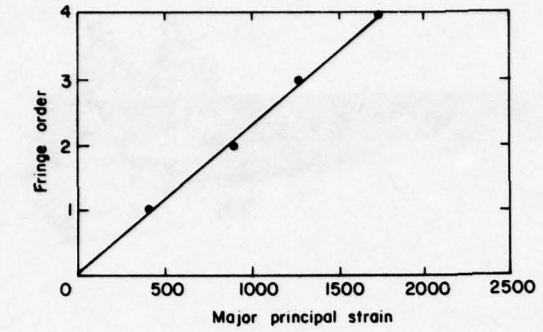

Gage sensitivity factor 440 X 10^{-6} strain/fringe.

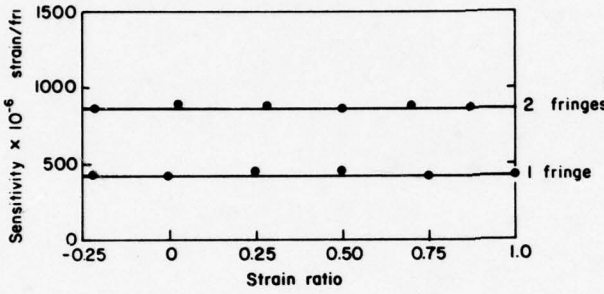

Gage sensitivity against strain ratio.

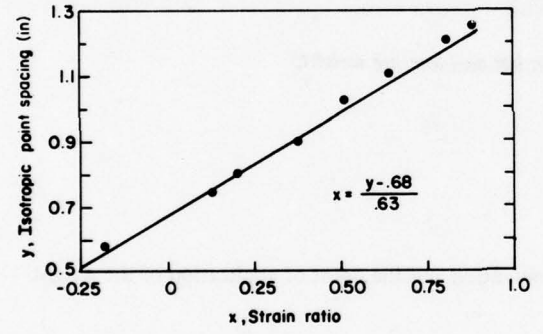

Determination of minor principal strain.

Figure 91. Calibration characteristics of a standard 2-in.-diameter plastic biaxial gage with a 0.2-in.-diameter central hole.

Photoelastic strainmeter

The photoelastic strainmeter described in Part I was developed principally for absolute rock stress measurements using the borehole overcoring technique. The gage was intended for measurements in relatively low stress fields (less than 2000 psi) and also to check the principal stress directions when other types of unidirectional instruments are being applied with the borehole overcoring technique.

The meter described by Hawkes[32] is identical to the photoelastic stressmeter except that it is constructed from birefringent plastic instead of glass and is usually much thinner. It is set using identical equipment to that described earlier to set the photoelastic stressmeter. Figure 92 shows a section through a photoelastic soft inclusion meter set into a rock slab using the long hole setting equipment illustrated in Figure 75.

In use the meter is set into a 1-1/2-in. borehole and then overcored by a larger (4-6 in. diameter) core drill. Expansion of the core upon relief of the in-situ stress causes the inclusion meter to be strained, and

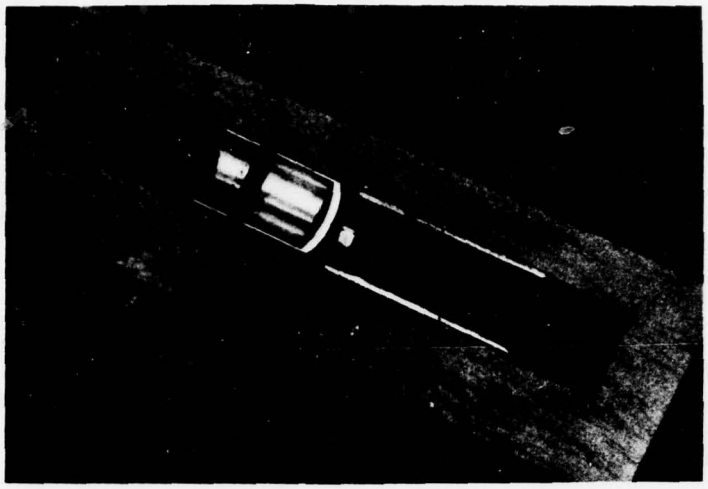

Figure 92. Section through soft inclusion gage (B) and cement chamber (A) after setting (F: cement bond).

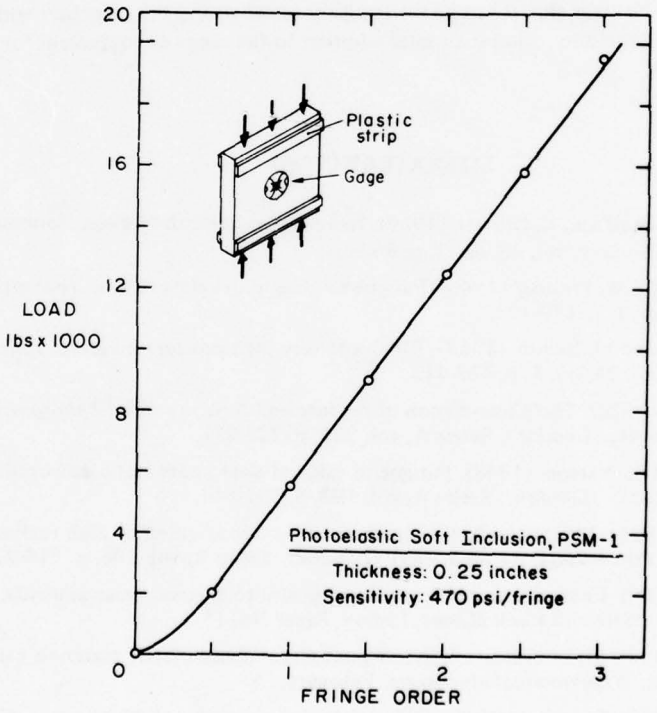

Figure 93. Calibration of photoelastic 'soft inclusion' gage in Barre granite.

the magnitude of the strains and their principal direction are obtained from the photoelastic patterns, as described in Part I.

The standard sensitivity factor is given by equation 69 as

$$S_0 = (0.215 + 0.167\upsilon_g) f \frac{E_h}{E_g} .$$

For a soft inclusion 0.25 in. thick constructed from Photolastic Inc. PSM-1 ($\upsilon_g = 0.32, E_g = 0.42 \times 10^6$ psi, $f = 44.1$ psi/fringe/in.) the sensitivity factor S_0 is given by

$$S_0 = 111.5 \times 10^{-6} \; E_h \text{ psi/fringe} \tag{92}$$

Figure 93 shows the results of a calibration test of the meter in Barre granite giving a sensitivity of 470 psi/fringe. For stress levels up to 1200 psi the average tangent modulus of Barre granite loaded in the same direction was measured at 3.9×10^6. From eq 92 the sensitivity is given by $S_0 = 435$ psi/fringe, which is close to the measured value.

For absolute rock stress measurements the main drawback to the use of the photoelastic soft inclusion is the length of time required after setting the gage before a reading can be taken. No fast-acting cements have yet been found that will satisfactorily bond the gage and at the same time remain fluid for the setting procedure.

The gage has the advantage that it can be made highly sensitive and this, together with the ease with which it indicates the stress direction, makes it a useful addition to the range of equipment for use with borehole overcoring techniques.

LITERATURE CITED

33. Argon, H.S., I. Hord and E. Orowan (1960) Indentation strength of glass. *Journal of the American Ceramics Society*, vol. 43, no. 2, p. 86-96.

34. Baker, T.C. and F.W. Preston (1946) Fatigue of glass under static loads. *Journal of Applied Physics*, vol. 17, no. 1, p. 170-178.

35. Bridgman, P.W. and I. Simon (1953) Effects of very high pressure on glass. *Journal of Applied Physics*, vol. 24, no. 4, p. 403-413.

36. Griffith, A.A. (1920) The phenomenon of rupture and flow in solids. *Philosophical Transactions, Royal Society (London)*, Series A, vol. 221, p. 225-251.

37. Gurney, K. and S. Pearson (1948) Fatigue of mineral glass under static and cyclic loading. *Proceedings, Royal Society (London)*, Series A, vol. 192, p. 537-544.

38. Harris, F.C. (1924) The photoelastic constants of glass as affected by high temperature and by lapse of time. *Proceedings, Royal Society (London)*, Series A, vol. 106, p. 718-723.

39. Hawkes, I. (1969) Photoelastic strain gages and in situ rock stress measurements. International Symposium on Stress in Rock Masses, Lisbon, Paper No. 15.

40. Hawkes, I. (1969) Stress evaluation in low-modulus and viscoelastic materials using photoelastic glass inclusions. *Experimental Mechanics*, February.

41. Hawkes, I. (1969) The photoelastic unidirectional stressmeter: A borehole rock stress gauge. CRREL Special Report 134.

42. Hawkes, I. and J.A. Hooper (1969) Photoelastic load cells for civil engineering structures. *Civil Engineering* (London), vol. 64, p. 660-664.

43. Hawkes, I. and M. Mellor (1970) Uniaxial testing in rock mechanics laboratories. *Engineering Geology*, vol. 4, no. 3, p. 177-285.

LITERATURE CITED (Cont'd)

44. Hoek, E. (1963) Experimental study of rock stress problems in deep level mining. *Proceedings, 1st International Conference on Experimental Mechanics,* 1961, p. 177-194.

45. Hogg, J.R. (1969) The measurement of stress, strain, and load, using photoelastic transducers. Ph.D. thesis, University of Sheffield.

46. Holland, J.A. and W.E.S. Turner (1932) A study of the breaking strength of glass. *Journal of the Society of Glass Technology,* vol. 22, p. 225-251.

47. Holland, J.A. and W.E.S. Turner (1940) The effect of sustained loading on the breaking strength of sheet glass. *Journal of the Society of Glass Technology,* vol. 24, p. 46-57.

48. Hondros, G. (1959) The evaluation of Poisson's ratio and the modulus of materials by the Brazilian (indirect tensile) test. *Australian Journal of Applied Science,* vol. 10, p. 243-268.

49. Hooper, J.A. (1966) The measurement of stress in concrete using optical transducers. ME thesis, University of Sheffield.

50. Hooper, J.A. (1972) The theory and development of load cells incorporating photoelastic glass disc transducers. Ph.D. thesis, University of Sheffield, 142 p. Also: The theory and design of photoelastic load gauges incorporating glass element transducers. *International Journal of Rock Mechanics and Mining Sciences,* vol. 9, p. 363-401.

51. Hooper, J.A. (1971) The failure of glass cylinders in diametral compression. *Journal of the Mechanics and Physics of Solids,* vol. 19, p. 179-200.

52. Howland, R.C.T. and A.C. Stevenson (1933) Biharmonic analysis in perforated strip. *Philosophical Transactions, Royal Society (London),* Series A, vol. 232, p. 155-222.

53. Jessop, H.T. (1921) On Cornu's method of determining the elastic constants of glass. *Philosophical Magazine,* vol. 42, p. 551-568.

54. Kunert, K. (1961) Spannungsverteilung im Halbraum bei elliptischer Flachenpressungsverteilung uber einer rechteckigen Druckflache. *Forsch. Ing. Wes,* vol. 27, no. 6, p. 165-174.

55. Leeman, E.R. (1964) Rock stress measurements using the trepanning stress-relieving technique. *Mine and Quarry Engineering,* June, p. 250-255.

56. Mesnager, M. (1913) Détermination complète sur une modèle reduit des tensions qui se produirant dans un ouvrage. *Ann Pont. Chauss,* vol. 15, no. 4, p. 133-186.

57. Moore, D.R. (1967) The measurement of ground movements in bord and pillar workings. ME thesis, University of Sheffield.

58. Morley, A. (1954) *Strength of materials.* London: Longmans, Green & Co. Ltd.

59. Murgatroyd, J.B. and R.F.R. Sykes (1947) The delayed elastic effect in silicate glass at room temperature. *Journal of the Society of Glass Technology,* vol. 31, no. 141, p. 17-35.

60. Nikholayef, A.F. (1964) Synthetic polymers and plastics. Ed, Khimia, Moscow.

61. Phillips, P. (1905) The slow stretch in rubber, glass, and metal wires, when subjected to constant pull. *Philosophical Magazine,* vol. 9, p. 513-531.

62. Popov, E.P. (1947) Discussion of "Critical stresses in a circular ring," by E.A. Ripperger and N. Davies. *Transactions of the American Society of Civil Engineers,* vol. 112, p. 631-634.

63. Rabbets, J.W. (1968) The effect of temperature changes on the performance of the photoelastic glass insertion stressmeter. Unpublished report, Postgraduate School of Mining, University of Sheffield.

64. Rose, H. (1969) An investigation of stressmeter cements. Unpublished report, Postgraduate School of Mining, University of Sheffield.

65. Rose, H. and A. Roberts (1966) The measurement of in-situ stress, strain, and load, by optical techniques. U.S.Army European Research Office, Final Technical Report, Contract 91-591-EUC.

66. Saltuklaroglu, M. (1968) The determination of loads on mine support systems. Ph.D. thesis, University of Sheffield.

67. Savin, G.N. (1961) Stress concentration around holes. Oxford: Pergamon Press.

LITERATURE CITED (cont'd)

68. Savur, S.R. (1925) On the stress-optical coefficients for direct tension and pressure measured in glass. *Philosophical Magazine*, vol. 50, p. 453-463.

69. Shand, E.B. (1954) Experimental study of the fracture of glass. I. The fracture process. *Journal of the American Ceramic Society*, vol. 37, no. 2, p. 52-60.

70. Stephen, R.M. and D. Pirtz (1963) Application of birefringent coating to the study of strains around circular inclusions in mortar prisms. *S.E.S.A. Exp. Mech.*, vol. 3, no. 4, p. 91-97.

71. Trumbachev, V.F. and G.A. Katkov (1966) Experimental application of photoelastic coatings for the determination of stresses and loads on the supports of mining excavations. *International Journal of Rock Mechanics and Mining Science*, vol. 3, p. 337-347.

72. Van Zee, A.F. and H.M. Noritake (1958) Measurement of the stress-optical coefficient and rate of stress release in commercial soda-lime glasses. *Journal of the American Ceramic Society*, vol. 41, no. 5, p. 164-175.

73. Waxler, R.M. (1953) The stress-optical constant of plate glass. *Glass Industry*, vol. 34, p. 258-259.

74. Skilton, D. (1971) Behaviour of rigid inclusion stressmeters in viscoelastic rock. *International Journal of Rock Mechanics and Mining Sciences*, vol. 8, p. 283-289.

75. Buswell, H.J., D.R. Moore and A. Owens (1974) The use of a high modulus inclusion gage in non-linear viscoelastic materials. *Experimental Mechanics*, vol. 14, no. 7, p. 274-280.

APPENDIX: EXAMPLES OF PHOTOELASTIC LOAD CELLS

The major application of photoelastic transducers has been to evaluate loads, stresses and strains in civil engineering type structures and in mines. In this appendix specific examples of load cells are described together with some applications.

Photoelastic load cells

As discussed in Part II, photoelastic load cell designs can be broken down into two main categories: Those in which a glass disk carries the full load to be measured (glass disk load cells) and those in which a glass disk shares the load with a deforming steel body (steel body load cells). The following brief discussion of various photoelastic load cell designs is not intended to be comprehensive, but is presented to show the versatility of the technique.

Glass disk load cells

A wide range of glass disk load cells have been developed for purposes as diverse as measuring hydraulic pressures and measuring the loads on scaffolding.

The sensitivity S_0 of such load cells can be determined from eq 18 as

$$S_0 = \frac{P}{n} = \frac{D\pi\lambda}{8C} \quad \text{(for transmitted light)} \tag{A1}$$

$$= \frac{D\pi\lambda}{16C} \quad \text{(for reflected light)} \tag{A2}$$

where P is the applied load, C is the stress coefficient of the glass, λ is the light wavelength and D is the disk diameter.

Note that the sensitivity is not a function of the disk length. This is a very important advantage in that it is not necessary to apply the loads uniformly along the disk length to obtain accurate readings. For soda lime glass, $C = 1.8824 \times 10^{-8}$ in.^{2}/lb, and thus eq A1 and A2 can be written

$$S_0 = .0882\, D\lambda \text{ lb/fringe (transmitted light)} \tag{A3}$$

$$S_0 = .0411\, D\lambda \text{ lb/fringe (reflected light)} \tag{A4}$$

where λ is in angstrom units and D is in inches.

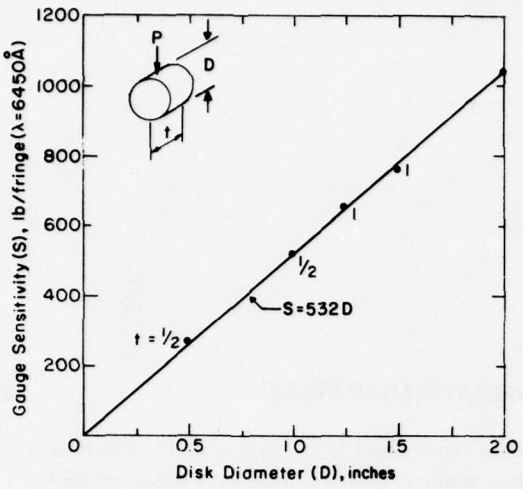

Figure A1. Relationship between glass disk load cell sensitivity (lb/fringe) and disk diameter.

Typically, for a red filter (λ = 6450 Å) the sensitivity of glass disk load cells is

$$S_0 = 532\,D \text{ lb/fringe (transmitted light)} \quad \text{(A5)}$$

$$S_0 = 266\,D \text{ lb/fringe (reflected light)} \quad \text{(A6)}$$

Figure A1 is a calibration graph of glass disk load cells under transmitted light (red filter, λ = 6450Å) showing excellent agreement with eq A5.

Scaffold tube load cell

Figure A2 illustrates the design of a simple scaffold load cell and shows a cell installed in a scaffolding frame. The cell is read by counting the fringes in the disk under transmitted light with the polarizing and analyzing filters built permanently in place. No attempt has been made in this cell to provide for compensation of the fringe orders when viewing, as the cells are intended to be used to obtain an overall picture of the loads in scaffold structures, rather than accurate individual readings. As the scaffold loads are expected to be generally low, a 1-in.-diameter, 0.75-in.-thick glass disk transducer is used to give a sensitivity of 532 lb/fringe over a range of approximately 0 to 2700 lb. In the event of overloading and consequent fracture of the disk the outer sleeve of the cell is designed to make direct contact with the scaffold tube and thereby maintain the structural integrity of the assembly. The cell is very simple to construct and no problems have been encountered in its use.

Mine roof/floor convergence meter

A convergence meter based on a glass disk load cell has been designed to monitor closure of mine workings where it is too dangerous for personnel to enter routinely but where it is possible to observe the measurement station.

In mines in sedimentary deposits or in saline evaporites the roof to floor closure is often on the order of several inches, and is measured by techniques employing conventional survey instruments and telescopic extensometers. In hard rock mines, the rock movements may be quite small, on the order of ¼ in., but are equally significant in relation to mine stability, particularly in mines subjected to rock bursts.

The meter illustrated in Figure A3 is intended primarily for use in hard rock mines. It is capable of reading convergence to a resolution of 1×10^{-4} in. over a range of 0.1 in. or alternately to 2×10^{-3} in. over a range of 0.25 in. It consists of a glass disk load cell (A) mounted in series with a number of spring washers (B) standing on a telescopic tube set (C). The length of the tubes can be adjusted to span between the roof and floor, and preloading of the load cell is achieved by turning the nut (D) to extend the shaft (E). When the convergence occurs the meter accepts load, deforming the spring washers and stressing the glass disk in the load cell. The reading of the load cell is proportional to the deformation of the washers and is thus a measure of convergence. The range of the meter can be varied from around 0.05 to 0.25 in. by changing the number or stiffness of the spring washers. The glass disk is typically 1.0 in. in diameter and 0.5 in. thick, giving a sensitivity of 266 lb/fringe (red light, reflected). The sensitivity of the meter with a given load cell depends upon the number and stiffness of the washers. For the design shown in Figure A3 the convergence C_m is given by

$$C_m = n(5N + 2) \times 10^{-3} \text{ in.} \quad \text{(A7)}$$

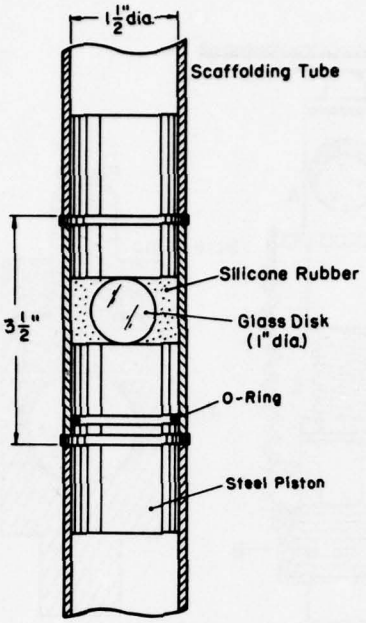

a. Basic design.

b. Cell positioned in scaffold.

Figure A2. Scaffold tube load cell.

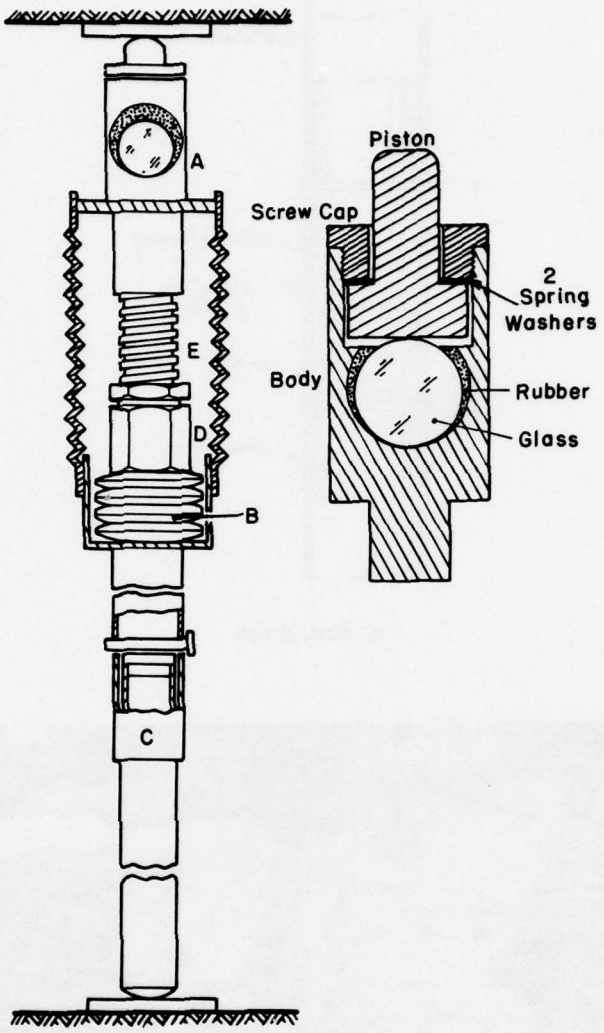

Figure A3. The stope stability meter.

where C_m is convergence in inches, n is the fringe order change and N the number of washers.

The meter can be read at distances up to 200 ft using a telescope and powerful light. The instrument is sensitive to temperature changes but this presents no great problem in mines as the temperature remains very constant.

In one application the meter was used to observe the effects on a mine roadway of the approach of other mine workings at a lower elevation, and to detect the onset of ground movement due to subsidence. The total range of measurement in this case was extended by resetting the meter to a new zero datum when the full extent of the available range had been expended.

The stope stability meter worked excellently and showed that the excavation in which it was installed remained stable until the approaching workings in the lower seam reached within an angle of "draw" equal to 32.5°. Thereafter, convergence at the measurement station continued steadily for the remainder of the project. Measurements were continued over a period of 6 months, in very wet conditions, during which time the meter functioned perfectly.

Photoelastic hydraulic pressure gage

The photoelastic hydraulic pressure gage is another example of a load cell in which the full load is carried by a glass disk. It was developed as a highly stable, stiff pressure gage for use under arduous conditions and as an indicator for "stiff" hydraulic flatjack type load cells. The gage illustrated in Figure A4 consists of a glass disk loaded diametrically by means of a piston which in turn is loaded by fluid pressure. The analyzing and polarizing filters are built permanently into this particular gage but they can be left out and the gage read using an external polariscope.

The sensitivity of the photoelastic hydraulic pressure gage for transmitted light is given by

$$S = 0.0822\, D\lambda \frac{4}{\pi d^2} \tag{A8}$$

where d is the diameter of the piston. When viewed by transmitted red light (6450 Å) the sensitivity of a hydraulic pressure gage is

$$S_0 = \frac{677.7\, D}{d^2} \text{ psi/fringe} \tag{A9}$$

where the glass disk diameter and the piston diameter are both in inches. The majority of the designs tested have a 1-in.-diameter disk and a 9/16-in.-diameter piston, giving a sensitivity of 2140 psi/fringe.

There have been numerous applications of the photoelastic hydraulic pressure gage. Hooper[49] describes the gage and its application in an apparatus for applying sustained loads to test specimens, for periods up to several years. His equipment required that a precisely known hydraulic pressure be applied to a piston loading a viscoelastic cylindrical test specimen. The pressure was measured by both a photoelastic hydraulic pressure gage and a 10-in.-diameter Bourdon tube test gage. It was thought that the Bourdon tube might show slight creep over a period of two years and the photoelastic gage was used to monitor this effect. However, over the two-year test period no discrepancies between the two gage readings were observed.

Saltuklaroglu[66] used 48 photoelastic pressure gages in a study to measure the loads on hydraulic jacks on a longwall coal face.

The distribution of load on the supports along the length of a longwall face varies considerably. Each unit carries a load which is dependent on the interaction between the support legs and the strata in contact with the legs. The loads also vary in time and space depending upon the operational working cycle and the location of the cutting and loading machine.

To study the variations of fluid pressure in such a hydraulic system by the use of conventional pressure gages is not practicable under the very arduous working conditions typical of longwall mine workings. Bourdon type gages are vulnerable to damage, and when damaged leak hydraulic fluid, which destroys the support's effectiveness.

When photoelastic fluid pressure gages were inserted into the chock hydraulic circuit, as illustrated in Figure A5, these disadvantages were entirely removed. Due to the compactness and inherent strength of the photoelastic gages it was possible to mount them on the valve control box situated at the front of each chock, in such a way as not to impede the normal operation of the chocks.

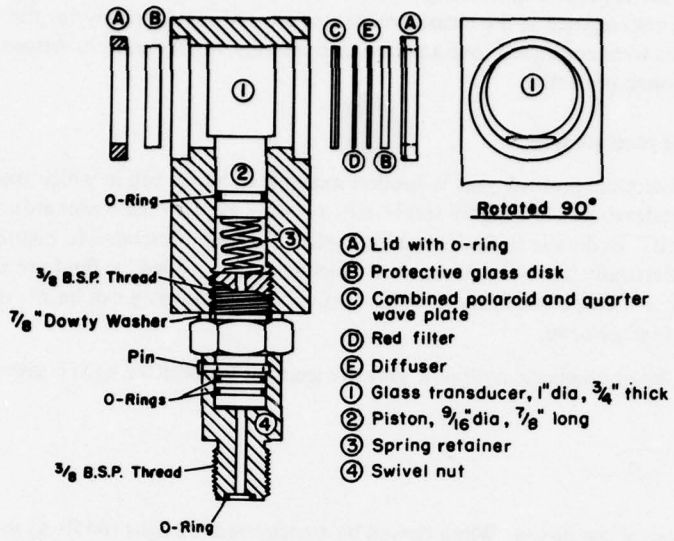

Figure A4. Photoelastic hydraulic pressure gage.

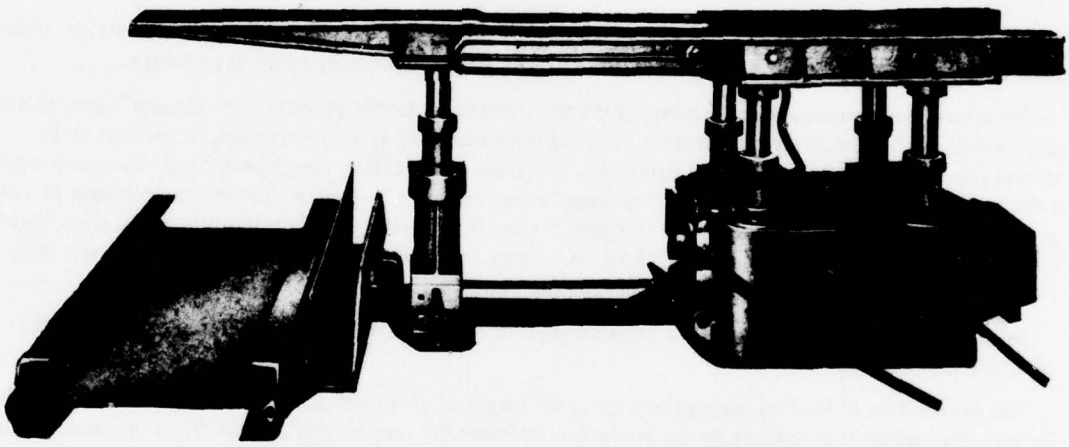

a. 3 1/4-in. bore five-leg Gullick chock.

Figure A5. Monitoring loads on hydraulic mine support using photoelastic hydraulic load gages.

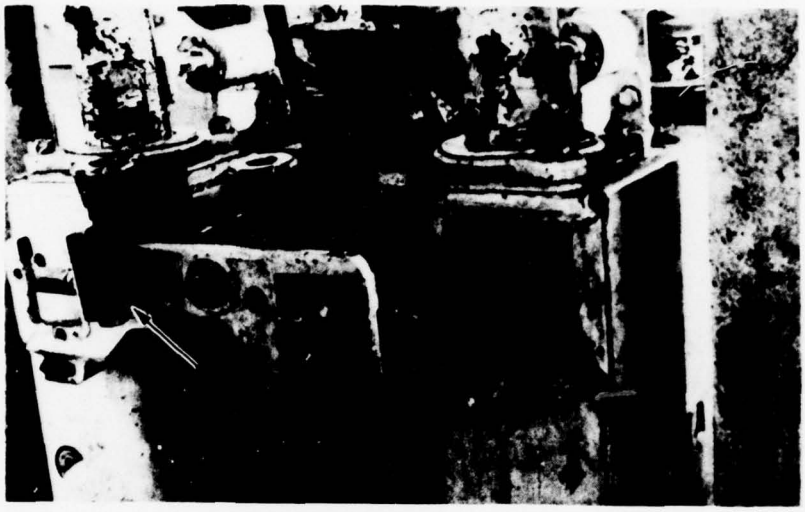

b. Arrangements for mounting gages. Arrow points to gage.

Figure A5 (cont'd).

Variations of load on the chocks were observed during the working cycle, with readings of pressure being taken in the hydraulic circuit of each leg. The readings were related to face conditions such as caving conditions, locations of machines, and phase of the working cycle. During the course of a six-month investigation several of the gages failed by mechanical fracture of the glass, possibly due to fluid "hammer" in the hydraulic circuit when shock loads were transmitted to the chocks from the strata. The damage to the gages had no effect on the working performance of the supports concerned, which continued to function as before, without loss of fluid from the gages.

Hydraulic borehole pressure cells

The photoelastic hydraulic gage has also been adapted to monitor the change in hydraulic pressure induced in a flatjack prestressed into a borehole in rock or coal. In such gages the pressure readings are a measure of rock stress change. The basic device, as described by Miller and Sporcic[81], consists of a thin flatjack encapsulated in a polyester resin cement to form a cylinder approximately 1 ft long by a little less than 2 in. in diameter. The cell is filled with hydraulic fluid, and after insertion into a borehole it is pressurized to bring it into contact with the borehole walls. The effects of change of load in the strata into which the cell has been inserted can then be observed in terms of the change of pressure in the hydraulic system.

However, the cells as designed by Miller and Sporcic had certain disadvantages arising from the use of Bourdon type pressure gages and recorders on the hydraulic system. These gages are bulky and vulnerable to damage, and when damaged leak hydraulic fluid which causes false readings. In addition, the pressure changes to be measured only give rise to small oil displacements, and as most Bourdon tube type gages are soft and require significant oil flow into them with increase in pressure, the overall sensitivity of the flatjack is low. By replacing the Bourdon type pressure gage with a photoelastic fluid pressure gage these disadvantages are removed. Figure A6a illustrates the gage and Figure A6b the flatjack component before encapsulation in epoxy resin. Typically the cell described by Skilton[82] is 1-1/2 in. in diameter by 8 in. long.

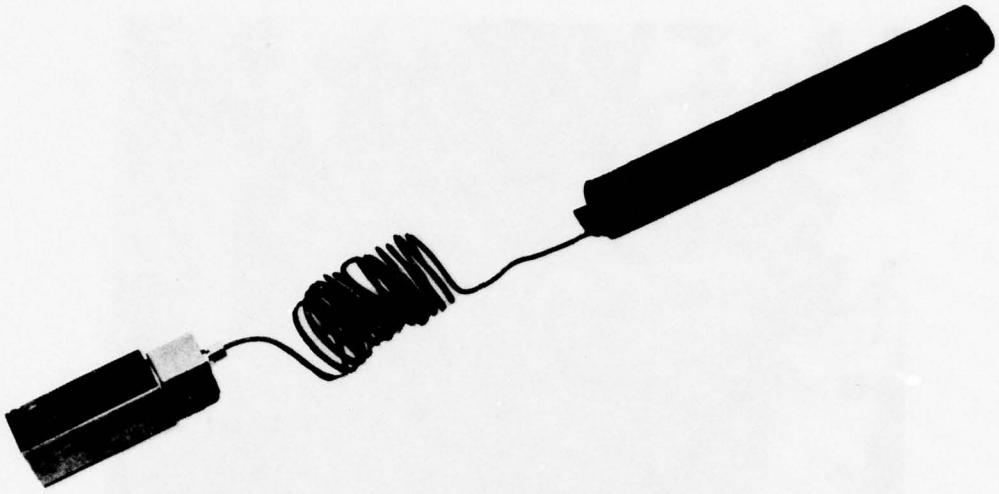

a. Borehole pressure cell with photoelastic hydraulic pressure gage.

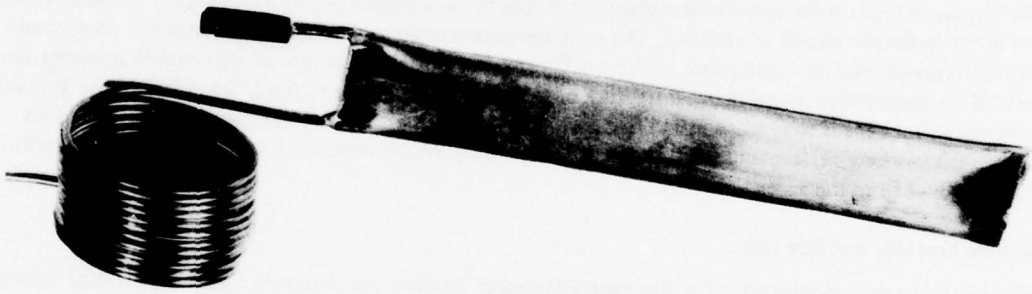

b. Basic flatjack design.

Figure A6. Photoelastic hydraulic borehole pressure cell.

When in use the photoelastic-hydraulic pressure cell is pushed to the back of the borehole, and then withdrawn 1 ft to avoid complications caused by the stress concentration at the back of the hole. It is then coupled to the hydraulic system, pressurized to approximately 2000 psi (this pressure being maintained for 15 min), and then reduced to the particular initial setting pressure desired. Finally the isolating valve is closed and the pressure cell, complete with its gage, is disconnected from the hand pump and feed pipe. Stress changes in the rock or coal around the borehole can then be monitored in terms of the pressure changes as read by the photoelastic gage.

Calibration of the borehole pressure cell consists of relating the change in observed hydraulic pressure to change of stress in the rock, for various initial setting pressures.

The ratio of the change in rock stress to the change in cell pressure is the sensitivity factor of the cell.

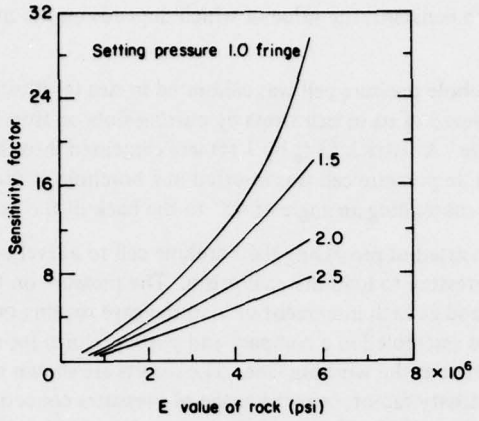

a. Effect of modulus of elasticity of the host rock and the initial setting pressure on the sensitivity of the borehole pressure cell.

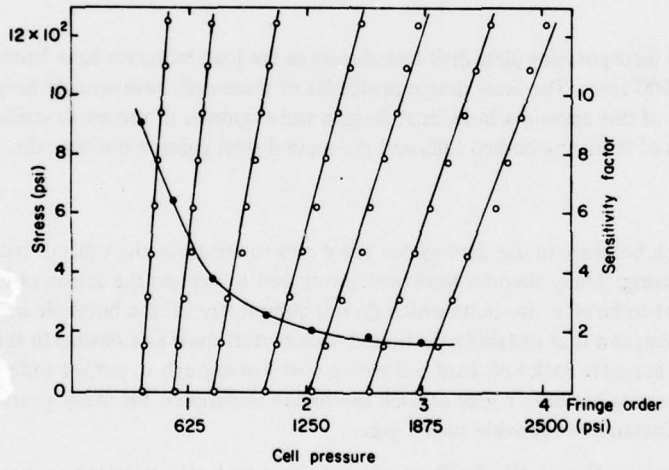

b. Calibration characteristics in Mansfield sandstone.

Figure A7. Calibrations of photoelastic hydraulic borehole pressure cell.

Materials capable of being cut into suitable specimens for compression testing can be used to calibrate the gage in the laboratory. However, coal, being friable, requires that the calibration be made by an in situ method.

Skilton[83] gives the results of laboratory calibrations performed on six rock types ranging in modulus from 10^6 to 6×10^6 psi. The composite effect of the E value of the host material, and the effect of variation in the setting pressure on the sensitivity of the cell, are summarized in Figure A7a. The relationship between the cell pressure, as registered by the fringe count in the glass disk, and the change in rock stress is shown in Figure A7b for various setting pressures in one of the rocks tested.

It will be noted that the cell displays a linear response to the change in host stress, but the sensitivity factor is not the same for all initial setting pressures. However, when the setting pressure exceeds 2 fringes the sensitivity factor approaches a constant, the value of which depends on the modulus of elasticity of the host material.

For use in coal pillars the borehole pressure cell was calibrated in situ (as illustrated in Fig. A8a). A segment of a coal pillar was first relieved of its in situ stress by cutting slots on three sides, to enclose a prism 3 ft high by 3 ft deep by 1 ft wide. A flatjack (3 ft by 1 ft) was cemented into the horizontal slot at the base of this prism, and the borehole pressure cell was inserted in a borehole at the center of the prism, the back of the cell being at a depth subtending an angle of 45° to the back of the bottom slot.

The calibration procedure consisted of presetting the borehole cell to a level of one fringe order and then periodically raising the flatjack pressure to load the coal prism. The pressure on the flatjack system was also read on a photoelastic gage and at each increment of load the gage reading on the borehole pressure cell was noted. All the apparatus was assembled in a compact and portable form for easy transportation in the mine and for convenient application at the working face. The results are shown in Figure A8b. The cell response was linear, giving a sensitivity factor, over the range of pressures concerned, of 1.10. The modulus value of the coal ranged from 0.40 -0.60 X 10^6 psi and the result of the in situ calibration tied in reasonably well with the laboratory calibrations on the other rock types.

Several postgraduate students at Sheffield University have used these hydraulic cells to study the effects of various mining operations on the development of loads on small support pillars, and to observe the stress concentrations produced in the strata ahead of the extraction faces in longwall working (Bannerjee[76], Skilton[83], Ergen[77]).

Steel body load cells

Steel body load cells incorporating glass disk transducers as the load indicator have been built and tested with load ranges up to 600 tons. The basic design principles of these cells have already been discussed in detail; in the remainder of this appendix individual designs and examples of use are described. The first section describes examples of steel ring bodied cells and the second steel column bodied cells.

Rock bolt load cell

Many millions of rock bolts are in use throughout the world to reinforce the walls of rock excavations in mining and civil engineering. Many theories have been developed to explain the action of rock bolts but it is commonly agreed that to be effective bolts which do not completely fill the borehole into which they are set must be under tension, and that instability in bolted rock reveals itself as a change in tension in the bolt. The development of an accurate rock bolt load cell with a cost low enough to permit widespread use as a control gage for bolted strata has been a goal of rock mechanics researchers for many years. The photoelastic rock bolt load cell is an attempt to provide such a gage.

The basic gage is shown in Figure A9. In Figure A10 the gage is shown mounted on a rock bolt with a washer, spherical seating and an end plate, to ensure uniform loading. The gage consists of a hollow steel cylinder with a transverse hole to allow the stem of the rock bolt to pass through. A glass disk is mounted in one half of the cylinder, as shown in Figure A10, such that when the body deforms under the applied load the deformation is conveyed to the disk. The disk can be preloaded in the body by a set screw and wedge mechanism.

The rock bolt load cell has been extensively tested by Saltuklaroglu[66] for the effects of loading conditions and general stability. Figure A11 shows his test setup and the results of some of the tests. One of the major problems when mine rock bolt load cells are being used is compensation for the effects of eccentric loading, as the rock face is rarely plane to the axis of the rock bolt. Saltuklaroglu was able to demonstrate that up to 8½° of eccentric loading could be tolerated with a photoelastic rock bolt load cell assembly without appreciable error. Due to flattening of the glass disk during the initial loading stages the load/fringe order

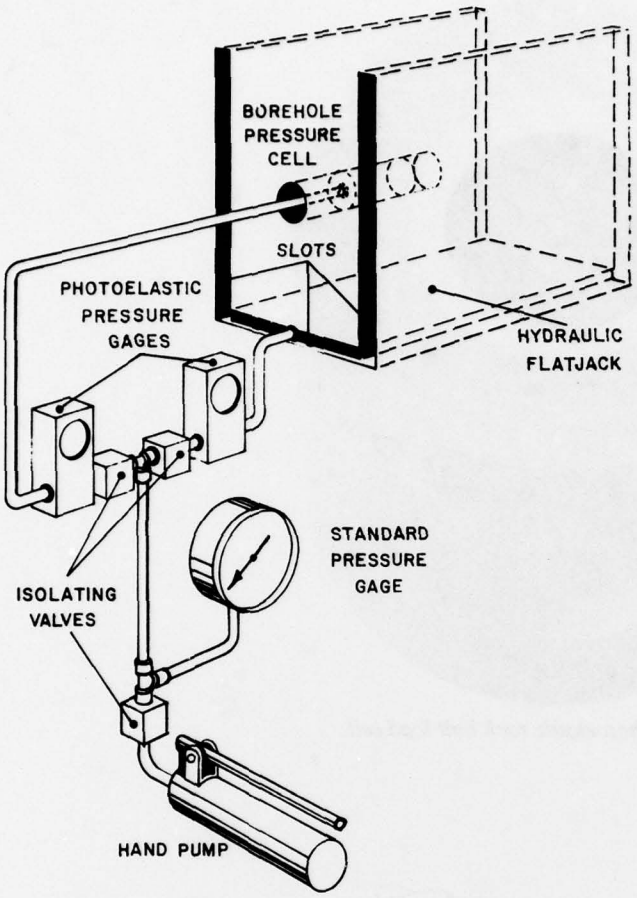

a. Test set up.

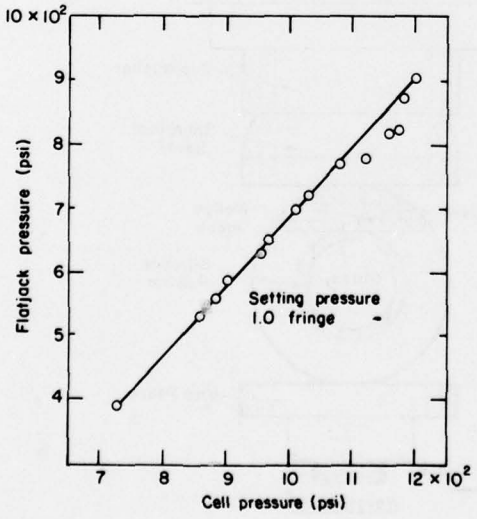

b. Calibration characteristics.

Figure A8. In situ calibration of a photoelastic hydraulic borehole pressure cell in Barnsley hard coal.

Figure A9. Photoelastic rock bolt load cell.

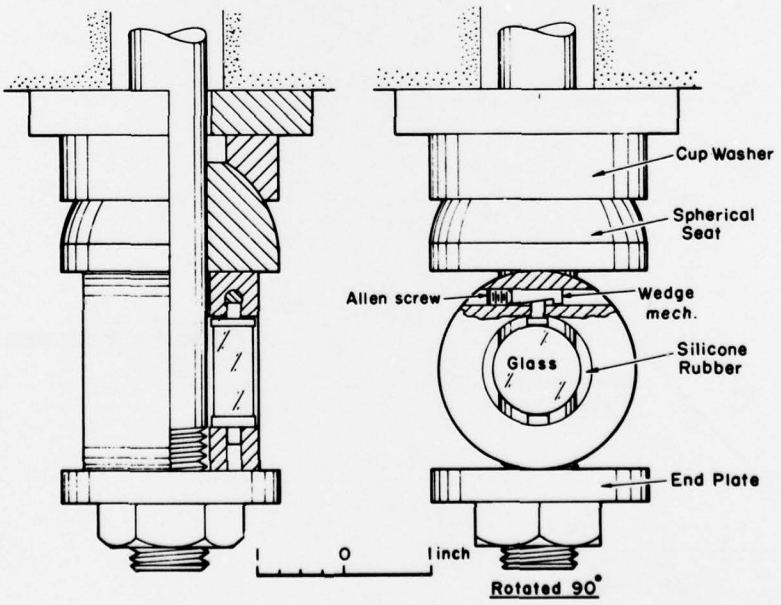

Figure A10. Design of rock bolt dynamometer.

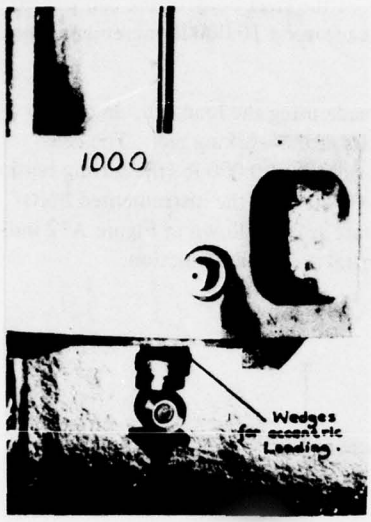

a. Manner of calibration under eccentric loading.

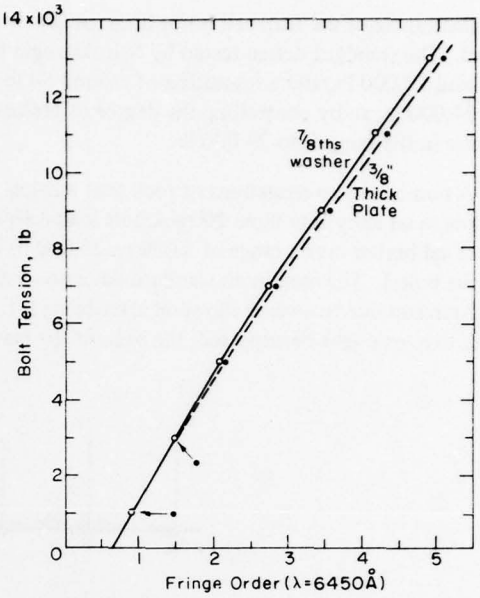

b. The effect of bolt-end washer design on the sensitivity of the rock bolt dynamometer.

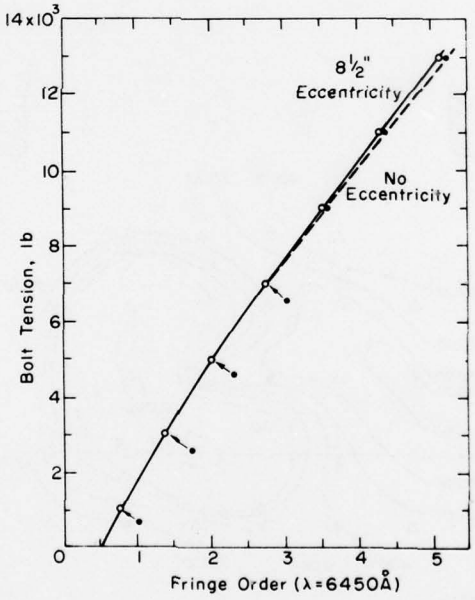

c. The effect of eccentric loading on the sensitivity of the photoelastic rock bolt dynamometer.

Figure A11. Calibration characteristics of the photoelastic rock bolt load cell. (After Saltuklaroglu.[66])

characteristic of the load cell is not linear at low fringe orders and a preload of at least 1 fringe should be used. The standard design tested by Saltuklaroglu had a sensitivity of 2,750 lb/fringe, a reading range of around 10,000 lb, and a resolution of around 50 lb. The working range of the steel body of the cell was up to 24,000 lb, so by controlling the degree of preload the cell could be read over a 10,000-lb increment anywhere in the range 0 to 24,000 lb.

A number of investigations of rock bolt tension changes have been made using the load cell. In one example in an anhydrite mine 20 rock bolt load cells were installed on bolts at the working face. The cells were calibrated over a range of 5,000 to 25,000 lb with a preload of 4 fringes at 20,000 lb (the setting tension in the bolts). The maximum standard deviation was 0.177 fringe at 11,000 lb. All the instrumented bolts lost tension due to anchor slip soon after being set. The tension loss contour lines shown in Figure A12 indicate that, as might be expected, the bulk of the loss occurred in the central area of the junction.

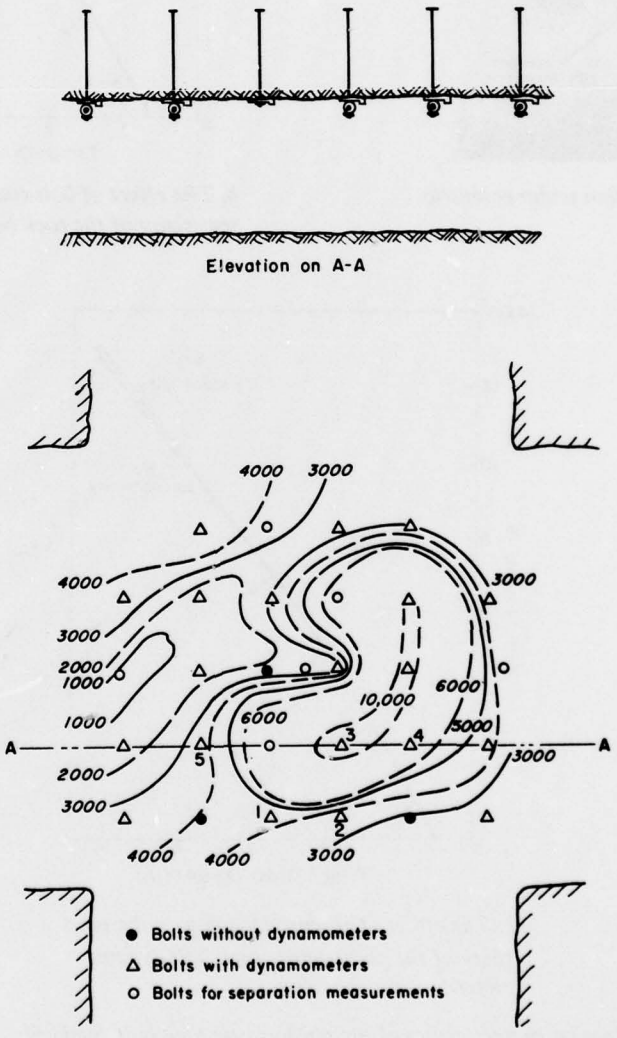

Figure A12. Plot of bolt tension loss in a room and pillar mine.

Earth pressure load cell

Another example of a ring body load cell is shown in Figure A13. This particular cell, described by Hooper[79], was designed to measure changes in earth pressure under a concrete raft over long periods of time. Details of the calibration characteristics of this 10-ton load cell are given in Figure 64. The cell was mounted at the center of a large concrete piston flush-mounted with the underside of the raft as shown in Figure A14. A tube led from the surface to a chamber around the cell so that it could be read using the specially designed polariscope illustrated in Figure A15.

A slotted square-section steel tube containing an adjustable inclined mirror was fastened to the end of a 40-in. length of 0.75-in.-diameter steel pipe, the upper end of which was provided with a screwed connection. Three additional lengths of pipe were provided to enable the unit to be lowered to a depth of 11 ft. Attached to the side of the square sectioned tube was one arm of a lazy-tongs mechanism, the adjacent arm of which was connected to the end of a 0.125-in.-diameter steel rod. Vertical movement of this rod induced the linkage mechanism to extend or retract, as required. Three additional screwed extension rods enabled the lazy-tongs to be operated from the surface of the foundation raft.

An aluminum box containing lightbulbs was fixed to a horizontal spindle located at the closed end of the lazy tongs. Also incorporated in the light box was a combined polarizer and quarter wave plate, together with a diffusing screen.

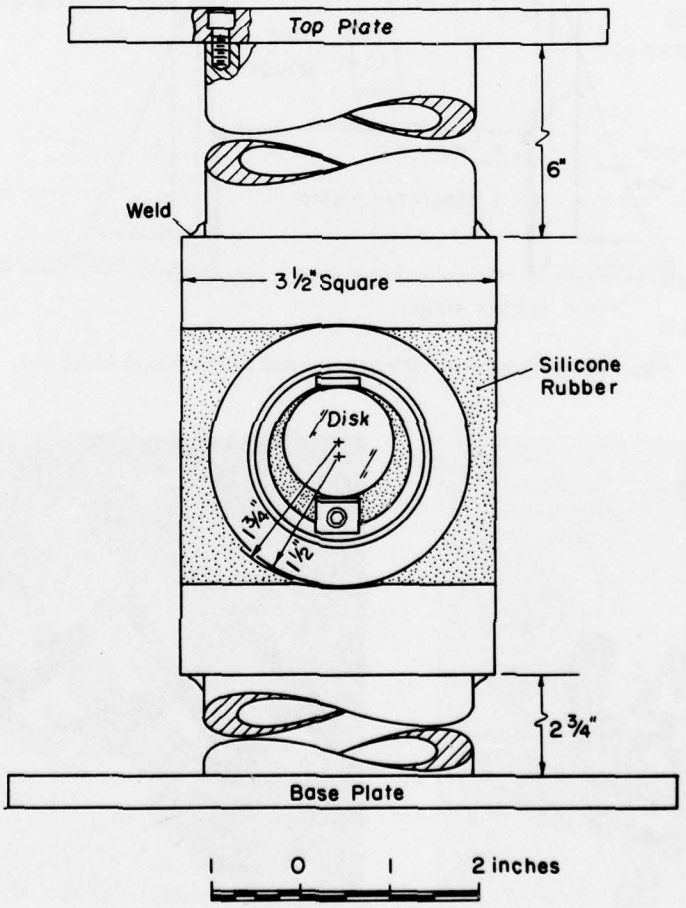

Figure A13. Steel ring body load cell for measuring earth pressures. (After Hooper[79])

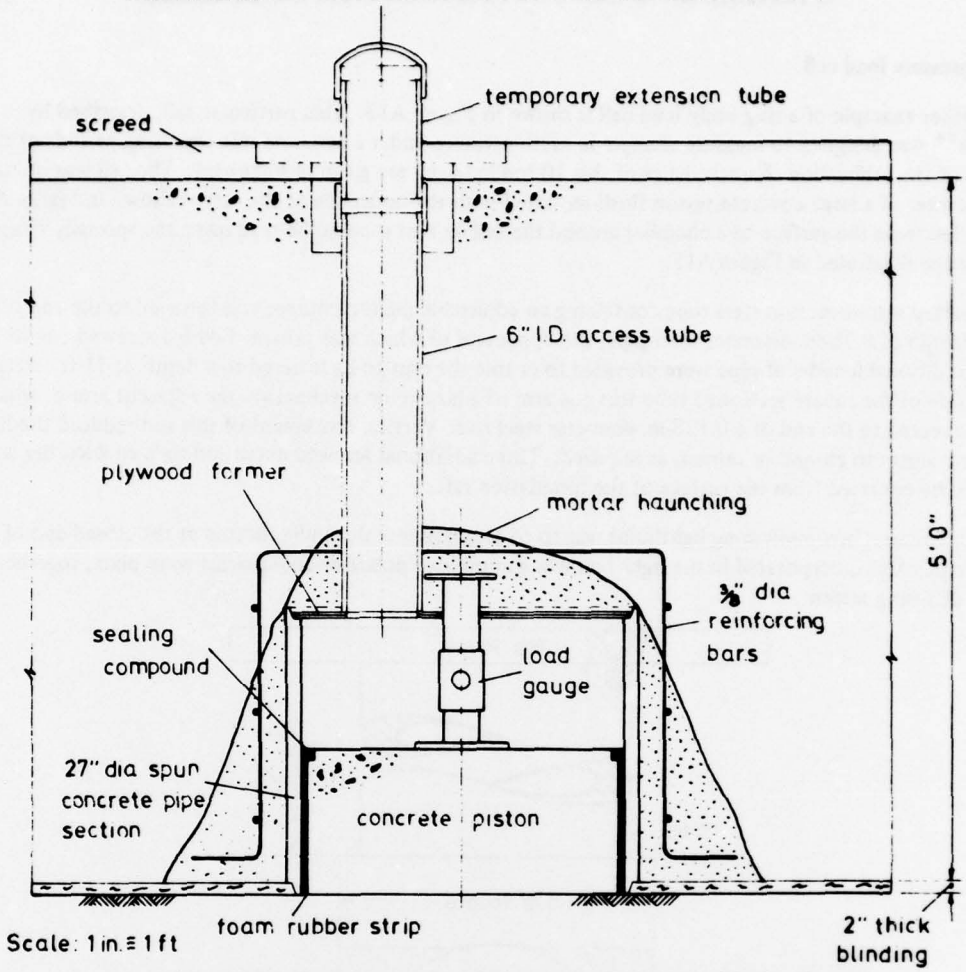

Figure A14. Positioning of earth pressure cells in tower block raft.

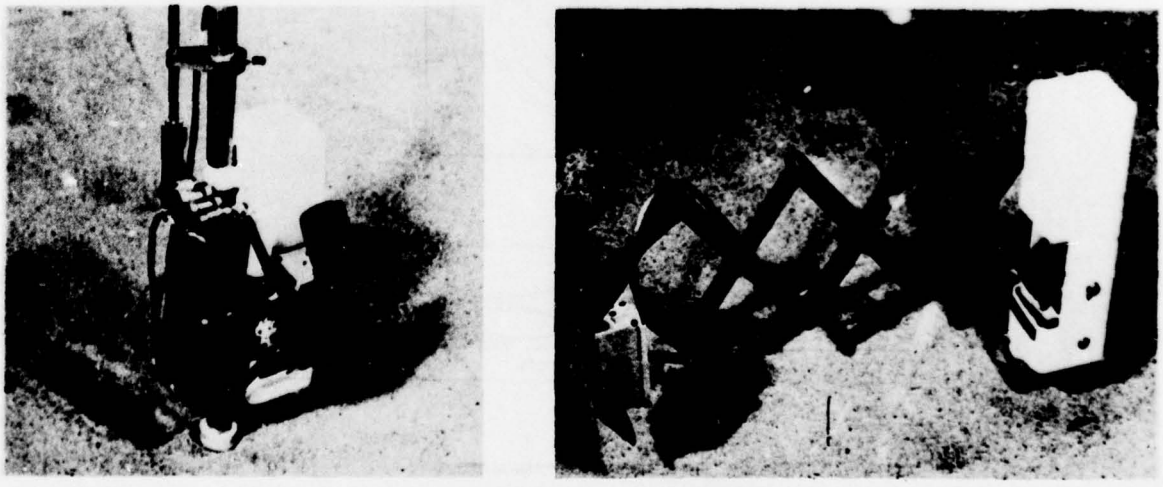

a. Linkage mechanism retracted. *b. Linkage mechanism extended.*

Figure A15. Viewer for earth pressure and pile load cells.

The load cell was read by lowering the retracted light unit down the 6-in.-diameter access tube until it rested on the concrete piston of the earth pressure cell. The lazy-tongs were then extended by depressing the control rod and then the light box was positioned at the back of the gage to be read. The fringe order was then measured from the surface by observing the fringe pattern visible in the mirror when viewed through a hand-viewer.

Three earth pressure cells as described were installed in the summer of 1964 in the pile-raft foundation supporting a tower block in central London and were all functioning well after two years. Two of the cells were still functioning the last time they were read in 1973 after 6 years. It is not clear why one of the cells failed but it is thought to be due to a buildup of sludge around the cell; the units had to be pumped out prior to reading. The results of the study indicated that the stress on the foundation built up to around 20 psi as the building was constructed over a period of 3 years and then settled down to a slightly lower contact pressure (Hooper[80]).

Cable and chain tensometers

Another example of a ring body load cell is the photoelastic cable and chain tensometer illustrated in Figure A16a. In this load cell, which is designed to be installed as a permanent link in the chain or cable, the diametral deformation of the ring is applied to the glass disk transducer at right angles to the loading direction, as illustrated in Figure 58d. In this load cell the polarizing/analyzing filters are built into the faceplate, so to read the fringe order it is merely necessary to shine a light into the viewing aperture. In a second version the polarizing and quarter wave plate are mounted independently to permit goniometric (tardy) compensation as illustrated in Figure A16b. In the example shown, the fringe reading is 4.22, which with this particular tensometer represents a load of 16,900 lb. The tensometers illustrated in Figure A16a have a reading range of 25,000 lb (12½ tons) and a resolution of ± 1000 lb without compensation and ± 100 lb with compensation.

On account of its robust nature this particular tensometer has found an application in the mining industry for measuring the clutch-slipping force levels on coal cutting machinery and the like.

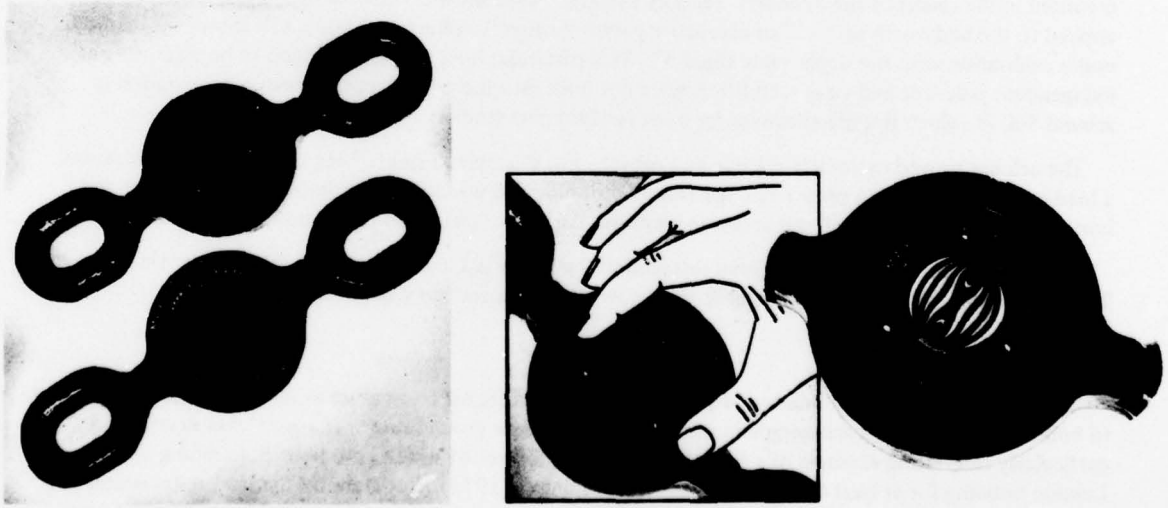

a. Chain and cable tensometer. *b. Tensometer fitted with a movable viewer for fringe compensation.*

Figure A16. Photoelastic chain and cable load cells.

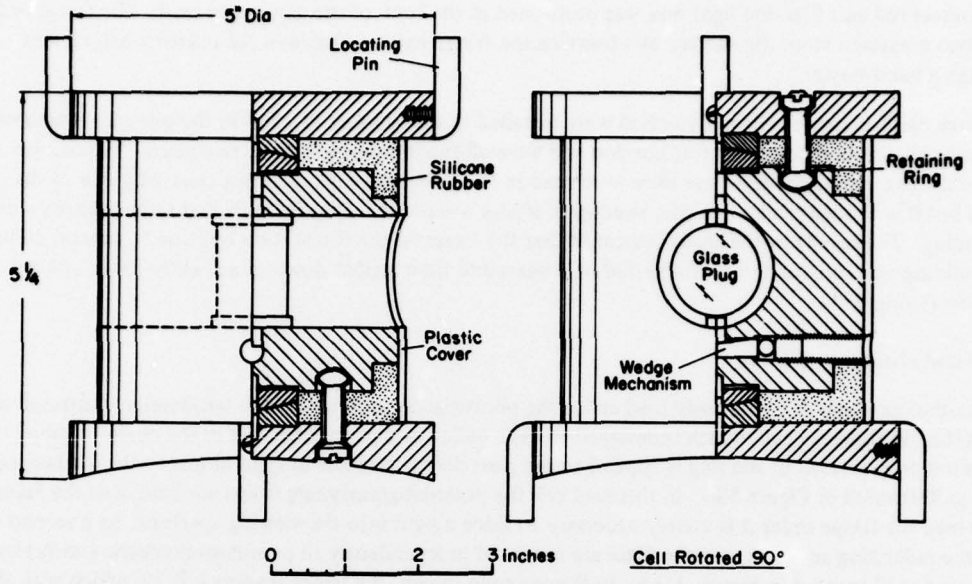

Figure A17. Photoelastic pit prop load cell.

Pit prop load cell

The measurement of load buildup on mine supports presents severe problems because of the difficult environment and the difficulty of ensuring controlled loading conditions for the cell. Figure A17 shows the design of a compact 50-ton range photoelastic load cell designed to overcome these problems. Load is transmitted to a cylindrical steel body through two spherical seatings where it is sensed by a glass disk transducer mounted in the center of the cylinder. Tests by Fisekci[78] have shown that with this design loads can be applied to the body with up to 5° of eccentricity without significant error. Figure A18 shows the load cell under calibration with the upper plate tilted 5°. This particular load cell was intended to be read using an independent polarizer and viewer, so filters were not built into the cell. Accuracy with compensation is around 500 lb, which is quite adequate for mine roof support studies.

The cell has proved extremely reliable and robust. For example, Fisekci[78] reports that on one occasion a load cell was placed on a prop 1 ft away from a shot hole and was subsequently blasted several feet and buried in a rock pile. The cell was recovered without damage or change in calibration characteristics.

Load cells of similar design have been installed in the Victoria Line extension of the London Underground Transport system and in a cargo tunnel at Heathrow Airport where they continue to function.

Pile load cell

The measurement of load buildup in piles is particularly difficult to measure as the loads take several years to build up and the cell is submerged in what is often corrosive groundwater. Hooper[79] has described a particularly interesting example of a 600-ton pile load cell, three of which have been functioning under a London building for at least 6 years (as of the last readings in 1973). For stability the load cell was constructed from six 100-ton load cells rigidly clamped between two massive end plates (Fig. A19). The complete assembly, after calibration, was then built into the pile, 5 ft below a raft supporting the structure

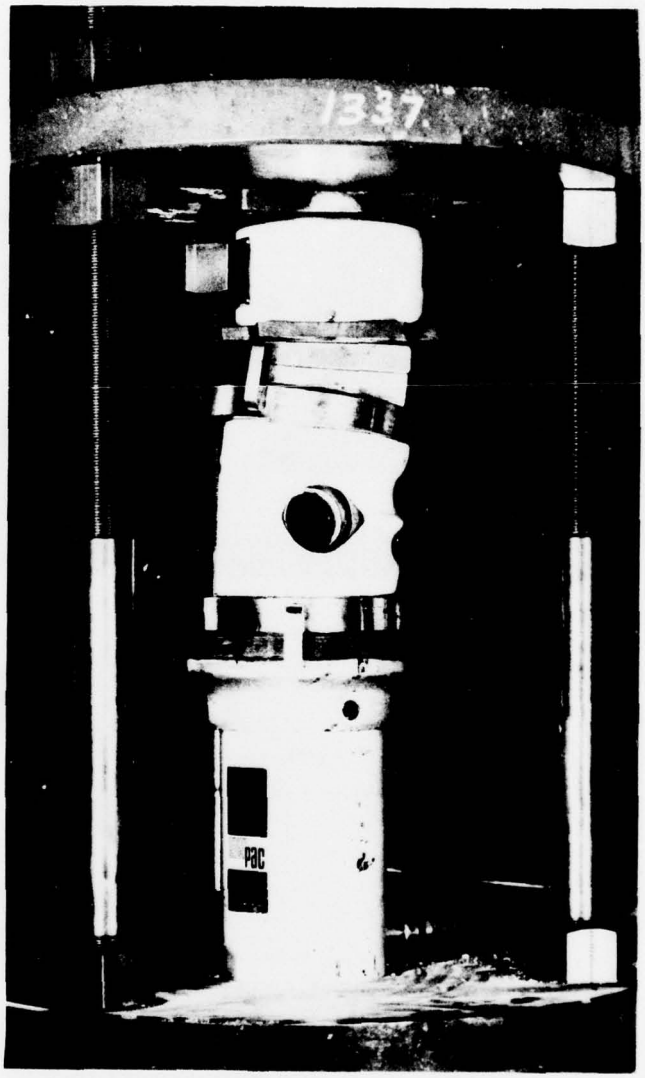

Figure A18. Pit prop load cell under eccentric loading tests.

(Fig. A20). A pipe connecting the center of the load cell to the upper surface of the raft permitted access for the view discussed earlier (Fig. A14 and A15).

As mentioned above, the cells had to be pumped out prior to reading, but they all functioned well, with the readings stabilizing at around 350 tons after 3 years. (For complete details Hooper's paper should be studied.)

Cable load cell

The construction of hollow-bodied load cells for monitoring the loads on large cables and prestressing strand presents design problems if the glass disk transducer is to be used, as great care must be taken to equalize the load distribution in the body. In the photoelastic cable load cell this has been achieved by the

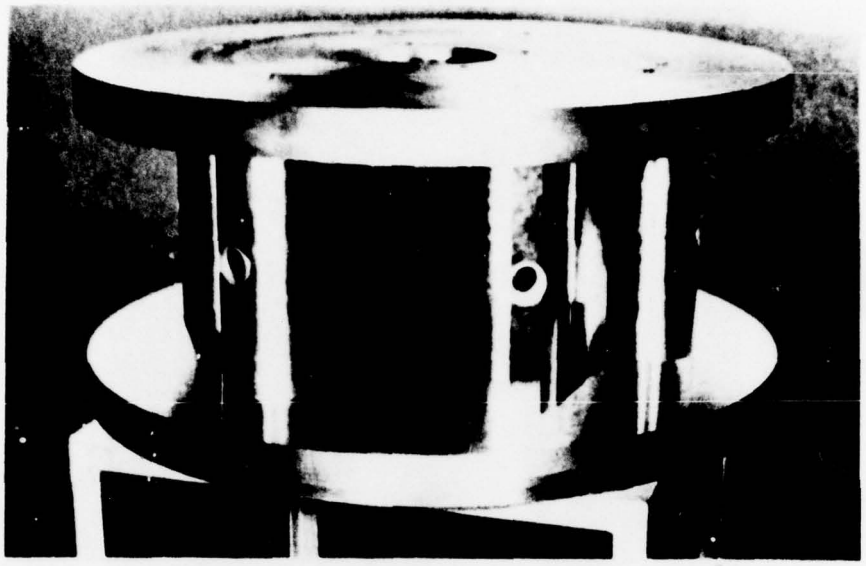

a. Load cell assembled prior to application.

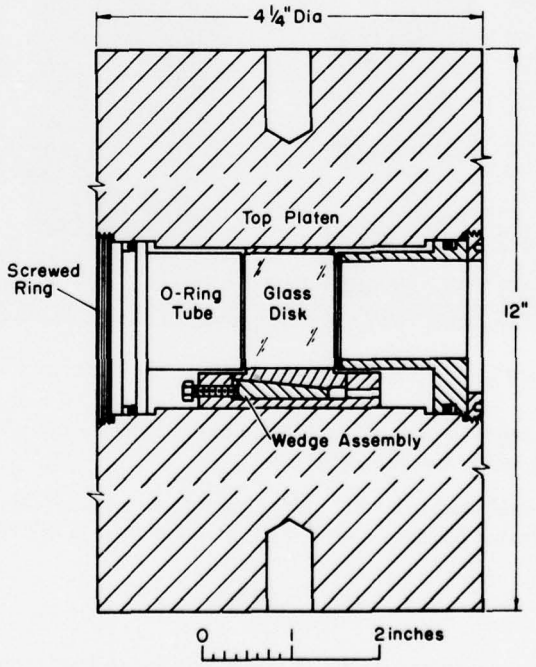

b. Design details of individual 100-ton cell.

Figure Al 9. Photoelastic 600-ton pile load cell.

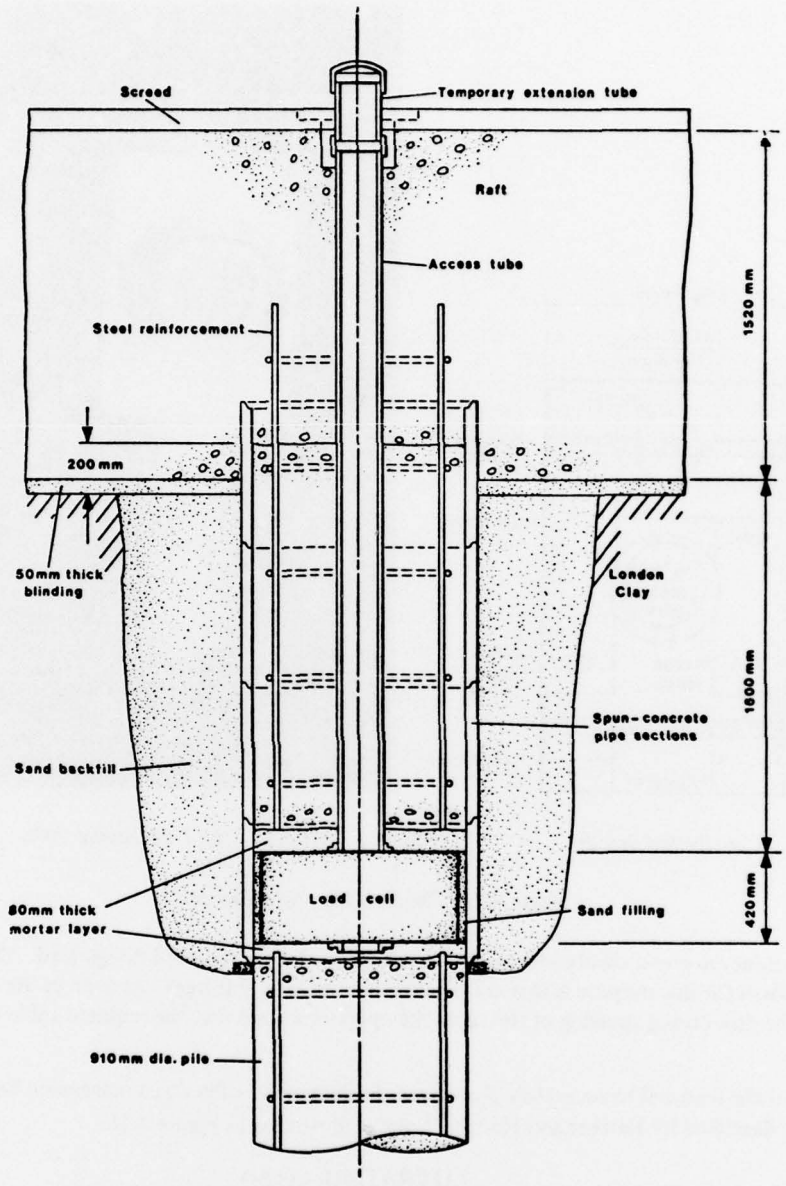

Figure A20. Positioning the 600-ton pile load cells in a pile.

use of four hardened steel rollers, two at each end of the body with the pairs at right angles to each other as illustrated in Figure A21a. With this arrangement an eccentric loading of up to 4° can be tolerated without introducing significant errors. Figure A21b shows the load cells undergoing eccentric loading tests.

The load range of the cell illustrated in Figure A21 is 0 to 65 tons, and within this range the cell is sensibly linear at 10,000 lb/fringe. Tardy compensation gives a reading accuracy of ± 200 lb. The technique of using this cell differs from that previously described, since it is not used to measure a range of load but to indicate when a desired tension has been reached. The initial preload of the glass disk transducer can be varied to enable the cell to be used over different load ranges. The cell is adjusted prior to installation in

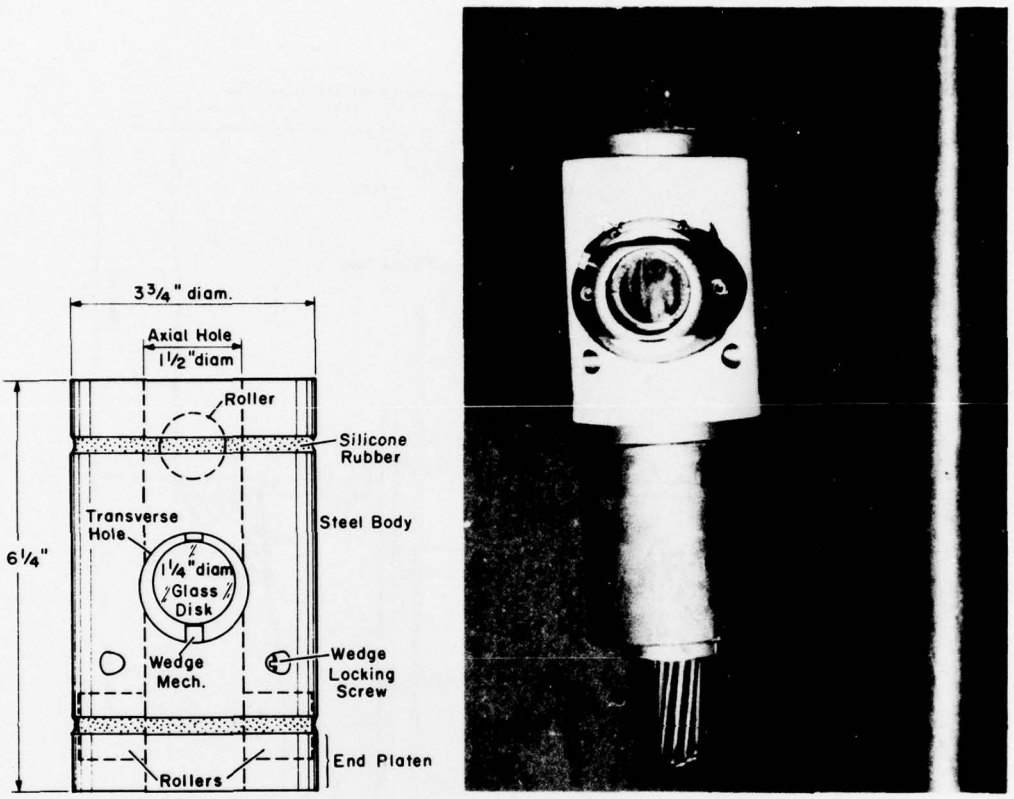

a. Design details. *b. Undergoing tests.*

Figure A21. Photoelastic cable load cell.

a testing machine, to give a clearly identifiable fringe pattern at the required design load. The fringe pattern normally chosen for this purpose is that corresponding to exactly 2 fringes. As soon as the second fringe appears in the disk during stressing of the cable the operator knows that the required cable tension has been reached.

The use of the load cell to accurately pretension the supportive cables of a suspension bridge using this technique is described by Hawkes and Hooper[42] and is illustrated in Figure A21c.

LITERATURE CITED

76. Bannerjee, S.P. (1969) A study of some fundamental factors influencing the occurrence of coal outbursts in mines. Ph.D. Thesis, University of Sheffield.

77. Ergen, I. (1967) Investigation of strata pressures in mines using hydraulic pressure cells. M. Eng. Thesis, University of Sheffield.

78. Fisekci, M.Y. (1965) The determination of strata pressures and support loads in mines. M. Eng. Thesis, University of Sheffield.

79. Hooper J. (1973) Field instrumentation for long term measurement of pile load and raft contact pressure. *Civil Engineering and Public Works Review*, 68, May, p. 438-446.

80. Hooper J. (1973) Observations on the behaviour of a piled-raft foundation on London clay, *Proc. Instn. Civ. Engrs.*, vol. 55 (Dec), p. 855-877.

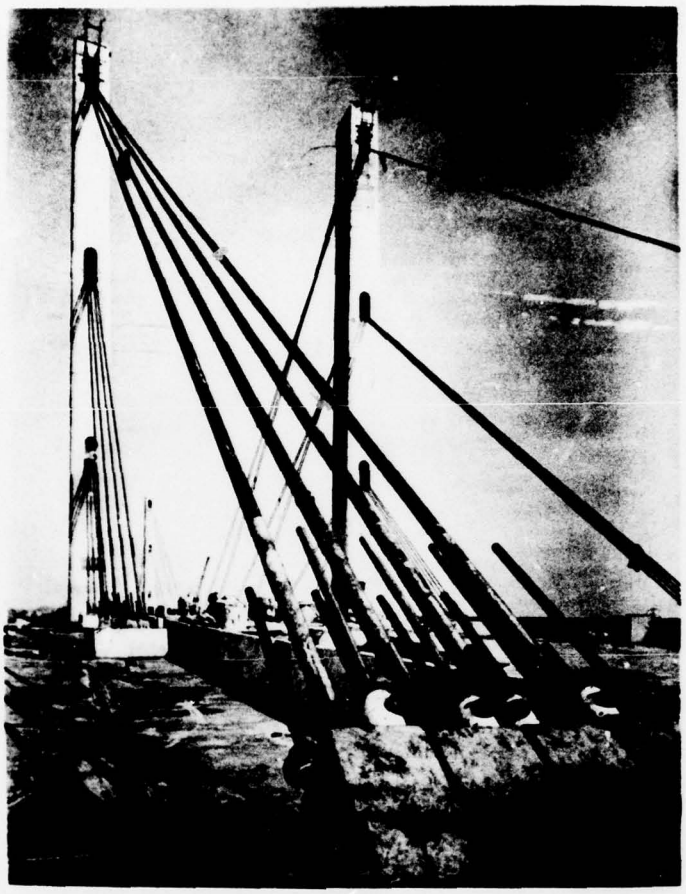

c. Photoelastic load cells in use to tension the cables of a suspension bridge.

Figure A21 (cont'd).

LITERATURE CITED (Cont'd)

81. Miller, T.C. and R. Sporcic (1965) Development of a hydraulic device for measuring relative pressure changes in coal during mining. U.S. Bureau of Mines, RI 6571.

82. Skilton, D. (1968) Determination of stress variations in coal. *Mining Magazine*, Feb., vol. 118, no. 2.

83. Skilton, D. (1966) In-situ stress measurements in mines. M. Eng. Thesis, University of Sheffield.

☆ U. S. GOVERNMENT PRINTING OFFICE: 1979--601-585--87